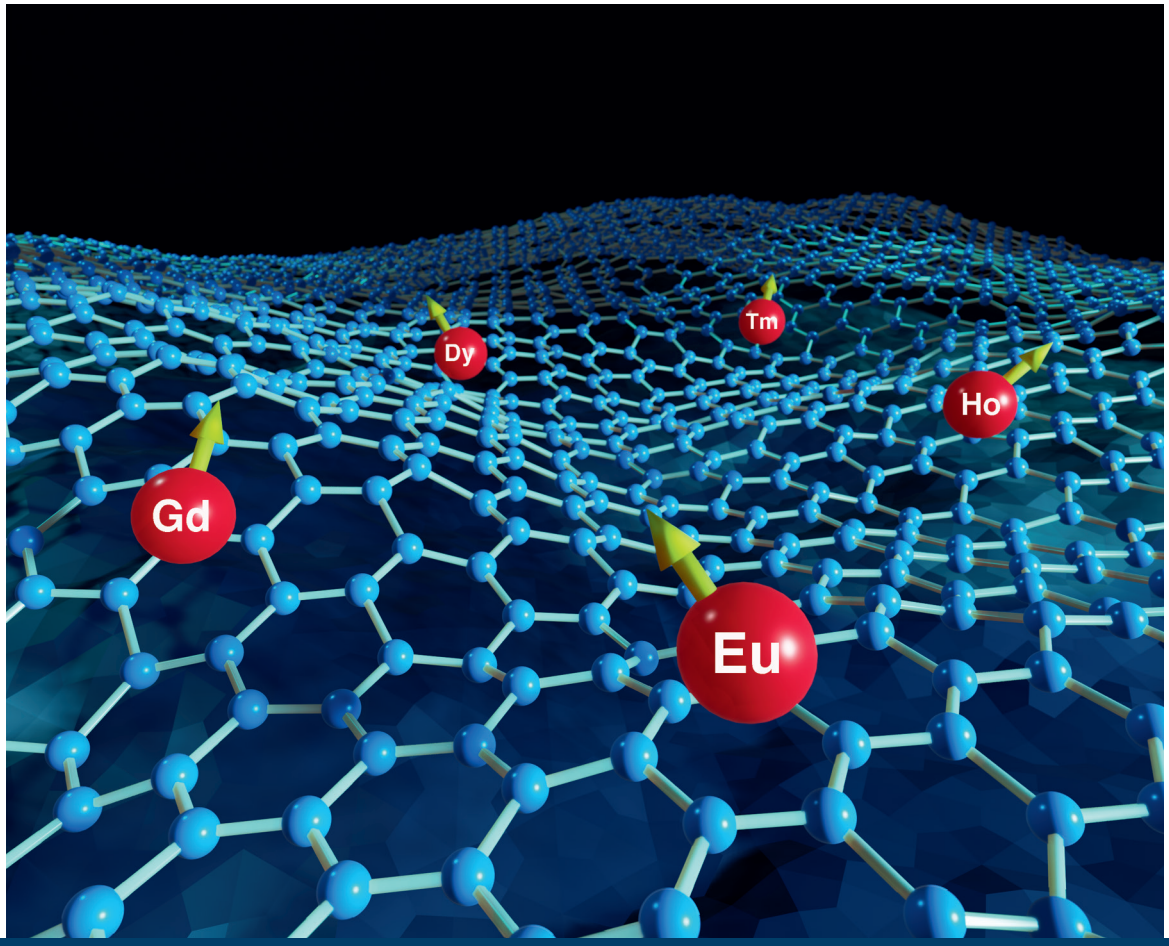

Rare-earth atoms on two-dimensional materials: *ab initio* investigation of magnetic properties

Johanna Paulina Carbone

Schlüsseltechnologien / Key Technologies
Band / Volume 279
ISBN 978-3-95806-740-0

Mitglied der Helmholtz-Gemeinschaft

JÜLICH
Forschungszentrum

Rare-earth atoms on two-dimensional materials: *ab initio* investigation of magnetic properties

Von der Fakultät für Mathematik, Informatik und Naturwissenschaften der RWTH Aachen University zur Erlangung des akademischen Grades einer Doktorin der Naturwissenschaften genehmigte Dissertation

vorgelegt von

Johanna Paulina Carbone, M.Sc.

aus

Düsseldorf, Deutschland

Berichter: Universitätsprofessor Dr. rer. nat. Stefan Blügel

Universitätsprofessor Dr. rer. nat. Markus Morgenstern

Tag der mündlichen Prüfung: 14.12.2023

Forschungszentrum Jülich GmbH
Peter Grünberg Institut (PGI)
Quanten-Theorie der Materialien (PGI-1/IAS-1)

Rare-earth atoms on two-dimensional materials: *ab initio* investigation of magnetic properties

Johanna Paulina Carbone

Schriften des Forschungszentrums Jülich
Reihe Schlüsseltechnologien / Key Technologies Band / Volume 279

ISSN 1866-1807 ISBN 978-3-95806-740-0

Bibliografische Information der Deutschen Nationalbibliothek.
Die Deutsche Nationalbibliothek verzeichnet diese Publikation in der
Deutschen Nationalbibliografie; detaillierte Bibliografische Daten
sind im Internet über http://dnb.d-nb.de abrufbar.

Herausgeber und Vertrieb:	Forschungszentrum Jülich GmbH Zentralbibliothek, Verlag 52425 Jülich Tel.: +49 2461 61-5368 Fax: +49 2461 61-6103 zb-publikation@fz-juelich.de www.fz-juelich.de/zb
Umschlaggestaltung:	Grafische Medien, Forschungszentrum Jülich GmbH
Druck:	Grafische Medien, Forschungszentrum Jülich GmbH
Copyright:	Forschungszentrum Jülich 2024

Schriften des Forschungszentrums Jülich
Reihe Schlüsseltechnologien / Key Technologies, Band / Volume 279

D 82 (Diss. RWTH Aachen University, 2023)

ISSN 1866-1807
ISBN 978-3-95806-740-0

Vollständig frei verfügbar über das Publikationsportal des Forschungszentrums Jülich (JuSER)
unter www.fz-juelich.de/zb/openaccess.

To my mother Regina, my father Carlo, and my brother Giulio

Zusammenfassung

Die Adsorption einzelner magnetischer Atome und atomar dünner magnetischer Schichten auf Oberflächen und zweidimensionalen Materialien bietet eine einzigartige Möglichkeit zur Konstruktion hochkompakter und effizienter Nanostrukturen mit potenziellen Anwendungen in der Spintronik und Spin-Orbitronik. Diese Arbeit verwendet Berechnungen basierend auf der Dichtefunktionaltheorie, um unser Verständnis der Physik der $4f$ Elektronen zu vertiefen, indem sie die wesentlichen Eigenschaften von Seltenerd-Atomen untersucht, die auf zweidimensionale Materialien adsorbiert sind. Diese Untersuchungen liefern wertvolle Erkenntnisse über magnetische Anisotropie und verwandte Phänomene und werfen Licht auf das komplexe Zusammenspiel von Faktoren wie Spin-Bahn-Kopplung, Symmetrie, Kristallfeld und topologischen Merkmalen, welche das beobachtete Verhalten bestimmen. Die vielversprechenden Ergebnisse betonen die Bedeutung einer weiteren Erforschung solcher Systeme, um den gezielten Entwurf und die Anpassung magnetischer Nanostrukturen zu realisieren.

Die Untersuchung beginnt mit der Analyse der Eigenschaften von Seltenerd-Atomen, die auf einer Graphen-Monoschicht adsorbiert sind und sich somit in einem hexagonalen Kristallfeld befinden. Die berechneten elektronischen und magnetischen Eigenschaften sowie die Energieabhängigkeit von der Magnetisierungsrichtung zeigen, dass selbst auf einem strukturell einfachen Material wie Graphen die Energieabhängigkeit stark anisotrop ist und Werte von mehreren meV erreichen kann. Die Berechnung von Multiplett-Aufspaltungen anhand bewerteter Kristallfeldparameter zeigt Unterschiede zwischen ganzzahligen und halbzahligen Spin-Systemen auf. Im ersten Fall treten tunnelgespaltene Zustände auf, während die halbganzzahligen Spin-Systeme durch Symmetrie gegen die Bildung solcher Zustände geschützt sind. Dennoch kann die Quantentunnelung der Magnetisierung in beiden Spin-Systemen stattfinden, angetrieben von verschiedenen Faktoren wie Streuereignissen mit Substrat-Phononen und Leitungselektronen. Insgesamt hängt die magnetische Anisotropie signifikant vom entsprechenden Seltenerd-Atom ab und kann durch Anwendung äußerer mechanischer Spannung als Mittel zur Manipulation modifiziert werden, während die elastischen Eigenschaften von der Magnetisierungsrichtung abhängen. Diese Beobachtungen bieten wertvolle Einblicke in die magnetoelastischen und magnetostrukturellen Eigenschaften der Materialien. Zusätzlich wird die Bedeutung einer präzisen theoretischen Beschreibung der $4f$ Elektronen in einer Diskussion über ihre Orbitalbesetzung betont, da dies erhebliche Auswirkungen auf die magnetischen Anisotropieeigenschaften hat. Eine Konzentrationsreduktion der magnetischen Atome zeigt in der anschließenden Analyse, dass sich die elektronische Struktur verändern kann, was zu neuartigen Eigenschaften, wie der Entstehung von flachen Bändern in der Nähe der Fermi Energie führt.

Das Ziel der Studie besteht außerdem darin, experimentelle Bedingungen realitätsgetreuer in der Simulation nachzubilden, indem sie die Auswirkungen eines metallischen Substrats auf die magnetischen Eigenschaften der Seltenerd- /Graphen-Systeme analysiert. Die Ergebnisse legen nahe, dass die magnetischen Eigenschaften durch das metallische Substrat minimal beeinflusst oder erheblich beeinträchtigt werden können, abhängig von der Entfernung zwischen den Komponenten und den magnetischen Eigenschaften des Substrats selbst. Daher kann die Auswahl des Metallsubstrats sowohl die Untersuchung der inhärenten magnetischen Eigenschaften des zweidimensionalen Seltenerd-Materials ermöglichen als auch die Manipulation dieser Eigenschaften erleichtern.

Abschließend führt die Arbeit Untersuchungen bezüglich Seltenerd-Atomen auf einer Monoschicht eines Übergangsmetall-Dichalkogenid durch, und erweitert damit den wissenschaftlichen Kenntnisstand der potenziellen Szenarien, in denen $4f$ Elektronen interagieren und von verschiedenen Umgebungen beeinflusst werden können. Dieser Abschnitt zeigt, dass eine große magnetische Anisotropie entweder eine hohe oder niedrige Bedeckung des magnetischen Atoms erfordert, abhängig von seiner Chemie und $4f$ Besetzung. Darüber hinaus zeigen die Ergebnisse, dass die spezielle Kombination aus hoher Magnetisierung, starker Spin-Bahn-Kopplung und Symmetrieeigenschaften zur Entstehung nicht-trivialer topologischer Merkmale in der Bandstruktur führen kann. Diese Merkmale vereinen sich zu einer endlichen Berry-Krümmung im reziproken Raum, was vielversprechende Möglichkeiten für die Realisierung anomaler Hall-Plattformen in diesen Systemen bietet.

Abstract

The adsorption of single magnetic atoms and atomic-thin magnetic layers on surfaces and two-dimensional materials presents a unique opportunity for the construction of highly compact and efficient nanostructures, with potential applications in spintronics and spin-orbitronics. This thesis employs density functional theory-based calculations to deepen our understanding of the physics of $4f$ electrons by investigating the essential characteristics of rare-earth atoms adsorbed onto two-dimensional materials. These investigations provide valuable insights into magnetic anisotropy and related phenomena, shedding light on the complex interplay between factors such as spin-orbit coupling, symmetry, crystal field, and topological features that govern observed behaviors. The promising results obtained highlight the importance of further exploration of such systems with the ultimate aim of designing and tailoring magnetic nanostructures.

The analysis begins by examining the properties of rare-earth atoms adsorbed on a graphene monolayer, resulting in them being situated within a hexagonal crystal field. The calculated electronic and magnetic properties, as well as the energy dependence on the magnetization direction, reveal that even on a structurally simple material like graphene, the energy dependence is highly anisotropic and can reach values of several meV. The calculation of multiplet splittings from evaluated crystal field parameters indicates differences between integer and half-integer spin systems. In the former case, tunnel-split states are found, whereas half-integer spin systems are symmetry-protected against the formation of such states. Nevertheless, quantum tunneling of magnetization can take place in both spin systems, driven by various factors like scattering events involving substrate phonons and conduction electrons. Overall, the magnetic anisotropy is found to be significantly dependent on the specific rare-earth atom and can be modified by applying external mechanical strain as a tool for manipulation, while the elastic properties rely on the direction of magnetization. These observations offer valuable insights into the magnetoelastic and magnetostriction properties of the materials. Additionally, the importance of obtaining a precise theoretical description of the $4f$ electrons is emphasized in a discussion on their orbital occupation, as it has a considerable impact on the magnetic anisotropy properties. Upon diluting the magnetic atoms, subsequent analysis demonstrates that the electronic structure can be altered, resulting in the appearance of novel properties such as flat bands in the vicinity of the Fermi energy.

The study also aimed to simulate experimental conditions more accurately by analyzing the impact of a metallic substrate on the magnetic properties of the rare-earth/graphene systems. The findings suggest that the magnetic properties can be minimally influenced or considerably impacted by the metallic substrate, depending on the distance between the components and the magnetic prop-

erties of the substrate itself. Therefore, the selection of the metal substrate can allow for either the examination of the inherent magnetic characteristics of the two-dimensional rare-earth material or facilitate the manipulation of these properties.

Finally, the thesis outlines investigations with regards to rare-earth atoms adsorbed onto a monolayer of transition-metal dichalcogenide, broadening the potential scenarios in which $4f$ electrons can interact and be influenced by different environments. It will be demonstrated that achieving a large magnetic anisotropy requires either a high or low coverage of the magnetic atom, depending on its chemistry and $4f$ occupation. Furthermore, the results reveal that the combination of a large magnetization, strong spin-orbit coupling, and symmetry properties can lead to the emergence of non-trivial topological features in the band structure. These features merge into a finite Berry curvature in reciprocal space, which presents promising opportunities for realizing anomalous Hall platforms in these systems.

Contents

Chapter 1

Introduction

In recent years, there has been an increasing interest in exploring and developing novel two-dimensional (2D) materials with the aim of expanding our fundamental understanding of the underlying physics and advancing practical applications. A broad range of systems has been extensively investigated in the literature, including van der Waals (vdW) materials [1] such as graphene and graphene-like materials (*e.g.*, hexagonal boron nitride [2]), 2D transition metal dichalcogenides (TMDCs) [3] like MoS_2, WS_2, $MoSe_2$, WSe_2, and metal halides [4, 5]. These systems exhibit unique properties arising from intrinsic effects such as spin-orbit coupling, symmetry-related phenomena, electronic correlations, and magnetic interactions, which can be further coupled by stacking different monolayers on top of each other [6–10]. By controlling various factors such as the assembling sequence, chemical composition, and stacking angle, a diverse range of properties can be engineered. For instance, twisting layers can result in incommensurate structures that exhibit unique quantum effects, as demonstrated by several recent studies [11–13]. This leads to the development of novel materials that hold potential for use in the latest generation of electronics, spintronics, and optics devices [14–18]. Moreover, the modulation of properties by varying the constituents of the system enables a comprehensive understanding of the respective roles played by different factors within the system.

Significant progress has also been made in the research area of atomically thin magnetic materials [19, 20] in understanding their intrinsic magnetic properties and manipulation through structure/composition engineering and external stimuli, such as strain, light-induced phenomena, or gating [21–26]. Magnetism can generally emerge in 2D-materials either intrinsically or due to external factors such as vacancies, doping, or strain induction. [27]. Another strategy involves atomic impurities, such as single atoms or molecules deposited on top [28–31], which is similar to constructing vdW heterostructures that exploit the proximity effect. In this context, rare-earth atoms used for this technique could be an intriguing platform to stabilize magnetic phases in 2D.

While the choice of investigating 2D-materials is easily justifiable due to the extensive range of properties and manipulation possibilities they offer, the selection

of rare-earth atoms (or $4f$-atoms) as the magnetic source may raise questions. In these atoms, magnetism arises from the $4f$ electrons, which can generate substantial magnetic moments (both spin and orbital) and possess a high degree of localization, protecting the $4f$ magnetic moment from excessive hybridization effects caused by the surrounding chemical environment that could destabilize the magnetization. Nevertheless, interactions between $4f$ electrons and other electrons can occur through weaker hybridizations, electrostatic interactions, or indirect interactions (via itinerant electrons), enabling the exploitation of their unique properties and leading to extraordinary effects on the environment. Additionally, electron correlation effects are significantly enhanced by the small distance between the $4f$ electrons due to their localization. The electron correlations lead to a multitude of complex properties, one of which is the remarkably large *magnetic anisotropy* observed in rare-earth based systems, which is driven by the large spin-orbit coupling that $4f$ electrons are subject to.

From these considerations, it can be inferred that the exploration of $4f$ electrons is a fascinating choice because of the complexity and richness of the phenomena involved. Theoretical treatments of these electrons pose significant challenges, making it difficult to decipher their effects, but also presenting unique opportunities for scientific exploration. Therefore, despite the challenges, investigating $4f$ electron phenomena holds great promise for advancing our understanding of the fundamental principles governing magnetism in condensed matter systems.

The aim of this study is to investigate through *ab initio* DFT calculations the underlying electronic and magnetic properties of rare-earth atoms on 2D-materials, with a particular focus on the phenomenon of magnetic anisotropy. The magnetic anisotropy arises from the interplay between the geometrical shape of the $4f$ charge cloud and the surrounding chemical environment via spin-orbit coupling. The 2D-substrate plays a fundamental role in generating a specific crystal field around the rare-earth atom, whose symmetry and chemical-physical properties constitute the second key ingredient in the generation of magnetic anisotropy. The present thesis analyzes two different 2D-materials, namely graphene (Gr) and WSe_2, as substrates for the $4f$-atoms.

The choice was based on three considerations: 1) they generate different local symmetries for the $4f$-atom; 2) while graphene represents a case of weak interaction from a chemical perspective, since there is no elemental variety and the Carbon atoms interact with an adsorbed atom only with the perpendicular oriented delocalized π orbitals, WSe_2 involves several types of orbitals in its interaction with the $4f$-atom; 3) graphene is an example of an almost spin-orbit coupling-free 2D-material, thus the effect solely arises from the $4f$-atom, while in WSe_2, the presence of heavy W atoms leads to spin-orbit coupling in addition to that of the rare-earth atom. In this study, the selected 2D-materials will serve as a basis for examining the electronic and magnetic properties induced by $4f$ electrons. The underlying concept involves addressing fundamental questions regarding $4f$ physics when rare-earth atoms are

adsorbed onto various substrate types, and exploring how this knowledge can be leveraged to manipulate magnetic properties in rare-earth based 2D-materials.

Before delving into the technical details about the chapter organization of this thesis, it is pertinent to address a fundamental question that arises: why is magnetic anisotropy significant?

Initially, it should be highlighted that establishing long-range magnetic order in 2D magnets can be challenging at finite temperatures due to the reduced dimensionality, unless the thermal fluctuations can be overcome. This can be achieved for example in 2D systems that possess a sufficiently large magnetic anisotropy [32].

In recent years, the advancement of computation power and data generation has highlighted the need for improved memory capacity in electronic devices. One promising solution for dense data storage is the use of single atoms deposited on 2D-materials or surfaces with large magnetic anisotropies [33]. These magnetic atoms can serve as information carriers, with their magnetization oriented in specific favored directions. The key requirement for stable information storage is magnetic stability, which is associated with large magnetic anisotropy, allowing the unit of information, or bit, to retain its state over long time periods and resist external perturbations, such as temperature fluctuations. At the quantum level, this stability requires long relaxation times for the atom's magnetization, corresponding to magnetic quantum states separated by significant energy gaps in the energy spectrum and protected from quantum tunneling of magnetization. Additionally, to avoid magnetization reversal, the atomic magnet should also be decoupled from the environment to prevent scattering of the spin with electrons and phonons.

In this context, lanthanide atoms have already shown their potential in molecular magnets [34–37], where the $4f$-atom is trapped in a molecular cage made out of specific ligands. Recently, single lanthanide atoms adsorbed on surfaces have demonstrated the ability to maintain their magnetic state, opening the path towards memory units at the atomic scale [38, 39].

This thesis aims to enhance our comprehension of magnetism in $4f$ systems by examining and comparing different rare-earth atoms under various conditions. The following is an overview of the thesis structure:

Chapter 2 of this thesis provides a theoretical overview of rare-earth physics, including electronic properties of isolated atoms and the effects of their adsorption onto a surface. The chapter reviews the concept of magnetic anisotropy and provide an introduction to crystal field theory, including the hexagonal crystal field Hamiltonian and its parameters. The multiplet splittings of $4f$ electrons in a hexagonal crystal field is explained, and the effect of quantum tunneling of magnetization on magnetic stability is discussed. Two spin systems, namely a half-integer spin system ($J = 7/2$) and an integer spin system ($J = 8$), are modeled to illustrate the differences between the two cases. The chapter also presents a method for deriving crystal field parameters of a hexagonal crystal field from the classical magnetic anisotropy constants, which can be computed from *ab initio* DFT calculations.

Chapter 3 offers insights into the main motivations behind the choice of the current research topic. This is accomplished by briefly reviewing the pioneering works from the literature and discussing the potential applications of $4f$-atoms on 2D-materials in the fields of magnetic bits and anomalous Hall conductors.

Chapter 4 explores the intricacies of a many-electron system, presenting the requisite theoretical groundwork for Density Functional Theory (DFT) and its extension through the Hubbard model within the DFT+U framework. These methods are necessary to enhance the description of $4f$ electrons, as exemplified in the case of Gd/Gr. The chapter concludes with an explanation of the theoretical background of the Full-Potential Linearized Augmented Plane-Wave method (FLAPW), which is implemented in the FLEUR code used for all calculations throughout the thesis.

Chapter 5 starts the analysis of the results obtained in the context of $4f$-atoms on a graphene monolayer. Firstly, the electronic and adsorption properties are examined, followed by an exploration of the magnetic properties, with a particular emphasis on magnetic anisotropy and a comparison between various rare-earth atoms. The systems under investigation include Eu and Gd, which are representatives of half-filled $4f$-shells, as well as Dy, Ho, and Tm, which are representatives of open $4f$-shells with stronger spin-orbit coupling effects. Subsequently, the discussion shifts to the computed multiplet splittings in the open $4f$-shell systems, which were obtained through the calculation of crystal field parameters based on the magnetic anisotropy constants. Additionally, it is demonstrated that the magnetic anisotropy can be engineered not only by changing the $4f$-atom but also by mechanical deformation. Consequently, the magnetic anisotropy behavior as a function of external strain is examined, allowing for the extraction of elastic force constants and vibrational frequencies of the graphene complexes.
The chapter provides an overview of the impact of Hubbard U on the computed

magnetic anisotropy and highlights the challenges when simulating such systems in the DFT+U framework. Furthermore, significant emphasis is given to the importance of accurate U values, thereby increasing awareness of the need for precision.
Further investigation of Dy/Gr includes a comparison between magnetic anisotropy in the Hund's rule $4f$ occupation and a non-Hund's rule occupation to illustrate the competition between crystal field effects and the intra-atomic exchange interaction. This section emphasizes once more the importance of accurately describing the $4f$ electrons, as it greatly affects the magnetic anisotropy properties.
Finally, the chapter concludes by examining the impact of rare-earth atom coverage (concentration on the graphene sheet), briefly exploring the electronic properties of a large simulation cell that corresponds to the isolated atomic limit of the $4f$-atoms.

Chapter 6 aims to establish a preliminary comprehension of how a metallic substrate can affect the magnetic anisotropy of Gd/Gr. The investigation focuses on two scenarios: the first involves a non-magnetic surface, while the second scenario involves a magnetic surface, in the Gd/Gr/Ir(111) and Gd/Gr/Co(111) systems, respectively.

Chapter 7 delves into the effects of $4f$-atoms adsorbed on a WSe_2 monolayer and aims to investigate the electronic and magnetic properties of Eu/WSe_2 while exploring the possibility of engineering spin and orbital properties for use as a platform for magnetotransport phenomena. The study commences with a high coverage situation of Eu atoms on the 2D-material, which creates sufficient proximity effects to generate prominent spin-orbit coupling effects, magnetic anisotropy, and stable ferromagnetism. These properties allow for the observation of anomalous Hall conductivity resulting from the tailored Berry curvature in the system. The impact of reducing the Eu coverage is then analyzed by simulating larger periodic cells.

Chapter 8 presents an analysis of the electronic and magnetic properties of Gd and Ho atoms on WSe_2. Gd is examined as an example of a different chemical behavior than Eu, while Ho is considered as an instance of an open $4f$-shell. This chapter discusses the impact of these two properties on magnetic anisotropy and spin-orbital properties in comparison with the previously studied Eu atom, both in high and low coverage scenarios on the 2D-material. Based on these observations, the chapter provides final considerations that could facilitate the manipulation of magnetic anisotropy through the $4f$-atom's nature and its coverage on the 2D-material in the future.

Chapter 9 concludes the comprehensive investigation of rare-earth atoms on 2D-materials, summarizing the key findings and insights gained.

Chapter 2

Magnetism of $4f$-atoms on 2D-materials

The following sections provide a comprehensive examination of rare-earth magnetism, starting with the electronic properties of individual rare-earth atoms and how they are affected by adsorption onto surfaces and 2D-materials. Crystal field theory is introduced to establish its connection to magnetic anisotropy, and subsequently utilized to model the influence of a hexagonal crystal field on systems with both integer and half-integer spins. Lastly, the chapter illustrates the process of determining crystal field parameters using the classical magnetic anisotropy energy functional. This method is later applied in Chapter 5 to DFT calculations of rare-earth atoms on graphene.

2.1 General aspects of electronic properties of rare-earth atoms

Magnetism is a property that arises in atoms characterized by unfilled (or "open") electron shells *i.e.* in presence of unpaired electron spins in specific orbitals. Orbital filling is determined by the simultaneous action of the classical repulsive Coulomb interaction between pairs of electrons and the pure quantum mechanical exchange interaction acting between electrons with parallel spins. The latter is a consequence of the identical nature of electrons and specifically of their classification as fermionic particles with half-integer spin. Hence, considering a many-body system of electrons, the respective wave function is antisymmetric with respect to the exchange of two particles, leading to the well known Pauli exclusion principle which prohibits two electrons to occupy the same state while having the same spin.

Unpaired electrons in atoms cause an imbalance in the spin density pointing in one direction compared to the spin density pointing in the opposite direction, generating thus a magnetic moment which in turn can spin-polarize the structures they are part of and/or interact with magnetic moments arising from other atoms in the sys-

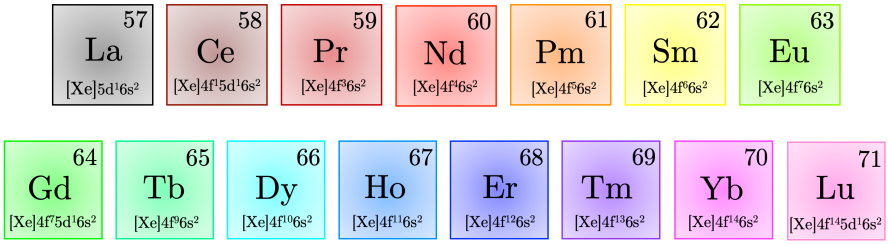

Figure 2.1: The lanthanide series: with increasing Z the $4f$-shell is filled and four exceptions present d valence electrons in the atomic limit, namely La, Ce, Gd and Lu.

tem, leading to a variety of magnetic phenomena exploitable in technological devices. In this perspective, rare-earth (RE) atoms are extraordinarily appealing due to the sequential filling of the $4f$-shell along the series, being the unpaired $4f$ electrons the source of large magnetic moments. Furthermore, rare-earths are heavy elements characterized by strong spin-orbit coupling (SOC), which plays a primary role in determining peculiar features in the electronic structure of some materials and is often strictly associated to a broad and heterogeneous spectrum of complex yet fascinating electronic and magnetic phenomena. For a more detailed discussion about SOC in rare-earths, see section 2.2.

Fig. 2.1 illustrates the lanthanide series with increasing atomic number Z and shows the electronic configuration for each element in the series. In general, lanthanides have electronic configuration $[\mathrm{Xe}]6s^2 4f^n$ with exception of La, Ce, Gd and Lu that tend to place one electron in the $5d$ orbital in order to get an empty, half-filled or completely filled $4f$-shell. Starting with Lanthanium, the $[\mathrm{Xe}]6s^2 5d^1$ configuration is favored with respect to the $5d^0 4f^1$, leading thus to a $4f^0$ state. However, as the atomic number increases, the $4f$ orbitals become more stable compared to the $5d$ orbitals due to their high penetration into the core. This leads to the additional electron in Ce occupying the $4f$-subshell, also driven by the stabilization gained when the spins of the $5d$ and $4f$ electrons are aligned. Subsequently, the $4f$-shell is gradually filled up through the series and the lanthanides have electronic configuration $[\mathrm{Xe}]6s^2 4f^n 5d^0$, $\mathrm{n} = 3-7$. At $Z = 63$, namely Eu, the $4f$-shell is half-filled and the following electron in Gd occupies the $5d$ orbital maintaining a half-filled $4f$-shell, $[\mathrm{Xe}]6s^2 4f^7 5d^1$. Nevertheless, with Tb the energy equation involving the interaction with other electrons and the nuclear charge, favors the displacement of the $5d$ electron into the $4f$-shell and the addition of the new electron into the same shell. Hence, the next elements present again a sequential filling of the $4f$ orbitals which leads to configurations $[\mathrm{Xe}]6s^2 4f^n 5d^0$ with $n = 9-14$ until $Z = 70$. Finally, Lu places the last electron inside of the $5d$ orbitals, being all the $4f$ states occupied.

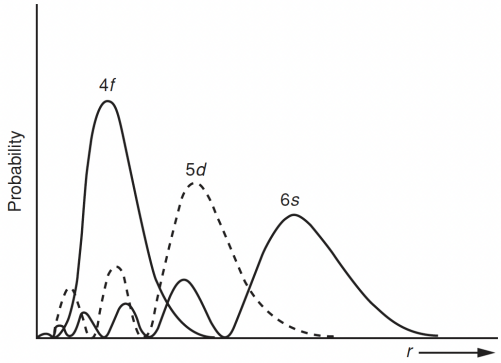

Figure 2.2: Hydrogenic squared radial wave functions for the $4f$, $5d$ and $6s$ orbitals of cerium, plotted as the probability to find an electron at distance r from the nucleus. (after [41, 42]).

The unfilled $4f$-shells in rare-earths are responsible for magnetic and spectroscopic properties of the compounds they are part of, while they are mostly not involved in chemical processes because of their localized nature. Instead, the chemical properties of rare-earth materials are determined by valence orbitals that are more extended in space (*e.g.* $6s$ and $5d$), and hence can hybridize with surrounding electrons of different species. In order to properly understand the electronic and magnetic properties of the RE-based 2D-materials that are investigated in this thesis, it is necessary to have a closer look at the wave functions describing the $4f$ electrons inside of single RE atoms. Considering a RE atom with atomic number Z, the respective non-relativistic Hamiltonian reads as [40]

$$\mathcal{H} = \sum_{i}^{Z}\left[-\frac{\hbar^2}{2m}\nabla_i^2 - \frac{Ze^2}{r_i}\right] + \frac{1}{2}\sum_{ij}^{Z}\frac{e^2}{|\boldsymbol{r_i} - \boldsymbol{r_j}|}, \tag{2.1}$$

where the first term describes the kinetic energy of the electrons, the second term corresponds to the attractive potential energy of the electron in the field of the positive charged nucleus, and the last term determines the electrostatic repulsion between pairs of electrons. Solving the corresponding Schrödinger equation

$$\mathcal{H}\Psi = E\Psi \tag{2.2}$$

gives the atomic eigenstates Ψ and energies E. Nevertheless, the solution to this eigenvalue problem presents difficulties associated to an accurate computation of all inter-electronic interactions in multi-electron systems and a variety of numerical procedures, including post-Hartree Fock [43] and DFT [44–46] methods have been developed in order to account, within limits, for the last term in Eq. (2.1). A brief overview will be provided here, with more details discussed in Chapter 4.

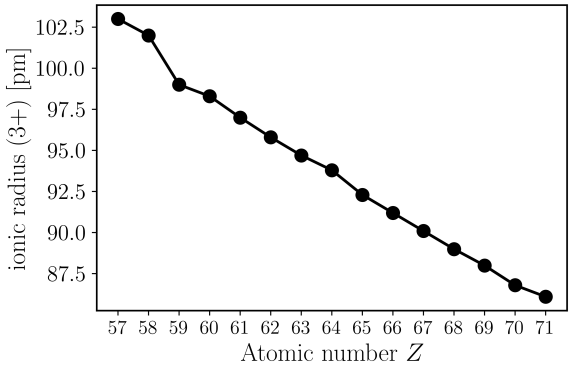

Figure 2.3: Ionic radius (for the Ln^{3+} state) as a function of the atomic number Z depicting the lanthanide contraction.

One way to simplify the problem is by replacing the electron-electron interaction with an effective potential that is experienced by each electron, effectively reducing the many-body problem into multiple single-particle problems. Taking into account the fermionic nature of electrons, the total eigenfunction Ψ can then be expressed as an antisymmetric wave function in the form of a Slater determinant:

$$\Psi(q_1, q_2, ..., q_N) = \frac{1}{\sqrt{N!}} \begin{vmatrix} \phi_1(q_1) & \phi_2(q_1) & \cdots & \phi_N(q_1) \\ \phi_1(q_2) & \phi_2(q_2) & \cdots & \phi_N(q_2) \\ \vdots & \vdots & \ddots & \vdots \\ \phi_1(q_N) & \phi_2(q_N) & \cdots & \phi_N(q_N) \end{vmatrix}. \tag{2.3}$$

Here, the coordinates q_i involve both spatial and spin coordinates, and N is the total number of electrons. Moreover, being the atomic potential rotationally-invariant, it is possible to express each single-electron function ϕ as a product of a radial function $R_{nl}(r)$, a spherical harmonic $Y_{lm}(\theta, \varphi)$ and a spin function χ_{m_s}, to construct a *spin-orbital*

$$\phi(q) = R_{nl}(r) Y_{lm}(\theta, \varphi) \chi_{m_s}, \tag{2.4}$$

where n is the principal quantum number, l is the angular momentum quantum number, m is the magnetic quantum number, and m_s corresponds to the spin of the electron. The single-particle eigenvalue problem becomes separable, and the radial function is solution of the radial Schrödinger equation,

$$\left[-\frac{\hbar^2}{2m} \frac{d^2}{dr^2} + \frac{\hbar l(l+1)}{2mr^2} + V(r) \right] r R_{nl}(r) = E r R_{nl}(r). \tag{2.5}$$

Fig. 2.2 illustrates the radial part of Eq. (2.4) for the $4f$, $5d$ and $6s$ orbitals of Ce in terms of probability of finding an electron, calculated as $4\pi r^2 R_{nl}^2$ at a distance r

from the nucleus. This permits to understand why $4f$ electrons play a limited role in chemical bonding, as they are spatially deep embedded within the atom compared to the more widely spread $5d$ and $6s$ valence electrons [42].

This high penetration of the $4f$ orbitals is also responsible for the *lanthanide contraction*, which consists in a decreasing atomic (and ionic) radius of the elements with increasing atomic number Z. This trend is illustrated in Fig. 2.3 for the ionic radii of the oxidation state Ln^{3+} of the lanthanides and is due to an incomplete shielding of the $n = 5, 6$ valence electrons by the penetrating $4f$ electrons from the increasing positive nuclear charge when protons are added along the series.

Coming back to Eq. (2.4), the spherical harmonics $Y_{lm}(\theta, \varphi)$ are solution of the angular Schrödinger equation,

$$\left[\frac{1}{\sin\theta}\frac{\partial}{\partial\theta}\left(\sin\theta\frac{\partial}{\partial\theta}\right) + \frac{1}{\sin^2\theta}\frac{\partial^2}{\partial\varphi^2}\right] Y_l^m(\theta,\varphi) = -l(l+1)Y_l^m(\theta,\varphi), \tag{2.6}$$

and are eigenfunctions of the the angular momentum operator $\boldsymbol{L}$ and its z component $\boldsymbol{L}_z$:

$$\boldsymbol{L}^2 Y_l^m(\theta,\varphi) = \hbar^2 l(l+1) Y_l^m(\theta,\varphi) \tag{2.7}$$

$$\boldsymbol{L}_z Y_l^m(\theta,\varphi) = \hbar m Y_l^m(\theta,\varphi), \tag{2.8}$$

where, $l = 0, ..., n-1$ and $m = -l, ..., l$. The spherical harmonics can be expressed in

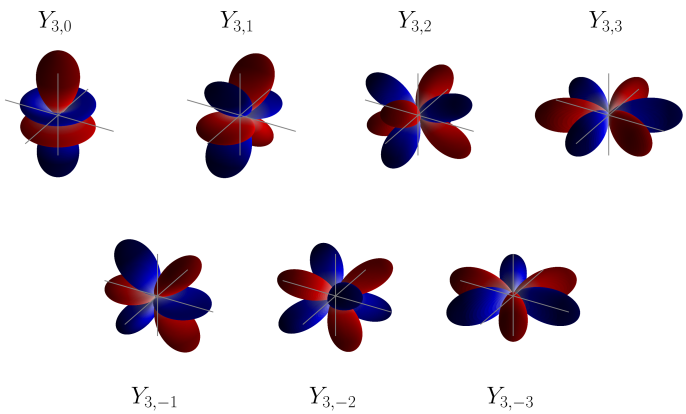

Figure 2.4: The $4f$ wave functions exhibit angular dependence, which can be described by spherical harmonics with a quantum number $l = 3$, and varying magnetic quantum number m. The positive values are depicted in red, while the negative values are shown in blue.

terms of associated Legendre polynomials $P_l^m(\cos\theta)$,

$$Y_l^m(\theta,\varphi) = (-1)^m \sqrt{\frac{(2l+1)(l-m)!}{4\pi(l+m)}} P_l^m(\cos\theta) e^{im\varphi}, \tag{2.9}$$

with

$$Y_l^{-m}(\theta,\varphi) = Y_l^{m*}(\theta,\varphi). \tag{2.10}$$

This equation gives the general shape of the orbitals *i.e.*, if squared, the angular probability to find the electron based on the quantum numbers l and m. Concerning the $4f$ orbitals, $l = 3$ and m assumes integer values $-l \leq m \leq l$. This combination of (l, m) generates highly anisotropic angular wave functions, as illustrated in Fig. 2.4, and play an important role in the determination of magnetic properties of materials involving REs.

Finally, the radial and angular parts in the single-particle wave functions, are multiplied by the spin function χ_{m_s} which is the eigenfunction of the spin operators $\boldsymbol{S}^2$ and $\boldsymbol{S}_z$

$$\boldsymbol{S}^2 \chi_{m_s} = \hbar^2 s(s+1) \chi_{m_s} \tag{2.11}$$

$$\boldsymbol{S}_z \chi_{m_s} = \hbar m_s \chi_{m_s} \tag{2.12}$$

with $s = 1/2$ and $m_s = \pm 1/2$.

2.2 Spin-orbit coupling

The spin-orbit coupling, which refers to the interaction between the magnetic field created by the electron's motion through an electric field and the electron spin, plays a crucial role in determining the energy spectrum of the $4f$ states in RE atoms and materials. As a result, it has a significant impact on their electronic and magnetic properties. It is well known that SOC manifests in lifting the spin degeneracies in atoms and solids, and can be formally derived by introducing a relativistic correction in the Schrödinger equation. This is done by considering the Dirac equation whose solution naturally includes the spin of the electron and its relativistic nature. The spin-dependent term in the relativistic Hamiltonian is the cause of spin-splitting of the otherwise double-degenerate spin-up and spin-down bands in solids. For an electron moving through an electric field $\boldsymbol{E}$ with momentum $\boldsymbol{p}$, the spin-orbit Hamiltonian can be written as

$$\mathcal{H}_{\mathcal{SO}} = -\frac{e\hbar}{(2mc)^2}\boldsymbol{\sigma}\cdot(\boldsymbol{E}\times\boldsymbol{p}) = -\frac{\mu_{\mathrm{B}}}{2}\boldsymbol{\sigma}\cdot\left(\frac{1}{c}\boldsymbol{E}\times\boldsymbol{v}\right) = -\frac{\mu_{\mathrm{B}}}{2}\boldsymbol{\sigma}\cdot\boldsymbol{B} \tag{2.13}$$

where e and m are the electron charge and mass, $\mu_{\mathrm{B}} = e\hbar/2mc$ is the Bohr magneton, and the spin of the electron is $\boldsymbol{\sigma} = 2\boldsymbol{S}/\hbar$, with $\boldsymbol{S}$ the spin angular momentum. Eq. (2.13) describes the interaction of the magnetic moment of the electron spin with the magnetic field arising from the orbital motion of the particle itself in an external potential. In the case of the orbital motion of an electron in an atom, we consider an electric field generated by the positive charge of the nucleus *i.e.* the potential is spherically symmetric. In the reference system of the moving electron, it experiences a magnetic field $\boldsymbol{B} = \frac{1}{c}(\boldsymbol{E}\times\boldsymbol{v})$ emerging from the Lorentz-transformed electric field (the electron perceives a dynamical positively-charged background), which will interact with the electron spin. In this situation, Eq. (2.13) rewrites as

$$\mathcal{H}_{\mathcal{SO}} = \frac{\hbar}{4m^2c^2}\frac{1}{r}\frac{dV}{dr}\boldsymbol{\sigma}\cdot(\boldsymbol{r}\times\boldsymbol{p}) = \frac{\hbar}{4m^2c^2}\frac{1}{r}\frac{dV}{dr}\boldsymbol{\sigma}\cdot\boldsymbol{l} = \xi\boldsymbol{\sigma}\cdot\boldsymbol{l}. \tag{2.14}$$

Here, ξ is the spin-orbit coupling constant and $\boldsymbol{l}$ is the orbital angular momentum that aligns antiparallel to the spin of the electron. In the vicinity of the atomic nucleus, the potential V in Eq. (2.14) exhibits a Coulomb-like shape $V \sim -\frac{Z}{r}$, where Z represents the atomic number. Consequently, the derivative of the potential is proportional to the atomic number Z, and it decreases as the distance from the nucleus increases. As a result, the spin-orbit coupling constant ξ is expected to have larger values for heavy elements and for electrons that are closer to the core. The additional interaction energy described by $\mathcal{H}_{\mathcal{SO}}$ can often be treated as a perturbation to the non-relativistic Hamiltonian, allowing to determine the energy corrections and the respective split spectrum.

2.2.1 LS coupling scheme

In multi-electron atoms, the Aufbau principle can be exploited to obtain the ground state electronic configuration in terms of shells, defined by the principal quantum

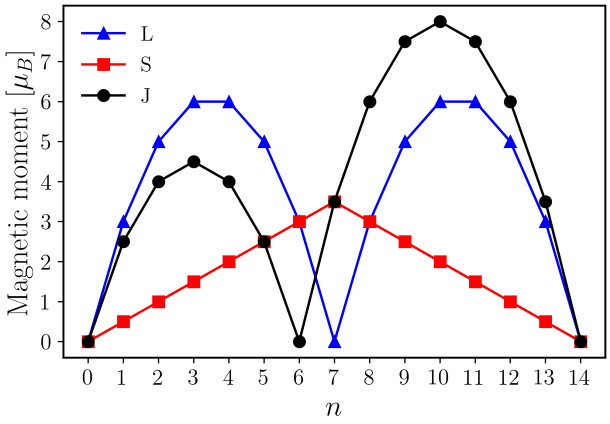

Figure 2.5: The total orbital angular momentum L, the total spin angular momentum S and the total angular momentum J as a function of the number n of $4f$ electrons in the Ln^{3+} state in lanthanides. The trend follows Hund's rules.

number n, and subshells defined by l (s,p,d,f,...). Nevertheless, in order to determine properties such as the the magnetic moment of an atom, it is necessary to take into consideration the fact that each electron in a subshell carries an orbital moment and a spin moment, and there are multiple approaches of combining these angular moments in a many-electron system. Hence, the overall challenge is to identify the lowest-energy state in a pool of different electronic state occupations for a given configuration. In order to find the solution, it is necessary to account for distinct interactions acting on and between electrons such as the electrostatic contributions from the nucleus and other electrons, exchange interactions and SOC. If SOC is relatively weak compared to the inter-electronic Coulomb interaction, then the Coulomb interaction first couples the individual orbital moments $\boldsymbol{l}_i$ and spin moments $\boldsymbol{s}_i$ of the electrons generating the total orbital angular momentum $\boldsymbol{L}$ and the total spin angular momentum $\boldsymbol{S}$:

$$\boldsymbol{L} = \sum_i \boldsymbol{l}_i, \quad \boldsymbol{S} = \sum_i \boldsymbol{s}_i, \tag{2.15}$$

with quantum numbers L and S. This coupling scheme is known as the *Russell-Saunders coupling* and is usually adopted for RE atoms. We define the z-components of the angular moments as $\boldsymbol{L}_z$ and $\boldsymbol{S}_z$, and the respective quantum numbers $M_L = \sum_i m_i$ ($-L \leq M_L \leq +L$) and $M_S = \sum_i m_{s_i}$ ($-S \leq M_S \leq +S$). Then SOC couples $\boldsymbol{L}$ and $\boldsymbol{S}$ to form the total angular momentum $\boldsymbol{J} = \boldsymbol{L} + \boldsymbol{S}$, and acts as a perturbation inducing further splitting of the energy levels, which are labeled by the quantum number J that assumes values $|L - S| \leq J \leq L + S$. The spectroscopic term is a label used to identify the atomic states based on the quantum numbers (LSJ), and writes as ${}^{2S+1}L_J$. The

different values of $L = 0, 1, 2, 3$ are conventionally addressed as S, P, D, F, and the spin multiplicity, given by $2S + 1$, reflects the number of possible J states for given values of L and S. The term symbol corresponding to the ground state can be determined following Hund's rules which summarize as [47–49]:

Hund's rules

- For a given electron configuration, the term with maximum spin multiplicity $(2S + 1)$ has the lowest energy.
- For a given multiplicity, the term with the largest value of the total orbital angular momentum quantum number L has the lowest energy.
- For a given term, in an atom with outermost subshell half-filled or less, the level with the lowest value of the total angular momentum quantum number J lies lowest in energy. If the outermost shell is more than half-filled, the level with the largest value of J will be the one with the lowest energy.

Fig. 2.5 illustrates the trends of L, S and J for the $4f^n$ configurations in the Ln^{3+} oxidation state along the lanthanide series.

By writing the multi-electron Hamiltonian as a spherical symmetric term and a perturbation,

$$\mathcal{H} = \mathcal{H}_0 + \mathcal{H}_{SO} = \mathcal{H}_0 + \xi \boldsymbol{L} \cdot \boldsymbol{S}, \tag{2.16}$$

it is easy to show the symmetries of $\mathcal{H}$, based on the commutation relations:

$$[\boldsymbol{L}_i, \boldsymbol{L}_j] = i\hbar\epsilon_{ijk}\boldsymbol{L}_k \quad [\boldsymbol{S}_i, \boldsymbol{S}_j] = i\hbar\epsilon_{ijk}\boldsymbol{S}_k \quad [\boldsymbol{L}^2, \boldsymbol{L}_j] = 0 \quad [\boldsymbol{S}^2, \boldsymbol{S}_j] = 0, \tag{2.17}$$

where ϵ_{ijk} is the Levi-Civita symbol. Indeed, $\mathcal{H}_{SO}$ does not commute with $\boldsymbol{L}_z$ and $\boldsymbol{S}_z$ and hence, the two z-components are not conserved quantities, and M_L and M_S are no longer good quantum numbers. Instead, $\mathcal{H}_{SO}$ commutes with $\boldsymbol{L^2}$, $\boldsymbol{S^2}$, $\boldsymbol{J^2}$ and $\boldsymbol{J}_z$ (z-component of $\boldsymbol{J}$) and their simultaneous eigenstates are classified by the quantum numbers J, L, S, J and J_z.

The magnetic moment of an atom can then be evaluated as [50]

$$\boldsymbol{m} = -\mu_B(g_L\boldsymbol{L} + g_S\boldsymbol{S}) = -\mu_B g_J \boldsymbol{J}, \tag{2.18}$$

where μ_B represents the Bohr magneton, $g_L = 1$ and $g_S \sim 2$ denote the orbital and spin g-factors respectively, and g_J refers to the total angular momentum g-factor. Moreover, atoms with $J \neq 0$ are characterized by a $(2J + 1)$-fold degenerate ground state, in which states are labeled by the quantum number J_z. The J_z states can be further split by breaking the spherical symmetry *e.g.* in a crystal field whose symmetry is dictated by the spatial arrangement of the constituent atoms.

2.3 Rare-earths atoms on surfaces

So far, only isolated RE atoms have been considered, for which each J energy level presents a $(2J+1)$-fold degeneracy of J_z states due to the rotational invariance of the atomic Hamiltonian with point symmetry $\mathcal{O}(3)$. Nevertheless, the present work deals with single RE atoms adsorbed on top of two-dimensional layers of different materials, where the underlying surface induces a symmetry breaking of the atomic states. When an atom is deposited on a surface, it experiences an electric field produced by the surrounding atomic charges, known as the crystal field (CF). The effect of the CF is a lowering of the spherical symmetry of the embedded atomic potential, and the new symmetry is dictated by the spatial arrangement of the neighboring atoms defining the surface, or in other words, by the chemical environment.
Examples of two different local crystal field symmetries are shown in Fig. 2.6, which depicts the two main situations that have been investigated throughout this work: a hexagonal C_{6v} and a trigonal C_{3v} crystal field. The C_{6v} point symmetry is characterized by 6 nearest neighbors located at the vertices of a hexagon, and hence related by rotations of 60° around the main rotation axis, while in the C_{3v} site the adatom is located at the center of two inequivalent triangles such that a rotation of 120° is needed to leave the system unaltered. These kind of atomic arrangements are found in several 2D-crystal structures, *e.g.* graphene-like structures [51–53] and transition metal dichalcogenides (TMDCs) [54, 55] and it will be shown that the symmetry of the CF plays an important role in determining the magnetic properties of the adsorbed RE atoms. For example, due to the interplay between large spin and orbital magnetic moments that lead to strong SOC and the interaction with the CF, the 4f electrons of a RE atom on top of a surface can exhibit prominent magnetic anisotropies.

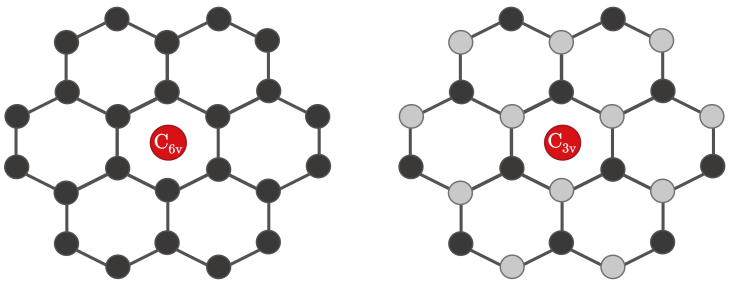

Figure 2.6: C_{6v} crystal field (left) and C_{3v} crystal field (right). Both symmetries exhibit a hexagonal arrangement of atoms, but in the C_{6v} case, the atoms in the 2D-material belong to the same chemical species (similar to graphene), while in the C_{3v} case, the central RE atom is surrounded by two different atom species.

2.3.1 Magnetic anisotropy

The magnetic anisotropy (MA) is a property of a system that describes the dependence of its magnetic properties on the direction of measurement. Samples that exhibit magnetic anisotropy are more easily magnetized along a specific direction, meaning that the magnetic anisotropy energy (MAE) represents the energy required to deflect the magnetization from the preferred direction. The latter is called the *easy-axis* and defines the direction of spontaneous magnetization *i.e.* the energetically most favored magnetic state, while the most unfavored direction is referred to as *hard-axis*. The phenomenon can be classified based on different sources:

Magnetocrystalline anisotropy is an intrinsic source of MA originating from the interaction between the local non-spherical charge cloud of the magnetic atom with the crystal field. The effect is driven by spin-orbit interaction. Closely related to the magnetocrystalline anisotropy is the *magnetoelastic anisotropy*, as it describes the change in magnetic properties of a material in response to external stress. This phenomenon arises due to the deformation of the crystal field surrounding magnetic atoms under stress, altering the interaction of the charge cloud with the surrounding environment.

Shape anisotropy is observed in non-spherical samples due to the demagnetizing field varying based on the direction, resulting in an easy-axis for the magnetization.

Exchange anisotropy is driven by the magnetic interaction that occurs at the interface between two distinct magnetically ordered layers, such as a ferromagnet and an antiferromagnet.

The following discussion will provide a more detailed exploration of both magnetocrystalline and magnetoelastic anisotropy.

2.3.1.1 Magnetocrystalline anisotropy (MCA)

When a RE atom is deposited on a 2D-material, the $4f$ charge will experience the CF generated by the nearest surface charges. For most of the lanthanides the $4f$ charge distribution is characterized by a non-spherical geometry due to the large angular moment $\boldsymbol{L}$ which is coupled through SOC to the large spin magnetic moment arising from unpaired $4f$ electrons. As a result, the orientation of the magnetic moment of the RE atom affects the interaction between the $4f$ charge distribution and the surrounding point charges in the crystal field.

When the magnetic moment is rotated, the $4f$ charge cloud will also rotate, leading to either a stronger or weaker electrostatic interaction with the crystal field, depending on whether the $4f$ distribution is oriented more towards or away from the surrounding point charges. This process translates into an angular dependence of the total energy of the system upon rotation of the magnetization. Exceptions are Eu and Gd for

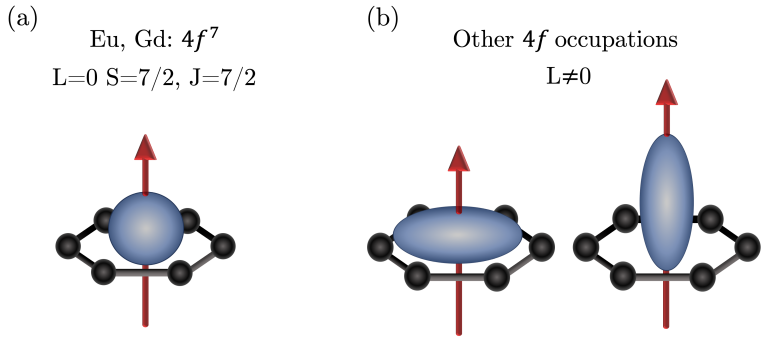

Figure 2.7: (a) In Eu and Gd the half-filed 4f-shell produces vanishing values of $\boldsymbol{L}$ reflecting in a spherical shape of the 4f charge distribution. (b) For other 4f occupations, the total orbital angular momentum is non-zero leading to oblate or prolate-like geometries of the 4f cloud which interact differently with the surrounding CF based on their orientation.

which the half-filled $4f^7$ shell leads to a vanishing $\boldsymbol{L}$, which reflects in an isotropic 4f charge cloud (See Fig. 2.7). Therefore, in these cases the magnetocrystalline anisotropy is expected to give only small contributions arising from the intra-atomic spin-orbit interaction. From these considerations, the MCA can be reduced to two key ingredients: the geometry of the 4f charge distribution and the symmetry of the CF.

The classical energy functional, $E_{an}(\theta,\varphi)$, describing how the total energy changes as a function of the magnetization direction, is written as a series of powers of the direction cosines of the magnetization vector, where only even powers are permitted because of the invariance of the anisotropy energy under time-reversal symmetry [56]. Moreover, the number of terms in the expansion depends on the specific crystallographic point-group. For example, for a *trigonal* symmetry the anisotropy energy is [57]

C_{3v} symmetry

$$\begin{aligned} E_{an}(\theta,\varphi) =& K_1 \sin^2\theta + K_2 \sin^4\theta + K_2' \sin^3\theta\cos\theta\cos(3\varphi) + K_3 \sin^6\theta \\ &+ K_4 \sin^6\theta\cos(6\varphi) + K_5 \sin^3\theta\cos^3\theta\cos(3\varphi), \end{aligned} \tag{2.19}$$

whereas for *hexagonal* symmetries $K_2' = K_5 = 0$, hence it reduces to

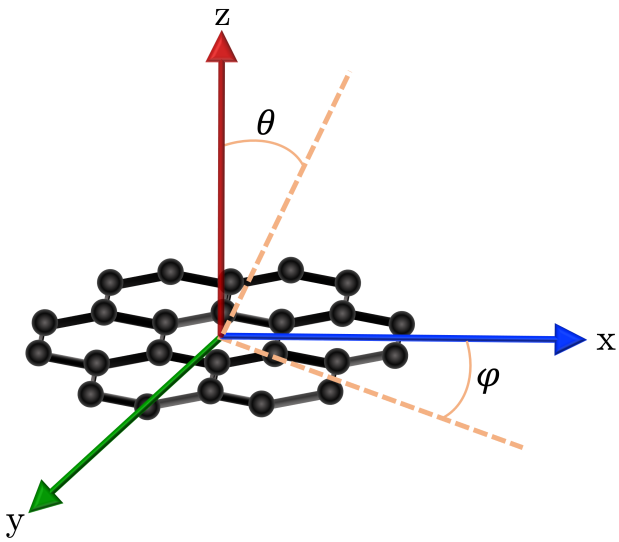

Figure 2.8: Coordinate system adopted in the investigation of MAE of RE atoms on 2D-materials: θ is the polar angle describing magnetization rotations from the z-axis towards the substrate plane; φ corresponds to the angle from the x-axis and relates to rotations of the magnetization in the plane of the 2D-material.

C_{6v} symmetry

$$E_{an}(\theta,\varphi) = K_1 \sin^2\theta + K_2 \sin^4\theta + K_3 \sin^6\theta + K_4 \sin^6\theta \cos(6\varphi). \tag{2.20}$$

In Eqs. 2.19 and 2.20, θ is the polar angle between the z-axis and the magnetization direction, and determines the energy change in the out-of-plane direction; φ instead is the azimuthal angle between the x-axis and the magnetization direction, defining the in-plane contributions to the MAE. Fig. 2.8 illustrates the coordinate system.

The K_i are the *magnetic anisotropy constants* and their values define the overall trend of the MAE. For example, in the case of a first-order anisotropy, $E_{an}(\theta,\varphi) = K_1 \sin^2\theta$, and the sign of K_1 determines the easy-axis: for $K_1 > 0$ the system presents an out-of-plane easy-axis, if $K_1 < 0$ the easy-axis is in-plane. The MAE of many magnetic materials is well described by the first term, however, in some instances, RE atoms can exhibit a more complex behavior that requires the use of higher-order terms to achieve an accurate description of the MAE.

A measure of the MA is the *magnetic anisotropy field*, which can be directly related to the constants K_i. In the case of an in-plane easy-axis with ($\theta = \pi/2$, $\varphi = 0.0$),

applying an external magnetic field $\mathbf{B} = [0, 0, B_z]$ along the z direction, will induce canting of the magnetization towards the magnetic field direction. The field needed to obtain a complete alignment of the magnetization along z corresponds to the magnetic anisotropy field, B_{an}. For an hexagonal system with magnetization M, the latter can be calculated starting from

$$E_{an+B_z}(\theta, \varphi) = K_1 \sin^2\theta + K_2 \sin^4\theta + K_3 \sin^6\theta + K_4 \sin^6\theta \cos(6\varphi) + M B_z \cos\theta, \quad (2.21)$$

where the last term accounts for the effect of an externally applied magnetic field along the z direction, resulting in the formation of a local minimum in the MAE curve at $\theta = 0$. Calculating the second derivative of Eq. 2.21 in $\theta = 0$ and equating it to 0, leads to

$$B_z = B_{an} = -\frac{2K_1}{M} \quad [\mathrm{T}]. \quad (2.22)$$

Typically the magnetization per atom is given in μ_B, where the conversion between eV/T and μ_B is 1 $\mu_\mathrm{B} \sim 5.788 \cdot 10^{-5}$ eV/T.

For an in-plane easy-axis $K_1 < 0$, such that B_{an} becomes positive. From Eq. 2.22 it can be observed that a magnetic field of at least B_{an} is required to align the magnetization of the material. Additionally, the larger the MAE, the more resistant the magnetization will be to being tilted by an external magnetic field. This property is crucial in the design of hard magnets.

2.3.1.2 Magnetoelastic anisotropy

Another effect explored in this thesis involves the coupling of the previously described MCA with elastic deformations of the sample, such as a linear distortion described by $\lambda = \Delta l/l_0 = (l - l_0)/l_0$, where l_0 represents the original length of the system and l represents the final length. There are two main phenomena which can be considered, one the reverse effect of the other: *magnetostriction effect* [58, 59] and the *magnetoelastic effect* [60, 61]. The magnetostriction effect involves changes in the structure or dimensions of a material in response to magnetization, resulting in different shapes for different magnetization directions. On the other hand, in the magnetoelastic effect, the application of an external stress (resulting in changes in the structure) can induce different magnetic properties, such as varying MA.

In the case of single RE atoms adsorbed on 2D-materials, the phenomenon can be again described in terms of SOC and CF effects: in the magnetoelastic coupling an external mechanical deformation (for example an applied pressure) induces changes in the crystal structure at the atomic level. In the framework of the RE atom, this consists in a displacement of the surrounding point charges that form the CF. This shift in the crystal field results in a different interaction between the 4f charge cloud and the crystal field compared to the unperturbed situation. This can lead to a new direction of the easy-axis as well as general changes in the MAE *i.e.* different

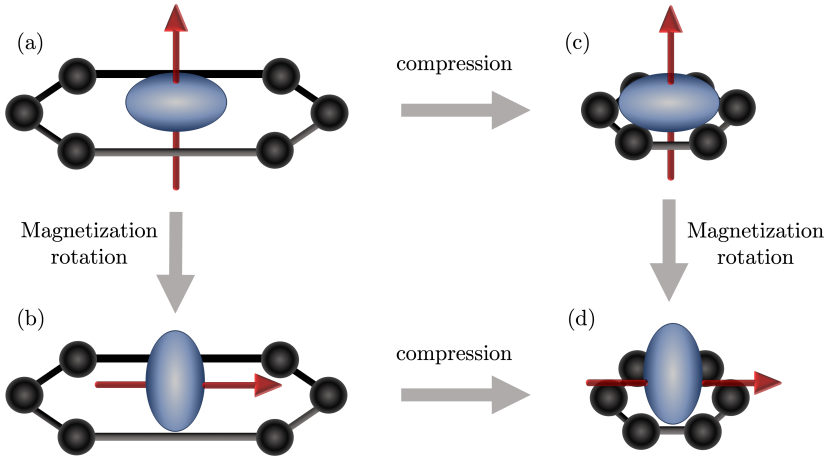

Figure 2.9: (a)-(c)-(d): Example of how an external strain can change the CF around the RE atom and consequently the MAE. (a)-(b)-(d): Example demonstrating how a change in magnetization direction can induce a structural transformation.

strains can induce different trends of $E_{an}(\theta, \varphi)$. Since the effect strictly relies on a non-spherical charge distribution around the atom, it is expected to be stronger for RE atoms with non-vanishing $\boldsymbol{L}$ values.

Fig. 2.9 sketches a simple example of an oblate charge density inside of an C_{6v} CF: from (a) to (b), the charge density is rotated by $\theta = \pi/2$ through SOC following the rotation of the magnetization, depicted by the red arrow. This rotation will result in a MAE due to the altered interaction with the CF after the rotation. From (a) to (c) the 2D-material undergoes an in-plane compression, causing the CF point charges to come closer to the charge cloud, leading to a change in the MAE compared to the relaxed structure. Tracing the arrows from (a) to (b) and then to (d) reveals an overall magnetostriction event, where a change in magnetization direction leads to a variation in the crystal structure around the magnetic atom. On the other hand, the path from (a) to (c) and then to (d) illustrates how a change in the crystal structure (such as compression) can induce a rotation of the magnetization direction, resulting in a magnetoelastic effect. In this example, the hexagonal symmetry is retained even after the mechanical deformation. However, the induced strain can also result in different symmetries of the CF around the RE atom and thus a transition to one crystallographic phase to another [62–64], requiring the use of distinct energy functionals $E_{an}(\theta, \varphi)$ to describe the MAE.

In general, the anisotropy energy of the system, which encompasses both the magnetocrystalline anisotropy energy and the magnetoelastic energy, can be represented as

a Taylor series with respect to the strain ε [65],

$$E_{\mathrm{MCA}} = (E_{\mathrm{MCA}})_0 + \sum_{i \geq j} \left(\frac{\partial E_{\mathrm{MCA}}}{\partial \varepsilon_{ij}} \right)_0 \varepsilon_{ij}. \tag{2.23}$$

The initial term characterizes the magnetocrystalline anisotropy unaffected by external factors and maintains the symmetry of the undistorted crystal field. On the other hand, the second term represents the variation in magnetic anisotropy energy induced by strain and may deviate from the symmetry depending on the type of distortion. Specifically, the strain is a tensor property that can be defined as $\varepsilon_{ij} = (\frac{\partial u_i}{\partial X_j} + \frac{\partial u_j}{\partial X_i})/2$, where $i, j = 1, 2, 3$ are the crystallographic directions, and the vector $\mathbf{u} = \mathbf{x} - \mathbf{X}$ represents the displacement from $\mathbf{X}$ to $\mathbf{x}$. Thus, the derivatives of $\mathbf{u}$ components with respect to $\mathbf{X}$ components characterize the distortion [66]. The explicit form of the strain tensor is given by

$$\varepsilon = \begin{bmatrix} \varepsilon_{xx} & \varepsilon_{xy} & \varepsilon_{xz} \\ \varepsilon_{yx} & \varepsilon_{yy} & \varepsilon_{yz} \\ \varepsilon_{zx} & \varepsilon_{zy} & \varepsilon_{zz} \end{bmatrix}, \tag{2.24}$$

and contains both normal strain components, which are ε_{xx}, ε_{yy}, and ε_{zz}, relative to a perpendicularly applied stress to the cross section of the material, as well as shear strain components ε_{ij}, where $i \neq j$, that are relative to a parallel applied stress to the cross section of the material. Moreover, the magnetoelastic energy terms in Eq. 2.23 can be written using directional cosines multiplied by the magnetoelastic coupling constants, which specify the magnitude of the magnetoelastic effect in different directions.

2.3.2 Crystal field theory

In the following, the CF effect on 4f electrons will be discussed in more detail. As previously mentioned, when the magnetic RE atom is adsorbed on a surface, the CF surrounding it induces splitting in the $(2J + 1)$-fold degenerate spectrum of the 4f electrons. This symmetry breaking modifies the magnetic properties and it is important to understand how the new symmetry affects the MA from a quantum point of view, in order to achieve an energetically stabilized magnetization. In the point charge model, the atoms constituting the CF are treated as point charges, and the electrostatic CF potential at a coordinate $\boldsymbol{r}$ close to the magnetic RE is evaluated as [40, 67]

$$V_{\mathrm{CF}}(\boldsymbol{r}) = \sum_i \frac{q_i}{|\boldsymbol{R}_i - \boldsymbol{r}|}. \tag{2.25}$$

Hence, $V_{\mathrm{CF}}(\boldsymbol{r})$ is directly proportional to the sum of point charges composing the CF, q_i, and inversely proportional to the distance between the charges and the RE atom at the center. It is important to note that this model corresponds to a simplified picture where overlap between neighboring wave functions is neglected. This approximation is suitable for highly localized 4f electrons, which are not typically involved in hybridization processes, but might not be appropriate when dealing with delocalized

Table 2.1: List of commonly occurring Legendre P_l^0 and associated Legendre (P_l^m, $m \neq 0$) polynomials.

$$P_2^0(\cos\theta) = \tfrac{1}{2}(3\cos^2\theta - 1)$$

$$P_2^2(\cos\theta) = 3(1 - \cos^2\theta)$$

$$P_4^0(\cos\theta) = \tfrac{1}{8}(35\cos^4\theta - 30\cos^2\theta + 3)$$

$$P_4^2(\cos\theta) = \tfrac{15}{2}(1 - \cos^2\theta)(7\cos^2\theta - 1)$$

$$P_4^3(\cos\theta) = 105(1 - \cos^2\theta)^{\frac{3}{2}}\cos\theta$$

$$P_4^4(\cos\theta) = 105(1 - \cos^2\theta)^2$$

$$P_6^0(\cos\theta) = \tfrac{1}{16}(231\cos^6\theta - 315\cos^4\theta + 105\cos^2\theta - 5)$$

$$P_6^2(\cos\theta) = \tfrac{105}{8}(1 - \cos^2\theta)(33\cos^4\theta - 18\cos^2\theta + 1)$$

$$P_6^3(\cos\theta) = \tfrac{315}{2}(1 - \cos^2\theta)^{\frac{3}{2}}(11\cos^3\theta - 3\cos\theta)$$

$$P_6^4(\cos\theta) = \tfrac{945}{2}(1 - \cos^2\theta)^2(11\cos^2\theta - 1)$$

$$P_6^6(\cos\theta) = 10395(1 - \cos^2\theta)^3$$

electrons. The CF potential in Eq. 2.25 is then expressed in terms of spherical harmonics since this permits to easily access to the matrix elements of the CF potential energy. In order to accomplish this, we define the angle α between $\boldsymbol{R}$ and $\boldsymbol{r}$, such that the quotient in Eq. 2.25 is represented as a sum of Legendre functions $P_l(\cos\alpha)$:

$$\frac{1}{|\boldsymbol{R}_i - \boldsymbol{r}|} = \sum_{l=0}^{\infty} \frac{r^l}{R_i^{(l+1)}} P_l(\cos\alpha) \quad R_i > r. \tag{2.26}$$

Table 2.1 lists some of the most commonly used Legendre and associated Legendre polynomials. Adopting the "Addition Theorem", the Legendre polynomials can be written in terms of spherical harmonics $Y_l^m(\theta,\varphi)$,

$$P_l(\cos\alpha) = \frac{4\pi}{(2l+1)} \sum_{m=-l}^{l} (-1)^m Y_l^{-m}(\theta_i,\varphi_i) Y_l^m(\theta,\varphi), \tag{2.27}$$

where (l, m) represent the orbital angular quantum number and the magnetic quantum number, while (θ_i,φ_i) and (θ,φ) denote the angular coordinates of $\boldsymbol{R}$ and $\boldsymbol{r}$, respectively.

Combining Eqs. 2.27 and 2.26 and plugging into Eq. 2.25, the potential generated by the charges q_i can be expressed as

$$V_{\mathrm{CF}}(\boldsymbol{r}) = \sum_i q_i \sum_l \frac{r^l}{R_i^{(l+1)}} \frac{4\pi}{(2l+1)} \sum_{m=-l}^{l} (-1)^m Y_l^{-m}(\theta_i, \varphi_i) Y_l^m(\theta, \varphi). \tag{2.28}$$

We then define

$$A_l^m = (-1)^m \frac{4\pi}{(2l+1)} \sum_i \frac{q_i}{R_i^{(l+1)}} Y_l^{-m}(\theta_i, \varphi_i), \tag{2.29}$$

which allows the potential to be rewritten as:

$$V_{\mathrm{CF}}(\boldsymbol{r}) = \sum_{l=0}^{\infty} \sum_{m=-l}^{l} A_l^m r^l Y_l^m(\theta, \varphi). \tag{2.30}$$

The A_l^m are defined as the crystal field parameters (CFP) and strictly depend on the symmetry of the CF. It is important to notice that the CF potential must be invariant under the symmetry operations of the point group defining the site.

2.3.2.1 Perturbing Crystal Field Hamiltonian

In $4f$ systems the SOC energy is much larger than the CF energy, hence the latter can be treated applying first-order perturbation theory and considering just the lowest lying J multiplet of the $4f$-shell. It is then possible to express the CF perturbation of the $4f$ electrons in the CF as [68]

$$\mathcal{H}_{\mathrm{CF}} = e \sum_i V_{\mathrm{CF}}(\boldsymbol{r_i}), \tag{2.31}$$

where the sum goes over the $4f$ electrons. One way to determine the expectation values of the CF Hamiltonian is direct integration between the $4f$ wave functions ϕ_l^m and $\mathcal{H}_{\mathrm{CF}}$

$$\langle \phi_l^{m_1} | \mathcal{H}_{\mathrm{CF}} | \phi_l^{m_2} \rangle, \tag{2.32}$$

where $l = 3$ and m_1, m_2 are the magnetic quantum numbers of the $4f$ states.

When calculating these matrix elements, it is necessary to deal with integrals that involve 3 spherical harmonics since also the single-electron wave functions, ϕ_l^m, of the $4f$ electrons are expanded in spherical harmonics (as shown in Eq. 2.4). Separating the radial from the angular part of the problem, the radial integral $\langle r^l \rangle$ is mostly considered numerically, while the angular part reduces to the evaluation of Gaunt integrals [69],

$$\langle Y_l^{m_1} | Y_{l'}^{m_3} | Y_l^{m_2} \rangle = \sqrt{\frac{(2l'+1)(2l+1)}{4\pi(2l+1)}} C(l'll|000) C(l'll|m_3 m_2 m_1). \tag{2.33}$$

Here, l' and m_3 are the angular momentum and magnetic quantum number of the CF potential. The C are the Clebsh-Gordan coefficients. The Wigner-Eckart theorem requires that in order to obtain non-zero matrix elements, Eq. 2.33 must contain the totally symmetric representation. The following rules can be used to determine which contributions result in non-zero matrix elements:

Selection rules

1. The integral vanishes unless $|l - l| \leq l' \leq 2l$ (triangle condition)
2. The integral vanishes unless $m_1 = m_2 + m_3$
3. The integral vanishes unless the inner product of Eq. 2.33 is even *i.e.* $l + l + l'$ is an even integer $\Longrightarrow$ for $4f$ electrons, with $2l = 6$, the value of l' must be an even integer.

Applying these conditions to $4f$ electrons with $l = 3$, the first rule indicates that the quantum number $l' \leq 6$, while the third rule results in l' taking values $0, 2, 4, 6$. The potential term with $l' = 0$ corresponds to spherical contributions to the field and does not induce any CF splitting in the $4f$ levels.

Concerning m_3, the permitted values are dictated by the CF symmetry and can be summarized as follows: for a C_{nv} symmetry, $m_3 = an$ with a integer and $m_3 \leq l'$. This can be derived from the application of symmetry operators of the CF point group to Eq. 2.30.

The aforementioned rules permit to understand where the expansion in Eq. 2.30 has to be stopped and which terms give rise to contributions to the CF splitting of $4f$ states in a specific CF symmetry.

2.3.2.2 Stevens Operator Equivalents Method

A more convenient method to evaluate the matrix elements of the crystal field implies the transformation of the spherical harmonics into functions of the total angular momentum operators called the "Operator Equivalents" [70]. The procedure involves the conversion of the spherical harmonics in Eq. 2.30 in cartesian coordinates, leading to $\mathcal{H}_{\mathrm{CF}} = e\sum_i V(x_i, y_i, z_i)$, where (x, y, z) are then replaced by $(\hat{J}_x, \hat{J}_y, \hat{J}_z)$ in a symmetrized fashion that considers the non-commuting property of $(\hat{J}_x, \hat{J}_y, \hat{J}_z)$. This is done by replacing the products of cartesian coordinates with all possible combinations of products of the $\hat{J}$ components and dividing by the number of combinations.
For example,

$$xy \longrightarrow \frac{1}{2}(\hat{J}_x\hat{J}_y + \hat{J}_y\hat{J}_x), \quad x^2 - y^2 \longrightarrow \hat{J}_x^2 - \hat{J}_y^2. \tag{2.34}$$

Therefore, considering states $|LSJJ_z\rangle$, the matrix element, for example, of $\sum_i(3z_i^2 - r_i^2)$, can be written as

$$\begin{aligned}\langle LSJJ'_z|\sum_i(3z_i^2 - r_i^2)|LSJJ_z\rangle \equiv& \alpha\langle r^2\rangle\langle LSJJ'_z|3\hat{J}_z^2 - \hat{J}(\hat{J}+1)|LSJJ_z\rangle \\ =& \alpha\langle r^2\rangle\langle LSJJ'_z|\hat{O}_2^0|LSJJ_z\rangle,\end{aligned} \tag{2.35}$$

where the factor α is the *Stevens factor* and depends on the quantum number l of the considered shell and on J of the considered RE element. The respective Stevens factors for 4^{th} ($l = 4$) and 6^{th} ($l = 6$) order terms are denoted as β and γ. A list of these values can be found in Table A.3 for RE ions. The operator $\hat{O}_2^0$ is the operator equivalent for $l = 2, m = 0$ in the specific example. If the procedure is carried out on the respective tesseral harmonics expressed in cartesian coordinates, the CF Hamiltonian can be written as

$$\mathcal{H}_{\text{CF}} = \sum_{l,m} A_l^m \alpha_l \langle r^l\rangle \hat{O}_l^m = \sum_{l,m} C_l^m \hat{O}_l^m, \tag{2.36}$$

with $C_l^m = \alpha_l A_l^m \langle r^l\rangle$ the convention commonly adopted to refer to the CFP. In this equation, $\hat{O}_l^m$ are the so-called *Stevens Operators*. As discussed, these operators are expressed in terms of total angular momentum operators and act on the J_z states of the central RE atom, removing their degeneracy. The calculation of the matrix elements of Eq. 2.36 gives thus rise to a multiplet structure of J_z states (corresponding to the specific J values of the RE atom) which become split by the CF energy.

2.4 Multiplet splitting of $4f$-states in a C_{6v} crystal field

In the present section, the CF theory will be discussed from the theoretical point of view in the specific case of interest of $4f$ electrons in an hexagonal CF. Chapter 5 will then apply the acquired knowledge to real systems of RE adatoms adsorbed on a graphene monolayer.

Based on the selection rules for non-zero matrix elements of Eq. 2.33, for a rare-earth atom experiencing a C_{6v} CF the respective crystal field Hamiltonian is given by [71, 72]

C_{6v} Crystal Field Hamiltonian

$$\mathcal{H}_{6v} = C_2^0\hat{O}_2^0 + C_4^0\hat{O}_4^0 + C_6^0\hat{O}_6^0 + C_6^6\hat{O}_6^6. \tag{2.37}$$

The explicit form of the operators $\hat{O}_l^m$ is reported in the following:

$$\hat{O}_2^0 = 3\hat{J}_z^2 - X$$

$$\hat{O}_4^0 = 35\hat{J}_z^4 - (30X - 25)\hat{J}_z^2 + 3X^2 - 6X$$

$$\hat{O}_6^0 = 231\hat{J}_z^6 - (315X - 735)\hat{J}_z^4 + (105X^2 - 525X + 294)\hat{J}_z^2 - 5X^3 + 40X^2 - 60X$$

$$\hat{O}_6^6 = \tfrac{1}{2}(\hat{J}_+^6 - \hat{J}_-^6),$$

with $X = J(J+1)$ and $\hat{J}_\pm = \hat{J}_x \pm i\hat{J}_y$ are the ladder operators. The operators with $m = 0$ contain even powers of $\hat{J}_z$ and $\hat{J}$ and are defined as the *uniaxial* CF operators. Their effect is to split the J_z states maintaining the degeneracy of those with the same absolute value $\langle J_z \rangle$. This gives rise to a specific energy landscape of the quantum states depending on the values of the CFP, and it determines the energy difference between the lowest and the highest lying states, the total zero field splitting (TZFS) [72]. This energy corresponds to the energy barrier that has to be overcome in order to observe a magnetization reversal from one magnetic state to the opposite one and is related to the classical MAE of Eq. 2.20.

By taking as an example the operator $\hat{O}_2^0$, it contains $\hat{J}(\hat{J}+1)$ that equally shifts all the states, and $\hat{J}_z^2$ that generates a parabolic dispersion of the states around $\langle J_z \rangle = 0$. The sign of C_2^0 determines the orientation of the parabola and thus it determines the easy-axis of the system in the case of a first-order anisotropy: for $C_2^0 > 0$ the easy-axis is in-plane, for $C_2^0 < 0$ the easy-axis is out-of-plane. How the sign of C_2^0 is precisely related to the first-order anisotropy constant is discussed in more detail in Section 2.4.4.

Fig. 2.10 shows the effect of the sign of C_2^0 in half-integer and integer spin systems. In the case of a half-integer J (Fig. 2.10 (a)) with $C_2^0 > 0$, the ground state will be

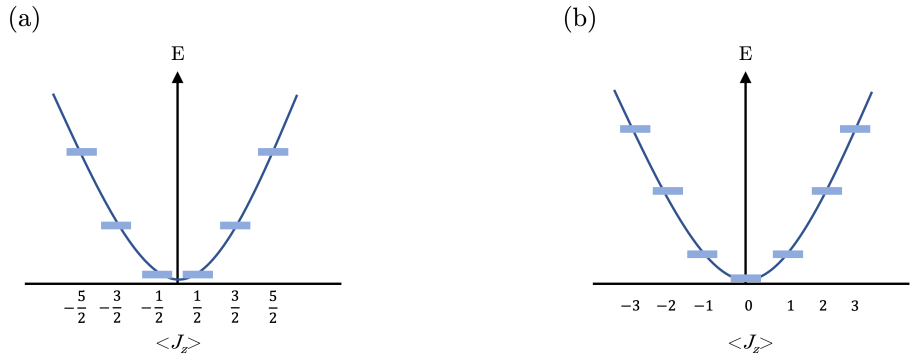

Figure 2.10: Effect of the sign of C_2^0 in half-integer and integer spin systems. (a) A half-integer J with $C_2^0 > 0$ leads to a double-degenerate ground state; inverting the sign has no effect on the degeneracy. (b) A integer J system with $C_2^0 > 0$ shows a single magnetic state at $\langle J_z \rangle = 0$, while $C_2^0 < 0$ produces a double-degeneracy of the ground state.

two-fold degenerate. Switching to $C_2^0 < 0$ maintains this degeneracy. On the other hand, when J is integer and $C_2^0 > 0$ (Fig. 2.10 (b)), the ground state is non-degenerate, as a single state at the lowest energy is found with $\langle J_z \rangle = 0$. If the sign is inverted, a double-degenerate ground state scenario arises.

The higher powers of $\hat{J}_z$ contained in $\hat{O}_4^0$ and $\hat{O}_6^0$ lead to a non-monotonic dispersion of the energy levels. Instead, the $\hat{O}_6^6$ operator, which depends on the ladder operators, is defined as a *transverse* operator that acts in the (xy) plane and mixes J_z states differing by $\Delta J_z = \pm 6, \pm 12$. Some of the newly generated mixtures can be tunnel-split doublets with quenched $\langle J_z \rangle$ value, whose effect is to significantly reduce the energy barrier for a spin-flip event inducing quantum tunneling of magnetization (QTM).

2.4.1 Quantum tunneling of magnetization and magnetic stability

For systems where $\mathcal{H}_{\mathrm{CF}}$ contains no transverse operators, the magnetization can in principle only be reversed by exceeding the entire energy barrier spanning from the lowest to the highest energy state(s). Instead, the presence of transverse operators can significantly reduce this energy barrier because of the generation of mixtures of states, some of which possibly lie at quenched $\langle J_z \rangle$. If states at $\langle J_z \rangle = 0$ form, the system no longer has to overcome the whole energy barrier, but can tunnel through the barrier via these states from one magnetic state towards the opposite one. For an hexagonal system,

$$\langle J_z = i | \hat{O}_6^6 | J_z = j \rangle \neq 0, \quad |i - j| = 6, 12 \tag{2.38}$$

meaning that the expectation value of $\hat{O}_6^6$ between two J_z states is non-zero when the J_z states differ by $\Delta J_z = \pm 6, \pm 12$. In this case, the states are coupled and a new wavefunction described as a superposition of the initial states is generated.

A simplified example of the process is depicted in Fig. 2.11 for $J = 4$: the states displayed in the same color are linear combinations of pure states differing by $\Delta J_z = \pm 6$, for example the $|J_z = -4\rangle$ couples to $|J_z = 2\rangle$ and $|J_z = -2\rangle$ is mixed with $|J_z = 4\rangle$. Similarly, $|J_z = -3\rangle$ and $|J_z = 3\rangle$ are mixed, and in this case two linear combinations are generated from the two initial states, a symmetric (in phase combination) and an antisymmetric (out of phase combination) one, both at $\langle J_z \rangle = 0$. These states are tunnel-split doublets and can yield QTM. In fact, if these states are ground states, QTM can happen directly since the system is located simultaneously at the left and at the right of the energy barrier [73]. If the tunnel-split doublets are not the ground state, they can nevertheless mediate QTM via excitation, *e.g.*, thermal excitation, phonon or conduction electron scattering events. These phenomena can induce transitions of the spin either directly to the tunnel-split doublet or to some excited states, from which the system then relaxes towards the opposite magnetization state via the tunnel-split doublets.

In order to stabilize the magnetization against reversal events, the optimal choice of the substrate is crucial both concerning the symmetry properties as well as the chemical and physical properties. From this point of view, a graphene monolayer is a

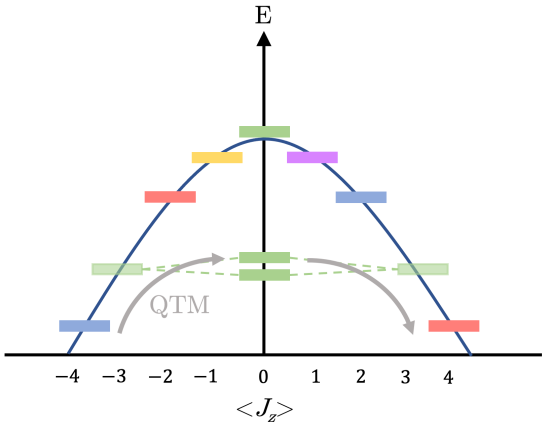

Figure 2.11: Example of a parabolic multiplet splitting for $J = 4$ in the presence of the transverse operator $\hat{O}_6^6$. Same colors indicate mixtures of states. The green states at $\langle J_z = 0 \rangle$ are tunnel-split states generated by the linear combinations of $|J_z = -3\rangle$ and $|J_z = 3\rangle$. The highest lying state corresponds to the $|J_z = 0\rangle$ state. States $|J_z = -1\rangle$ and $|J_z = 1\rangle$ are pure states.

suitable choice as a decoupling layer between the RE atom and a metallic/insulating surface in order to avoid scattering events. It is possible to achieve a stable magnetization also by a proper choice of the RE atom, *i.e.*, the total angular momentum J. As a matter of fact, half-integer spin systems are protected against the formation of doublets at $\langle J_z \rangle = 0$ by Kramer's degeneracy, rendering quantum tunneling of magnetization impossible through such states. Certainly, also for half-integer J systems an accurate analysis of the multiplet spectrum is necessary since magnetization reversal can be induced by other factors, *e.g.*, transitions induced by external perturbations.

These considerations are fundamental for the implementation of memory devices that rely on a hard and enduring magnetization. Therefore, the knowledge of the specific CFP in real materials as well as the general understanding of how the symmetry conditions along with varying J and CFP values affect the magnetic multiplets, is necessary to identify combinations of RE atoms and 2D-materials that are protected against magnetization reversal and thus promising candidates for magnetic units.

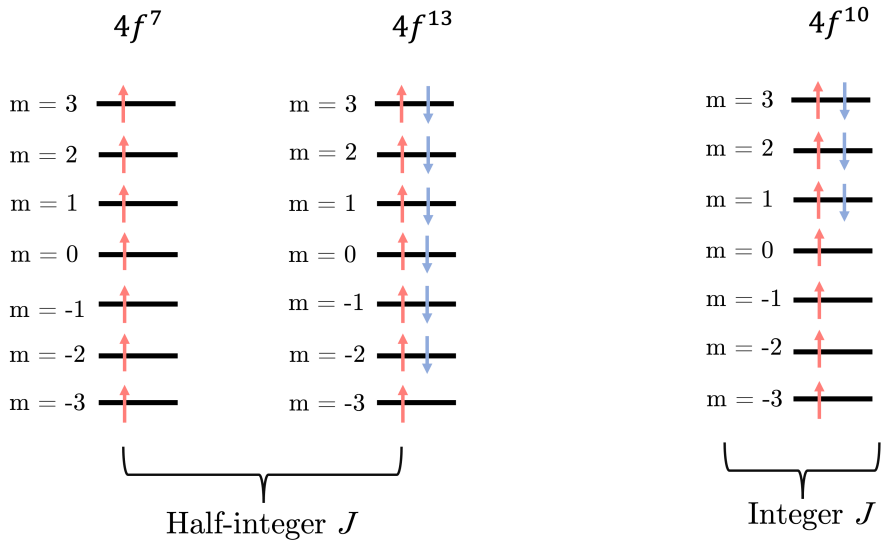

Figure 2.12: Different 4f occupations corresponding to different total angular momentum J values in the Hund's rules: $4f^7$ and $4f^{13}$ are associated to $J = 7/2$, $4f^{10}$ to $J = 8$.

2.4.2 Modelling of a C_{6v} crystal field Hamiltonian: integer and half-integer spin systems

In the following, the splitting effect of a C_{6v} crystal field will be analyzed by the implementation of a toy model. As examples, a half-integer and an integer J spin system have been chosen. The model contemplates the diagonalization of the CF Hamiltonian matrix with the symmetry of Eq. 2.37, where the CFP are given as input parameters and the elements $\langle J_z = i|\mathcal{H}_{6v}|J_z = j\rangle$ are evaluated following the tables in [67], which report the values of the elements $\langle J_z = i|\hat{O}_l^m|J_z = j\rangle$ for a constant J. As a half-integer spin system, the case of $J = 7/2$ will be discussed, which is associated to a half-filled $4f$-shell, namely $4f^7$ ($L = 0, S = 7/2$), as well as to a $4f^{13}$ occupation ($L = 3, S = 1/2$). Concerning the integer J case, a $J = 8$ system has been investigated, corresponding to a $4f^{10}$ occupation ($L = 6, S = 2$). These are sketched in Fig. 2.12.

2.4.2.1 Half-integer spin: $J = 7/2$

In order to compute the actual energy spectrum, we consider that for $J = 7/2$, $-7/2 \leq J_z \leq 7/2$, and the respective CF matrix elements are reported in the following:

$$\langle J_z = \frac{7}{2}|\mathcal{H}_{6v}|J_z = \frac{7}{2}\rangle = \langle J_z = -\frac{7}{2}|\mathcal{H}_{6v}|J_z = -\frac{7}{2}\rangle = 21C_2^0 + 420C_4^0 + 1260C_6^0$$

$$\langle J_z = \frac{5}{2}|\mathcal{H}_{6v}|J_z = \frac{5}{2}\rangle = \langle J_z = -\frac{5}{2}|\mathcal{H}_{6v}|J_z = -\frac{5}{2}\rangle = 3C_2^0 - 780C_4^0 - 6300C_6^0$$

$$\langle J_z = \frac{3}{2}|\mathcal{H}_{6v}|J_z = \frac{3}{2}\rangle = \langle J_z = -\frac{3}{2}|\mathcal{H}_{6v}|J_z = -\frac{3}{2}\rangle = -9C_2^0 - 180C_4^0 + 11340C_6^0$$

$$\langle J_z = \frac{1}{2}|\mathcal{H}_{6v}|J_z = \frac{1}{2}\rangle = \langle J_z = -\frac{1}{2}|\mathcal{H}_{6v}|J_z = -\frac{1}{2}\rangle = -15C_2^0 + 540C_4^0 - 6300C_6^0$$

$$\langle J_z = \frac{7}{2}|\mathcal{H}_{6v}|J_z = -\frac{5}{2}\rangle = \langle J_z = -\frac{7}{2}|\mathcal{H}_{6v}|J_z = \frac{5}{2}\rangle = \langle J_z = \frac{5}{2}|\mathcal{H}_{6v}|J_z = -\frac{7}{2}\rangle =$$
$$\langle J_z = -\frac{5}{2}|\mathcal{H}_{6v}|J_z = \frac{7}{2}\rangle = 360\sqrt{7}C_6^6.$$

It can be noticed that the only non-zero off-diagonal terms are those between states separated by $\Delta J_z = \pm 6$, as the $\hat{O}_6^6$ operator operator exclusively mixes these states. All other unlisted elements are zero, and the entire CF matrix can be represented in the schematic form illustrated in Fig. 2.13.

Diagonalizing the CF matrix, leads to the energy spectrum of the multiplets. All calculation outputs are plotted on an energy diagram in arbitrary units and each pure state is represented by an individual color. By setting all CFP to zero except C_2^0, one gets pure states at the permitted $\langle J_z\rangle$ values that arrange in a parabolic

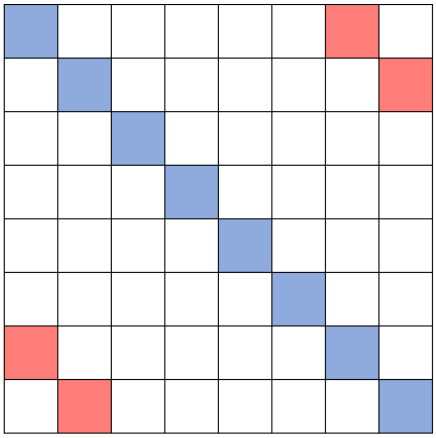

Figure 2.13: $\mathcal{H}_{6v}$ matrix for $J = 7/2$.

trend, as shown in Fig. 2.14 for $C_2^0 = \pm 1$, where the dashed lines are drawn on top to put in evidence the shape of the energy spectrum. The shape arises from the $\hat{O}_2^0$ operator that contains $\hat{J}_z^2$. Changing the sign of C_2^0 results in an inversion of the parabola, maintaining a two-fold degenerate ground state in both cases, as imposed by time-reversal symmetry for half-integer spins. The overall TZFS maintains the same value independently from the sign of C_2^0.

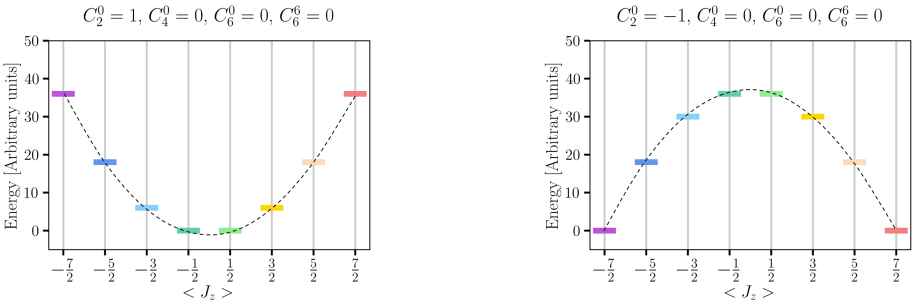

Figure 2.14: Magnetic multiplets for $J = 7/2$ in a first-order anisotropy with $C_2^0 = 1$ (left) and $C_2^0 = -1$ (right) while all other CFP are equal to zero. The dashed line serves as a guide to easier identify the dispersion.

Introducing the term $C_4^0 \hat{O}_4^0$ in the Hamiltonian leads to a higher order anisotropy of the magnetic states. This is illustrated in Fig. 2.15, where the diagonalization has been performed at fixed value of $C_4^0 = 1$ and for increasing values of C_2^0, while

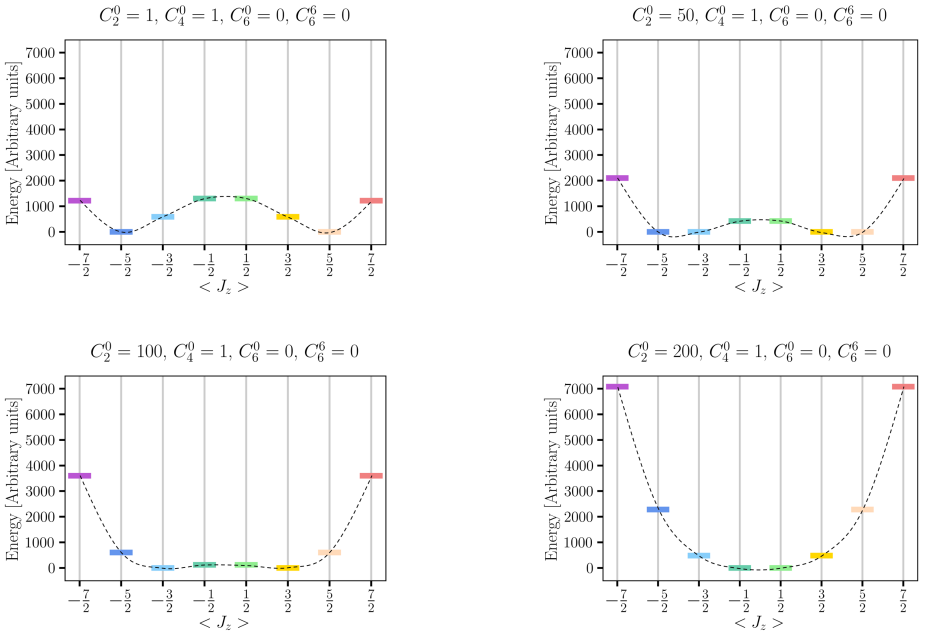

Figure 2.15: Magnetic multiplets for $J = 7/2$ and varying C_4^0/C_2^0, with C_2^0 taking values of $1, 50, 100, 200$. $C_4^0 = 1$ and C_4^0 is fixed to 1. The second term in Eq. 2.37 introduces local maxima and minima in the energy disposition of the states.

higher order terms are put to zero. It is seen that low ratios of C_4^0/C_2^0 in the order of 5×10^{-3} are needed in order C_4^0 to become negligible such that the states again form a parabolic trend. For higher values of C_4^0/C_2^0 the disposition of states forms progressively more anisotropic curves with increasing depth and height of the valleys and hills according to increasing value of C_4^0/C_2^0.

The effect of C_4^0 is better evidenced in Fig. 2.16 where the ratio C_2^0/C_4^0 goes up to 5 leading to bigger energy differences between the states and a larger TZFS. An inversion in sign of C_2^0 and C_4^0 is respectively shown in Fig. 2.17 and 2.18. Here it is seen that increasing the negative value of C_2^0 pushes the states towards a parabolic shape, which is reached for low absolute values of C_4^0/C_2^0 and inverted compared to Fig. 2.15. A similar effect is observed by comparison of Fig. 2.16 with Fig. 2.18 in the higher anisotropy example (larger values of C_4^0/C_2^0).

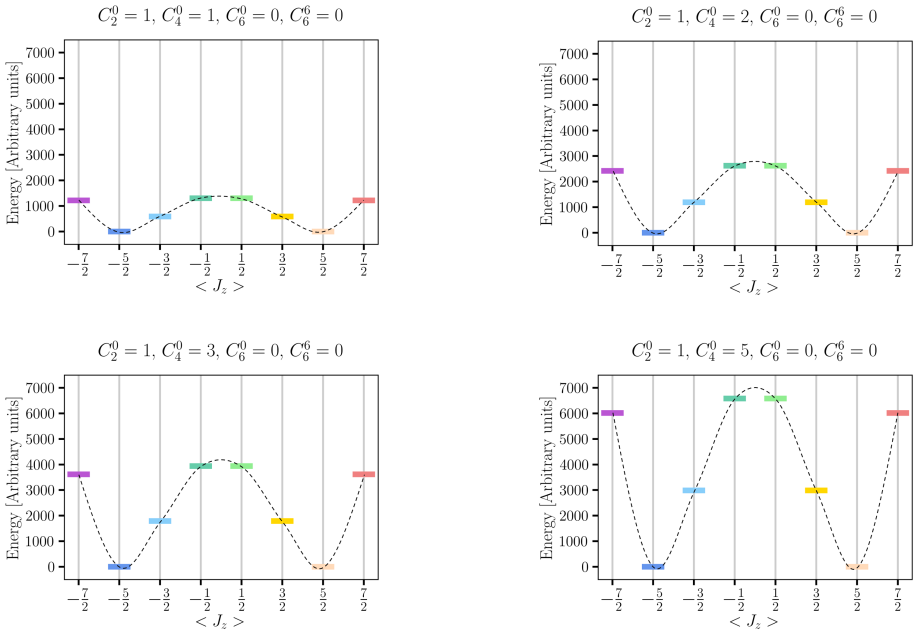

Figure 2.16: Magnetic multiplets for $J = 7/2$ for larger values of C_4^0/C_2^0. C_2^0 is fixed to 1 and C_4^0 takes values of $1, 2, 3, 5$.

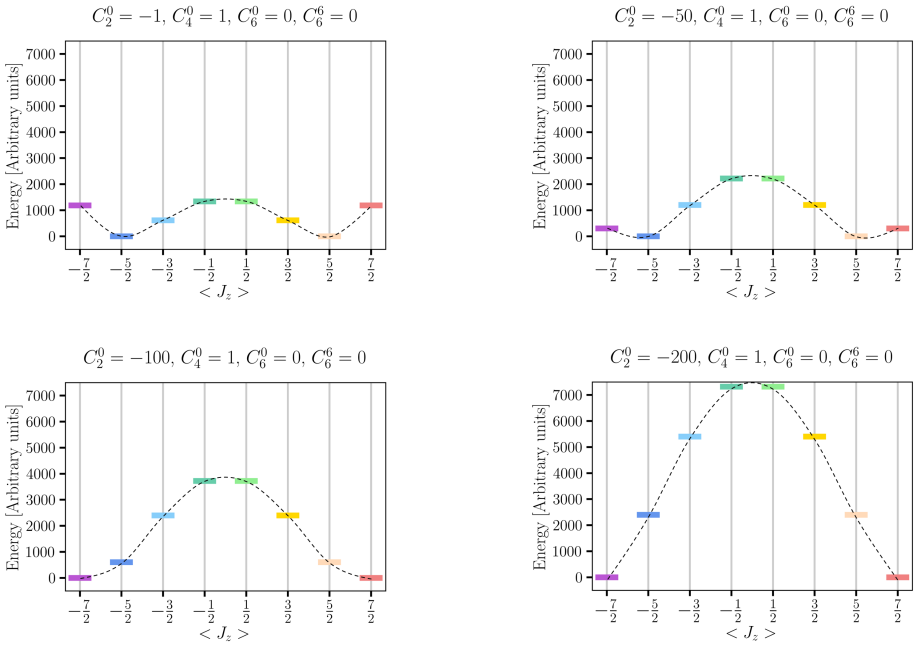

Figure 2.17: Magnetic multiplets for $J = 7/2$ and varying C_4^0/C_2^0 with negative C_2^0. C_2^0 is varied over negative values of $-1, -50, -100, -200$, and C_4^0 is fixed to 1.

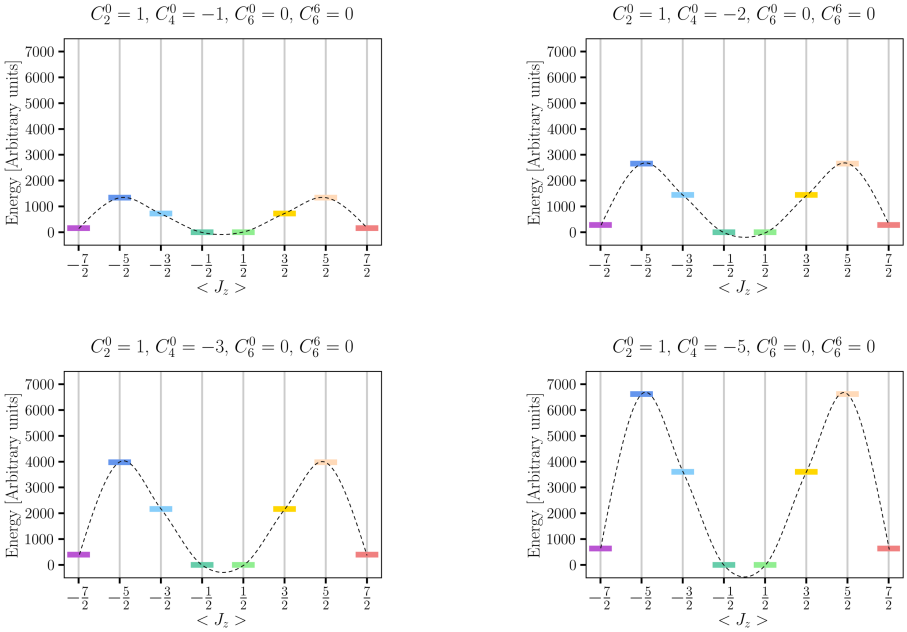

Figure 2.18: Magnetic multiplets for J = 7/2 and varying C_4^0/C_2^0 with negative C_4^0. C_2^0 is fixed to 1, while C_4^0 is varied over negative values of $-1, -2, -3, -5$.

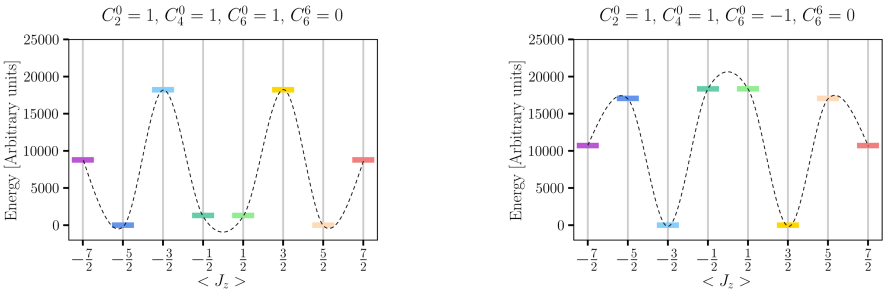

Figure 2.19: Magnetic multiplets for $J = 7/2$ with non-zero $C_6^0 = 1, -1$.

Fig. 2.19 shows the multiplet splitting for $C_2^0 = C_4^0 = C_6^0 = 1$ and $C_6^6 = 0$. The effect of the third term in Eq. 2.37 is to introduce further oscillatory behavior in the state dispersion, which is a consequence of highly anisotropic behavior.

The introduction of the CFP C_6^6 accounts for the hexagonal symmetry. Prior to examining the energy spectrum, group theoretical principles can be employed to predict how the $(2J+1)$-fold degeneracy of a spherically symmetric atom (with point group K_h) will be split into a sum of irreducible representations (IR) due to the hexagonal symmetry. The *great orthogonality theorem* [74] is a criteria for irreducibility,

$$\sum_{\nu=1}^{n} \chi^{(\Gamma)}(g_\nu)[\chi^{(\Gamma')}(g_\nu)]^* = n\delta_{\Gamma\Gamma'} \tag{2.39}$$

where $\chi^{(\Gamma)}(g_\nu)$ and $\chi^{(\Gamma')}(g_\nu)$ are characters of the symmetries g_ν belonging to the two representations Γ, Γ' of K_h and C_{6v}, respectively, and $n =$ is the number of symmetry operations ($n = 24$ in this case). Eq. 2.39 gives an orthogonality relationship between the characters, indicating the number of times each Γ' (in this case of the C_{6v} symmetry) is included in the reducible representation Γ (spherical symmetry K_h). Considering the character table for an isolated atom with $J = 7/2$ and of the C_{6v} point-group (Table A.1) in Appendix A, it is possible to deduce the splitting of the $(2J+1) = 8$ states:

$$K_h^{7/2} = \Gamma_7 + 2\Gamma_8 + \Gamma_9 \tag{2.40}$$

leading to 4 sets of double degenerate states, two sets of which belonging to the same IR, namely Γ_8.

In Fig. 2.20, panel (a) shows the energy spectrum calculated for this symmetry with arbitrary values of the CFPs as an illustrative example. The transverse operator $\hat{O}_6^6$ generates linear combinations of $|J_z = -\frac{7}{2}\rangle, |J_z = \frac{5}{2}\rangle$ and $|J_z = -\frac{5}{2}\rangle, |J_z = \frac{7}{2}\rangle$, which are represented by states of the same color (blue and red), and it can be noticed how the expectation value of these superpositions deviates from the pure state value. This

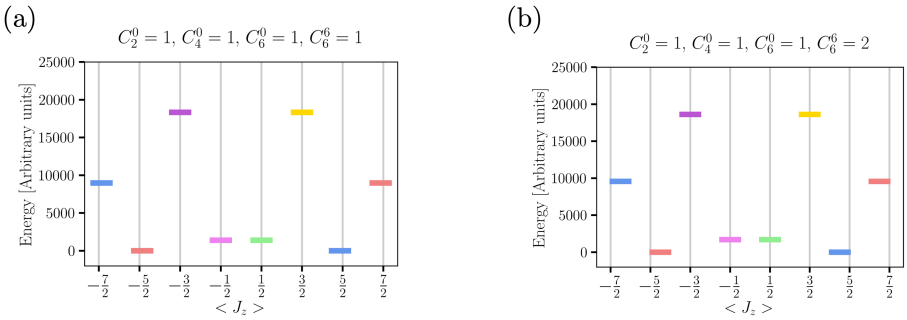

Figure 2.20: Magnetic multiplets for $J = 7/2$ with non-zero $C_6^6 = 1, 2$. From (a) to (b) the C_6^6 parameter increases and results in a larger shift of the mixtures in blue and red from the pure state expectation value $\langle J_z \rangle$.

deviation increases the stronger the mixing *i.e.* the larger C_6^6, as observed in Fig. 2.20 (b). Of fundamental importance is the fact that for half-integer spin systems, in the absence of an external magnetic field, the transverse operators can never generate mixtures with $\langle J_z \rangle = 0$, since states must maintain the two-fold degeneracy. This property is nevertheless lost in integer J systems.

Before delving into the modelling of an integer spin system, it is important to highlight that it is theoretically possible to determine the irreducible representations to which different J_z states belong within a given point group. This can be achieved by establishing appropriate basis functions and applying the symmetry operators. For instance, let's consider a symmetry group $\mathcal{G}$ defined by the operators $\hat{G}_k$, and a basis set composed of functions $\{\psi_1, ..., \psi_d\}$. The action of the symmetry operator $\hat{G}_k$ on one of the basis functions can be represented as a linear combination of the basis set:

$$\hat{G}_k |\psi_i\rangle = \sum_{k=1}^{d} G_{ki} |\psi_k\rangle, \quad i = 1, ..., d \quad \text{and} \quad \forall \hat{G}_k \in \mathcal{G}, \tag{2.41}$$

resulting in a new vector within the space. The expansion coefficients, which depend on the particular symmetry operation, determine the transformation or *representation matrix*. In fact, by multiplying Eq. 2.41 on the left by $\langle \psi_j |$, we obtain

$$\langle \psi_j | \hat{G}_k | \psi_i \rangle = \sum_{k}^{d} G_{ki} \langle \psi_j | \psi_k \rangle = \sum_{k}^{d} G_{ki} \delta_{kj}. \tag{2.42}$$

If the selected basis functions are orthogonal to each other, then Eq. 2.42 can be reformulated as

$$G_{ji}(k) = \langle \psi_j | \hat{G}_k | \psi_i \rangle. \tag{2.43}$$

Hence, the representation matrix can be determined by calculating the matrix elements between all possible pairs of basis functions.

2.4.2.2 Integer spin: $J = 8$

For systems with integer spin, the modifications that the multiplet spectrum undergoes with changing CFP are generally similar to those of half-integer spin systems. However, it will be demonstrated that in integer spin systems, magnetization reversal can be induced by QTM due to the influence of $\hat{O}_6^6$.

The CF matrix for a spin system with $J = 8$ has dimensions of 17×17, where J_z can take values $-8 \leq J_z \leq 8$. The matrix elements, which are listed in Appendix A.2, show that the $\hat{O}_6^6$ operator mixes states that differ in $\langle J_z \rangle$ by ± 6, while all non-listed elements are zero. As previously mentioned, the ground state for integer J can be non-degenerate or double-degenerate, depending on the sign and values of the CFP. This property is exemplified in Fig. 2.21, which represents a higher symmetry case than the C_{6v} due to the absence of the transverse operator.

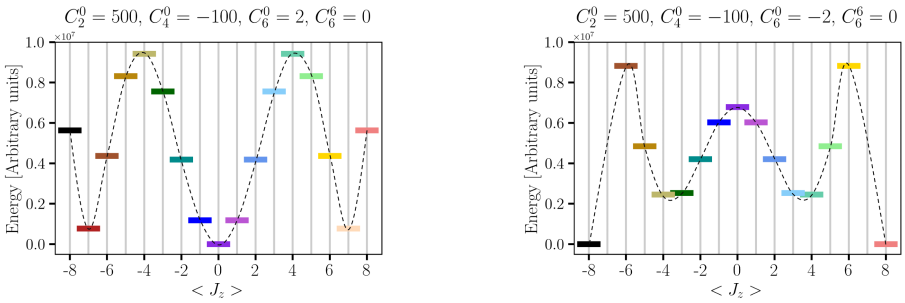

Figure 2.21: Example of a multiplet splitting for $J = 8$ without $\hat{O}_6^6$ operator: for integer spin systems the ground state can be composed by a single magnetic state or by two-degenerate states.

In order to consider a hexagonal CF, it is necessary to take into account also the $C_6^6\hat{O}_6^6$ contribution. Adopting similar symmetry considerations as in the half-integer case, the degeneracy of the J_z states in a C_{6v} CF can be predicted considering the character table in Table A.2 in Appendix A, where no double-group is necessary for an integer spin system. The resulting splitting can be described as several non-degenerate states and 6 sets of double-degenerate states belonging to the IR Γ_5 and Γ_6:

$$K_h^8 = \Gamma_1 + 2\Gamma_2 + \Gamma_3 + \Gamma_4 + 3\Gamma_5 + 3\Gamma_6. \tag{2.44}$$

Fig. 2.22 illustrates the result of diagonalizing $\mathcal{H}_{\mathrm{CF}}$ containing all the terms describing a C_{6v} CF adopting arbitrary CFP for the sake of example. In this case, there are no pure states as every wavefunction arises from linear combinations of several states. For example, the states in purple are superpositions of $|J_z = -8\rangle$, $|J_z = -2\rangle$ and $|J_z = 4\rangle$, and similarly for the other states. It is also clear that for integer J values quantum states at $\langle J_z\rangle = 0$ can form: the light green states emerge as a result of the mixing of three states, namely $|J_z = -6\rangle$, $|J_z = 0\rangle$, and $|J_z = 6\rangle$, one state is situated at around 1.1 energy units, while the other two are approximately at 0.8 energy units and appear to be in close proximity to each other. The dark green states, on the other hand, are examples of tunnel-split doublets. The latter result from the symmetric and antisymmetric linear combination of the $|J_z = -3\rangle$ state with the $|J_z = 3\rangle$ state (pictorically drawn in grey on top of the multiplet calculation). This kind of quantum states can drive QTM through excitation from the ground state, as the system can tunnel through the energy barrier to reach the opposite magnetic state, such as from $|J_z = -4\rangle$ to $|J_z = 4\rangle$. This is the fundamental difference from half-integer spin system, which are, in contrast, protected against the formation of such states. A last comment concerns the degeneracy of the multiplets which perfectly reflects the result obtained adopting the orthogonality theorem: 5 states are non-degenerate and 6 states are double-degenerate in energy.

From this discussion, it emerges that half-integer and integer spins behave differently when adsorbed in a hexagonal CF and it is essential to take into account the properties of the two types of spin systems to design hard magnets. Although half-integer

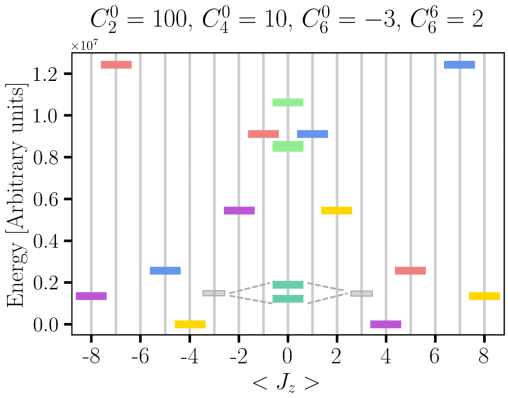

Figure 2.22: Magnetic multplet splitting for $J = 8$ with arbitrary CFP. States in the same color represent mixtures of several $|J_z\rangle$. In particular, the combinations of $|J_z = -3\rangle$ with $|J_z = 3\rangle$ leads to tunnel-split doublets at quenched $\langle J_z\rangle$.

spins are protected against the formation of tunnel-split doublets, the choice between integer or half-integer spin systems is not obvious since the magnetization can also be destabilized by transitions that do not involve states at $\langle J_z = 0 \rangle$. In this perspective, it is in necessary to induce high energy barriers between the magnetic states in order to prevent magnetization reversal and this can be achieved in both kinds of spin systems.

2.4.3 First-order perturbation effects: electron and phonon scattering

As previously mentioned, a magnetization reversal event can occur through processes that may not necessarily involve quantum tunneling via mixed states at $\langle J_z = 0 \rangle$. Therefore, it is crucial to calculate multiplet splittings and further explore how to control them based on the selection of the spin system and the crystal field. For instance, temperature effects can induce magnetization reversal and affect the magnetic stability. Two different mechanism can be distinguished in two different temperature regimes: At finite temperatures, magnetization reversal can occur through thermal activation, enabling the system to overcome the minimal energy barrier when the temperature is sufficiently high. This leads to an Arrhenius-like relationship for the magnetic lifetime under the condition that no external magnetic field is present. At lower temperatures, although the thermal energy may not be sufficient to overcome the energy barrier U (see Fig. 2.23), it can prompt excitations to metastable higher-energy states that enable thermally assisted quantum tunneling of the magnetization [73]. At the microscopic level, this phenomenon can involve scattering processes, such as interactions with the substrate's phonons and electrons. The mathematical representation employs operators $\hat{J}_z$, $\hat{J}_+$, and $\hat{J}_-$, which enable transitions between states with $\Delta J_z = 0, \pm 1$. In this first-order perturbation scenario, the operator $\hat{O}_6^6$ of a hexagonal crystal field facilitates the coupling between states of equal energy having angular momentum differences of $\Delta J_z = 0 \pm 6k, -1 \pm 6k, 1 \pm 6k$ (as detailed in Ref. [72]

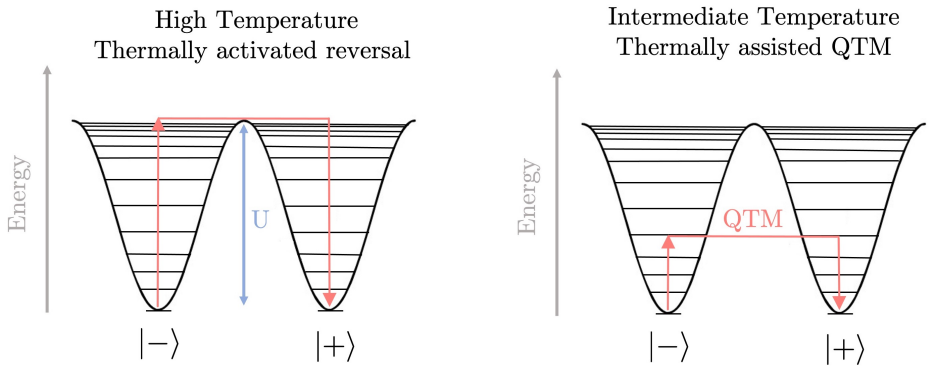

Figure 2.23: Visual representation depicting the mechanisms of magnetization reversal through thermal activation and thermally assisted quantum tunneling of magnetization.

and the corresponding PhD thesis [75]). Here, the parameter k assumes integer values depending on the total angular momentum J of the lanthanide. In the absence of an external magnetic field, this process thus involves the transition to a higher-energy state, from which subsequent quantum tunneling can take place. In the presence of a magnetic field, it can also directly induce transitions between opposite spin ground states.
It is important to mention that single atom spin systems can experience spin reversal events mediated by exchange interactions with itinerant electrons of the substrate, known as Kondo scattering [76–78]. These transitions between two ground states lead to relatively short lifetimes. This effect occurs in systems where the crystal field produces two degenerate ground states separated by $\Delta J_z = \pm 1$ transitions. To reduce this effect, one strategy is to separate the atomic spins from the conduction electrons, which can be achieved by introducing a decoupling layer.

2.4.4 Reverse-engineering the magnetic anisotropy: from classical to quantum

As discussed in the previous sections, the effects at the quantum level have a strong impact on magnetization reversal events of single rare-earth atoms deposited on a 2D-material. Thus, a classical formulation as described in Eq. 2.20 is not sufficient to achieve an exhaustive overview about the magnetic stability and a quantum-mechanical description is fundamental to determine the energy differences involved in possible transitions between different magnetic states. This translates in the necessity to determine the accurate values of the CFP and compute the respective multiplet structures to identify possible systems protected against magnetization reversal events and therefore appealing choices for stable magnetic units.

In the following, a simple approach that relates the classical magnetic anisotropy constants, K_i, to the quantum crystal field parameters, C_l^m, for a C_{6v} symmetry is proposed in the *reverse-engineering* framework. Since the classical energy functional $E(\theta, \varphi)$ can be straightforwardly computed (and thus the K_i) in the DFT picture discussed in section 4.2.1, the reverse-engineering represents a method to calculate the CFP from *ab initio*.

Following [79], the 4f electron density associated to a spin quantization axis aligned along $\hat{\mathbf{z}}$ can be defined as

$$\rho_{4f}^{\hat{\mathbf{z}}}(\mathbf{r}) = n_{4f}^{0}(r) \sum_{l=2,4,6} \mathcal{A}_l \left(\frac{2l+1}{4\pi} \right)^{1/2} Y_{l0}(\hat{\mathbf{r}}). \tag{2.45}$$

Here, $n_{4f}^{0}(r)$ denotes the radial charge density, $Y_{l0}(\hat{\mathbf{r}})$ represents spherical harmonics, and the $\mathcal{A}_l$ are numerical factors dependent on the total angular momentum J of the specific rare-earth and the corresponding Stevens factor [70, 80]. This expression can be extended for a general direction of the magnetic moment by replacing Y_{l0} with

$\sum_m e^{-im\varphi} d_l^{m0} Y_{lm}(\hat{\mathbf{r}})$, where the d_l^{m0} functions are related to the associated Legendre polynomials, P_l^m:

$$\begin{aligned} d_2^0 &= P_2^0(\cos\theta) \\ d_4^0 &= P_4^0(\cos\theta) \\ d_6^0 &= P_6^0(\cos\theta) \\ d_6^6 &= \frac{1}{\sqrt{12!}} P_6^6(\cos\theta) \\ d_6^{-6} &= \sqrt{12!} P_6^{-6}(\cos\theta). \end{aligned}$$

Considering a single rare-earth atom at the center of a C_{6v} CF, we assume that the contributions to the MAE fully arise from the $4f$ electrons and consider the limit in which the CF energy is small compared to the exchange field. In this scenario, the CF contribution can be treated as a first-order perturbation [81]. The CF potential is written as a linear combination of spherical harmonics, $V_{\mathrm{CF}}(\mathbf{r}) = \sum_{lm} V_{lm}(r) Y_{lm}(\hat{\mathbf{r}})$, and the expectation value can be expressed generally as:

$$E_{\mathrm{CF}} = \int \sum_{lm} \rho_{4f}(\mathbf{r}) V_{lm}(r) Y_{lm}(\hat{\mathbf{r}}) d\mathbf{r}, \tag{2.46}$$

which leads to [79]

$$E_{\mathrm{CF}} = \sum_{l=2,4,6} \mathcal{A}_l \sum_m (-1)^m B_l^{-m} e^{-im\varphi} d_l^{m0}(\theta). \tag{2.47}$$

The B_l^{-m} are the CFP in the Waybourne convention [82],

$$B_l^m = \left(\frac{2l+1}{4\pi}\right)^{1/2} \int r^2 n_{4f}^0(r) V_{lm}(r) dr, \tag{2.48}$$

and are closely related to the Stevens convention by a multiplicative factor dependent on (l, m), denoted as θ_l^m (note that this is different from the θ used to denote spherical coordinates), and the Stevens factor (α_l): $C_l^m = \theta_l^m \alpha_l B_l^m$. The derivation of the relationship between K_i and the CFP will be carried out in the B_l^m convention to ultimately be converted in the more accesible convention C_l^m of Eq. 2.37.

Expansion of Eq. 2.47 for a C_{6v} CF, leads to

$$E_{6v} = \mathcal{A}_2 B_2^0 d_2^0(\theta) + \mathcal{A}_4 B_4^0 d_4^0(\theta) + \mathcal{A}_6 B_6^0 d_6^0(\theta) + \mathcal{A}_6 B_6^6 (e^{-i6\varphi} d_6^6(\theta) + e^{i6\varphi} d_6^{-6}(\theta)). \tag{2.49}$$

Adopting the property

$$P_l^{-m} = (-1)^m \frac{(l-m)!}{(l+m)!} P_l^m, \tag{2.50}$$

it can be derived that $P_6^{-6} = \frac{1}{12!} P_6^6$ and $d_6^{-6} = \frac{1}{\sqrt{12!}} P_6^6$, which leads to

$$E_{6v} = \mathcal{A}_2 B_2^0 P_2^0(\theta) + \mathcal{A}_4 B_4^0 P_4^0(\theta) + \mathcal{A}_6 B_6^0 P_6^0(\theta) + \mathcal{A}_6 B_6^6 \frac{2}{\sqrt{12!}} P_6^6 \cos(6\varphi). \tag{2.51}$$

Plugging the definition of the P_l^m of Table 2.1 into Eq. 2.51, produces

$$\begin{aligned}
E_{6v} = \quad & \mathcal{A}_2 B_2^0 \frac{1}{2}(3\cos^2\theta - 1) \\
& + \mathcal{A}_4 B_4^0 \frac{1}{8}(35\cos^4\theta - 30\cos^2\theta + 3) \\
& + \mathcal{A}_6 B_6^0 \frac{1}{16}(231\cos^6\theta - 315\cos^4\theta + 105\cos^2\theta - 5) \\
& + \mathcal{A}_6 B_6^6 (\frac{-2\cdot 10395}{\sqrt{12!}}(\cos^2\theta - 1)^3)\cos(6\varphi) \\
= \quad & (\frac{3}{2}\mathcal{A}_2 B_2^0 - \frac{30}{8}\mathcal{A}_4 B_4^0 + \frac{105}{16}\mathcal{A}_6 B_6^0)\cos^2\theta \\
& + (\frac{35}{8}\mathcal{A}_4 B_4^0 - \frac{315}{16}\mathcal{A}_6 B_6^0)\cos^4\theta \\
& + (\frac{231}{16}\mathcal{A}_6 B_6^0)\cos^6\theta \\
& - \frac{2\cdot 10395}{\sqrt{12!}}\mathcal{A}_6 B_6^6(\cos^2\theta - 1)^3\cos(6\varphi) \\
& - \frac{1}{2}\mathcal{A}_2 B_2^0 + \frac{3}{8}\mathcal{A}_4 B_4^0 - \frac{5}{16}\mathcal{A}_6 B_6^6 \\
= \quad & K_1'\cos^2\theta + K_2' cos^4\theta + K_3'\cos^6\theta + K_4'\sin^6\theta\cos(6\varphi) + constant.
\end{aligned} \tag{2.52}$$

Considering now the conversion to $\sin\theta$ functions,

$$\begin{aligned}
\cos^2\theta &= 1 - \sin^2\theta \\
\cos^4\theta &= 1 - 2\sin^2\theta + \sin^4\theta \\
\cos^6\theta &= 1 - 3\sin^2\theta + 3\sin^4\theta - \sin^6\theta,
\end{aligned} \tag{2.53}$$

Eq. 2.52 becomes

$$\begin{aligned}
E_{6v} = \quad & K_1'(1 - \sin^2\theta) + K_2'(1 - 2\sin^2\theta + \sin^4\theta) \\
& + K_3'(-3\sin^2\theta + 3\sin^4\theta - \sin^6\theta) + K_4'\sin^6\theta\cos(6\phi) \\
= \quad & (-K_1' - 2K_2' - 3K_3')\sin^2\theta + (K_2' + 3K_3')\sin^4\theta \\
& - K_3'\sin^6\theta + K_4'\sin^6\theta\cos(6\phi) + constant.
\end{aligned} \tag{2.54}$$

This equation can then be written in the shape of Eq. 2.20 with

$$\begin{aligned} K_1 &= -K_1' - 2K_2' - 3K_3' = -\frac{3}{2}\mathcal{A}_2 B_2^0 - 5\mathcal{A}_4 B_4^0 - \frac{21}{2}\mathcal{A}_6 B_6^0 \\ K_2 &= K_2' + 3K_3' = \frac{35}{8}\mathcal{A}_4 B_4^0 + \frac{189}{8}\mathcal{A}_6 B_6^0 \\ K_3 &= -K_3' = -\frac{231}{16}\mathcal{A}_6 B_6^0 \\ K_4 &= K_4' = \frac{2 \cdot 10395}{\sqrt{12!}}\mathcal{A}_6 B_6^6. \end{aligned} \tag{2.55}$$

To conclude the derivation, we define $\theta_2^0 = 1/2$, $\theta_4^0 = 1/8$, $\theta_6^0 = 1/16$, $\theta_6^6 = \sqrt{231}/16$ as reported in [83] and

$$\begin{aligned} \mathcal{A}_2 &= J(J - \frac{1}{2}) \cdot \alpha_l \\ \mathcal{A}_4 &= J(J - \frac{1}{2})(J-1)(J - \frac{3}{2}) \cdot \alpha_l \\ \mathcal{A}_6 &= J(J - \frac{1}{2})(J-1)(J - \frac{3}{2})(J-2)(J - \frac{5}{2}) \cdot \alpha_l, \end{aligned} \tag{2.56}$$

with α_l the Stevens factor (α, β, γ for $l = 2, 4, 6$), defined in Table A.3 for the RE^{3+} ions in Appendix A.4. The magnetic anisotropy constants K_i in Eq. 2.55 are finally formulated in terms of $C_l^m = \theta_l^m \alpha_l^m B_l^m$ as

Reverse-engineering of CFP

$$\begin{aligned} K_1 &= -3f_2 C_2^0 - 40 f_4 C_4^0 - 168 f_6 C_6^0 \\ K_2 &= 35 f_4 C_4^0 + 378 f_6 C_6^0 \\ K_3 &= -231 f_6 C_6^0 \\ K_4 &= f_6 C_6^6. \end{aligned} \tag{2.57}$$

where $f_l = \mathcal{A}_l/\alpha_l$. The equations imply that the K_i values can be expressed as a linear combination of the CFP. Assuming a pure first-order anisotropy, all constants except K_1 are zero, resulting in only C_2^0 being non-zero. In this situation, C_2^0 determines the sign of the parabolic dispersion of the magnetic multiplets *i.e.* the easy-axis: if $C_2^0 < 0$, then the easy-axis is out-of-plane ($K_1 > 0$), whereas $C_2^0 > 0$ indicates an easy-plane anisotropy ($K_1 < 0$). Nevertheless, when dealing with open $4f$-shells higher order anisotropy terms must mostly be taken into account and the determination of the easy-axis is not trivial.

The result of Eq. 2.57 for hexagonal C_{6v} systems, shows that the calculation of the magnetic anisotropy constants K_i gives access to the CFP. In Chapter 5 this method will be applied to RE atoms adsorbed on a graphene monolayer, where starting from DFT calculations, the multiplet splitting of the systems were determined.

Chapter 3

Applications in spin-orbitronics

In this chapter, the use of rare-earth atoms on 2D-materials is explored, highlighting key studies that have influenced the current research. Specifically, two major applications are examined: the implementation of rare-earths as single-atom magnets and the potential of rare-earth-based materials as magnetotransport devices, as they show great promise for future electronics. Both of these applications demand the creation of significant magnetic anisotropies.

Since the discovery of graphene as first 2D-material, fundamental research has been successful in discovering 2D-structures with properties useful in fields including electronics, optics, energy and catalysis. These materials offer a wide range of electronic properties that can be manipulated through chemical composition and crystal structures, and can be experimentally realized using various methods [84–86]. The ability to engineer the properties of 2D-materials by using proximity effects between layers [87] or depositing single atoms [88–91] is particularly appealing. This allows for the combination of various properties, such as large SOC [92–94], magnetism [95–99], and topological properties [100–102], in one structure [103–105]. Through theoretical and experimental investigation, it is possible to create novel phenomena by optimizing the combination of elements in the system and this could potentially lead to the development of next-generation of spintronics devices [106].

While *spintronics* exploits the spin magnetic moment of atoms to build efficient platforms for electronic devices, *spin-orbitronics* concerns phenomena that arise from the interplay between the spin magnetic moment and the orbital magnetic moment of atoms. RE atoms are particularly well-suited for this due to their very large spin and orbital moments that are coupled through spin-orbit interaction.

Additionaly, as discussed in Section 2.1, the magnetization of RE atoms is localized and protected from the chemical environment, leading to a more stable f magnetic moment in comparison to a d magnetic moment. From the orbital perspective, the $4f$ filling leads to large $\boldsymbol{L}$ values that translate into anisotropic $4f$ distributions which interact with the CF without being quenched. Another advantage concerns the pos-

sibility to engineer the magnetic anisotropy by changing the orbital $4f$ filling, making RE atoms promising candidates for a variety of applications *e.g.* data storage and quantum technology.

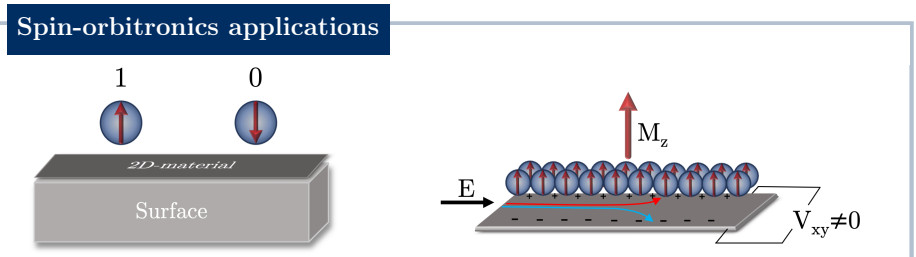

Figure 3.1: Example of two applications of RE atoms on 2D-materials in spin-(orbi)tronics: single atom magnets (left) and platforms for transport properties such as the anomalous Hall effect (right).

3.1 Single-atom magnets

Permanent magnets have a high resistance to fluctuation, allowing them to maintain stored data over time. This property is crucial for their use in efficient memory devices. For example, when a RE atom is adsorbed on a substrate, it acts as an isolated magnetic moment that spontaneously aligns along a preferred direction. If the energy required to rotate the magnetic moment is too high to be induced by external factors such at thermal excitations, the RE atom can serve as a hard magnet. Physically this is reflected in a large magnetic anisotropy energy along with long coherence times of the magnetization, which can be defined as a measure of the interval of time in which the magnetization preserves its value along a direction before decaying and losing the saved information. These systems permit the construction of magnets at the atomic scale, favoring a downscaling of the information units and, consequently, the possibility to increase the storage density per unit of surface [107].

These considerations are fundamental also at the quantum level, for example, in the generation of stable basic units in quantum information referred to as *qubits*. The primary distinction from classical computation, where information is encoded in $|1\rangle$ and $|0\rangle$ bits, is the possibility of utilizing spin states that are superpositions of these states $|1\rangle$ and $|0\rangle$, thereby taking advantage of the quantum nature of the spin. In this perspective, $4f$-elements on 2D substrates are promising candidates as quantistic information carriers [108, 109].

Recent research has aimed to gain a comprehensive understanding of the chemical hybridization, electronic transfer processes, magnetic interactions and anisotropy of

REs on 2D substrates, using both experimental and theoretical methods [78, 110–118]. The generation of single-atom magnets relies heavily on the magnetic anisotropy energy, which is the key ingredient in this process. Additionally, considering the highly localized nature of $4f$ magnetic moments, quantum effects must be taken into account, as they may induce magnetization reversal processes. The proposed research strategy is aimed at gaining a deeper understanding of how the magnetic anisotropy energy changes with the nature of the RE element and the symmetry and chemistry of the surrounding CF. The goal is to identify conditions that effectively prevent the occurrence of quantum tunneling of magnetization. Previous studies have laid the foundation for this research combining X-Ray Absorption Spectroscopy (XAS), X-Ray Magnetic Circular Dichroism (XMDC) and Scanning Tunneling Microscopy (STM) measurements with multiplet splittings calculations for RE atoms in different environments [72, 119, 120] and determining giant lifetimes of the $4f$ magnetizations [38, 76, 120–123].

In this context, graphene (Gr) is often utilized as a decoupling layer between a metallic or insulating surface and the RE atoms. Indeed, graphene interacts via van der Waals interactions which are remarkably weak compared to covalent bondings and reflect in larger distances from the substrate. As a result, by adsorption of a RE atom, it is possible to investigate RE/Gr systems which are not substantially affected by the vibrational modes and conduction electrons of the substrate. However, achieving this separation requires careful selection of the substrate, as the interaction between Gr and the substrate depends on the chemical composition of the latter [124–127]. For instance, it has been shown that Gr on top of Ir(111) results in a large vertical distance [127, 128] compared to other metals with minimal impact on the electronic structure of Gr, making Ir(111) a good substrate candidate for the study of RE single-atom magnets on Gr.

The use of Gr as a 2D-material is not restricted to its weak bonding characteristics. The hexagonal arrangement of the C atoms also generates a CF that can lead to stable magnetic ground states, and opens opportunities for manipulating the multiplet splittings. Additionally, the low density of states at the Fermi energy of Gr prevents scattering events of the magnetization and its negligible SOC means that the resulting MAE is dominated by the adsorbed RE atom.

Other applications involve depositing RE atoms on van der Waals materials with properties that differ from Gr, such as stronger SOC. The goal of this approach is to not only exploit the CF of the 2D-material but also to take advantage of proximity effects between layers, which can lead to phenomena that do not exist in the individual layers alone. Examples of suitable 2D-materials might involve TMDCs such as MoS_2, $MoSe_2$, WSe_2 that are composed of three atomic layers, in which one transition metal element (M) is bonded to chalcogen atoms (X) with stoichiometry MX_2. These 2D-materials are attractive due to the variety of electronic phases they exhibit, based on the chemical composition of M and X and the crystalline structure [129, 130]. These

phases range from semiconductors to conductors and superconductors [131–139]. A TMDC monolayer in 2H stacking inherently breaks inversion symmetry and, coupled with the intrinsic SOC stemming from the transition metal atom, results in various effects such as band splitting and valley degrees of freedom [140, 141] leading to valley and spin hall effects [142].

3.2 Magnetotransport phenomena

In general, TMDC monolayers represent an ideal platform for transport phenomena due to the possibility to tailor their chemical and structural properties, the SOC and magnetic properties *e.g.* via proximity effect by interfacing with a magnetic material. From this perspective, RE atoms can act as a magnetic source, inducing magnetization in the vdW material. This, in combination with SOC, is crucial for generating magnetotransport phenomena such as the anomalous Hall effect.

3.2.1 Anomalous Hall conductivity

The anomalous Hall effect (AHE) occurs when an electric field is applied to a ferromagnet, causing the electronic current to deflect perpendicular to the applied voltage. This effect arises from a combination of different factors such as net magnetization, spin-orbit coupling, and orbital hybridization, which lead to an additional contribution to the group velocity of electrons perpendicular to the electric field, which is absent in non-magnetic materials. A sketch of the effect is illustrated in Fig. 3.1. Empirically, The AHE is typically represented by an additional term in the Hall resistivity, ρ_H, which is proportional to the magnetization, M_z [143]:

$$\rho_H = R_0 H_z + R_s M_z. \tag{3.1}$$

The first term in the equation describes the classical Hall effect, with R_0 being the Hall coefficient and H_z the perpendicularly applied magnetic field, indicating a linear dependence on the latter in non-magnetic materials. The anomalous effect in ferromagnetic materials is accounted for by the second term, with R_s denoting the anomalous Hall coefficient, as it originates from the presence of magnetization even in the absence of an external magnetic field.

The *intrinsic* AHE solely depends on the band structure of the material, which can exhibit intricate features due to orbital hybridization and SOC-induced effects. To provide an accurate description of the AHE it is thus essential to incorporate topological concepts, such as the Berry curvature, that appropriately capture the geometrical characteristics of the electronic structure. On the other hand, contributions to the AHE that come from external sources involve the presence of impurities that cause scattering of electrons driven by spin-orbit coupling. This thesis focuses solely on the intrinsic AHE, which will be discussed in further detail below.

To understand the definition of the Berry curvature, we begin by introducing the Berry phase as the phase evolution of a complex vector as it is transported around a closed path, for example, the ground state of a quantum system when moved in the parameter space (such as the k-space). The resulting phase evolution is determined by the geometry of the parameter space.
Considering the Hamiltonian $\mathcal{H}$ of some system and its eigenstates $|n(\lambda(t))\rangle$, the adiabatic approximation [144] assumes the parameter $\lambda(t)$ to change slowly over time. This means that if the system is in the state $|n(\lambda(0))\rangle$ at $t = 0$, it will remain in the same state, up to a phase, at any later time t. In other words, the system is able to adapt to the gradual changes. Taking the Ansatz [145, 146]

$$\psi(t) = c(t)e^{-i\phi(t)}\,|n(\lambda(t))\rangle \tag{3.2}$$

where ϕ is the dynamical phase defined as

$$\phi(t) = \frac{1}{\hbar}\int_0^t E_n(\lambda(t'))dt', \tag{3.3}$$

while $c(t)$ allows for the potential existence of an extra phase beyond $\phi(t)$. Plugging Eq. 3.2 into the time-dependent Schrödinger equation

$$[i\hbar\partial_t - \mathcal{H}(\lambda(t))]\,|\psi(t)\rangle = 0, \tag{3.4}$$

results in

$$\begin{aligned} &i\hbar\dot{c}(t)e^{-i\phi(t)}\,|n(\lambda(t))\rangle + i\hbar c(t)[\cancel{-i\dot{\phi}(t)e^{-i\phi(t)}|n(\lambda(t))\rangle}] + i\hbar c(t)e^{-i\phi(t)}\partial_t\,|n(\lambda(t))\rangle \\ &\cancel{-c(t)e^{-i\phi(t)}E_n\,|n(\lambda(t))\rangle} = 0, \end{aligned} \tag{3.5}$$

where the cancellation occurs from $\dot{\phi}(t) = E_n(t)/\hbar$. This yields the following expression,

$$\dot{c}(t)\,|n(\lambda(t))\rangle + c(t)\partial_t\,|n(\lambda(t))\rangle = 0, \tag{3.6}$$

which multiplied with $\langle n(\lambda(t))|$ on the left leads to

$$\dot{c}(t) = ic(t)\,\langle n(\lambda(t))|i\partial_t n(\lambda(t))\rangle\,. \tag{3.7}$$

We define $\mathcal{A}_n(t) = \langle n(\lambda(t))|i\partial_t n(\lambda(t))\rangle$ as the Berry connection "in time", and the solution of Eq. 3.7 is

$$c(t) = e^{i\gamma(t)}, \tag{3.8}$$

with $\gamma(t)$ the Berry phase defined as

$$\gamma(t) = \int_0^t \langle n(\lambda(t'))|i\partial_{t'} n(\lambda(t'))\rangle = \int_0^t \mathcal{A}_n(t')dt'. \tag{3.9}$$

Expressing the Berry phase in terms of the parameter λ is then a straightforward task by noticing that $\partial_t |n(\lambda(t))\rangle = \dot{\lambda}\partial_\lambda |n(\lambda(t))\rangle$. Thus, $\mathcal{A}_n(t) = \dot{\lambda}\mathcal{A}_n(\lambda)$, with $\mathcal{A}_n(\lambda) = \langle n(\lambda)|i\partial_\lambda n(\lambda)\rangle$ defined as the Berry connection in parameter space (the time dependence is intrinsic, meaning that the functions $\mathcal{F}(\lambda)$ are defined as $\mathcal{F}(\lambda(t))$). By utilizing $d\lambda = \dot{\lambda}dt$, a variable substitution can be made to the λ-parameter space:

$$\gamma(t) = \int_{\lambda(0)}^{\lambda(t)} \langle n(\lambda)|i\partial_\lambda n(\lambda)\rangle \, d\lambda = \int_{\lambda(0)}^{\lambda} \mathcal{A}_n(\lambda) d\lambda, \tag{3.10}$$

showing that the Berry phase solely depends on the path in parameter space. More generally, for multiple changing parameters $\boldsymbol{\lambda} \equiv (\lambda_1, \lambda_2, \lambda_3, ..., \lambda_N)$ the Berry phase writes as

$$\gamma = \oint_\Gamma i \langle n(\boldsymbol{\lambda})|\nabla_{\boldsymbol{\lambda}} n(\boldsymbol{\lambda})\rangle \cdot d\boldsymbol{\lambda} = \oint_\Gamma \boldsymbol{\mathcal{A}}(\boldsymbol{\lambda}) \cdot d\boldsymbol{\lambda}, \tag{3.11}$$

and depends only on the chosen path. The Berry curvature is then defined as the curl of the Berry connection

$$\boldsymbol{\Omega}(\boldsymbol{\lambda}) = \nabla_{\boldsymbol{\lambda}} \times \boldsymbol{\mathcal{A}}(\boldsymbol{\lambda}), \tag{3.12}$$

and applying Stokes' theorem for a closed path Γ that delimits the surface $\mathcal{S}$, the Berry phase is defined as

$$\gamma = \oint_\Gamma \boldsymbol{\mathcal{A}}(\boldsymbol{\lambda}) \cdot d\boldsymbol{\lambda} = \int_{\mathcal{S}} \boldsymbol{\Omega}(\boldsymbol{\lambda}) \cdot d\boldsymbol{S}. \tag{3.13}$$

Eq. 3.13 illustrates that the relationship between $\boldsymbol{\mathcal{A}}(\boldsymbol{\lambda})$ and $\boldsymbol{\Omega}(\boldsymbol{\lambda})$ is the same as the connection between the vector potential $\boldsymbol{A}(\boldsymbol{r})$ and the magnetic field $\boldsymbol{B}(\boldsymbol{r})$ in real-space.

Berry curvature in crystals

Consequently, when the parameter space $\boldsymbol{\lambda}$ is defined by the reciprocal space of a crystal structure, where the parameters are the wavevectors $\boldsymbol{k}$, the Berry curvature can be interpreted as an effective magnetic field in k-space. For each band n, the value of $\boldsymbol{\Omega}_n(\boldsymbol{k})$ is well-defined and it provides a local description of its geometric properties.

In the case of a 2D reciprocal space (k_x,k_y), the Berry connection associated with band n is defined in terms of periodic part of the Bloch's function, $u_{n\boldsymbol{k}}$:

$$A_{nk_x}(\boldsymbol{k}) = \langle u_{n\boldsymbol{k}}|i\partial_{k_x} u_{n\boldsymbol{k}}\rangle, \quad A_{nk_y}(\boldsymbol{k}) = \langle u_{n\boldsymbol{k}}|i\partial_{k_y} u_{n\boldsymbol{k}}\rangle. \tag{3.14}$$

The Berry phase then writes as

$$\gamma_n = \oint \boldsymbol{\mathcal{A}}_n(\boldsymbol{k}) \cdot d\boldsymbol{k}, \tag{3.15}$$

and the Berry curvature is given by

$$\Omega_{n\boldsymbol{k}} = \partial_{k_x}\mathcal{A}_{nk_y}(\boldsymbol{k}) - \partial_{k_y}\mathcal{A}_{nk_x}(\boldsymbol{k}) = -2\mathrm{Im}\left\langle \partial_{k_x} u_{n\boldsymbol{k}} | \partial_{k_y} u_{n\boldsymbol{k}} \right\rangle . \tag{3.16}$$

One common method to calculate the Berry curvature, and hence the intrinsic anomalous Hall conductivity, is through the use of the Kubo formula [143, 147, 148] based on linear response theory [149], which for each band n can be written as:

$$\Omega_{n\boldsymbol{k}} = -2\hbar^2 \sum_{m\neq n} \mathrm{Im}\left[\frac{\langle u_{n\mathbf{k}} | v_x | u_{m\mathbf{k}} \rangle \langle u_{m\mathbf{k}} | v_y | u_{n\mathbf{k}} \rangle}{(E_{n\mathbf{k}} - E_{m\mathbf{k}})^2} \right], \tag{3.17}$$

where v_x and v_y are the x and y components of the velocity operator. The summation is over the eigenstates with eigenvalues $E_{n\boldsymbol{k}}$. This equation indicates that features of the Berry curvature will manifest in reciprocal space, where bands are separated in energy, due to effects such as SOC.

Moreover, the evaluation of the Berry curvature for all occupied bands can be obtained using the following equation, where the Fermi-Dirac distribution $f_{n\boldsymbol{k}}$ has been introduced:

$$\Omega_{\boldsymbol{k}} = \sum_n f_{n\boldsymbol{k}} \Omega_{n\boldsymbol{k}}. \tag{3.18}$$

The intrinsic anomalous Hall conductivity can then be obtained by integrating Eq. 3.18 over the Brillouin zone (BZ) [150]

Anomalous Hall conductivity

$$\sigma_{\mathrm{AHC}} = \frac{e^2}{\hbar} \int_{BZ} \frac{d^2k}{(2\pi)^2} \Omega_{\boldsymbol{k}}. \tag{3.19}$$

When computing integrals over the BZ, symmetry is crucial in determining the values of properties. In general, if the structural inversion symmetry is broken, the Berry curvature will have equal magnitude but opposite sign at opposite k-points, resulting in a zero value of the intrinsic AHC upon integration over the BZ. However, if time-reversal symmetry is also broken, then the Berry curvature will be different at opposite k-points, allowing for a non-zero AHC. As a result, ferromagnetic materials are particularly interesting for this purpose.

In summary, by carefully choosing the elements in a system and designing the band structure with symmetry considerations, orbital hybridizations, and spin-orbit coupling effects in mind, it is possible to create materials that exhibit anomalous Hall conductivity.

Chapter 4

The Many-Body Problem: *ab initio* methods

The many-body problem refers to the difficulties in understanding and predicting the behavior of materials composed by a large number of electrons. The complexity stems from the numerous interactions between electrons, making the Schrödinger equation impossible to solve exactly. To overcome this, approximate and computational techniques are employed to solve the equation and deduce the properties of many-electron systems. The sections that follow detail the computational approaches that have been adopted throughout this thesis to calculate electronic and magnetic properties of rare-earth atoms on 2D-materials.

For many-electron systems, the Hamiltonian can be written as

$$\mathcal{H} = \mathcal{T}_e + \mathcal{T}_N + \mathcal{V}_{eN} + \mathcal{V}_{ee} + \mathcal{V}_{NN} \tag{4.1}$$

where the terms are defined below with distances $r_{ij} = |\boldsymbol{r_i} - \boldsymbol{r_j}|$, and nuclear charges denoted by Z [151]:

$$\mathcal{T}_e = -\sum_i \frac{\hbar^2}{2m_e}\nabla_i^2, \qquad \text{kinetic energy of electrons with mass } m_e$$

$$\mathcal{T}_N = -\sum_k \frac{\hbar^2}{2m_k}\nabla_k^2, \qquad \text{kinetic energy of nuclei with mass } m_k$$

$$\mathcal{V}_{eN} = -\sum_i \sum_k \frac{e^2 Z_k}{r_{ik}}, \qquad \text{electron-nucleus electrostatic potential}$$

$$\mathcal{V}_{ee} = \sum_{i<j} \frac{e^2}{r_{ij}}, \qquad \text{electron-electron electrostatic potential}$$

$$\mathcal{V}_{NN} = \sum_{k<l} \frac{e^2 Z_k Z_l}{r_{kl}}, \qquad \text{nucleus-nucleus electrostatic potential.}$$

In the listed contributions, there are many coordinates and interactions that indicate a mutual dependence among the particles. To simplify the problem, a common

method is to separate the motion of the electrons from the motion of the nuclei using the Born-Oppenheimer approximation [152, 153]. This is possible because the nuclei are much heavier than the electrons, so their coordinates can be assumed fixed in the electronic framework. This allows the electronic configuration to instantly adapt to the nuclear motion. Practically, one can thus solve the electronic equation separately from the nuclear equation assuming an external nuclear potential for the electronic problem.

However, the presence of electron interaction term implies that the dynamics of all electrons are interdependent, and to accurately describe the system, it is necessary to consider all interactions. However, due to the complexity and the infinite computational resources required, various computational methods are employed to approximate these correlation effects. Density Functional Theory (DFT), shown schematically Fig. 4.1, is an example of such a method. It is extensively employed in computational materials science and is widely recognized as a fundamental approach for simulating quantum mechanical systems, alongside the Hartree-Fock methods.

The Hartree-Fock method for an N-particle system involves breaking down the N-particle electronic Schrödinger equation into N individual single-particle equations [154]. In the approach of treating each electron individually, an important approximation is introduced where an average potential field is considered for each electron resulting from the presence of all other electrons. This field is supposed to approximately mimic the repulsive electron-electron interactions. The ground state wavefunction is assumed to be a single Slater determinant composed of the N single-electron wavefunctions, which comply with the antisymmetry condition, thus allowing the method to include the exchange-correlation energy. Despite its limitations, the Hartree-Fock method is often used as a starting point for more advanced methods that attempt to account for electrostatic correlations between electrons in the so-called post-HF methods. Nevetherless, due to the computational demands of post-HF methods, especially when applied to systems with a large number of atoms, such as periodic systems, DFT methods are mostly employed when simulating crystal structures.

4.1 Density Functional Theory: a short review

Density functional theory offers a significant advantage by replacing the wavefunction of an N-electron system with an electron density, greatly reducing the number of variables from $3N$ (3 for each electron) to just 3. This simplification is relevant when considering the electronic problem of a system composed of N interacting electrons, described by the Hamiltonian $\mathcal{H} = \mathcal{T}_e + \mathcal{V}_{ee} + \mathcal{V}_{ext}$. Here, $\mathcal{T}_e$ represents the kinetic energy, $\mathcal{V}_{ee}$ denotes the electron-electron interaction, and $\mathcal{V}_{ext}$ accounts for the external potential originating from the nuclei.

At the core of DFT lie the Hohenberg-Kohn theorems, which establish its theoretical

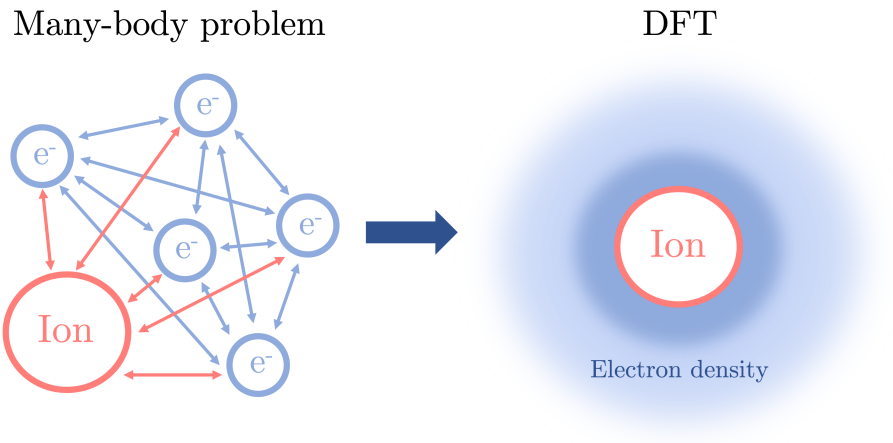

Figure 4.1: The DFT philosophy consists to approximate the vast number of interactions of a complex system considering an electronic charge distribution around the nuclei. Each electron feels an effective field produced by the other electrons.

foundation. The first theorem asserts that the electron density uniquely determines the external potential within which the electrons are confined. This implies a one-to-one correspondence between the electron density and the external potential. As a direct consequence of this theorem, the total energy of the system becomes a unique functional of the electron density. The second theorem builds upon this by stating that the electron density that minimizes the energy functional corresponds to the exact ground state density, subject to the constraint that the total number of electrons remains fixed. [155]:

Hohenberg-Kohn theorems

1. $E = E[n(\boldsymbol{r})]$
2. $E[n(\boldsymbol{r})] \geq E[n_{\mathrm{GS}}(\boldsymbol{r})] = E_{\mathrm{GS}}$.

These two formulations translate into a one-to-one mapping between the ground state wavefunction and the ground state electron density, meaning it is sufficient to calculate the electron charge density to determine ground state properties. However, due to the lack of explicit definition of the electron density and the form of the total energy functional in the Hohenberg-Kohn theorems, a practical strategy employed in DFT calculations, inspired by Kohn and Sham [156], is to construct a fictitious system of

non-interacting electrons. This approach aims to emulate the behavior of the actual interacting system by introducing a potential that describes electronic interactions. The potential is designed in a manner that ensures the ground state density of the fictitious system matches the ground state density of the real system.

Considering Eq. 4.1 for the electronic problem, the energy functional of the real interacting system can be expressed as a sum of the kinetic energy of the electrons, the Coulomb interactions between electrons and the interactions of the electrons with the external nuclear potential:

$$E[n] = T_e[n] + V_{ee}[n] + V_{eN}[n] = T_e[n] + V_{ee} + \int V_{ext}(\boldsymbol{r})n(\boldsymbol{r})d\boldsymbol{r}. \tag{4.2}$$

In the non-interacting system the first two terms in Eq. 4.2 are replaced by the kinetic term and two contributions that describe the electron interactions

$$T_e[n] + V_{ee}[n] = T_e^0[n] + E_{\mathrm{H}}[n] + E_{\mathrm{XC}}[n]. \tag{4.3}$$

Here, the kinetic energy is simply the sum over the electrons of the individual contributions

$$T_e^0[n] = -\frac{\hbar^2}{2m_e}\sum_i \int \psi_i^* \nabla_i^2 \psi_i d\boldsymbol{r}, \tag{4.4}$$

where the single-electron wave functions $\psi_i(\boldsymbol{r})$ have been introduced and their use will be discussed later. The second term, $E_{\mathrm{H}}[n]$, describes the electrostatic interaction between charge densities and is called the *Hartree* functional

$$E_{\mathrm{H}}[n] = \frac{e^2}{2}\iint \frac{n(\boldsymbol{r})n(\boldsymbol{r}')}{|\boldsymbol{r}-\boldsymbol{r}'|}d\boldsymbol{r}d\boldsymbol{r}' = \frac{e^2}{2}\int V_{\mathrm{H}}(\boldsymbol{r})n(\boldsymbol{r})d\boldsymbol{r}. \tag{4.5}$$

Lastly, the energy functional $E_{\mathrm{XC}}[n]$ is the exchange-correlation functional and corresponds to the energy difference between the real interacting system and the non-interacting system. Hence, it incorporates all missing quantum-mechanical effects and writes as

$$E_{\mathrm{XC}}[n] = T_e[n] + V_{ee}[n] - T_e^0[n] - E_{\mathrm{H}}[n]. \tag{4.6}$$

The exchange-correlation functional is not known and must be approximated as part of the DFT workflow. One of the major challenges in DFT is identifying an accurate exchange-correlation functional that can effectively capture the effects at the quantum level as the accuracy of DFT calculations directly depends on this quantity. Examples of some commonly adopted E_{XC} functionals include the Local Density Approximation (LDA) [157]

$$E_{\mathrm{XC}}^{\mathrm{LDA}} = \int \epsilon_{\mathrm{XC}}^{\mathrm{LDA}} n(\boldsymbol{r})d\boldsymbol{r} \tag{4.7}$$

where $\epsilon_{\mathrm{XC}}^{LDA}$ is the exchange-correlation energy of the homogeneous electron gas of density $n(\boldsymbol{r})$. LDA assumes that the density varies slowly in space, making it possible to approximate the charge density of the system at a specific point with the charge

density of a homogeneous gas. The exchange contribution can be determined analytically, while the correlation contribution can be estimated through methods such as statistical quantum mechanics simulations. To account for inhomogeneities of the electron density in real systems, other methods that include a gradient $\nabla n(\boldsymbol{r})$ correction have been developed and are classified as Generalized Gradient Approximations (GGA). The final Kohn-Sham energy functional can thus be written as

$$E[n] = T_e^0[n] + E_H[n] + E_{\mathrm{XC}} + \int V_{ext}(\boldsymbol{r}) n(\boldsymbol{r}) d\boldsymbol{r}. \tag{4.8}$$

which has to be minimized with the constraint that the total number of electrons N is fixed,

$$N = \int n(\boldsymbol{r}) d\boldsymbol{r}. \tag{4.9}$$

Defining the respective Lagrangian functional

$$\mathcal{L}[n] = E[n] - \lambda \left[\int n(\boldsymbol{r}) d\boldsymbol{r} - N \right] \tag{4.10}$$

and imposing $\delta\mathcal{L}[n] = 0$, leads to the condition for the interacting system:

$$\frac{\delta T_e^0}{\delta n} + \frac{\delta E_{\mathrm{H}}}{\delta n} + \frac{\delta E_{\mathrm{XC}}}{\delta n} + V_{ext}(\boldsymbol{r}) - \lambda = 0. \tag{4.11}$$

In the non-interacting system, an effective potential V_{KS} is added to simulate all the electron-electron interactions, resulting in a charge density that is identical to that of the real system. The respective minimization is

$$\frac{\delta T_e^0}{\delta n} + V_{\mathrm{KS}} - \lambda = 0. \tag{4.12}$$

Since V_{KS} must be equivalent to the real-system potential, it is possible to define the Kohn-Sham potential as

$$V_{\mathrm{KS}} = \frac{\delta E_{\mathrm{H}}}{\delta n} + \frac{\delta E_{\mathrm{XC}}}{\delta n} + V_{ext}(\boldsymbol{r}), \tag{4.13}$$

with

$$V_{\mathrm{H}} = \frac{\delta E_{\mathrm{H}}}{\delta n} = e^2 \int \frac{n(\boldsymbol{r}) d\boldsymbol{r}}{|\boldsymbol{r} - \boldsymbol{r}'|}, \quad \text{and} \quad V_{\mathrm{XC}} = \frac{\delta E_{\mathrm{XC}}}{\delta n}. \tag{4.14}$$

The approach involves solving a set of N single-particle equations, known as the Kohn-Sham equations, in a self-consistent field (SCF) manner,

$$\underbrace{\left[-\frac{\hbar^2 \nabla^2}{2m_e} + V_{\mathrm{KS}} \right]}_{\mathcal{H}_{\mathrm{KS}}} \psi_i(\boldsymbol{r}) = \varepsilon_i \psi_i(\boldsymbol{r}), \tag{4.15}$$

where $\mathcal{H}_{\mathrm{KS}}$ is the single-particle Kohn-Sham Hamiltonian and $\psi_i(\boldsymbol{r})$ are the single-particle wave functions with eigenenergies ε_i. The starting point of the method is

the construction of the wave functions $\psi_i(\boldsymbol{r})$ as linear combinations of a set of basis functions $\phi_j(\boldsymbol{r})$

$$\psi_i(\boldsymbol{r}) = \sum_j c_{ji}\phi_j(\boldsymbol{r}). \tag{4.16}$$

The charge density can then be evaluated from the single-electron wave functions

$$n(\boldsymbol{r}) = \sum_i^N |\psi_i(\boldsymbol{r})|^2, \tag{4.17}$$

and adopted to calculated an initial guess of the Kohn-Sham potential and thus the Hamiltonian. It is then possible to solve iteratively the Kohn-Sham equations, which lead to new wave functions that are used to calculate an improved charge density that will serve as input for a new cycle. The procedure repeats until some convergency criteria is met: the input and output charge densities are compared after each iteration and if the difference is small enough, then the output value is the ground state density and it is used to compute in the variational formalism the total energy of the system which corresponds approximately to the total energy of the real system. A sketch of the SCF cycle is shown in Fig. 4.4.

4.1.1 Spin Density Functional Theory

The present work aims to determine the magnetic properties of RE-systems, hence it is necessary to extend the above described DFT workflow to include the spin degree of freedom [158, 159], in order to simulate and observe fundamental magnetic phenomena driven by the RE atoms. In the spin-polarized case, the electrons are unrestricted, meaning electrons with opposite spins are not restricted to share the same spatial wave function, as sketched in Fig. 4.2. As a result, it is necessary to consider not only the scalar charge density, $n(\boldsymbol{r})$, but also the magnetization density, $\boldsymbol{m}(\boldsymbol{r})$, which is a 3-component vector.

When extending DFT to the spin-polarized case, Hohenberg-Kohn theorems now require the determination of a ground state density that is dependent on both the charge and magnetization density. The spin density matrix is introduced as a 2×2 matrix that can be decomposed into the scalar contribution and the vector contribution [160]:

$$\underline{n}(\boldsymbol{r}) = \frac{1}{2}(n(\boldsymbol{r})\underline{I} + \underline{\boldsymbol{\sigma}} \cdot \boldsymbol{m}(\boldsymbol{r})) = \frac{1}{2}\begin{pmatrix} n(\boldsymbol{r}) + m_z(\boldsymbol{r}) & m_x(\boldsymbol{r}) - im_y(\boldsymbol{r}) \\ m_x(\boldsymbol{r}) + im_y(\boldsymbol{r}) & n(\boldsymbol{r}) - m_z(\boldsymbol{r}) \end{pmatrix}, \tag{4.18}$$

where the underlined notation indicates matrices and the bold represents vectors. $\underline{I}$ is a 2×2 unit matrix and $\underline{\boldsymbol{\sigma}}$ is a vector of the Pauli matrices:

$$\sigma_x = \begin{pmatrix} 0 & 1 \\ 1 & 0 \end{pmatrix}, \quad \sigma_y = \begin{pmatrix} 0 & -i \\ i & 0 \end{pmatrix}, \quad \sigma_z = \begin{pmatrix} 1 & 0 \\ 0 & -1 \end{pmatrix}. \tag{4.19}$$

Restricted vs. unrestricted DFT

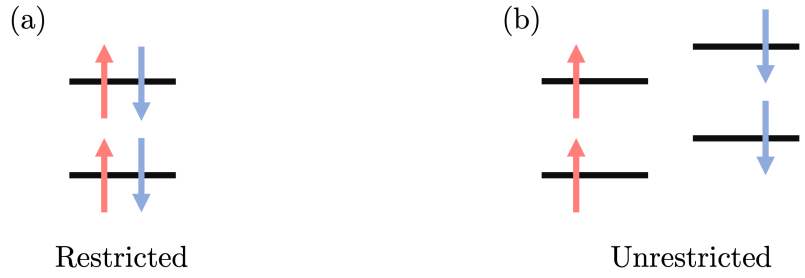

Figure 4.2: (a) Restricted DFT: electrons with opposite spin occupy the same spatial wave function. (b) Unrestricted DFT: electrons with opposite spin can occupy different spatial wave functions.

The components $n^{\alpha\beta}(\boldsymbol{r})$ of Eq. 4.18,

$$n^{\alpha\beta}(\boldsymbol{r}) = \frac{1}{2}(n(\boldsymbol{r})\delta^{\alpha\beta} + m_x(\boldsymbol{r})\sigma_x^{\alpha\beta} + m_y(\boldsymbol{r})\sigma_y^{\alpha\beta} + m_z(\boldsymbol{r})\sigma_z^{\alpha\beta}), \tag{4.20}$$

depend on the electronic density and magnetization density defined as

$$n(\boldsymbol{r}) = \sum_{\alpha} n^{\alpha\alpha}(\boldsymbol{r}), \quad \boldsymbol{m}(\boldsymbol{r}) = -\mu_B \sum_{\alpha\beta} \underline{\boldsymbol{\sigma}}^{\alpha\beta} n^{\alpha\beta}(\boldsymbol{r}), \tag{4.21}$$

where the spin indices, denoted as α and β, can take on two possible values, namely up $\uparrow$ and down $\downarrow$. In the Kohn-Sham formalism, the energy functional now depends on both the charge density and the magnetization density [161],

$$\begin{aligned} E[n^{\alpha\beta}(\boldsymbol{r})] = T_e^0[n^{\alpha\beta}(\boldsymbol{r})] + \frac{e^2}{2} \iint \frac{n(\boldsymbol{r})n(\boldsymbol{r}')}{|\boldsymbol{r}-\boldsymbol{r}'|} d\boldsymbol{r}d\boldsymbol{r}' \\ + \sum_{\alpha\beta} \int V_{ext}^{\alpha\beta} n^{\alpha\beta}(\boldsymbol{r}) + E_{\mathrm{XC}}[n^{\alpha\beta}(\boldsymbol{r})]. \end{aligned} \tag{4.22}$$

From this it is seen that only the Hartree energy depends on the total charge density, while all other contributions depend on the spin. When considering spin-polarized DFT, the external potential, V_{ext}, now includes not only the potential from the nuclei, but also the effects of an external magnetic field. This arises naturally when extending the Schrödinger equation to include relativistic effects through the use of the Dirac equation for an electron moving in an electromagnetic field. When solving this equation in the non-relativistic limit (where the electron's speed is much smaller

than the speed of light), it results in contributions to the Hamiltonian in the form $-\underline{\boldsymbol{\sigma}} \cdot \boldsymbol{B}$, which describe the interaction between the spin and the magnetic field.

As in standard DFT, in order to determine the ground state spin-density matrix, it is necessary to introduce single-particle wave functions in order to define $\mathcal{H}_{\mathrm{KS}}$. However, the main difference from the restricted case is that these wave functions are now determined by spin-dependent spatial wave functions or *spin-orbitals*. In the general case, the Kohn-Sham equations for a spin density matrix in the form of Eq. 4.18 are associated to an external potential,

$$\underline{V}_{ext}(\boldsymbol{r}) = V_{ext}(\boldsymbol{r})\underline{I} + \mu_{\mathrm{B}}\underline{\boldsymbol{\sigma}} \cdot \boldsymbol{B}(\boldsymbol{r}), \tag{4.23}$$

and exchange-correlation potential

$$\frac{\delta E_{\mathrm{XC}}}{\delta \underline{n}(\boldsymbol{r})} = V_{\mathrm{XC}}(\boldsymbol{r})\underline{I} + \mu_{\mathrm{B}}\underline{\boldsymbol{\sigma}} \cdot \boldsymbol{B}_{\mathrm{XC}}(\boldsymbol{r}). \tag{4.24}$$

Solution of the respective Kohn-Sham equations leads to the spin density matrix

$$n^{\alpha\beta}(\boldsymbol{r}) = \sum_i \psi_i^{*\alpha}(\boldsymbol{r})\psi_i^{\beta}(\boldsymbol{r}). \tag{4.25}$$

When the spin density matrix is diagonal, it indicates that the magnetic fields, including both external and exchange contributions, align in the direction of the z-axis. This situation characterizes a collinear spin system, where the magnetic moments are aligned exclusively along the z-axis. As a result, the Kohn-Sham equations can be decoupled into two distinct equations, one for each spin direction (up $\uparrow$ and down $\downarrow$). Expressing the functionals in terms of single-particle wave functions, for example the kinetic energy functional for each spin writes as

$$\begin{aligned} T_e^0[n^{\uparrow}(\boldsymbol{r})] &= -\frac{\hbar^2}{2m_e}\sum_i \int \psi_i^{*\uparrow}\nabla_i^2\psi_i^{\uparrow}d\boldsymbol{r} \\ T_e^0[n^{\downarrow}(\boldsymbol{r})] &= -\frac{\hbar^2}{2m_e}\sum_i \int \psi_i^{*\downarrow}\nabla_i^2\psi_i^{\downarrow}d\boldsymbol{r}, \end{aligned} \tag{4.26}$$

with $n^{\uparrow}(\boldsymbol{r})$ and $n^{\downarrow}(\boldsymbol{r})$ the spin-up and spin-down charge densities

$$\begin{aligned} n^{\uparrow}(\boldsymbol{r}) &= \sum_i^{N_{\uparrow}} |\psi_i^{\uparrow}(\boldsymbol{r})|^2 \\ n^{\downarrow}(\boldsymbol{r}) &= \sum_i^{N_{\downarrow}} |\psi_i^{\downarrow}(\boldsymbol{r})|^2, \end{aligned} \tag{4.27}$$

and minimizing the energy functional subject to the constraint of conservation of the number of particles, the Kohn-Sham equations for each spin are obtained:

$$\left[-\frac{\hbar^2}{2m_e}\nabla_i + V_{eff}^{\uparrow}(\boldsymbol{r})\right]\psi_i^{\uparrow}(\boldsymbol{r}) = \varepsilon_i^{\uparrow}\psi_i^{\uparrow}(\boldsymbol{r}) \tag{4.28}$$

$$\left[-\frac{\hbar^2}{2m_e}\nabla_i + V_{eff}^{\downarrow}(\boldsymbol{r})\right]\psi_i^{\downarrow}(\boldsymbol{r}) = \varepsilon_i^{\downarrow}\psi_i^{\downarrow}(\boldsymbol{r}), \tag{4.29}$$

and solved simultaneously, following the standard DFT prescription. In Eqs. 4.28 and 4.29, V_{eff} represents the effective potential, which encompasses the Hartree term, the external potential, and the exchange-correlation term. The total charge density is defined as the sum of the spin-up and spin-down densities, while the magnetization density becomes the difference between the spin-up and spin-down densities:

$$\begin{aligned} n(\boldsymbol{r}) &= n^{\uparrow}(\boldsymbol{r}) + n^{\downarrow}(\boldsymbol{r}) = \sum_{i}^{N_{\uparrow}} |\psi_i^{\uparrow}(\boldsymbol{r})|^2 + \sum_{i}^{N_{\downarrow}} |\psi_i^{\downarrow}(\boldsymbol{r})|^2 \\ m_z(\boldsymbol{r}) &= n^{\uparrow}(\boldsymbol{r}) - n^{\downarrow}(\boldsymbol{r}) = \sum_{i}^{N_{\uparrow}} |\psi_i^{\uparrow}(\boldsymbol{r})|^2 - \sum_{i}^{N_{\downarrow}} |\psi_i^{\downarrow}(\boldsymbol{r})|^2. \end{aligned} \tag{4.30}$$

Finally, the spin magnetic moment per unit of volume is defined as the integral over V of the magnetization density,

$$m_{spin} = \int_V (n^{\uparrow}(\boldsymbol{r}) - n^{\downarrow}(\boldsymbol{r}))d\boldsymbol{r} \tag{4.31}$$

and is defined in units of μ_{B}.

4.2 The Hubbard Model

The previous sections outlined the use of standard DFT as an effective approach for calculating properties of a wide range of materials, particularly in solids with high electron mobility, such as metals. However, it is widely recognized that DFT is not able to accurately describe strongly-localized electrons, as the limited spatial distribution leads to stronger interactions and a correlated dynamics. In statistical terms this means that the probability to find an electron at one coordinate and another electron at a second position, differs from the product of the two individual probabilities. The shortcomings of DFT are rooted in the way it handles many-body interactions, which are represented as functionals of the electron charge density, and the use of approximate exchange-correlation functionals, along with a single-particle treatment in solving the Kohn-Sham equations. These observations are critical when simulating the behavior of $4f$ electrons in RE atoms, as these electrons have a highly restricted spatial distribution and cannot be accurately described within the DFT picture.

A straightforward model that allows for a more accurate characterization of $4f$ electrons (and in general, correlated materials) is the *Hubbard model*, which can easily be integrated into the DFT process (as discussed in Section 4.2.1).

The Hubbard model

The fundamental idea behind the Hubbard model is to introduce a correction that accounts for the missing on-site electron-electron interactions. The Hubbard model views the atoms in a crystal as distinct sites that can accommodate a maximum of two electrons with opposite spins, as dictated by the Pauli exclusion principle. This means that each site can hold one electron with either spin-up or spin-down, or two electrons with opposite spins. The Hubbard Hamiltonian can be formally written in second quantization notation as the sum of two terms that capture the dynamics of the electrons in the lattice [162]:

$$\mathcal{H}_{Hubbard} = t \sum_{\langle i,j\rangle,\sigma} (c^{\dagger}_{i,\sigma} c_{j,\sigma} + h.c.) + U \sum_{i} n_{i,\uparrow} n_{i,\downarrow}. \tag{4.32}$$

The notation used includes $\langle i, j\rangle$ for the nearest-neighbor sites, $c^{\dagger}_{i,\sigma}$ is the creation operator of an electron at site i and spin σ, $c_{j,\sigma}$ is the annihilation operator of an electron at site j and spin σ and $n_{i,\sigma}$ is the number operator for electrons on site i and with spin σ. In Eq. 4.32 the first term describes the hopping of an electron from one atomic site to another with amplitude t, which is determined by the bandwidth of the valence states. The second term represents the strong Coulomb repulsion that occurs between electrons occupying the same atomic site, which is described by the parameter U, also known as the Hubbard U. The Hubbard U term is only applied to electrons on the same site, in order to account for the strong localization of the electrons of interest, and this is mathematically represented by the product of the occupation numbers on that site. A sketch of the model is depicted in Fig. 4.3.

The model predicts a transition from a metallic phase to an insulating phase based on the ratio of U/t. When $t >> U$ the extension of neighboring orbitals is such that the electrons are free to move through the crystal, and standard DFT is sufficient to achieve a good description of the electronic properties. Conversely, when $t << U$, the hopping of electrons is not energetically favored due to the strong Coulomb repulsion from double occupancy, causing the electrons to remain localized at their atomic sites. This results in insulating behavior and isolated magnetic moments.

4.2.1 DFT+U

The DFT+U method can be utilized to improve the description of the ground state properties of correlated electron systems by incorporating the Hubbard model into the DFT cycle. This is achieved by adding a U parameter to the treatment of localized electrons, such as the $4f$ electrons, while continuing to describe all delocalized electrons using conventional DFT methods.

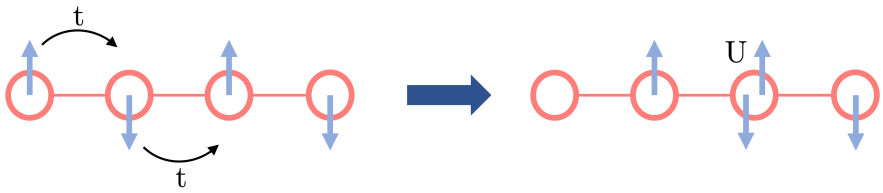

Figure 4.3: The Hubbard model can be schematized as follows: electrons can move from one atomic site to a neighboring site with kinetic energy t. When a site is occupied by two electrons, the Coulomb interaction between them is described by the parameter U.

DFT+U method

The method involves a combination of the standard DFT functional, $E_{\mathrm{DFT}}[n(\boldsymbol{r})]$, and the Hubbard functional, $E_{Hubbard}[n^{I\sigma}_{mm'}]$, which contains the electron-electron interactions between the localized electrons as described within the Hubbard model. However, to avoid double-counting problems, it is necessary to subtract the functional $E_{\mathrm{dc}}[n^{I\sigma}]$ from the formulation, as the DFT part already accounts for a part of the correlation energy:

$$E_{\mathrm{DFT}+U}[n(\boldsymbol{r})] = E_{\mathrm{DFT}}[n(\boldsymbol{r})] + E_{Hubbard}[n^{I\sigma}_{mm'}] - E_{\mathrm{dc}}[n^{I\sigma}]. \tag{4.33}$$

More precisely, the Hubbard term is dependent on the occupation numbers of the localized orbitals, which are identified by the indices I, σ, and m, consistent with the fact that the U correction is only applied to the localized electrons. Here, I represents the atomic site, σ denotes the spin index, and m corresponds to the localized state. The occupation numbers can be computed as the projections of the Kohn-Sham orbitals, ψ^{σ}_{kv}, onto the localized states, $\phi^{I}_{m'}$. This is expressed as follows:

$$n^{I\sigma}_{mm'} = \sum_{k,v} f^{\sigma}_{kv} \langle \psi^{\sigma}_{kv} | \phi^{I}_{m'} \rangle \langle \phi^{I}_{m} | \psi^{\sigma}_{kv} \rangle , \tag{4.34}$$

where f^{σ}_{kv} stands for the Kohn-Sham occupation as determined by the Fermi-Dirac distribution and k, v, and σ refer to the k-point, band, and spin indices, respectively. I and m are used to identify the atomic site and the localized states at a given atom I.

The functional $E_{\mathrm{dc}}[n^{I\sigma}]$ in Eq. 4.33 is approximated as a mean-field evaluation of the Hubbard energy functional and different formulations are currently available. Considering the case of a Hubbard correction in the form $\frac{1}{2}U\sum_{m,\sigma\neq m'\sigma'} n^{I\sigma}_{m} n^{I\sigma'}_{m'}$, with a total number of electrons $N^{I} = \sum_{m,\sigma} n^{I\sigma}_{m}$, then the DFT+$U$ energy functional writes as

$$E_{\mathrm{DFT}+U} = E_{\mathrm{DFT}} + \sum_{I} \left[\frac{U^{I}}{2} \sum_{m,\sigma\neq m'\sigma'} n^{I\sigma}_{m} n^{I\sigma'}_{m'} - \frac{U^{I}}{2} N^{I}(N^{I}-1) \right], \tag{4.35}$$

with $n_m^{I\sigma} = n_{mm'}^{I\sigma}$. The last term in this equation is the double-counting term. From this equation, the orbital energies can be evaluated by taking the derivative of the DFT+U energy functional with respect to the occupation number of a specific state [163]:

$$\varepsilon_m^{I\sigma} = \frac{\partial E_{\mathrm{DFT}+U}}{\partial n_m^{I\sigma}} = \varepsilon_{\mathrm{DFT}} + U^I\left(\frac{1}{2} - n_m^{I\sigma}\right). \tag{4.36}$$

It is evident that the U term results in an energy shift of $-U/2$ for occupied orbitals ($n_m^{I\sigma} = 1$) and an energy shift of $U/2$ for unoccupied orbitals ($n_m^{I\sigma}$=0). Similarly, the DFT+U potential is obtained deriving the energy functional with respect to the charge density of a specific orbital resulting again in a $U^I\left(\frac{1}{2} - n_m^{I\sigma}\right)$ term that determines a positive (repulsive) Hubbard potential if the orbital is less than half-filled ($n_m^{I\sigma} < 1/2$), and negative (attractive) when the orbital is more than half-filled ($n_m^{I\sigma} > 1/2$).

The drawback with Eq. 4.35 is that it is not invariant under rotation of the atomic basis set used for defining the occupation numbers, resulting in a dependence on the choice of the basis set. To address this problem, a rotationally-invariant formulation has been proposed in [164, 165], which eliminates the dependence on the atomic basis set and resembles the HF prescription:

$$\begin{aligned} E_{Hubbard}[n_{mm'}^{I\sigma}] = &\frac{1}{2}\sum_{\{m\},\sigma,I}\{\langle m, m''|V_{ee}|m', m'''\rangle\, n_{mm'}^{I\sigma} n_{m''m'''}^{I-\sigma} \\ &+(\langle m, m''|V_{ee}|m', m'''\rangle - \langle m, m''|V_{ee}|m''', m'\rangle) n_{mm'}^{I\sigma} n_{m''m'''}^{I\sigma}\}. \end{aligned} \tag{4.37}$$

In the limit of fully-occupied orbitals where each orbital is either fully-occupied or empty, the double-counting term resulting from this approximation applied to Eq. 4.37 reduces to

$$E_{\mathrm{DC}}[n_{mm'}^{I\sigma}] = \sum_I \{\frac{U^I}{2} N^I(N^I - 1) - \frac{J^I}{2}\left[N^{I\uparrow}(N^{I\uparrow} - 1) + N^{I\downarrow}(N^{I\downarrow} - 1)\right]\}. \tag{4.38}$$

This result is often referred to as the *Fully-localized limit* (FLL). Here, $N^I = N^{I\uparrow} + N^{I\downarrow}$ and U and J represent the screened Coulomb and exchange parameters, respectively.

It is possible to determine the matrix elements of the electron-electron interaction terms of Eq. 4.37 by describing the atomic orbitals ϕ in terms of a product of a radial and a spherical harmonic function as illustrated in Eq. 2.4.

$$\langle m, m''|V_{ee}|m', m'''\rangle = \int d\boldsymbol{r} \int d\boldsymbol{r}' \phi_{lm}^*(\boldsymbol{r})\phi_{lm'}(\boldsymbol{r})\frac{1}{|\boldsymbol{r} - \boldsymbol{r}'|}\phi_{lm''}^*(\boldsymbol{r}')\phi_{lm'''}(\boldsymbol{r}'). \tag{4.39}$$

As already discussed, by the combination of Eq. 2.26 and Eq. 2.27, the Coulomb kernel $1/|\boldsymbol{r}-\boldsymbol{r}'|$ can be expanded in spherical harmonics, which inserted in Eq. 4.39, leads to the formulation of the matrix elements:

$$\begin{aligned} U_{mm''m'm'''} &= \langle m, m''|V_{ee}|m', m'''\rangle = \sum_k a_k(m, m', m'', m''')F^k \\ J_{mm''m'''m'} &= \langle m, m''|V_{ee}|m''', m'\rangle = \sum_k a_k(m, m''', m'', m')F^k, \end{aligned} \tag{4.40}$$

where the factors a_k are given by:

$$a_k(m, m', m'', m''') = \frac{4\pi}{2k+1}\sum_{q=-k}^{k}\langle lm|Y_k^q|lm'\rangle\langle lm''|Y_k^{q*}|lm'''\rangle\,. \tag{4.41}$$

Here, k is the angular moment of the potential and is restricted to the range $0 \le k \le 2l$ (similarly, to the selection rules described in Section 2.3.2), where is l the angular moment of the localized orbitals. The Slater integrals, on the other hand, determine the radial part of Eq. 4.40 as follows:

$$F^k = \int dr \int dr' r^2 r'^2 R_{nl}^2(r)\frac{r_<^k}{r_>^{(k+1)}}R_{nl}^2(r') \tag{4.42}$$

where $r_<$ and $r_>$ are the smaller and larger radial distance between r and r' [166]. In the case of d electrons, F^0, F^2, and F^4 are necessary, whereas for f electrons, the F^6 term is also required.

Going now back to the definition of the double-counting functional as a mean-field picture of the Hubbard term, the U and J parameters in Eq. 4.38 can be defined as averages of the integrals in Eq. 4.40 over the localized states of fixed quantum number l:

$$\begin{aligned} U &= \frac{1}{(2l+1)^2}\sum_{m,m'}\langle m, m'|V_{ee}|m, m'\rangle \\ J &= \frac{1}{2l(2l+1)}\sum_{m\neq m',m'}\langle m, m'|V_{ee}|m', m\rangle \end{aligned} \tag{4.43}$$

where equations 4.43 are linked to the Slater integrals, which can be calculated and utilized to evaluate the V_{ee} integrals. The determination of Hubbard U and exchange parameter J is usually done in a semi-empirical manner by comparing with experimental results. Alternative methods involve the first-principle calculations of Hubbard U via for example Random Phase Approximation [167–169] or linear response theory [170]. However, the DFT+U method is limited in that the values depend on various factors like the type of atoms, the crystal structure, and magnetic properties, making them not easily transferable from one system to another or between different codes.

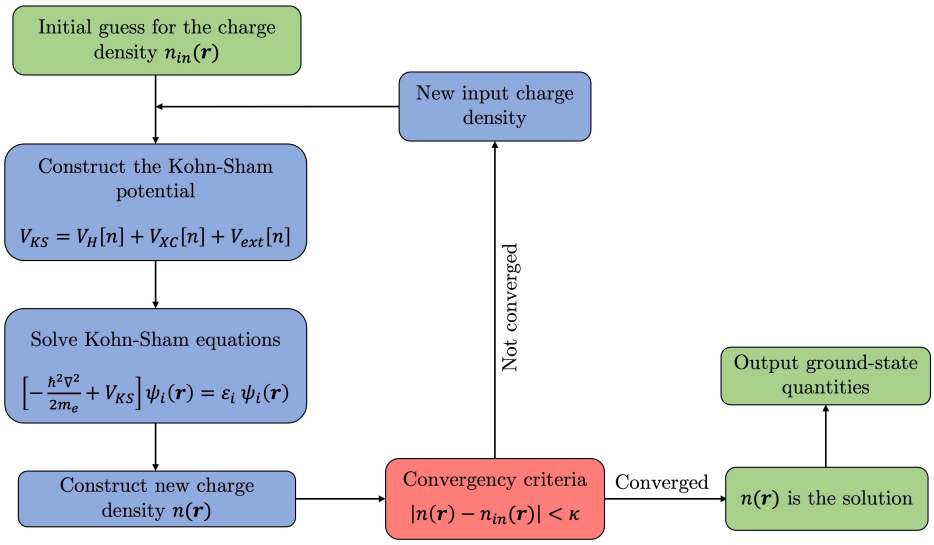

Figure 4.4: DFT self-consistent cycle.

Effect of the Hubbard U

In Fig. 4.5, the impact of increasing values of the Hubbard U on the $4f$ states of a Gd atom deposited on graphene is displayed via simulations performed adopting the FLEUR code (See Section 4.3). The top half of the plots displays the density of states (DOS) for the spin-up channel, while the bottom half shows the spin-down channel DOS. The total DOS (TDOS) of the system (Gd/Gr) is shown in grey, with the d and f states of the Gd adatom plotted in blue and red, respectively. In general, it can be seen that applying a Hubbard correction results in a larger energy splitting between the spin-up and spin-down $4f$ peaks. Precisely, in the standard DFT calculation, a magnetic moment of the Gd atom of 7.016 μ_B is calculated and the $4f$ spin-down peak lies at the Fermi energy suggesting a metallic character of the $4f$ electrons. This indicates that standard DFT is not accurate in the description of the localized $4f$ electrons. Applying a correction of U = 3 eV, the effect is to push the spin-up states lower in energy and the spin-down states away from the Fermi energy, leading to a magnetic moment of 7.235 μ_B, thus increasing the localization of the $4f$ electrons. Finally, in the U = 6.7 eV case, the $4f$ peaks are separated by an energy gap of ~ 11 eV leading to a magnetic moment of 7.319 μ_B and a fully insulating behavior of the localized $4f$ states.
This example highlights the importance to incorporate a correction into the DFT procedure in order to obtain a more accurate representation of the $4f$ electrons and the resulting properties.

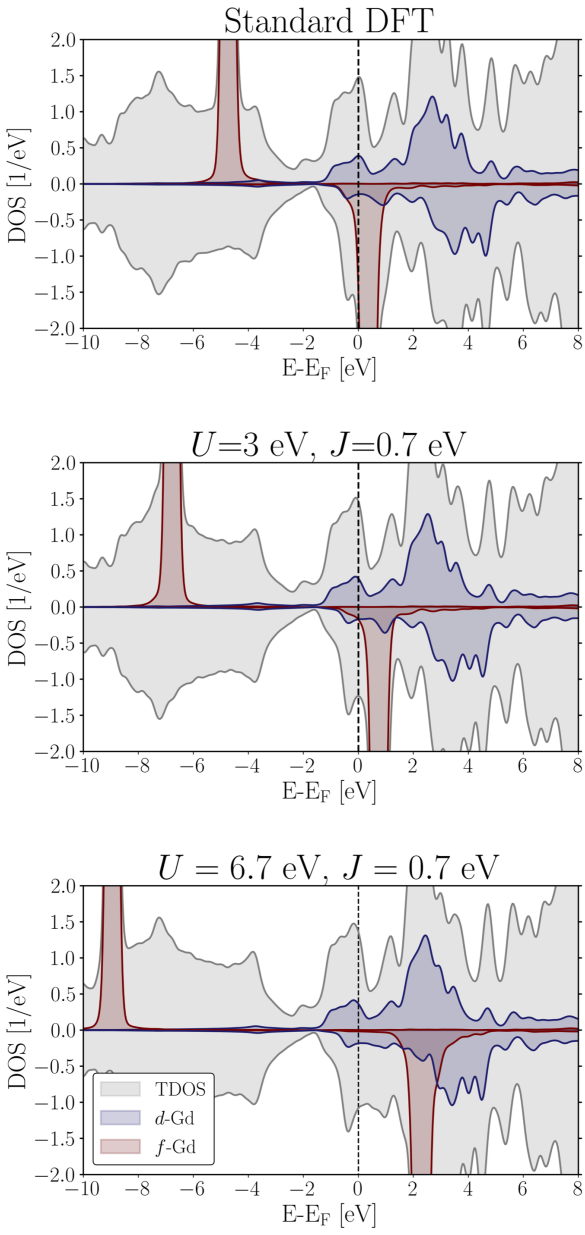

Figure 4.5: Effect of the Hubbard U correction on the $4f$ states of a Gd/Gr system calculated in the DFT framework. The $4f$ peaks get separated in energy the bigger the U value and are pushed away from the Fermi energy resulting in an localized and insulating character.

4.3 Full-potential linearized augmented plane-wave method

The variational principle offers a method to obtain the solution to the eigenvalue problem for a set of N states, given by the equation

$$\mathcal{H}\left|\psi_i\right\rangle = \varepsilon_i \left|\psi_i\right\rangle, \quad i = 1, ..., N. \tag{4.44}$$

This principle guarantees that energies obtained using approximate wave functions are higher than or equal to the exact energy solution. For the purposes of DFT calculations, the wave function $|\psi_i\rangle$ can be expressed as a linear combination of basis functions:

$$\left|\psi_i\right\rangle = \sum_j^L c_{ji} \left|\phi_j\right\rangle. \tag{4.45}$$

By inserting Eq. 4.45 in Eq. 4.44 and multiplying by $\langle\phi_k|$ on the left, this leads to

$$\sum_j^L c_{ji} \left\langle\phi_k|\mathcal{H}|\phi_j\right\rangle = \varepsilon_i \sum_j^L c_{ji} \left\langle\phi_k|\phi_j\right\rangle, \quad i = 1, ..., N \tag{4.46}$$

and the problem transforms into a generalized Hermitian matrix eigenvalue problem,

$$\sum_j^L c_{ji}\mathcal{H}_{kj} = \varepsilon_i \sum_j^L S_{kj}, \quad i = 1, ..., N \tag{4.47}$$

where c_{ji} is the j-th coefficient in the expansion of the i-th eigenfunction, ε_i is the i-th eigenvalue, while the Hamiltonian matrix $\mathcal{H}_{kj}$ and the overlap matrix S_{kj} have the same dimension as the number of basis functions L. The set of equations can be expressed in a compact form as:

$$\mathbf{HC} = \mathbf{SC}\boldsymbol{\varepsilon} \tag{4.48}$$

where $\mathbf{C}$ is the matrix of the expansion coefficients and $\boldsymbol{\varepsilon}$ is a diagonal matrix of the N ε_i eigenenergies corresponding to the eigenfunctions $|\psi_i\rangle$. Computationally, the selection of the basis set has a significant impact on both the cost of the computation and the accuracy of the results. Different techniques can be used to represent the target wave functions and the choice is largely dependent on the problem at hand. Some common methods include the Linear Combination of Atomic Orbitals (LCAO), where molecular orbitals are expressed as linear combinations of known atomic orbitals, typically in the form of Slater Type Orbitals (STO), Gaussian Type Orbitals (GTO) [171–173], or related variants, which are frequently used in quantum chemistry.

For periodic systems, the wave functions are typically described differently as the atomic character of the orbitals is partially lost, particularly for spatially delocalized electrons. According to Bloch's theorem, the wave functions in a periodic potential, labelled by the band index n and the Bloch vector $\boldsymbol{k}$, can be expressed as a product of a plane wave and a function with the same periodicity as the Bravais lattice:

$$\psi_{n\boldsymbol{k}}(\boldsymbol{r}) = u_{n\boldsymbol{k}}(\boldsymbol{r})e^{i\boldsymbol{k}\cdot\boldsymbol{r}}, \tag{4.49}$$

where $u_{n\boldsymbol{k}}(\boldsymbol{r}) = u_{n\boldsymbol{k}}(\boldsymbol{r} + \boldsymbol{R})$, $\boldsymbol{R}$ being a lattice vector. The periodic part can be expressed in terms of plane waves

$$u_{n\boldsymbol{k}}(\boldsymbol{r}) = \sum_{\boldsymbol{G}} c_{n\boldsymbol{k}}^{\boldsymbol{G}} e^{i\boldsymbol{G}\cdot\boldsymbol{r}}, \tag{4.50}$$

which leads to a description of the wave function as a linear combination of plane waves in the Fourier series:

$$\psi_{n\boldsymbol{k}}(\boldsymbol{r}) = \sum_{\boldsymbol{G}} c_{n\boldsymbol{k}}^{\boldsymbol{k},\boldsymbol{G}} e^{i(\boldsymbol{k}+\boldsymbol{G})\cdot\boldsymbol{r}}. \tag{4.51}$$

In this equation, $\boldsymbol{G}$ is a reciprocal lattice vector and $c_{n\boldsymbol{k}}^{\boldsymbol{k},\boldsymbol{G}}$ are the expansion coefficients. The cut-off for the expansion is usually selected by considering the fact that the contribution of higher $|\boldsymbol{k} + \boldsymbol{G}|$ terms is small. This cut-off is set using the criterion $|\boldsymbol{G} + \boldsymbol{k}| \leq \boldsymbol{K}_{max}$. To achieve the optimal balance between accuracy and computational cost, it is thus important to make a careful choice of the value of $\boldsymbol{K}_{max}$. However, it is important to note that the wave functions undergo significant changes in the vicinity of the atomic nucleus, with core electrons exhibiting peaks and valence electrons characterized by wavy features. This translates into the requirement of high cut-off values. In the *frozen core* approach, the core electrons are encoded in an approximate and smooth potential (pseudopotential) so that the remaining wave functions exhibit minimal spatial variation. This approach allows for the use of smaller basis sets and although computationally efficient, it often results in a loss of precision. Alternative methods include the core region in the calculations and are referred to as *all-electron* methods.

FLAPW

In the field of DFT, the Full-Potential Linearized Augmented Plane-Wave (FLAPW) method is widely recognized as one of the most precise all-electron methods available, due to its full treatment of both valence and core electrons. The FLAPW method can be understood as a successor of the Augmented Plane-Wave (APW) method, where the full treatment is accomplished by dividing the space into two distinct regions, namely the muffin-tin (MT) spheres (which do not overlap), around each atom, and the interstitial region (IR) located between the atoms, as depicted in Fig. 4.6.

To gain a comprehensive understanding of the FLAPW method, it is valuable to briefly discuss the key assumptions made within the APW framework. In this context, the potential inside of the MT is considered to be atomic-like *i.e.* spherical, allowing for the use of atomic basis functions. On the other hand, the IR is characterized by a slowly varying or constant potential, which can be described by plane waves.

The electron wave functions in the Kohn-Sham method are expressed as linear combinations of basis functions, in the following form [174–177]:

$$\psi_{n\boldsymbol{k}}(\boldsymbol{r}) = \sum_{|\boldsymbol{k}+\boldsymbol{G}|\leq \boldsymbol{K}_{max}} c_{n\boldsymbol{k}}^{\boldsymbol{k}+\boldsymbol{G}} \phi_{\boldsymbol{G}}(\boldsymbol{k},\boldsymbol{r}), \tag{4.52}$$

$$\phi_{\boldsymbol{G}}(\boldsymbol{k},\boldsymbol{r}) = \begin{cases} \dfrac{1}{\sqrt{V}} e^{i(\boldsymbol{k}+\boldsymbol{G})\cdot\boldsymbol{r}} & \text{IR region} \\ \displaystyle\sum_{L} a_L^{\alpha\boldsymbol{G}}(\boldsymbol{k}) u_l^{\alpha}(r^{\alpha}, E) Y_L(\hat{\boldsymbol{r}}^{\alpha}) & \text{MT region} \end{cases} \tag{4.53}$$

where V is the unit cell volume, $L = (l, m)$ indicates the orbital and magnetic quantum numbers, α represents the atomic index at position τ^{α}, and $\boldsymbol{r}^{\alpha} = \boldsymbol{r} - \tau^{\alpha}$ is the position vector relative to atom α. The MT basis functions are constructed from a combination of a spherical harmonic, $Y_L(\hat{\boldsymbol{r}})$, solution to the spherical potential, and a radial function u_l, which solves the radial Schrödinger equation (Eq. 2.5 with $R_{nl} = u_l$).

To ensure the continuity of the basis functions at the boundary of the MT, the coefficients $a_L^{\alpha\boldsymbol{G}}$ are determined by matching the functions at the boundary of the two regions. Additionally, the radial functions are dependent on the band energy E, making the problem non-linear, since E should be determined in a self-consistent way. To address this issue, the energy derivative of the radial function, $\dot{u}_l^{\alpha}(r^{\alpha}, E_l^{\alpha})$, is introduced as an augmentation inside of the MT region, which is now described by the radial function u_l and its derivative.

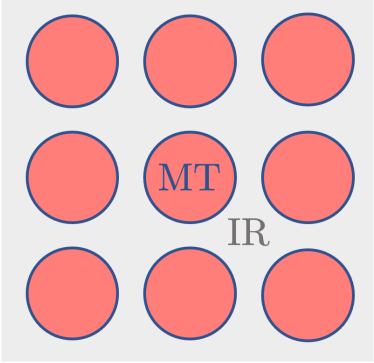

Figure 4.6: The space in the (FL)APW method is divided into two parts: the muffin-tin (MT) spheres, centered around each atom (represented in red), and the interstitial region (IR) in between the spheres (represented in grey).

This can be interpreted as a a Taylor expansion around the parameter E_l, thus linearizing the problem [174, 178] by the introduction of deviations around this value. In this way, it is possible to write

$$u_l^\alpha(r^\alpha, E) = u_l^\alpha(r^\alpha, E_l^\alpha) + (E - E_l^\alpha)\dot{u}_l^\alpha(r^\alpha, E_l^\alpha) + \mathcal{O}((E - E_l^\alpha)^2), \tag{4.54}$$

which leads to an error of $(E-E_l)^2$ in the wavefunction. In this linearized-formulation (LAPW), the basis set becomes:

LAPW basis set

$$\phi_{\boldsymbol{G}}(\boldsymbol{k}, \boldsymbol{r}) = \begin{cases} \dfrac{1}{\sqrt{V}} e^{i(\boldsymbol{k}+\boldsymbol{G})\cdot\boldsymbol{r}} & \text{IR region} \\ \displaystyle\sum_L \left[a_L^{\alpha\boldsymbol{G}}(\boldsymbol{k}) u_l^\alpha(r^\alpha, E_l^\alpha) + b_L^{\alpha\boldsymbol{G}}(\boldsymbol{k})\dot{u}_l^\alpha(r^\alpha, E_l^\alpha)\right] Y_L(\hat{\boldsymbol{r}}^\alpha) & \text{MT region} \end{cases} \tag{4.55}$$

and the coefficients $a_L^{\alpha\boldsymbol{G}}$ and $b_L^{\alpha\boldsymbol{G}}$ are obtained by enforcing continuity of the basis functions and the derivatives at the MT boundary in terms of value and slope. In the light of the above considerations, in FLAPW calculations, it is necessary to converge the total energy with respect to the $\boldsymbol{K}_{max}$, representing the number of basis functions in the IR region, and l_{max}, which determines the maximum number of terms in the expansion inside of the MT. Finally, the LAPW method can be extended to consider a *full* potential in the two regions, without shape-approximations as discussed in [179]. This can be achieved by relaxing the conditions of a spherical potential in the MT region and a constant potential in the IR region.

For the purpose of this thesis, all studies were performed using the FLEUR code [180], an open-source code based on density functional theory that implements the all-electron full-potential linearized augmented plane-wave method.

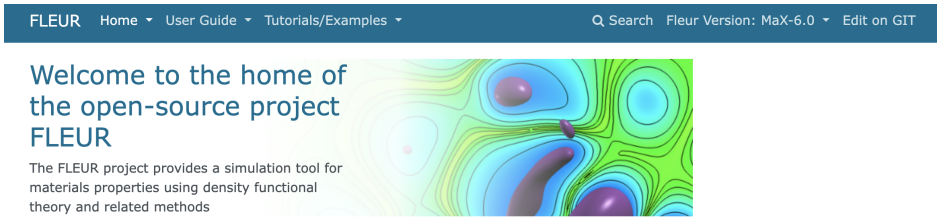

Figure 4.7: Homepage of FLEUR: https://www.flapw.de

Chapter 5

Electronic and magnetic properties of $4f$-adatoms on a graphene monolayer

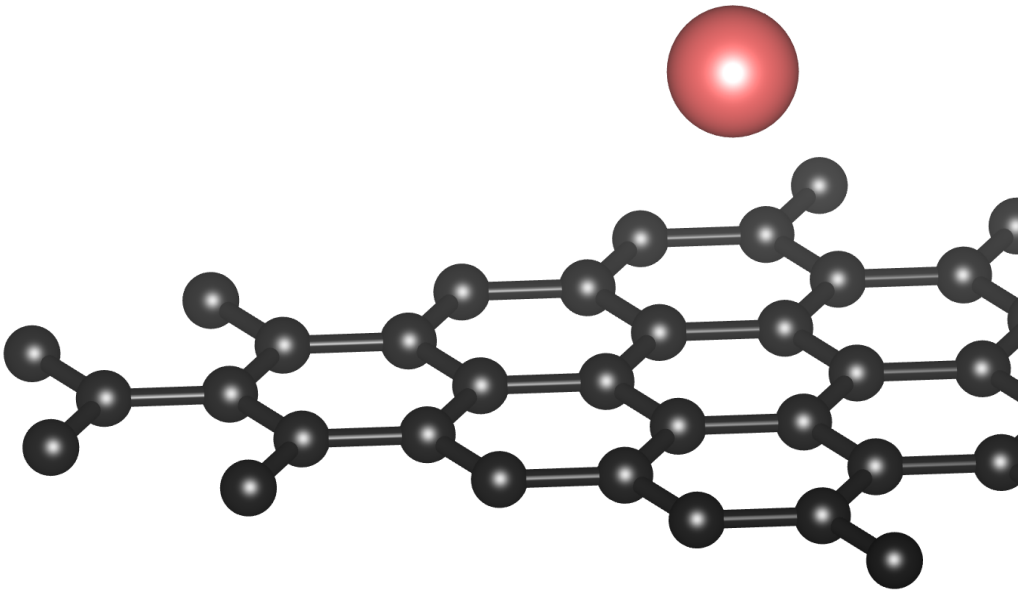

The focus of this chapter is to analyze the electronic and magnetic properties of five selected rare-earth atoms (Eu, Gd, Dy, Ho and Tm) on graphene. These elements include both half-filled and "heavy" rare-earth atoms with more than half-filled $4f$-shells. The chapter specifically explores the magnetic anisotropy properties and the reverse-engineering technique is used to compute the CFP for the highly-anisotropic systems. The findings for Dy, Ho and Tm can be found in the manuscript "Magnetic properties of $4f$ adatoms on graphene: Density functional theory investigations" by Johanna P. Carbone, Juba Bouaziz, Gustav Bihlmayer, and Stefan Blügel [181].

In the group of the selected RE atoms, Eu and Gd both have a half-filled $4f$-shell, leading to large spin magnetic moments but vanishing orbital moments. Eu is characterized by a valence electron configuration of $4f^7 6s^2$, while Gd has one additional d electron, $4f5d^1 6s^2$, which contributes to chemical bonding due to its larger spatial extension.

On the other hand, Dy, Ho and Tm are selected as representatives of heavy rare-earths, and exhibit spin and orbital moments that vary based on the occupation of the $4f$ orbitals. Their valence configurations can be represented as $4f^{10}6s^2$, $4f^{11}6s^2$, and $4f^{13}6s^2$, respectively. This requires the consideration of Coulomb-like correlations in addition to exchange correlation in determining the $4f$ orbital filling.

The second key-element is the 2D-material. In the context of single-atom magnets, the choice of graphene as a 2D-material is driven by its ability to decouple from underlying substrates, its hexagonal symmetry, and its minimal SOC. These properties render RE/Gr systems suitable for examining magnetic anisotropy effects caused by varying $4f$ occupations.

The present chapter will be organized as follows:

- The general electronic properties of RE on $\sqrt{3}\times\sqrt{3}$ graphene, including chemical adsorption and electronic structure, are addressed in Section 5.1. This section is divided into two parts: 1) the analysis of Eu/Gr and Gd/Gr, which are characterized by half-filled $4f$-shells; 2) the examination of more complex systems Dy/Gr, Ho/Gr, and Tm/Gr with increasing $4f$ occupancy.

- The analysis of magnetic anisotropy of the selected RE/Gr systems is presented in Section 5.2. The focus of the section is then directed towards the systems of Dy/Gr, Ho/Gr, and Tm/Gr, which exhibit highly anisotropic behavior due to the strong interplay between spin and orbital moments. To extract the magnetic anisotropy constants, the total energy curves are fitted, and the obtained values are subsequently used to evaluate crystal field parameters and the corresponding multiplet splittings for each system. The behavior of magnetic anisotropy energy

is studied with respect to the variation in the applied perpendicular strain and modification of the Hubbard U.

– The case of Dy/Gr deviating from Hund's rules is analyzed in Section 5.3, highlighting the importance of an accurate description of $4f$ electrons in determining magnetic anisotropy.

– Section 5.4 focuses on the effect of dilution of the rare-earth atoms by comparing the $\sqrt{3} \times \sqrt{3}$ simulation cell with a larger 4×4 simulation cell, providing an overview of the electronic structure based on the packing density of the magnetic atom.

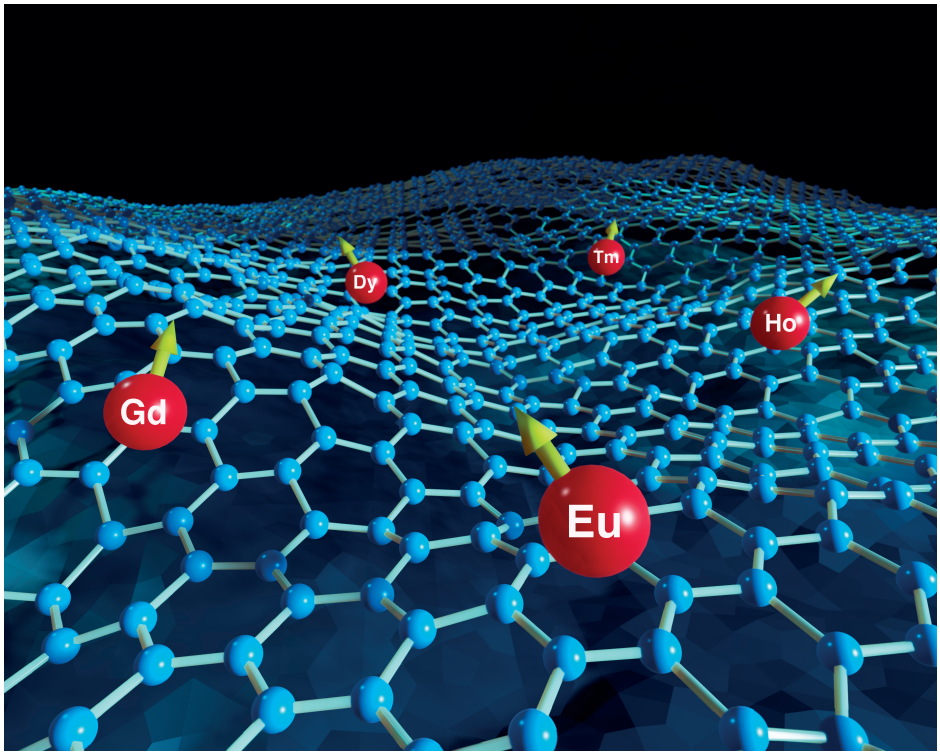

A graphical representation illustrating the investigated magnetic rare-earth atoms adsorbed on a monolayer of graphene. Credit for the design of this image goes to Daniele Valente.

5.1 Electronic properties of rare-earth adatoms on $\sqrt{3} \times \sqrt{3}$ graphene

Computational details

All presented results were obtained in the DFT+U framework as implemented in FLEUR, within the FLAPW method. The calculations were performed in a $\sqrt{3} \times \sqrt{3}$ simulation cell containing 6 C atoms and one rare-earth atom, with lattice constant taken equal to the experimental value (2.46 Å) times $\sqrt{3}$. The selection of the simulation cell is supported by both experimental and theoretical studies of the coverage of rare-earth atoms on graphene, which has been found to stabilize superstructures at a coverage of 33.3% ML [182, 183]. The value of the maximal angular momentum inside of the MT spheres was set to l_{max} = 10 for the rare-earth atoms and l_{max} = 6 for the C atoms, while in the IR region the cut-off for the plane-wave expansion was set to K_{max} = 4.5 a_0^{-1} (with a_0 the Bohr radius). The SCF cycle convergency was achieved using the GGA exchange-correlation functional in the Perdew, Burke, and Ernzerhof (PBE) prescription [184], in a 20 × 20 k-point mesh. Concerning the Hubbard U and J, the following values are used in the FLL limit : U = 6.7 eV, J = 0.7 eV for Eu and Gd; U = 7 eV, J = 0.82 eV for Dy; U = 7.03 eV, J = 0.83 eV for Ho; and U = 7.1 eV, J = 0.86 eV for Tm. These parameters were selected referring to previous studies that have shown that values $U \sim 7$ eV can accurately reproduce experimental observations, such as coehesive and magnetic properties, as well as electronic spectra [185]. The parameters were chosen in reference to [186, 187] for the half 4f-shells in Eu and Gd, [114] for Ho, [78, 117] for Dy and following the semiempirical formulas in [188] for Tm.

5.1.1 Eu and Gd on $\sqrt{3} \times \sqrt{3}$ graphene

The electronic properties of Eu and Gd adsorbed on graphene were studied without considering the effect of spin-orbit coupling in the DFT calculations. This is due to the fact that the 4f-shell of these elements has a half-filled occupation, leading to a negligible value for the orbital moment. For each 4f-adatom, three different adsorption sites were investigated, including the Top-site (on top of a C atom), the Bridge-site (at the midpoint between two C atoms), and the Hollow-site (at the center of a hexagonal ring formed by 6 C atoms). These sites are shown in Fig. 5.1. For each of the sites, structural relaxations were performed to determine the perpendicular distance (along the z direction, as described in Fig. 2.8) of the RE atom from the Gr monolayer. Upon reaching a state of minimal energy and vanishing forces, the adsorption energy at each relaxed distance, d_0, was computed as the energy difference between the interacting system (RE/Gr) and the sum of the total energies of the individual RE and Gr components,

$$\mathrm{E}_{ads} = \mathrm{E}_{\mathrm{RE/Gr}} - \mathrm{E}_{\mathrm{RE}} - \mathrm{E}_{\mathrm{Gr}}, \tag{5.1}$$

Figure 5.1: $\sqrt{3} \times \sqrt{3}$ supercell of graphene depicting the three possible adsorption sites of the RE atom: "T" for top, "H" for hollow, and "B" for bridge.

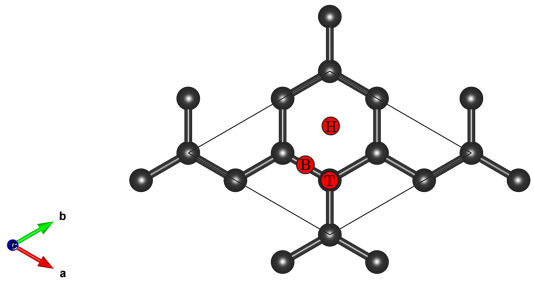

which represents the energy involved in the formation of the complex. Table 5.1 summarizes the ground state properties for the tested adsorption sites at the equilibrium distance d_0. Based on the examination of the adsorption energies, it can be concluded that the magnetic RE atom shows a preference for the H-site, as the magnitude of the energy involved is greater compared to the T- and B-sites. The B-site appears to be the second most favorable position for both systems. This observation can be argued based on the delocalization of the charge, which has been calculated for Eu/Gr and is shown in Fig. 5.2. Here, for each adsorption site the differential charge density, calculated as $n_{\mathrm{Eu/Gr}} - n_{\mathrm{Gr}} - n_{\mathrm{Eu}}$, is plotted on two different crystallographic planes, namely (010) and (001). For the (001) plane, two slices at different heights, h_1 and h_2, are evidenced. The red regions indicate a gain in charge density, while the blue ones correspond to a loss of charge density. By comparison between the three situations on

Site	E_{ads} [eV]	d_0 [Å]	d_{occ}	f_{occ}	$m_s^{\mathrm{RE}}[\mu_{\mathrm{B}}]$	$m_s^{\mathrm{tot}}[\mu_{\mathrm{B}}]$
Eu adatom on graphene						
H	−0.620	2.540	0.332	6.908	7.054	7.393
T	−0.436	2.740	0.226	6.911	7.039	7.332
B	−0.451	2.725	0.230	6.911	7.043	7.378
Gd adatom on graphene						
H	−1.435	2.236	0.866	7.017	7.319	7.860
T	−0.777	2.426	0.769	7.010	7.352	7.932
B	−0.871	2.387	0.795	7.012	7.374	7.964

Table 5.1: Ground state properties for Eu and Gd on Gr for the three adsorption sites: adsorption energy in eV, adsorption distance in Å, d and f occupation of the magnetic RE atom, spin magnetic moment of the RE atom in μ_{B}, and total spin magnetic moment of the RE/Gr system in μ_{B}. Calculations were performed without SOC.

the (001) plane, in the H-site the charge transfer happens between the RE adatom and the 6 nearest neighbors, whereas in the B-site, only 2 nearest C atoms participate, and in the T-site, primarily the C atom underneath is involved and to a lesser extent, the 3 surrounding C atoms. In general, the trend suggests that the interaction is stronger the more C atoms are close to the adatom, such that more charge is involved in the

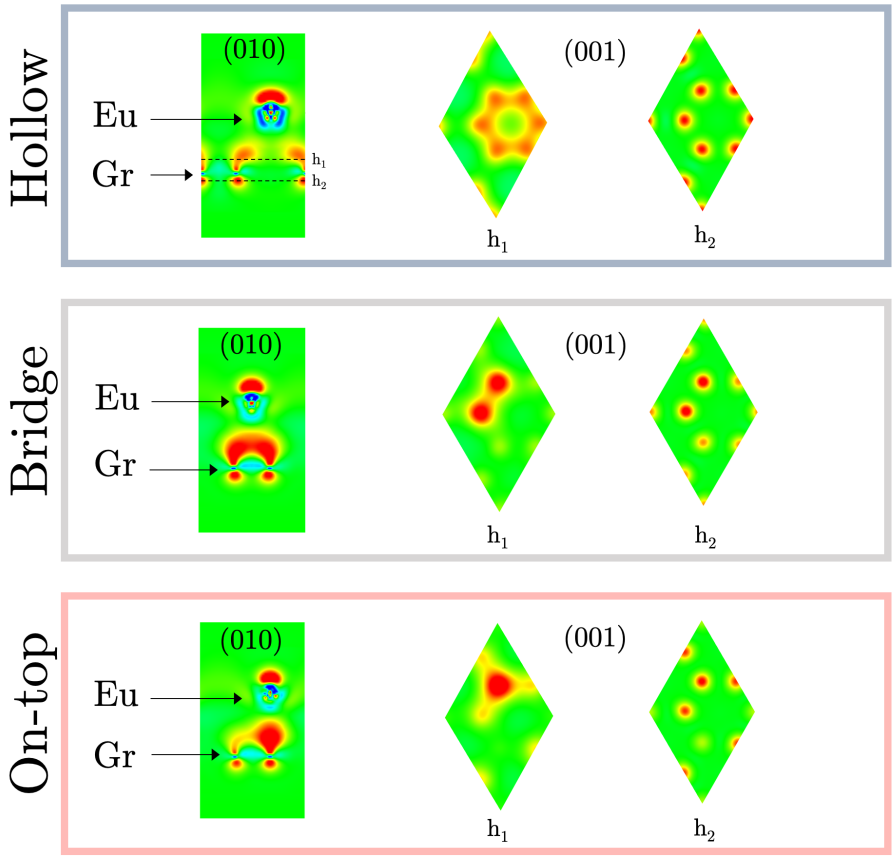

Figure 5.2: Differential charge densities of Eu/Gr on the three adsorption sites. The results are in two different planes, with the (010) plane on the left and the (001) plane on the right. From the results, a correlation can be established between the number of nearest neighbors and the stability of the system, with the H-site showing the highest stability, followed by the B and T-sites.

bonding. In particular, the hybridization is most likely to interest the out-of-plane p_z orbitals of Gr with the delocalized $5d$ orbitals of the RE. The preferred adsorption site is related to the distance between the RE and graphene, with the RE tending to adsorb closer to the monolayer in the H-site, and the relaxed distance being largest in the T-site. Moreover, a systematic trend of increasing bonding strength towards the graphene monolayer with a larger d occupation in the RE atom is observed, as seen by comparing E_{ads} and d_{occ} for the different sites. This correlation is a result of the chemical bonding being determined by delocalized valence electrons.

As a result of the previous discussion, the following analyses will focus on the H-site. The spin magnetic moment of the RE atom is primarily determined by the localized $4f$ electrons, which tend to follow Hund's rules in a half-filled manner. This results in a spin moment of the RE being close to 7 μ_B in both cases, with any deviations arising from intra-atomic spin-polarization. The d spin-polarization of the REs can be evaluated by subtracting the charge densities in the MT sphere, $n_{d\uparrow} - n_{d\downarrow}$, and results in ~ 0.110 μ_B for Eu and ~ 0.310 μ_B for Gd. The magnetic moment of the whole RE/Gr complex is dominated by the magnetic moment of the RE, which also causes spin-polarization in the substrate, especially in the IR region, which is composed mostly of the strongly delocalized π orbitals of Gr that interact with the d electrons of the RE. The magnetic moment associated with this region can be obtained by subtracting the total magnetic moment of the RE/Gr complex and the magnetic moment of the RE, $\Delta m = m_s^{\mathrm{tot}} - m_s^{\mathrm{RE}}$, resulting in 0.339 μ_B for Eu and 0.541 μ_B for Gd.

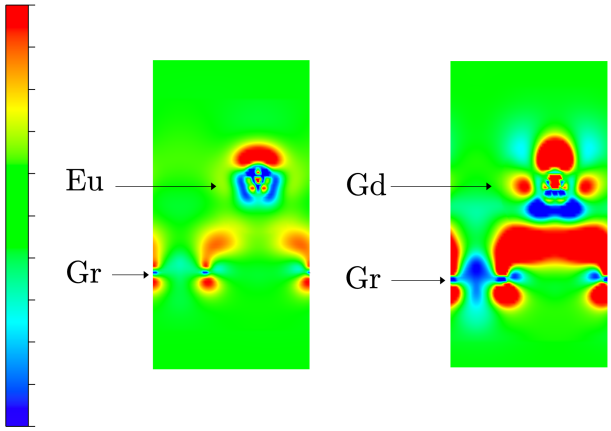

Figure 5.3: Differential charge density of Eu/Gr and Gd/Gr plotted in the (010) crystallographic plane. The values have been plotted on the same color scale ranging from a maximum saturation level of +0.004 (red) and a minimum of −0.004 (blue).

By comparing Eu/Gr with Gd/Gr, it is seen that the adsorption of Gd onto Gr is in general favored compared to Eu, and can be explained by the additional 5d electron of Gd in its outer valence shell. This is evidenced by plotting on the same color scale the differential charge density for the two systems, as in Fig. 5.3. The Gd complex exhibits more charge delocalization both towards the nearest C atoms, as well as towards the second nearest C atoms, which translates into an overall larger adsorption energy. In this regard, Eu exhibits more ionic characteristics in its bonding with the Gr monolayer, while Gd displays more covalent properties. The presence of an extra d electron in Gd results in a larger magnetic moment m_s^{Gd} compared to m_s^{Eu}, resulting in stronger spin-polarization in the system. This can be seen by examining the electronic structures of the two systems. Figs. 5.4 (a) and (b) show the spin-polarized density of states (DOS) for Eu/Gr and Gd/Gr, respectively. The total DOS is shown in grey, whereas the d and f states of the RE atom are depicted in blue and red, respectively. The upper panel (DOS ≥ 0) refers to the spin-up channel, while the bottom panel (DOS ≤ 0) corresponds to the spin-down channel. The localized nature of the 4f states is clearly visible, with the spin-up channel appearing at ~ -2.5 eV for Eu/Gr and at ~ -9 eV in Gd/Gr, much deeper in energy. Nevertheless, both systems display an unoccupied spin-down peak with a gap of $\Delta E \sim 11$ eV from the occupied

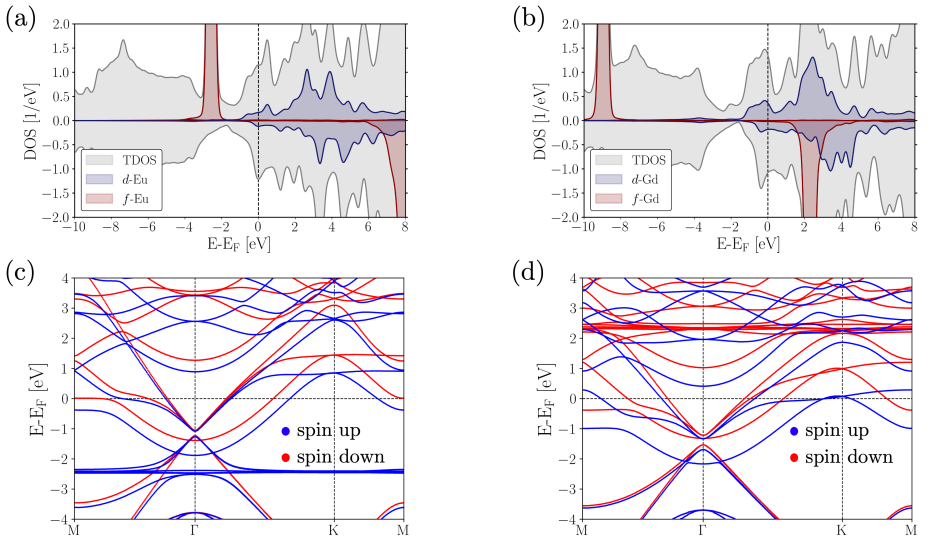

Figure 5.4: Spin-resolved DOS for Eu/Gr (a) and Gd/Gr (b): upper and lower panel represent the majority and minority states, respectively. The total DOS is shown in grey, the f states in red and the d states in blue. The calculated spin-polarized band structures are shown in (c) for Eu/Gr and in (d) for Gd/Gr. Calculations were performed without SOC.

peak. Furthermore, both systems show evidence of d electron occupation, with Gd having a slightly higher DOS near the Fermi energy, due to its extra d contribution as discussed previously in Table 5.1. The unequal spin-up and spin-down TDOS reveals the induced spin-polarization from the large magnetic moments of the RE atoms to the graphene substrate. This spin-polarization can be observed not only in the regions of the f states but also near the Fermi energy, and can be further analyzed in the spin-polarized band structures as shown in Figs. 5.4 (c) and (d), where the blue bands represent the spin-up channel and the red bands the spin-down channel.

Here, the presence of very flat bands can be observed at ~ −2.5 eV for Eu and ~ 2.3 eV for Gd, which correspond to the occupied and unoccupied $4f$ states respectively. Note that the unoccupied $4f$ states of Eu and the occupied $4f$ states of Gd are not visible in the given energy range. It is evident that the presence of the RE atoms induces some spin-polarization into the graphene monolayer, with this effect being more pronounced in Gd compared to Eu due to its larger magnetic moment. The phenomenon can be evinced by taking approximately the energy difference between the spin-up and the spin-down bands, which is enhanced in the Gd/Gr case. This represents a manifestation of exchange splitting that has been generated within the graphene monolayer as a result of its proximity to magnetic atoms. The $\sqrt{3} \times \sqrt{3}$ simulation cell, whose reciprocal lattice is shown in black in Fig. 5.5 along with the reciprocal space of the 1×1 unit cell in red, causes the high symmetry points of K and K' to fold into the Γ point, resulting in the emergence of the Dirac cone at this point. The symmetry of the $\sqrt{3} \times \sqrt{3}$ supercell breaks the sublattice symmetry of graphene by inducing the hybridization of electrons with different valley indices. This inter-valley coupling, also known as *intervalley scattering*, is a well-studied phenomenon in both theoretical and experimental works [189–192]. The mixing of the two inequivalent K and K' points of the primitive graphene at the Γ point makes them indistinguishable and leads to the sublattice symmetry breaking, introducing a difference in the effective

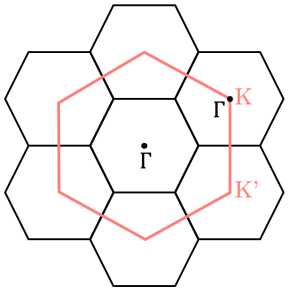

Figure 5.5: A visual representation of the reciprocal lattice of the $\sqrt{3} \times \sqrt{3}$ supercell and of the 1×1 unit cell of graphene, highlighted in black and red respectively.

potential felt by the sublattices of graphene. Consequently, the Dirac cone undergoes an energy splitting, which shows similarities to a spin-orbit coupling splitting. The size of the band gap depends on the strength of the intervalley mixing and can be tuned to allow for the opening of non-trivial gaps, leading to potentially useful electronic properties in graphene-based devices.

5.1.2 Dy, Ho and Tm on $\sqrt{3} \times \sqrt{3}$ graphene

The focus now shifts to RE/Gr systems with open 4f-shells, where correlation effects are particularly pronounced. The study involved Dy, Ho and Tm adsorbed on Gr, and as a natural consequence of the large orbital moments of these RE atoms, the following results have been obtained considering SOC inside of the MT regions. The outcomes of the study, including the adsorption energies and distances, the d and f occupation, the spin and orbital magnetic moments and the total spin magnetic moment of the RE/Gr complex are summarized in Table 5.2. The stability of the RE/Gr system follows a similar pattern as previously observed for Eu and Gd, with the H-site being the favored position for the RE atom on the Gr monolayer. This tendency has been noted in numerous other studies of RE/Gr, such as in references [182, 193, 194]. Again, the comparison between different adsorption sites reveals that the stability of the RE/Gr system increases as the RE atom gains more d electrons,

Site	E_{ads} [eV]	d_0 [Å]	d_{occ}	f_{occ}	$m_s^{RE}[\mu_B]$	$m_l^{RE}[\mu_B]$	$m_s^{tot}[\mu_B]$
Dy adatom on graphene							
H	−0.545	2.493	0.262	9.891	4.040	5.876	4.174
T	−0.074	2.741	0.189	9.901	4.024	5.904	4.115
B	−0.086	2.695	0.194	9.900	4.033	5.902	4.163
Ho adatom on graphene							
H	−0.476	2.499	0.250	10.881	3.045	5.905	3.150
T	−0.339	2.731	0.177	10.886	3.034	5.925	3.091
B	−0.344	2.729	0.177	10.886	3.038	5.922	3.113
Tm adatom on graphene							
H	−0.399	2.471	0.237	12.867	1.027	3.000	1.072
T	−0.280	2.805	0.143	12.878	1.020	2.987	1.043
B	−0.286	2.793	0.145	12.878	1.022	2.988	1.048

Table 5.2: Ground state properties for Dy, Ho and Tm on Gr for the three adsorption sites: adsorption energy in eV, adsorption distance in Å, d and f occupation of the magnetic RE atom, spin magnetic moment of the RE atom in μ_B, orbital magnetic moment of the RE atom in μ_B, and total spin magnetic moment of the RE/Gr system in μ_B. Calculations were performed in presence of SOC.

resulting in a decrease in the perpendicular distance between the RE atom and the Gr monolayer, which is lowest for the H-site. The Dy/Gr complexes with Dy adsorbed onto T and B sites appear to be unstable, as evidenced by their significantly smaller adsorption energies, which are an order of magnitude lower than those observed for the H-site and for the other RE/Gr systems. It is noteworthy that the systems with open $4f$-shells have a d occupation that is closer to that seen in Eu/Gr, rather than Gd/Gr, indicating a tendency towards ionic bonding with the Gr monolayer. In general, the RE atom undergoes a semiatomic-like behavior, maintaning its orbital and spin moments as dictated by Hund's rules and acquiring d electrons from the interaction with the substrate.

With regard to the preferred adsorption site, the H-site, the calculation of the d spin-polarization yields values of 0.04 μ_B for Dy, 0.03 μ_B for Ho, and 0.01 μ_B for Tm. This gradual decline in spin-polarization is a reflection of the decrease in the spin moment of the f electrons, from Dy to Tm. Additionaly, the m_s^{tot} is inversely proportional to the f occupation for late-series REs, and exhibits deviation from the f magnetic

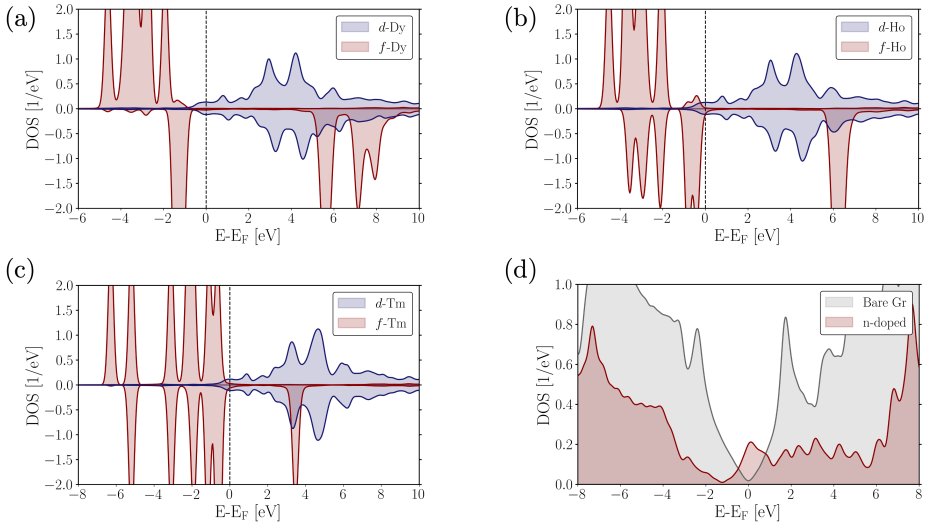

Figure 5.6: Spin-polarized density of states of the d (blue) and f (red) electrons of (a) Dy (b) Ho and (c) Tm, on top of graphene. The upper half of the plots displays the majority states, while the lower panel is relative to the minority states. The value $E - E_F = 0$ corresponds to the Fermi energy. (d) DOS of n-doped graphene (shown is the contribution of the MT of the carbon atoms) in the Ho/Gr system (red) and DOS of bare graphene (grey).

moment. This deviation stems from both the intra-atomic $f-d$ spin-polarization, which increases with the d occupation of the RE and the f magnetic moment, and the induced spin-polarization from m_s^{RE} to the IR region, where mostly delocalized π-orbitals of Gr and d electrons of the RE atom are found. The induced magnetization in this region is proportional to the RE's spin moment, with estimated values of 0.125 μ_{B} for Dy/Gr, 0.094 μ_{B} for Ho/Gr, and 0.036 μ_{B} for Tm/Gr.

In Fig. 5.6 (a) to (c), the spin-resolved DOS for the $5d$ and $4f$ electrons of the three systems reveal the semiatomic-like behavior of the REs, with d occupation appearing around the Fermi energy. The overall metallic behavior of the RE/Gr systems is attributed to n-doping from the REs towards the Gr, driven by the hybridization between d electrons of the RE and p_z electrons of Gr. Fig. 5.6 (d) compares the DOS of the C muffin-tins of Ho/Gr (red) to the total DOS of bare graphene (grey) to illustrate this n-doping. The energy difference between the Dirac points of the two cases estimates the magnitude of the n-doping to be around ~ 1.4 eV. As for the $4f$ states, they occupy a large energy window with a gap separating the occupied and unoccupied states, where the occupied states are close to the Fermi energy. The localization of these states leads to values of spin and orbital moments adhering closely to Hund's rules, as presented in Table 5.2. The aforementioned characteristics, including f-localization, spin-polarization, and doping effects, are also visible in the band structures illustrated in Appendix B, where the contributions of the RE atoms and C atoms are separated and displayed in the left and right, respectively, for each RE/Gr system.

5.1.3 Overview: trends with $4f$-filling

Figure 5.7 shows the variation of the adsorption energy (E_{ads}) and distance (d_0), as well as the properties at equilibrium distance, presented in tables 5.1 and 5.2, with respect to the RE atom, *i.e.*, the $4f$ occupancy. An examination of E_{ads} in relation to d_{occ} indicates that the bonding between the RE atoms and Gr is stronger with higher $5d$ occupancy in the valence shell. While Gd exhibits the strongest bonding towards Gr due to the presence of higher $5d$ occupancy in the valence shell, the behavior of Eu, Dy, Ho, and Tm is comparable, exhibiting a slight decrease in d_{occ} along the series, which corresponds to a declining E_{ads}, reflecting the more ionic character of the interaction with the substrate. In terms of the perpendicular equilibrium distance d_0, the exceptional strength of Gd's bonding to the substrate manifests itself in its closest proximity. Conversely, the decreasing trend observed from Eu to Tm can be attributed to the lanthanide contraction, whereby the decreasing atomic radii of the rare-earth metals leads to a decrease in the equilibrium distance to enable adsorption onto Gr. Ultimately, the $4f$ orbital filling increases along the series, resulting in an inverse relationship with the RE spin magnetic moment according to Hund's rules. As a result, the total magnetic moment of the RE/Gr complex follows the same trend as m_s^{RE}, but it is slightly shifted towards higher values due to the induced spin-polarization from the $4f$ magnetic moment.

Systematic trends

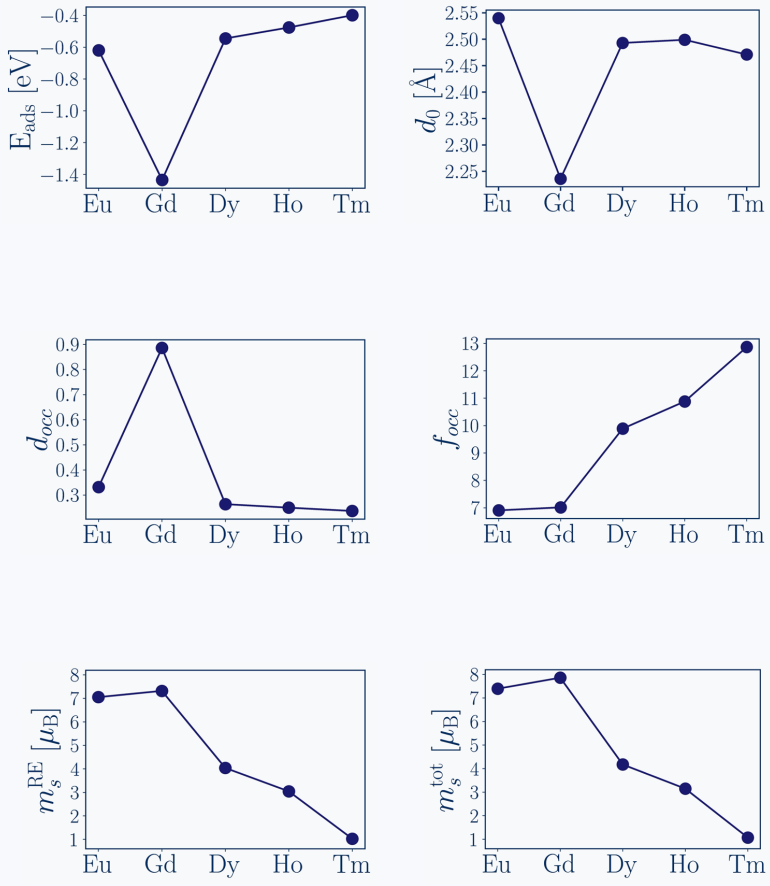

Figure 5.7: Systematic trends of Eu, Gd, Dy, Ho and Tm upon adsorption on graphene in the H-site.

5.2 Magnetic anisotropy of rare-earth adatoms on $\sqrt{3} \times \sqrt{3}$ graphene

To calculate the energy required for magnetization rotation, *i.e.* the MAE, it is essential to incorporate spin-orbit coupling in all calculations. This is because the rotation of magnetization results in a corresponding rotation of the orbital magnetic moment, which alters the alignment of the $4f$ charge cloud in the RE and causes it to interact differently with the surrounding crystal field. To determine the out-of-plane MAE, the total energy of the systems is computed self-consistently by incrementally rotating the magnetization, in steps of 10°, from the z-axis to the x-axis. Similarly, to determine the in-plane MAE, the magnetization is rotated from the x-axis to the y-axis. By fitting the curves obtained with Eq. 2.20 for a hexagonal symmetry, where θ represents the polar angle relative to the out-of-plane rotation and φ represents the azimuthal angle describing the in-plane rotation, the anisotropy constants K_i are evaluated.

In Fig. 5.8, the MAE curves for Eu/Gr and Gd/Gr are displayed, showing blue points for DFT+U calculations and a red curve for fitting. The energy values for all data

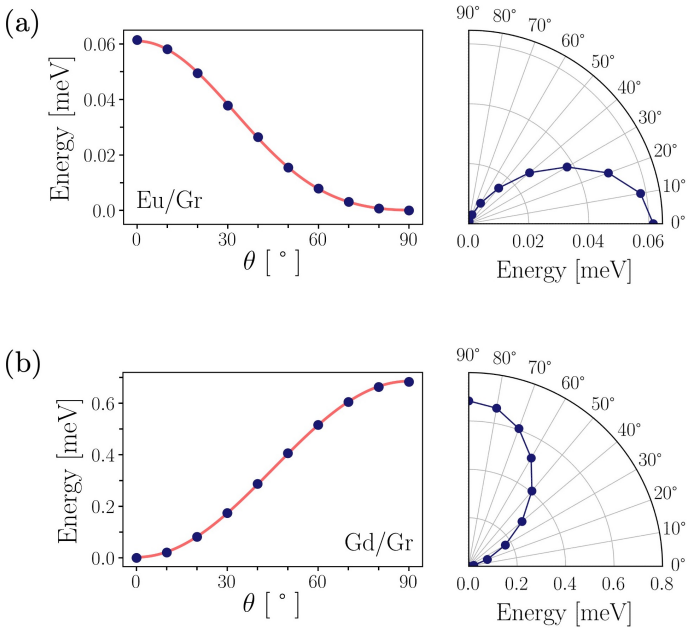

Figure 5.8: MAE out-of-plane curves for Eu/Gr (a) and Gd/Gr (b) and respective polar plots.

points are scaled so that the minimum energy value is zero. Additionally, each curve is accompanied by a polar plot as an alternative representation.

It is evident that both systems exhibit low-order anisotropy, as confirmed by fitting the Eu/Gr curve with K_1 and K_2, and that of Gd/Gr with K_1. The values of these constants, provided in Tab. 5.3, reveal that K_1 is the dominant term. Additionally, the Eu/Gr system presents an in-plane easy-axis, where the magnetic ground state corresponds to the magnetization at $\theta = 90°$, related to a $K_1 < 0$.

In contrast, the Gd/Gr system is distinguished by an out-of-plane easy-axis, with the energy minimum located at $\theta = 0°$ and $K_1 > 0$. Upon comparing the energy scales, it is evident that the MAE in Eu/Gr is one order of magnitude lower than that of Gd/Gr. This discrepancy is attributed to the additional $5d$ electron present in Gd, which hybridizes with the CF and generates supplementary contributions to the MAE, apart from the $4f$ effect. Moreover, as previously observed, the bonding between Gd and Gr involves the $5d$ electron, causing Gd to approach the CF more closely than Eu, resulting also in a stronger $4f$-CF interaction.

The estimated energy required to switch the magnetization from the easy-axis to the hard-axis (perpendicular for Eu and in-plane for Gd) are $\Delta E \sim 0.06$ meV and $\Delta E \sim 0.7$ meV for Eu/Gr and Gd/Gr, respectively, where $\Delta E = |E_\parallel - E_\perp|$. This difference in the MAE is also reflected in the values of K_1, which are larger for Gd/Gr than for Eu/Gr, indicating a larger first-order magnetic anisotropy.

Fig. 5.9 provides an analysis of the magnetic anisotropy in open $4f$-shell systems. The figure includes out-of-plane curves in panels (a)-(c) and corresponding polar plots for an alternate representation, as well as in-plane MAE curves in panels (d)-(f). The red lines show the fitted curves used to extract the anisotropy constants K_i, which are presented in Tab. 5.3. Compared to Eu and Gd, the open $4f$-shell systems exhibit a significant anisotropic nature, requiring all four K_i terms in the energy expansion to describe the MAE curves. The in-plane MAE curves reflect the six-fold symmetry of the Gr substrate, which causes the energy to repeat as $E(\varphi) = E(\varphi \pm \pi/3)$. Hence, the shape of these curves is fitted with $K_4 \sin 6\varphi$, where the amplitude and sign of the oscillations depend on the K_4 values.

By inspecting Table 5.3, the first-order constants (K_1 and K_2) are approximately one order of magnitude greater than K_3, while the in-plane constants (K_4) contribute the least, being two orders of magnitude weaker than the first orders. Nonetheless, Tm/Gr displays a deviation from the general trend, as K_3 and K_4 exhibit similar magnitudes. The magnetic anisotropy of Dy/Gr is illustrated in Fig. 5.9 (a) and (d), which indicates a preference for an in-plane ($\theta_{min} = 90°, \varphi_{min} = 0°$) easy-axis.

The energy difference from the perpendicular magnetization direction is is estimated to be approximately ΔE = 2 meV, whereas the energy barrier for the magnetization switching from the easy-axis to the θ = 0° direction is calculated to be as high as 5.3 meV. Referring to the MAE curves of Ho/Gr, an intermediate easy-axis at angles (θ_{min} = 42.67°, φ_{min} = 30°) is observed, which results in a canted magnetization direction. The energy difference between the perpendicular and parallel magnetization directions, ΔE, is about 2 meV, whereas the energy required for complete alignment of magnetization with the perpendicular and in-plane directions is approximately 6 meV and 8 meV, respectively. The out-of-plane curve of Tm/Gr exhibits a similar shape to that of Ho/Gr, and an absolute energy minimum observed at a tilted magnetization angle of (θ_{min} = 39.08°, φ_{min} = 0°). The energy difference ΔE is approximately 3.8 meV, and the energy required to align the magnetization along the perpendicular and in-plane directions are 2.64 meV and 6.22 meV, respectively.

The values of ($\theta_{min}, \varphi_{min}$) that correspond to the absolute energy minima mentioned earlier are determined by minimizing the energy functions that contain all terms up to K_4, using the extracted K_i parameters. The complete 3D energy surfaces, representing for each system the function $E(\theta, \varphi)$, can be visualized in Fig. 5.10 and the respective absolute minimum coordinates are listed in Table 5.4. The curvature

Unit	K_1	K_2	K_3	K_4
Eu adatom on graphene				
meV	−0.101	0.040	-	-
K	−1.172	0.464	-	-
Gd adatom on graphene				
meV	0.683	-	-	-
K	7.926	-	-	-
Dy adatom on graphene				
meV	15.355	−18.918	1.536	−0.441
K	178.187	−219.534	17.825	−5.118
Ho adatom on graphene				
meV	−27.734	32.218	−2.591	0.360
K	−321.840	373.875	−30.067	4.178
Tm adatom on graphene				
meV	−13.285	16.720	0.146	−0.158
K	−154.166	194.028	1.694	−1.834

Table 5.3: Magnetic anisotropy constants obtained via fitting of DFT+U data depicted in Fig. 5.8 for Eu and Gd and Fig. 5.9 for Dy, Ho and Tm. The values are reported in meV and K.

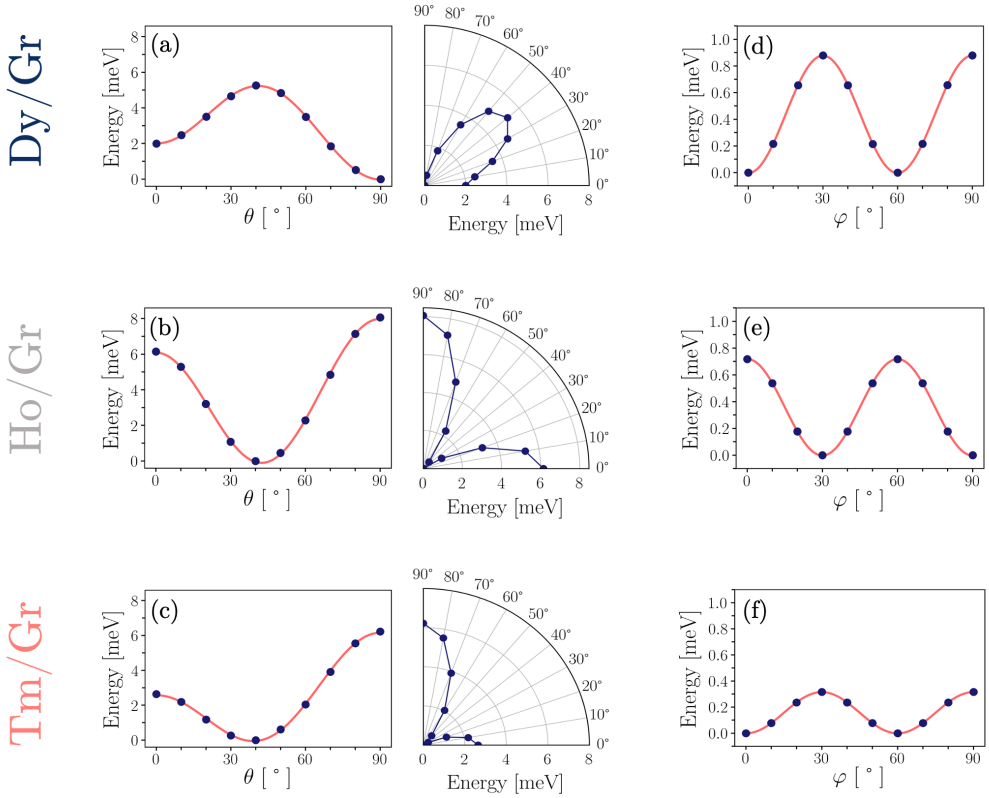

Figure 5.9: Out-of-plane magnetic anisotropy energy curves for Dy (a), Ho (b) and Tm (c) on graphene: the total energy is plotted against the angle between the perpendicular magnetization and the tested magnetization direction. An alternative representation of the DFT+U data in a polar plot for the computed systems is given besides. In-plane magnetic anisotropy energy curves for Dy (d), Ho (e) and Tm (f) on graphene: the total energy is plotted against the angle between the x-axis and the tested in-plane magnetization direction. Full dots indicate the DFT+U data, while the full lines display the fitting curves.

of the $E(\theta, \varphi)$ landscapes can be accounted for in terms of the magnetic anisotropy constants K_i. The relationships between the constants and the curvature can be

Figure 5.10: 3D MAE surfaces: the total energy is plotted as a function of the angular coordinates (θ, ϕ) adopting the fitted K_i values.

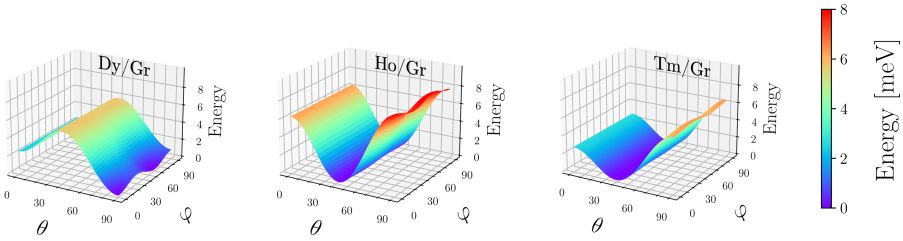

derived by first finding the zeros of $\frac{\partial E_{an}}{\partial \theta}$, which occur at $\theta = 0°, 90°$ and for $\sin^2\theta = -K_1/2K_2$. By examining the second derivative of the energy equation, disregarding K_3 and K_4, the following relationships can be established:

1. $$\frac{\partial^2 E_{an}}{\partial \theta^2}|_{\theta=0°} = 2K_1 \tag{5.2}$$

   leading to a convex behavior for $K_1 > 0$ (Dy) and concave behavior for $K_1 < 0$ (Ho and Tm).

2. $$\frac{\partial^2 E_{an}}{\partial \theta^2}|_{\theta=90°} = -2K_1 - 4K_2 \tag{5.3}$$

   giving rise to a convex behavior for Dy and concave behavior for Ho and Tm.

3. $$\frac{\partial^2 E_{an}}{\partial \theta^2}|_{\sin^2\theta=-\frac{K_1}{2K_2}} = -2K_1\left(\frac{2K_2 + K_1}{K_2}\right) \tag{5.4}$$

   The term in parenthesis is positive for all RE/Gr complexes, indicating that the curvature is solely determined by K_1. This defines an energy hill if $K_1 > 0$ (Dy) and an energy valley if $K_1 < 0$ (Ho and Tm).

RE/Gr	θ_{min}	φ_{min}
Dy/Gr	90°	$0° \pm n \cdot 60°$
Ho/Gr	42.67°	$30° \pm n \cdot 60°$
Tm/Gr	39.08°	$0° \pm n \cdot 60°$

Table 5.4: Polar (θ) and azimuthal (φ) angular coordinates corresponding to the ground state magnetization direction (easy-axis) for each open 4f-shell system. The variable n appearing in φ_{min} is an integer number, $n = 0, 1, 2, 3...$

Figure 5.11: Magnetization densities of the RE/Gr systems, calculated as $n_\uparrow - n_\downarrow$. The plots are to scale and with varying isosurface values for visualization.

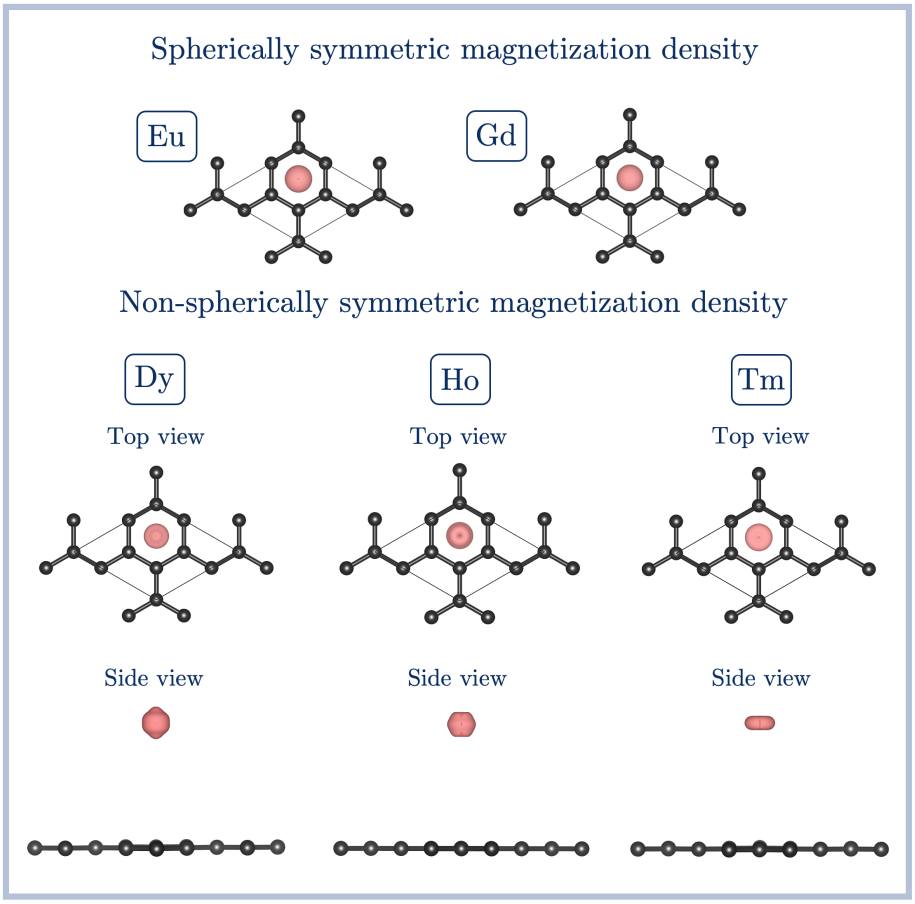

Regarding the in-plane MAE curves, it is noteworthy that Dy and Tm exhibit the same negative sign of the fourth-order anisotropy constant (K_4), which manifests as energy minima at 0° with a periodicity of 60°. In contrast, Ho displays a positive K_4 sign, leading to energy minima at 30° with the same periodicity. Furthermore, the magnitude of the oscillations is directly proportional to the absolute value of K_4, with Dy displaying the largest value, followed by Ho and Tm.

When comparing half-filled $4f$-shells with open $4f$-shells, it becomes apparent that there are significant differences in the energies associated with magnetic anisotropy.

Specifically, in Eu/Gr and Gd/Gr, much lower energies are required to rotate the magnetization, and the anisotropies follow a simpler lower-order trend. In contrast, open 4f systems exhibit larger energy scales and more complex trends due to the non-spherical nature of the 4f charge cloud. By examining the magnetization densities, which were obtained by subtracting the spin-up and spin-down charge densities and are illustrated in Fig. 5.11, one can qualitatively discern a difference between half-filled 4f-shells and open 4f-shells. Specifically, the magnetization density of half-filled 4f-shells appears nearly spherical due to the cancellation of angular momentum, whereas that of open 4f-shells exhibits a non-spherical shape, indicating an anisotropic distribution in space.

5.2.1 Reverse-engineering of the crystal field parameters

After computing the magnetic anisotropy constants via fitting of *ab initio* DFT+U calculations, it is possible to reverse-engineer the CFP as described in Eq. 2.37 following the recipe given in Eq. 2.57, *i.e.* as linear combinations of the K_i values. These parameters where calculated at equilibrium distance from the Gr monolayer for the highly-anisotropic open 4f-shell REs systems and are tabulated in Table 5.5. The CFP values were determined using Hund's rules to obtain the ground state J value, which is $J = 8$ for Dy, $J = 15/2$ for Ho, and $J = 7/2$ for Tm. Tables reporting the respective CFP in the standard convention $A_l^m = C_l^m/\alpha_l$ and in the Waybourne convention $B_l^m = C_l^m/\alpha_l\theta_l^m$ are provided in Appendix B.2. The CFP values enable access to the matrix elements of the CF Hamiltonian $\mathcal{H}_{6v}$ for each J value, as reported in [67]. By diagonalizing the CF matrix, the eigenstates and eigenvalues of $\mathcal{H}_{6v}$ can be obtained, which form the magnetic multiplet spectrum of the RE/Gr system being studied. The results for Dy/Gr, Ho/Gr and Tm/Gr are displayed in Fig. 5.12. Each plot features grey lines that identify the possible J_z values ranging from $-J$ to $+J$

Unit	C_2^0	C_4^0	C_6^0	C_6^6
Dy adatom on graphene				
meV	0.025	$-1.717 \cdot 10^{-4}$	$-7.381 \cdot 10^{-8}$	$-4.895 \cdot 10^{-6}$
K	0.290	$-1.992 \cdot 10^{-3}$	$-8.565 \cdot 10^{-7}$	$-5.680 \cdot 10^{-5}$
Ho adatom on graphene				
meV	−0.039	$3.904 \cdot 10^{-4}$	$1.992 \cdot 10^{-7}$	$6.394 \cdot 10^{-6}$
K	−0.451	$4.530 \cdot 10^{-3}$	$2.312 \cdot 10^{-6}$	$7.419 \cdot 10^{-5}$
Tm adatom on graphene				
meV	−0.190	$9.229 \cdot 10^{-3}$	$-8.026 \cdot 10^{-6}$	$-2.006 \cdot 10^{-3}$
K	−2.205	0.107	$-9.314 \cdot 10^{-5}$	$-2.327 \cdot 10^{-2}$

Table 5.5: Crystal field parameters obtained via reverse-engineering from the magnetic anisotropy constants K_i. The values are reported in meV and K.

in steps of 1. States sharing the same color correspond to mixtures of states that differ by $\Delta J_z = \pm 6, \pm 12$, and are subject to deviations from the pure state $\langle J_z \rangle$ value, depending on the strength of the mixing operator $\hat{O}_6^6$.

For Dy/Gr with $J = 8$ (Fig. 5.12 (a)), the C_2^0 parameter gives rise to a single ground state at $\langle J_z \rangle = 0$, but the non-monotonic behavior of the spectrum can be attributed to the higher contributions. Specifically, the C_6^6 parameter, generates linear combinations of the states:

$$|J_z = -8\rangle, |J_z = -2\rangle, |J_z = 4\rangle$$

$$|J_z = -7\rangle, |J_z = -1\rangle, |J_z = 5\rangle$$

$$|J_z = -6\rangle, |J_z = 0\rangle, |J_z = 6\rangle$$

$$|J_z = -5\rangle, |J_z = 1\rangle, |J_z = 7\rangle$$

$$|J_z = -4\rangle, |J_z = 2\rangle, |J_z = 8\rangle$$

$$|J_z = -3\rangle, |J_z = 3\rangle.$$

Of note are the mixtures of $(|J_z = -6\rangle, |J_z = 0\rangle, |J_z = 6\rangle)$ in orange (the state at ~ 8 meV corresponds to a doublet) and $(|J_z = -3\rangle, |J_z = 3\rangle)$ in red, which appear at quenched $\langle J_z \rangle$ value. Generally speaking, these kind of states can give rise to spin-flipping events via quantum tunneling, which are prevented in this case by the non-degenerate magnetic ground state. In terms of symmetry representations, there are six sets of double-degenerate states belonging to the Γ_5 and Γ_6 representations (see Tab. A.2). Additionally, there are five non-degenerate states located at $\langle J_z \rangle = 0$ and belonging to the representations Γ_i, where $i = 1, 2, 3, 4$.
Upon comparing the CFP of Dy/Gr in A_l^m notation with those in Ref. [117], where similar orbital and spin magnetic moments were obtained for Dy/Gr/Ir(111) within the DFT+Hubbard-I framework, a good agreement is observed for the largest coefficients, *i.e.*, $(A_2^0, A_4^0) = (-11.287, 5.156)$ meV. However, some deviations were noticed in the smaller contributions, $(A_6^0, A_6^6) = (0.057, 3.765)$ meV.

In the case of the half-integer spin systems Ho/Gr (Fig. 5.12 (b)) and Tm/Gr (Fig. 5.12 (c)), Kramers degeneracy determines a double degeneracy of the states such that no mixtures at $\langle J_z \rangle = 0$ can form. According to the orthogonality theorem, Ho/Gr presents three sets of double-degenerate states belonging to Γ_7, three to Γ_9 and two to Γ_8 (character table listed in Tab. A.1), while in the case of Tm/Gr the hexagonal field induces a splitting of one Γ_7 set, one Γ_9 set and two sets of Γ_8, all double-degenerate (character table in Tab. A.1). This implies that these systems are are not subject to spin-reversal through tunnel-split doublets, and in absence of external perturbations, the system has to overcome the whole energy barrier spanning from one ground state to the other in order to undergo a spin-flip event. Nevertheless, the spin reversal can occur through alternative phenomena, such as scattering with

phonons and electrons at finite temperatures. For Ho/Gr the lowest lying states appear at ~ $\langle J_z \rangle$ = ±11/2, while for Tm/Gr at ~ $\langle J_z \rangle$ = ±5/2, and again the actual expectation value deviates because of the presence of a finite transverse term. In the case of Ho/Gr, the energy barrier separating the two ground states is substantial, approximately ~ 14 meV, which corresponds to an activation barrier of U= 162 K in the expression for the relaxation time $\tau \propto e^{U/k_B T}$, where k_B is the Boltzmann constant and T the temperature. However, interactions with substrate phonons can establish a connection between these two states and the closest accessible states via thermal excitation. Specifically, these accessible states are characterized by $\langle J_z \rangle$ = ±13/2 and are positioned at an energy gap of roughly ΔE ~ 1.8 meV (21 K), from which assisted quantum tunneling is possible. Shifting focus to the Tm/Gr system, the doubly degenerate ground states possess an expectation value of $\langle J_z \rangle$ ~ ±5/2. Overcoming the entire energy barrier separating these ground states would require an energy of 209 K (equivalent to 18 meV). Furthermore, there exists an energy gap of 95 K (approximately ~ 8.2 meV) to the first excited state at $\langle J_z \rangle$ = ±3/2, which is inherently protected against quantum tunneling. From these arguments it can be concluded that among the two systems studied with out-of-plane anisotropy, Tm/Gr is probably the

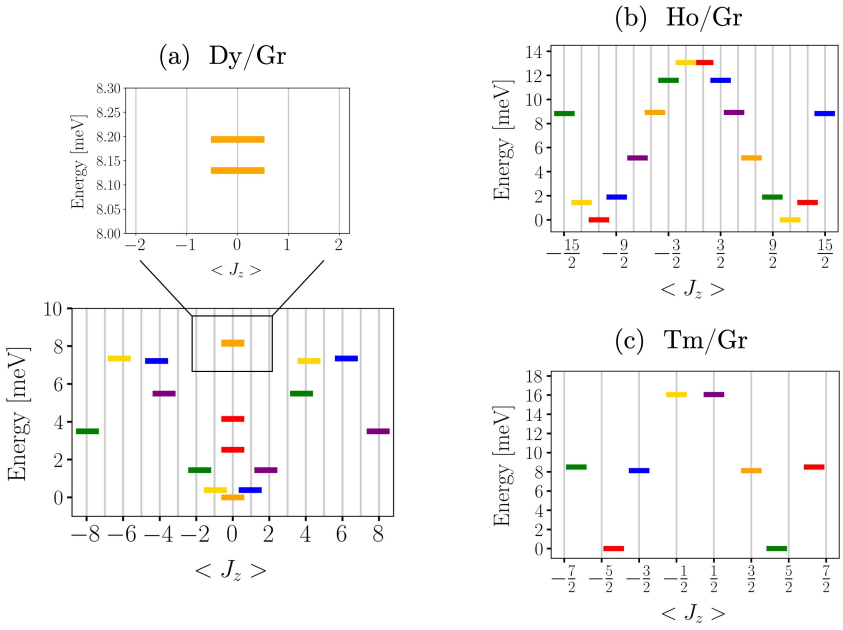

Figure 5.12: Multiplet splitting of (a) Dy/Gr, (b) Ho/Gr and (c) Tm/Gr, adopting the CFP values obtained from reverse-engineering via the magnetic anisotropy constants. States in the same color correspond to linear combinations of $|J_z\rangle$ differing by ΔJ_z = ±6, ±12.

most stable with respect to magnetization reversal. In general, it can be observed how the quantum framework qualitatively aligns with the classical magnetization rotation. Upon rotation of the magnetic spin moment in the RE atom, the orbital moment follows due to spin-orbit coupling. In the LSJ coupling picture, this induces a rotation of the total angular momentum J, thus the projection J_z assumes different values with different energies. Additional investigations are detailed in Appendix B.3, where phase diagrams were created for $J = 7/2,\ 8,\ 15/2$ to identify the magnetic ground state within a specific range of CFP values for C_4^0 and C_6^0.

5.2.2 Magnetoelastic coupling

The correlation between the geometric characteristics of the $4f$ charge distribution and the magnetic anisotropy energy implies that strain can be utilized to induce modifications in the magnetic anisotropy of RE/Gr systems. The application of external pressure leads to the displacement of atoms in the crystal structure, causing a rearrangement of the charge density. In the presence of spin-orbit coupling, this displacement can induce a rotation of the spin magnetic moment, resulting in new magnetic properties. The mechanical deformation in Fig. 5.14 is modeled by modifying the perpendicular distance between the RE adatom and the Gr monolayer. Three distances are considered, including a compressed state, where the distance is $d/d_0 = 0.96$ (−4% strain), the equilibrium distance with $d/d_0 = 1.0$ (no induced strain), and a stretched state where $d/d_0 = 1.04$ (+4% strain). From an experimental perspective, this shift in distance can be achieved, for instance, by modifying the chemical reactivity or the charge state of the graphene sheet through intercalation of dopands between graphene and the substrate [195–197].

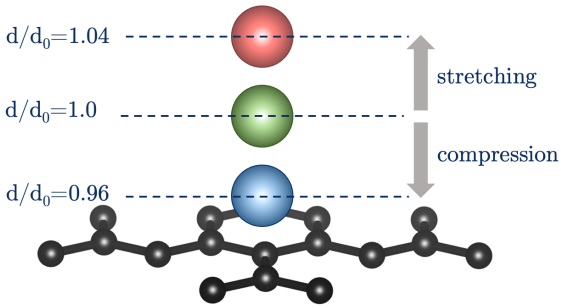

Figure 5.13: Illustration of the set-up used to simulate a mechanical strain perpendicular to the plane of a graphene substrate. Note that distances in this illustration are provided for conceptual purposes only.

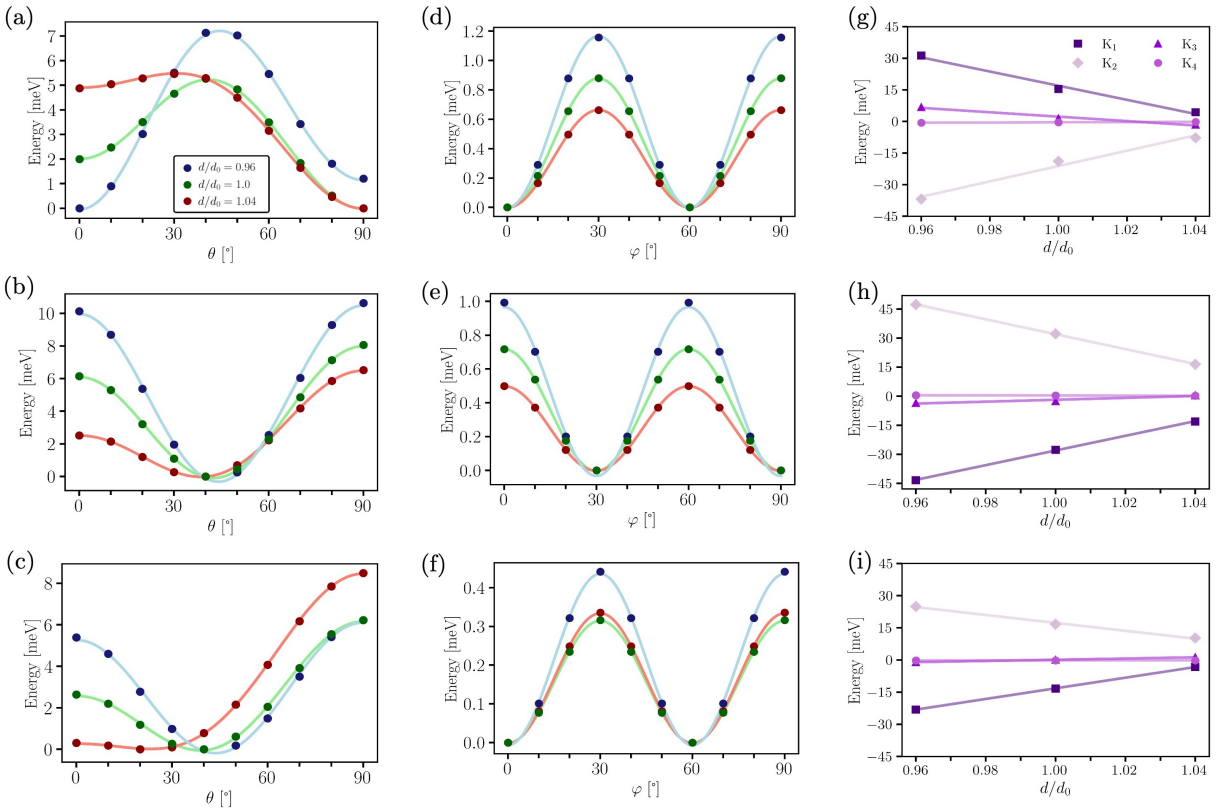

Figure 5.14: MAE curves (out-of-plane and in-plane) for different distances, namely $d/d_0 = 0.96, 1.0, 1.04$ (blue, green and red respectively) of the rare earth adatoms from the graphene monolayer. (a) and (d) correspond to the out-of-plane and in-plane curves of Dy/Gr; (b) and (e) correspond to the out-of-plane and in-plane curves of Ho/Gr; (c) and (f) correspond to the out-of-plane and in-plane curves of Tm/Gr. For each system, the last column (Figures (g)-(i)) shows the respective magnetic anisotropy constants K_i ($i = 1, 2, 3, 4$) obtained via the fitting of the MAE curves. Specifically, (g) shows the K_i for Dy/Gr, (h) for Ho/Gr and (i) for Tm/Gr. Points correspond to DFT+U data while lines to the fitting curves.

For each of the three distances and systems, the MAE curves for both the out-of-plane (Figures (a)-(c) in Fig. 5.14) and in-plane (Figures (d)-(f) in Fig. 5.14) directions are obtained through total energy self-consistent calculations (represented by points), and then fitted with Eq. 2.20 (represented by lines). The results for Dy/Gr are shown in the first row (Figures (a) and (d)), Ho/Gr in the second row (Figures (b) and (e)), and Tm/Gr in the last row (Figures (c) and (f)). The magnetic anisotropy constants as a function of induced strain for each RE/Gr complex are presented in the last column of each row (Figs. 5.14 (g)-(i)). Given the significant impact of the $4f$ charge cloud shape, notable effects are expected in systems possessing non-zero orbital angular momentum. Accordingly, the following discussion is focused on Dy/Gr, Ho/Gr, and Tm/Gr systems.

When analyzing the out-of-plane curves, it is observed that the magnitude of the MAE grows as the adatom approaches the substrate. This behavior is attributed to the stronger crystal field that the impurity experiences as it gets closer to the substrate. The absolute values of the anisotropy constants K_i, which are fitted to the total energy points up to K_3, exhibit a linear increase as the distance decreases. The presence of the three contributions leads to anisotropic energy curves with canted easy-axis in the case of Ho/Gr and Tm/Gr. When comparing the values among the systems, K_1 takes positive values for all distances in Dy/Gr, while it is negative for Ho/Gr and Tm/Gr. This is consistent with the hills/valleys generated in the curves, with the energy hill becoming steeper for Dy/Gr with smaller distances, and the energy valley becoming more pronounced for Ho/Gr and Tm/Gr. Regarding K_2, the sign is opposite in Dy/Gr compared to Ho/Gr and Tm/Gr, and the absolute value

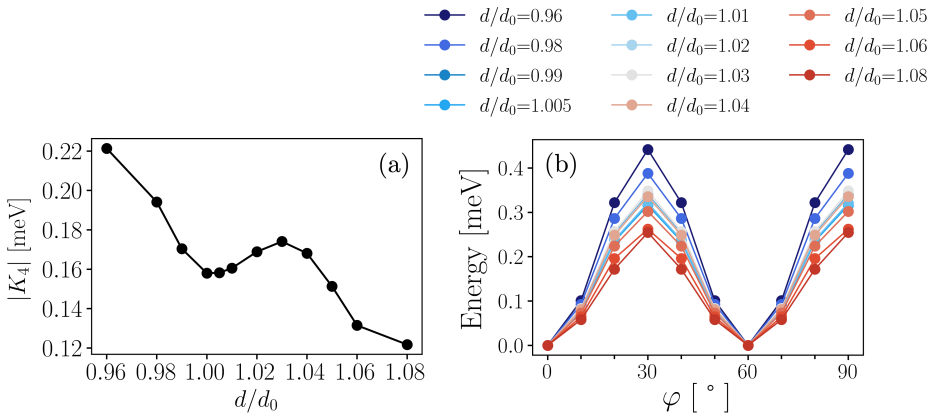

Figure 5.15: (a) $|K_4|$ of Tm/Gr for distances ranging from d/d_0 = 0.96 to d/d_0 = 1.08 from the graphene sheet *i.e.* from −4% to +8% of perpendicular strain. (b) In-plane MAE curves calculated with DFT+U for different perpendicular strains of Tm on Gr.

is slightly larger than that of K_1 in all systems. A similar analysis is applicable to K_3, where the main difference lies in the magnitude, which is 6.821 meV for Dy/Gr compared to −3.434 meV for Ho/Gr and −1.032 meV for Tm/Gr at $d/d_0 = 0.96$. While Ho/Gr and Tm/Gr maintain a canted easy-axis with the minimum slightly shifting towards larger θ values with compression, Dy/Gr undergoes a significant change in the easy-axis from in-plane at $d/d_0 = 1.0, 1.04$ to out-of-plane at $d/d_0 = 0.96$.

Moving to the in-plane curves, Fig. 5.9 shows a periodic trend with a periodicity of 60°. The amplitudes of the $\sin 6\varphi$ behavior are controlled by the constant K_4, and they increase as the adatom is moved closer to Gr. However, a deviation from this trend is observed for Tm/Gr, where the modulus of K_4 is slightly stronger for $d/d_0 = 1.04$ compared to $d/d_0 = 1.0$.To gain insight into this behavior, the absolute value of K_4 was evaluated for several other strains, as shown in Fig. 5.15. The results reveal a non-linear trend, with the value increasing from $d/d_0 = 1.08$ to $d/d_0 = 1.03$ before reaching a maximum. Then, from $d/d_0 = 1.03$ to $d/d_0 = 1.0$, $|K_4|$ decreases before increasing again at higher compressions. The values shown in Fig. 5.15 for K_4 were obtained by first calculating the in-plane MAE curves for each of the strains, and then fitting them using the method described earlier. The following tables present the reversed-engineered CFP C_l^m for the strain values of $d/d_0 = 0.96, 1.04$ in conjunction with the corresponding K_i values for Dy/Gr (blue tables), Ho/Gr (grey tables), and Tm/Gr (red tables).

$d/d_0 = 0.96$

Unit	K_1	K_2	K_3	K_4
meV	31.243	−36.872	6.821	−0.583
K	362.560	−427.882	79.154	−6.765
Unit	C_2^0	C_4^0	C_6^0	C_6^6
meV	0.017	$-2.691 \cdot 10^{-4}$	$-3.278 \cdot 10^{-7}$	$-6.471 \cdot 10^{-6}$
K	0.197	$-3.123 \cdot 10^{-3}$	$-3.804 \cdot 10^{-6}$	$-7.510 \cdot 10^{-5}$

$d/d_0 = 1.04$

Unit	K_1	K_2	K_3	K_4
meV	4.345	−7.719	−1.539	−0.332
K	50.422	−89.575	−17.859	−3.853
Unit	C_2^0	C_4^0	C_6^0	C_6^6
meV	0.035	$-1.071 \cdot 10^{-4}$	$7.395 \cdot 10^{-8}$	$-1.866 \cdot 10^{-6}$
K	0.406	$-1.243 \cdot 10^{-3}$	$8.582 \cdot 10^{-7}$	$-2.165 \cdot 10^{-5}$

Table 5.6: Dy/Gr: Magnetic anisotropy constants and crystal field parameters at $d/d_0 = 0.96$ and $d/d_0 = 1.04$. The values are reported in meV and K.

$d/d_0 = 0.96$				
Unit	K_1	K_2	K_3	K_4
meV	−43.329	47.289	−3.434	0.500
K	−502.812	548.766	−39.850	5.802
Unit	C_2^0	C_4^0	C_6^0	C_6^6
meV	−0.043	$5.815 \cdot 10^{-4}$	$2.640 \cdot 10^{-7}$	$8.88 \cdot 10^{-6}$
K	−0.450	$6.748 \cdot 10^{-3}$	$3.064 \cdot 10^{-6}$	$1.030 \cdot 10^{-4}$
$d/d_0 = 1.04$				
Unit	K_1	K_2	K_3	K_4
meV	−13.005	16.497	0.486	0.250
K	−150.917	191.440	5.640	2.901
Unit	C_2^0	C_4^0	C_6^0	C_6^6
meV	−0.041	$2.413 \cdot 10^{-4}$	$-3.737 \cdot 10^{-8}$	$4.440 \cdot 10^{-6}$
K	−0.476	$2.800 \cdot 10^{-3}$	$-4.337 \cdot 10^{-7}$	$5.152 \cdot 10^{-5}$

Table 5.7: Ho/Gr: Magnetic anisotropy constants and crystal field parameters at $d/d_0 = 0.96$ and $d/d_0 = 1.04$. The values are reported in meV and K.

$d/d_0 = 0.96$				
Unit	K_1	K_2	K_3	K_4
meV	−23.109	24.977	−1.032	−0.221
K	−268.169	289.846	−11.976	−2.565
Unit	C_2^0	C_4^0	C_6^0	C_6^6
meV	−0.135	$1.267 \cdot 10^{-2}$	$5.673 \cdot 10^{-5}$	$2.806 \cdot 10^{-3}$
K	−1.567	0.147	$6.583 \cdot 10^{-4}$	0.033
$d/d_0 = 1.04$				
Unit	K_1	K_2	K_3	K_4
meV	−3.260	10.204	1.244	−0.168
K	−37.831	118.413	14.436	−1.950
Unit	C_2^0	C_4^0	C_6^0	C_6^6
meV	−0.312	$6.661 \cdot 10^{-3}$	$-6.838 \cdot 10^{-5}$	$-2.133 \cdot 10^{-3}$
K	−3.621	0.077	$-7.935 \cdot 10^{-4}$	−0.025

Table 5.8: Tm/Gr: Magnetic anisotropy constants and crystal field parameters at $d/d_0 = 0.96$ and $d/d_0 = 1.04$. The values are reported in meV and K.

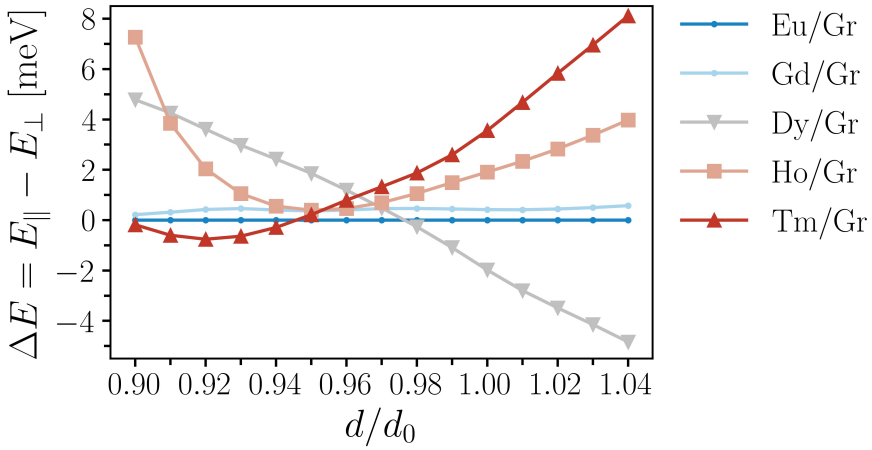

Figure 5.16: This figure depicts the magnetic anisotropy energy as a function of the distance between the RE element and the graphene layer. Gd and Eu are also shown for comparison. The calculation was performed using DFT+U. The energy difference between the parallel and perpendicular energy components ($E_{\parallel} - E_{\perp}$) is plotted on the y-axis.

To further analyze the behavior of each RE/Gr system, the change in $\Delta E = E_{\parallel} - E_{\perp}$ as a function of strain has been investigated. The range of values was scanned from $d/d_0 = 0.90$ to $d/d_0 = 1.04$ with a step of 0.01, and the results are presented in Fig. 5.16. Positive values of ΔE indicate a favored out-of-plane magnetization (along the z-axis), while negative values correspond to an in-plane (x-axis) magnetization.

Ho/Gr and Tm/Gr exhibit similar trends where the magnetic anisotropy energy, ΔE, decreases gradually as the adatom approaches the graphene sheet from larger distances until it reaches a minimum, and then increases again for stronger compressions. The distinguishing factor between the two systems is the location of the minimum value, which is shifted towards smaller relative distances, d/d_0, for Tm/Gr. Additionally, Tm/Gr experiences a sign change in ΔE in a narrow range of strain when highly compressed, ultimately favoring an in-plane magnetization. The variable magnetic behavior observed in these systems under external induced strain could have potential applications in the design of magneto-mechanical nano devices that rely on pressure-induced magnetization transitions [198–200]. In contrast, Dy/Gr exhibits a distinct behavior, where the trend appears linear, with ΔE starting from negative values at $d/d_0 = 1.04$ and increasing towards positive values upon compression. As a result, there is a transition in the preferred direction of magnetization from in-plane under large tensile strains to out-of-plane under compressive strains, with the transition occurring in the range of $d/d_0 = 0.98$ to $d/d_0 = 0.97$. The figure also depicts the

Table 5.9: Dissociation energy D_e , the b parameter and the equilibrium distance d_0 obtained by fitting with Eq. 5.5 the curves in Fig. 5.17. The parameters are listed for each RE/Gr complex and magnetization direction.

M direction	D_e [eV]	b [1/bohr]	d_0 [Å]
Dy adatom on graphene			
perpendicular	0.833	3.482	2.481
parallel	0.861	3.369	2.491
Ho adatom on graphene			
perpendicular	1.179	2.762	2.479
parallel	0.731	3.587	2.472
Tm adatom on graphene			
perpendicular	0.311	4.696	2.449
parallel	0.398	4.467	2.436

trend for Eu/Gr and Gd/Gr, which lack magnetoelastic behavior due to the half-filled $4f$-shell. Consequently, as compared to open $4f$-shells, ΔE remains nearly constant and close to zero.

Fig. 5.17 illustrates the total energy curves of each RE/Gr system as a function of strain, for both parallel and perpendicular magnetization directions. The curves have been vertically shifted to set the lowest energy to 0 eV and are limited to a small range of strains around the equilibrium distances. The DFT+U calculations are represented by dotted points, while the continuous lines correspond to the fitting using a Morse anharmonic potential in the form [201, 202]

$$V(r) = D_e \left(1 - e^{-b(d-d_0)}\right)^2 . \tag{5.5}$$

The equation utilized to carry out the fitting involves several parameters. Specifically, D_e refers to the potential's depth relative to the dissociation energy, while d denotes the distance between the RE and Gr, and d_0 represents the equilibrium distance. Additionally, the parameter b is utilized to determine the width of the potential well.

The values of these parameters are listed in Table 5.9. Notably, the anharmonic potential exhibits a dependence on the magnetization direction, which is apparent from the diverse characteristics of the potential well. In terms of the equilibrium distances, the influence of magnetostriction is evident in the differences of approximately 0.01 Å when comparing the perpendicular magnetization direction to the in-plane direction. By treating the RE/Gr complex as a diatomic molecule, it is possible to model the vibrational modes close to the energy minima in the ground state potential well and determine the stiffness against deformation and vibrational frequencies. The force constant at equilibrium distance, k_e, can be evaluated from the fitted values as

$k_e = 2b^2 D_e$, and the respective vibrational frequency can then be calculated using the equation:

$$\nu = \frac{1}{2\pi}\sqrt{\frac{k_e}{\mu}}. \tag{5.6}$$

The reduced mass of the RE/Gr complex, denoted as μ, is calculated using the equation $\mu = \frac{m_{\mathrm{Gr}} m_{\mathrm{RE}}}{(m_{\mathrm{Gr}} + m_{\mathrm{RE}})}$, where m_{RE} represents the atomic mass of the RE atom, and m_{Gr} represents the mass of the graphene in the simulation cell. For instance, Dy has an atomic mass of 162.5 amu, Ho has an atomic mass of 164.93 amu, and Tm has an atomic mass of 168.93 amu. The simulation cell consists of six carbon atoms with a total mass of 72.066 amu. The reduced mass is then converted to Kg using the conversion factor $1.6605 \cdot 10^{-27}$, and the force constant k_e, initially measured in eV/bohr^2, is converted to N/m by multiplying the values by $\frac{1.602 \cdot 10^{-19}}{(5.2918 \cdot 10^{-11})^2}$.

In this way, the vibrational frequencies can be obtained in units of s^{-1}, providing important information on the mechanical and dynamic properties of the RE/Gr system. Table 5.10 presents the computed values of k_e and ν for each system and magnetization direction. It can be observed that the vibrational properties exhibit slight variations depending on the magnetization direction. An out-of-plane magnetization in Dy/Gr yields higher k_e and ν values, indicating greater resistance to deformation when perpendicularly magnetized. In contrast, Ho/Gr and Tm/Gr exhibit larger k_e and ν values for an in-plane magnetization. Among the examined materials, Tm/Gr has the lowest force constants and vibrational frequencies, indicating weaker bonding towards the substrate and greater malleability compared to the other systems. Specifically, the force constant values follow the trend $k_e(\mathrm{Dy}) > k_e(\mathrm{Ho}) > k_e(\mathrm{Tm})$, reflecting the adsorption energies and d occupations.
Taking into account the magnetic bistability observed in the multiplet spectra of Ho/Gr and Tm/Gr (Fig. 5.12), there exists a separation between the two ground states with energy gaps of approximately $\Delta E \sim 14$ meV and $\Delta E \sim 18$ meV, respectively. When converting the vibrational frequencies of the rare-earth atoms' modes into vibrational energies, values ranging from $h\nu = 60-70$ meV are obtained. This implies that magnetization reversal due to adatom vibrations, which would necessitate $\Delta E = h\nu$, is unlikely.

RE/Gr	$k_{e\perp}$	$k_{e\parallel}$	$\nu_\perp \cdot 10^{-13}$	$\nu_\parallel \cdot 10^{-13}$
Dy/Gr	1155.54	1118.13	1.879	1.848
Ho/Gr	1029.05	1076.14	1.769	1.809
Tm/Gr	784.72	908.63	1.539	1.656

Table 5.10: Elastic force constants k_e (N/m) and the respective vibration frequencies ν (s^{-1}) calculated with perpendicular and parallel magnetization for each RE/Gr system.

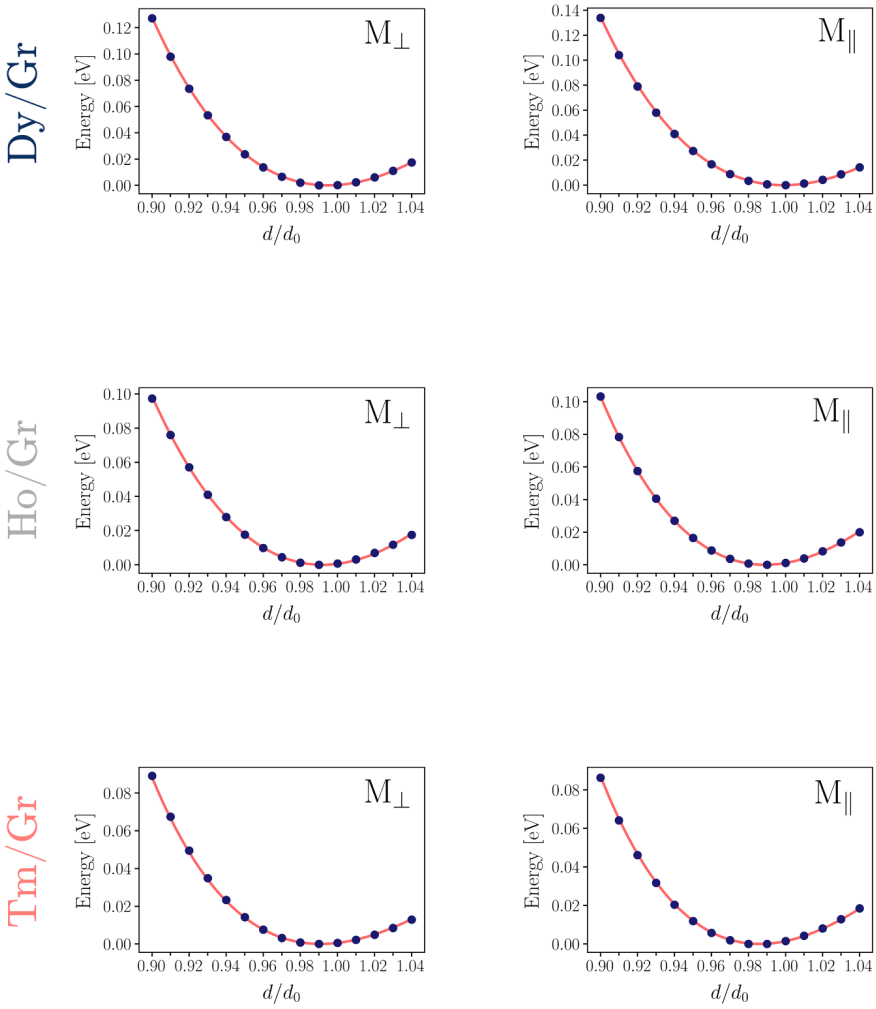

Figure 5.17: Total energy curves for each system as a function of d/d_0, ranging from 0.90 to 1.04, with perpendicular and in-plane magnetization directions. The blue dots represent the DFT+U data, while the red continuous lines are the fitting functions obtained with Eq. 5.5. The parameters D_e, b, and the precise equilibrium distance d_0 are determined from each fitting.

5.2.3 How is the MAE affected by the Hubbard U?

This section investigates the influence of the Hubbard U parameter on the out-of-plane magnetic anisotropy energy curves. The total energy curves as a function of θ are studied for three distinct U values in each system. One value is consistent with the previous analyses (approximately 7 eV), while the other two differ by 2 eV, with one being smaller and the other larger.

Figs. 5.18, 5.19, and 5.20 present the results for Dy/Gr, Ho/Gr, and Tm/Gr, respectively, along with the spin-polarized 4f and 5d DOS for each U value (in red and blue, respectively). Additionally, Gd/Gr is included as a half-filled 4f representative in Fig. 5.21. The blue curves correspond to the values used throughout this study, while the red and green curves represent the results obtained using smaller and larger U values, respectively.

Overall, it can be observed that as the Hubbard U parameter decreases, the 4f states (depicted in red in the spin-resolved DOS) move closer to the Fermi energy. As a result, they are more exposed to other high-energy valence states and interact more strongly with the environment, generating larger MA effects. This trend is exemplified by the Dy/Gr system, where the red curve corresponding to U = 5 eV reaches higher energy values than for higher U values.
In the case of Ho/Gr and Tm/Gr, the shift of the 4f states is even causing them to lie on the Fermi energy, indicating metallic behavior. Therefore, the MAE curves obtained with small U values are not reliable and larger values must be used.

For $U \sim 9$, the MAE curves have similar energy scales to the $U \sim 7$ case. Additionally, for Dy/Gr, the minima and maximum are close to the U = 7 eV value, and for Ho/Gr and Tm/Gr, the canted easy-axis is also obtained with a larger Coulomb parameter. Thus, it can be concluded that values of $U \sim 7$ eV are sufficient to obtain the electronic and magnetic properties of 4f-atoms quantitatively and qualitatively.

Fig. 5.21 illustrates the situation of the half-filled 4f-shell of Gd. The choice of the U value does not significantly affect the MAE in this case. This can be attributed to the fact that the occupied 4f states are located deep in energy away from the Fermi energy in all cases. Therefore, the MAE primarily arises from the 5d occupation, which is always spin-polarized due to the large 4f magnetic moment.

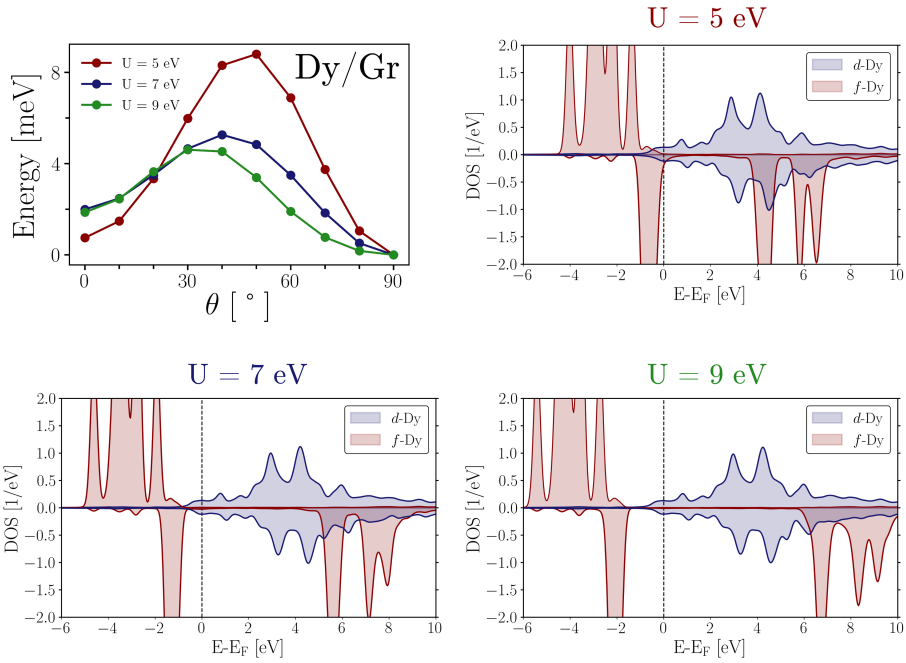

Figure 5.18: Dy/Gr: dependence of the out-of-plane MAE curve and spin-polarized DOS on the Hubbard U value. The red curve corresponds to U = 5 eV, the blue curve to U = 7 eV, and the green curve to U = 9 eV.

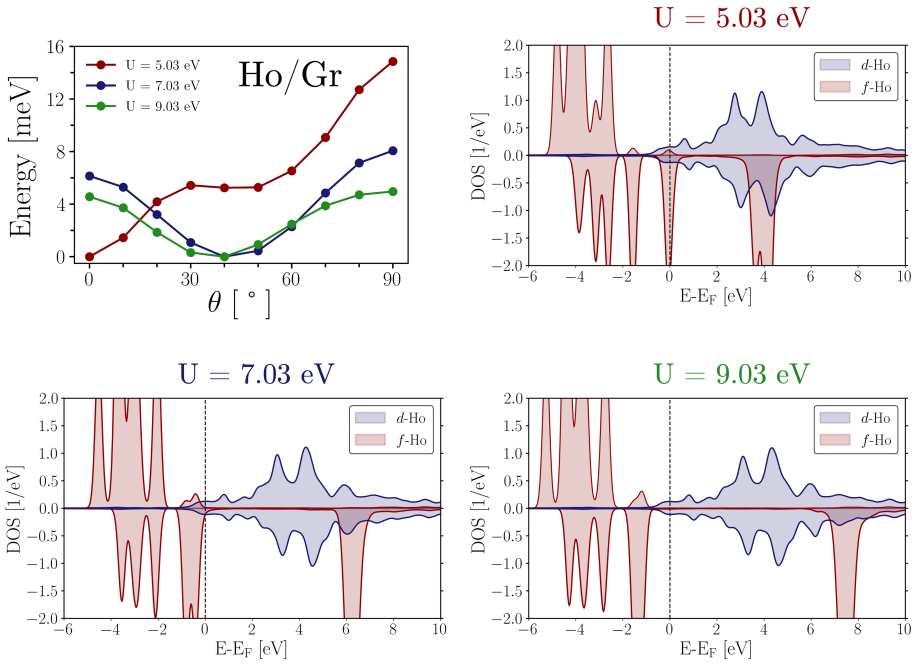

Figure 5.19: Ho/Gr: Dependence of the out-of-plane MAE curve and spin-polarized DOS on the Hubbard U values. The red curve corresponds to U = 5.03 eV, the blue curve to U = 7.03 eV, and the green curve to U = 9.03 eV.

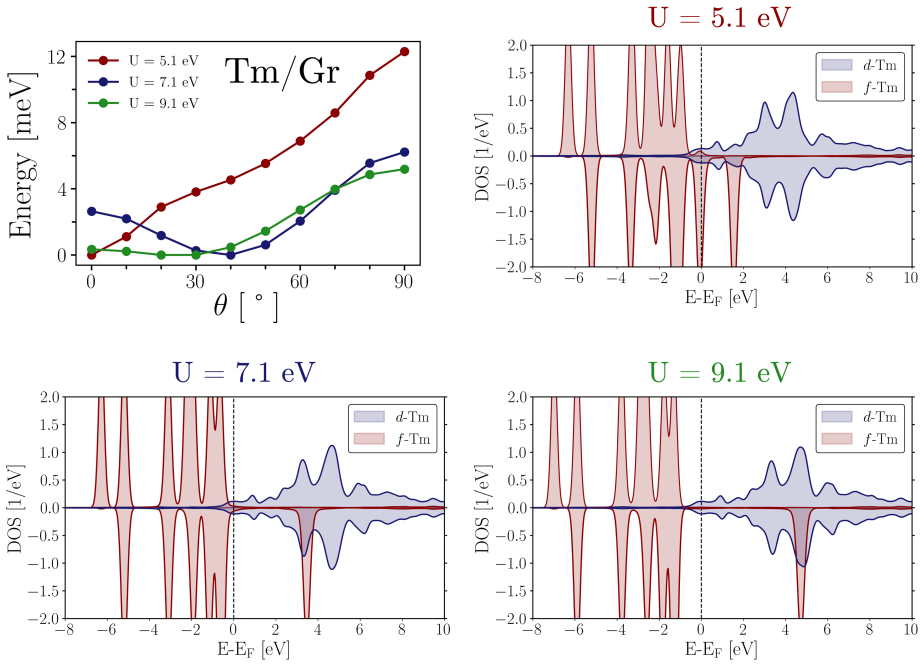

Figure 5.20: Tm/Gr: Dependence of the out-of-plane MAE curve and spin-polarized DOS on the Hubbard U values. The red curve corresponds to U = 5.1 eV, the blue curve to U = 7.1 eV, and the green curve to U = 9.1 eV.

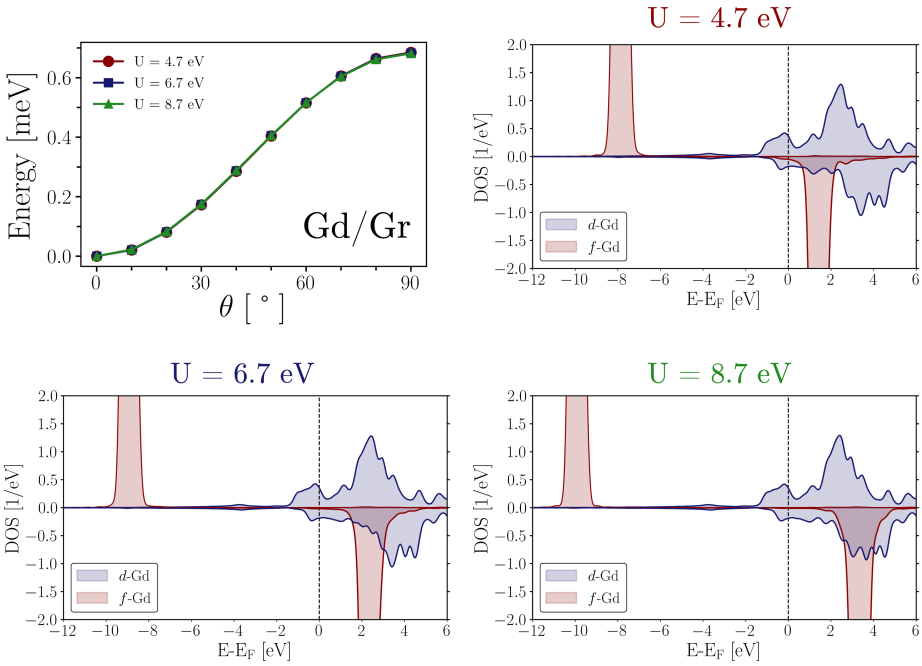

Figure 5.21: Gd/Gr: Dependence of the out-of-plane MAE curve and spin-polarized DOS on the Hubbard U values. The red curve corresponds to U = 4.7 eV, the blue curve to U = 6.7 eV, and the green curve to U = 8.7 eV.

5.3 The case of Dy deviating from Hund's rules

In the sections discussed earlier, all systems displayed a Hund's rule $4f$ occupation. However, upon further analysis, it was found that in the case of Dy/Gr, a $4f^{10}$ occupation can result in a distinct orbital occupation. Specifically, one majority spin electron migrates from the $m_l = 1$ orbital to the $m_l = 0$ orbital, resulting in the quenching of the orbital moment of Dy to $m_l = 5\ \mu_B$. This phenomenon can be attributed to the competition between the crystal field effects and the Hund's exchange interaction, leading to an orbital rearrangement.

Table 5.11 shows that the overall $4f$ occupation remains around 10 electrons with a spin magnetic moment of 4.033 μ_B, which is similar to Hund's rules. However, the orbital magnetic moment is reduced to 4.903 μ_B, which breaks Hund's second rule of maximizing the total orbital angular momentum. Consequently, the total angular momentum of Dy/Gr is $J = 7$ instead of $J = 8$ as per the Hund's rules. Specifically, the energy difference calculated between the two observed magnetic states is 0.28 eV in favor of the $J = 7$ situation. To examine the impact of this orbital rearrangement on the magnetic properties, the out-of-plane and in-plane magnetic anisotropy curves were evaluated in the $J = 7$ configuration and are depicted in Fig. 5.22. The anisotropic behavior deviates from the $J = 8$ case (as seen in Fig. 5.9) due to the altered geometrical shape of the $4f$ charge when one $4f$ electron is moved to the $m_l = 0$ orbital. This difference can be visualized in Fig. 5.23. Upon examination of Fig. 5.22, it can be observed that the out-of-plane curve demonstrates a minimum at a canted angle of $\theta = 51.82°$ and displays significant deviations from the $J = 8$ state as the system moves from 0° to 90°. While the $J = 8$ state presented an energy hill, the $J = 7$ state exhibits an energy valley. This phenomenon can be attributed to the magnetic anisotropy constants, which are compared in Table 5.12 for both magnetic states.

The in-plane magnetic anisotropy energy curve exhibits a notable increase in energy, comparable in magnitude to the out-of-plane curve, and represents the largest in-plane anisotropy among the studied systems. This enhanced contribution in the in-plane direction can be attributed to the significant value of K_4, which induces a notable shift in the energy minimum from the pure out-of-plane value. Specifically,

d_{occ}	f_{occ}	$m_s^{RE}[\mu_B]$	$m_l^{RE}[\mu_B]$	$m_s^{tot}[\mu_B]$
0.260	9.898	4.033	4.903	4.168

Table 5.11: Ground state properties for Dy with orbital moment ~ 5 μ_B ($J = 7$) on top of Gr in the H-site: d and f occupation of the magnetic RE atom, spin magnetic moment of the RE atom in μ_B, orbital magnetic moment of the RE atom in μ_B, and total spin magnetic moment of the RE/Gr system in μ_B. Calculations have been performed in presence of SOC.

Table 5.12: Dy/Gr: Magnetic anisotropy constants for the $J = 7$ and $J = 8$ magnetic states. The values are reported in meV.

State	K_1	K_2	K_3	K_4
$J = 7$	−14.29	13.10	−1.76	1.16
$J = 8$	15.36	−18.92	1.54	−0.44

the minimum for the out-of-plane energy ($\frac{\partial E_{an}}{\partial \theta}|_{\varphi=0^\circ}$) occurs at $\theta = 51.82^\circ$, while the global minimum ($\frac{\partial E_{an}}{\partial \theta}|_{\varphi=30^\circ}$) occurs at 57.93° due to the effect of K_4.

To offer a qualitative explanation for the substantial K_4 value, one can consider the spin-down 4f charge density, which is the distinguishing feature between the $J = 8$ and $J = 7$ states, computed for an in-plane magnetization direction, as depicted in Fig. 5.23. The $J = 7$ magnetic configuration reveals a more significant density in the xy-plane relative to the $J = 8$ state, which lacks such distinct poles parallel to the substrate. Thus, the $J = 7$ configuration results in a stronger interaction of the 4f charge with the hexagonal crystal field. These results highlight the importance of a meticulous evaluation of the 4f orbital occupation in rare-earth based systems in low dimensions. This is also important if one wants to use the above proposed reverse-engineering method to determine the CFP, since it holds only valid in the context of a Hund's rule occupation, *i.e.* when the interelectronic repulsion and SOC effects dominate and the crystal field can be treated as a perturbation.

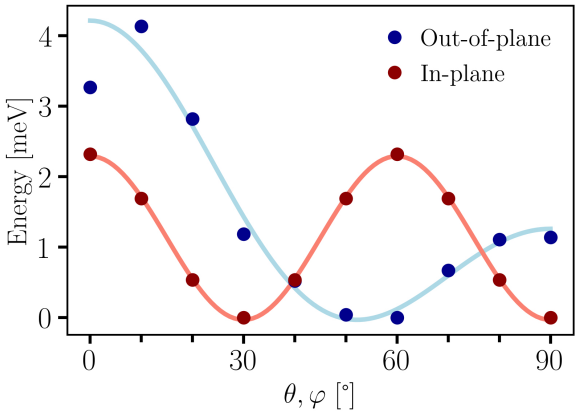

Figure 5.22: The figure shows the out-of-plane (blue) and in-plane (red) magnetic anisotropy energy curves for Dy/Gr with Dy having an orbital moment of $m_l = 5\ \mu_B$. The blue dots represent the DFT+U energies, while the lines indicate the fitting.

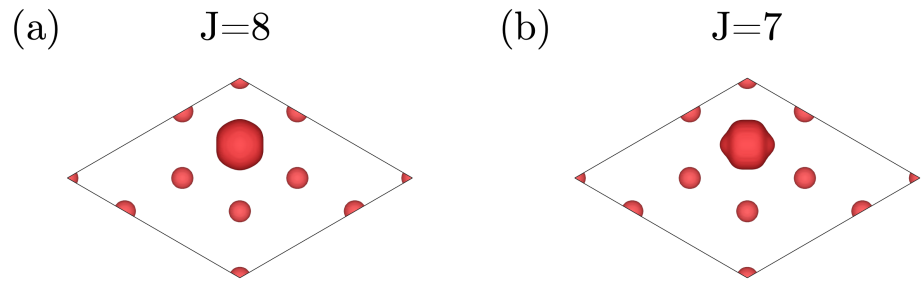

Figure 5.23: Top view of the charge density of the spin-down channel of Dy/Gr with in-plane magnetization for the two different orbital moments: (a) $m_l = 6$ μ_B ($J = 8$) (b) $m_l = 5$ μ_B ($J = 7$).

5.4 Diluted rare-earth atoms: 4×4 graphene supercell

In order to investigate the effect of varying concentrations of rare-earth atoms adsorbed onto the Gr sheet, a 4×4 supercell containing 33 atoms (32 C atoms and 1 RE atom) was simulated, with the magnetic adatom positioned in the H-site. This configuration corresponds to a much more diluted RE concentration, with one RE adatom per 32 C atoms instead of one per 6 C atoms. The perpendicular distance between the RE and Gr atoms was held constant, matching the value obtained from the smaller $\sqrt{3} \times \sqrt{3}$ simulation cells.

The ground state electronic properties of Eu and Gd without SOC, as well as those of the open $4f$-shells in the presence of SOC, are presented in Table 5.13. Commencing the discussion with a comparison of the d electron occupations in the two simulation cells, it can be observed that in all instances, the d_{occ} is lower in the 4×4 cell as compared to the $\sqrt{3} \times \sqrt{3}$ configuration. Specifically, for Eu, the d_{occ} is 0.196 as opposed to 0.332; for Dy, it is 0.181 in contrast to 0.262; for Ho, it is 0.165 compared to 0.250; and for Tm, it is 0.155 as against 0.237 in the $\sqrt{3} \times \sqrt{3}$ cell. The sole exception to this trend is Gd/Gr, where the dilute configuration yields almost a full d electron (0.935 d electrons) in the valence shell, as compared to a fraction of 0.866 observed in the higher coverage scenario ($\sqrt{3} \times \sqrt{3}$). These observations provide evidence of a transition towards a more atomic-like nature of the magnetic $4f$-adatoms. The increased separation between RE atoms reduces the delocalized charge for each RE-RE interaction as well as the electrons involved in the RE-Gr interaction, resulting in a reduced metallic behavior of the RE layer. This transformation is reflected in a shift from a RE monolayer to a more isolated atomic configuration.
Specifically, Gd tends to retain its $5d$ electron in the valence configuration, making it less available for bonding and thus resulting in weaker interaction with Gr and the surrounding Gd atoms. In contrast, all the other RE atoms acquire fewer d electrons

from the environment, leading to reduced interaction. The transition from metallic to atomic behavior is also reflected in the 4f orbital occupation, which exhibits a slight increase across all cases, with a stronger trend towards following the Hund's rules.

From the perspective of the spin magnetic moment of the RE atoms (m_s^{RE}), it is noted that their values are higher of around 0.1 μ_{B} in the dilute situation, which can be attributed to the presence of induced $f-s$ spin polarization (see Table 5.14) that is absent in the high-coverage state. In the case of Gd/Gr, the value of m_s^{RE} is roughly 0.41 μ_{B} larger in the 4×4 supercell than in the $\sqrt{3}\times\sqrt{3}$ cell, driven by both the $f-s$ spin polarization and the enhanced $f-d$ spin polarization. These effects are observable in Fig. 5.24, which displays the s (green), d (blue), and f (red) states of the RE adatom for each system, in addition to the TDOS (grey). Additionally, a zoomed-in view of the s states around the Fermi energy is provided for each RE/Gr system. Here, it can be noticed how the 4f peaks shift deeper to lower energies compared to the $\sqrt{3}\times\sqrt{3}$ cell, reflecting the isolated-atom picture. The appearance of a sharp occupied spin-up s peak just before the Fermi energy is especially noteworthy. This feature can also be observed in other studies in the literature for large simulation cells, including 4×4 [193, 203] and 5×5 [204] supercells.
The appearance of the sharp s peak seems to be linked to the RE atoms nearing the dilute limit, as demonstrated by simulating a single RE atom per simulation cell and gradually reducing the lattice parameter from that of the 4×4 Gr supercell (four times the unit cell) to simulate the progression from an isolated atom to a monolayer. Fig. 5.25 illustrates the evolution of the s peak of an Eu atom for various lattice parameters: $a/a_0 = 1.0$ corresponds to the dilute state of the Eu atom as in a 4×4 Gr cell, where a_0 is the lattice constant of this supercell; $a/a_0 = 0.84, 0.72, 0.67$ correspond to smaller distances between the magnetic atoms, resulting in denser packings. It can be observed that as the RE atom becomes more isolated, the s peak becomes narrower. Conversely, in high-concentration situations, the s electrons tend to be more widely spread out in energy. The observed behavior also appears to affect the spin-polarization, as the difference between the two spin channels (the upper panel being spin-up and the lower panel being spin-down) becomes more pronounced when the magnetic adatom is diluted.

RE/Gr	d_{occ}	f_{occ}	$m_s^{\mathrm{RE}}[\mu_{\mathrm{B}}]$	$m_l^{\mathrm{RE}}[\mu_{\mathrm{B}}]$
Eu/Gr	0.196	6.924	7.125	-
Gd/Gr	0.935	7.012	7.724	-
Dy/Gr	0.181	9.915	4.156	5.916
Ho/Gr	0.165	10.913	3.159	5.936
Tm/Gr	0.155	12.901	1.163	2.989

Table 5.13: Ground state properties of RE/Gr in a 4×4 supercell: d and f occupations, spin m_s^{RE} and orbital m_l^{RE} magnetic moments.

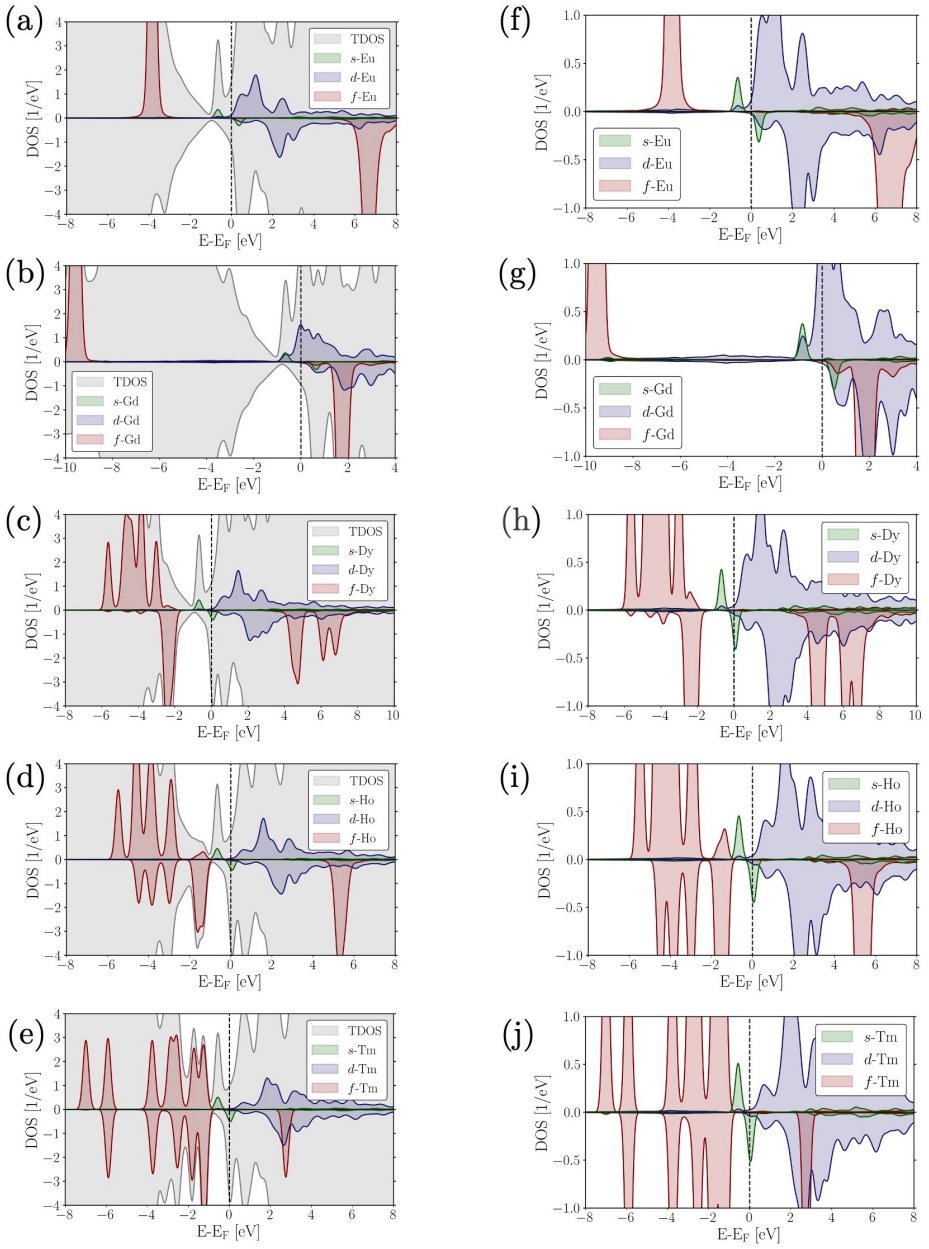

Figure 5.24: Spin-resolved DOS in the 4×4 supercells: panels (a) to (e) display the s, d, f states of the RE and the TDOS; panels (f) to (j) show a zoom of the RE states.

Table 5.14: Spin magnetic moments of the s, d and f electrons of the 4×4 RE/Gr systems.

RE/Gr	m_s^s [μ_B]	m_s^d [μ_B]	m_s^f [μ_B]
Eu/Gr	0.126	0.061	6.906
Gd/Gr	0.135	0.609	6.951
Dy/Gr	0.140	0.032	3.966
Ho/Gr	0.141	0.024	2.980
Tm/Gr	0.140	0.014	1.002

This slight enhancement in the spin magnetic moment, compared to the $\sqrt{3} \times \sqrt{3}$ supercell, may have an impact on magnetic anisotropy, but generally, the contribution of valence electrons to the MAE is a small fraction, approximately 10%, of the total interaction energy between the RE atom and the crystal field.

The computed unfolded bandstructure of 4×4 Eu/Gr in Fig. 5.26 clearly indicates the presence of a narrow s state in the system at ~ -0.7 eV. To emphasize the Dirac cone of the carbon structure, the chosen k-path runs along Γ–K–K'–Γ. The shift of the Dirac point towards lower energies from the Fermi energy suggests an n-doping of the Gr from the lanthanide by approximately ~ 0.7 eV. At a slightly higher energy than the Dirac point, a very flat band corresponding to the s electrons of Eu is visible, with its unoccupied spin-down counterpart located at ~ 0.4 eV. Flat bands exhibit a constant energy across the Brillouin zone, resulting in electrons with low kinetic energy. These electrons are highly localized, which can give rise to novel behaviors such as high electron density or strong electron-electron interactions. These proper-

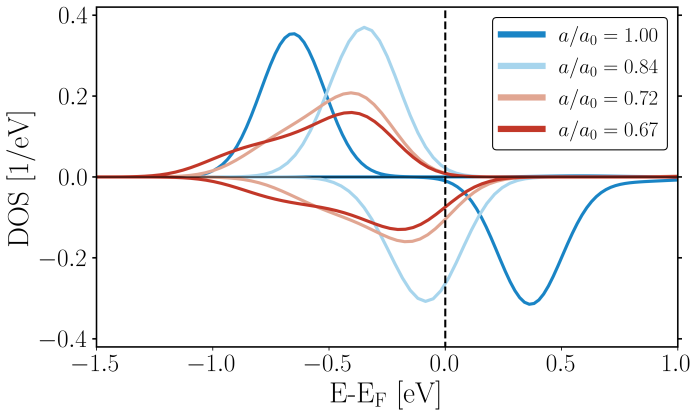

Figure 5.25: Evolution of the s peak with the distance between magnetic Eu atoms expressed as a function of the 4×4 supercell lattice constant of Gr.

ties have been linked to the emergence of superconductivity. The s state of the REs on graphene has the potential to form strongly correlated electronic states, making the observation of the flat band in the 4×4 RE/Gr systems a significant finding that warrants further investigation. The behavior of electrons in flat bands is a subject of great interest for the development of novel electronic and optoelectronic devices, and the investigation of flat bands can pave the way for new discoveries in the field.

Moreover, the magnetic anisotropy can be in first approximation explained as originating from the electrostatic interaction between the non-spherical charge density, primarily determined by the orbital magnetic moment, and the crystal field of graphene. Given the minor changes observed in the orbital moments m_l^{RE} (Table 5.13) in comparison to the $\sqrt{3} \times \sqrt{3}$ supercell, significant deviations in the magnetic anisotropy are not expected. From another perspective, the electron redistribution within the valence orbitals observed in the 4×4 case can alter the interaction between the RE atom with graphene, resulting in a small change in the perpendicular distance between the RE atom and graphene. Consequently, this affects the crystal field generated by Gr and experienced by the RE atom. Nonetheless, as illustrated in Fig. 5.14 and Fig. 5.16, it is evident that the magnetic anisotropy (and the respective constants K_i) trend remains approximately linear in the vicinity of $d/d_0 = 1$.

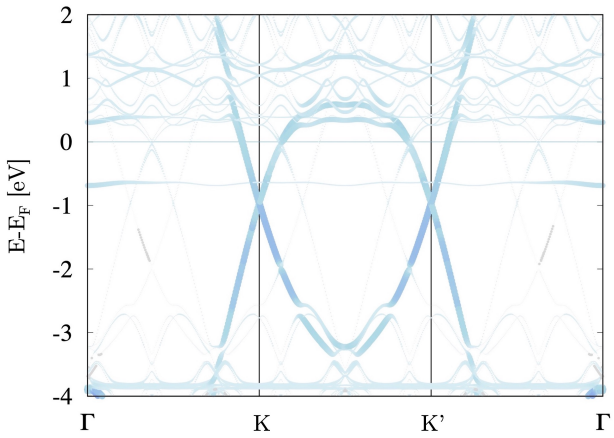

Figure 5.26: Unfolded band structure of the 4×4 supercell of Eu/Gr along the Γ–K-K'–Γ path, highlighting the Dirac cones at K and K'. The calculation was performed without SOC.

Chapter 6

The effect of a metallic substrate: Gd/Gr/Ir(111) and Gd/Gr/Co(111)

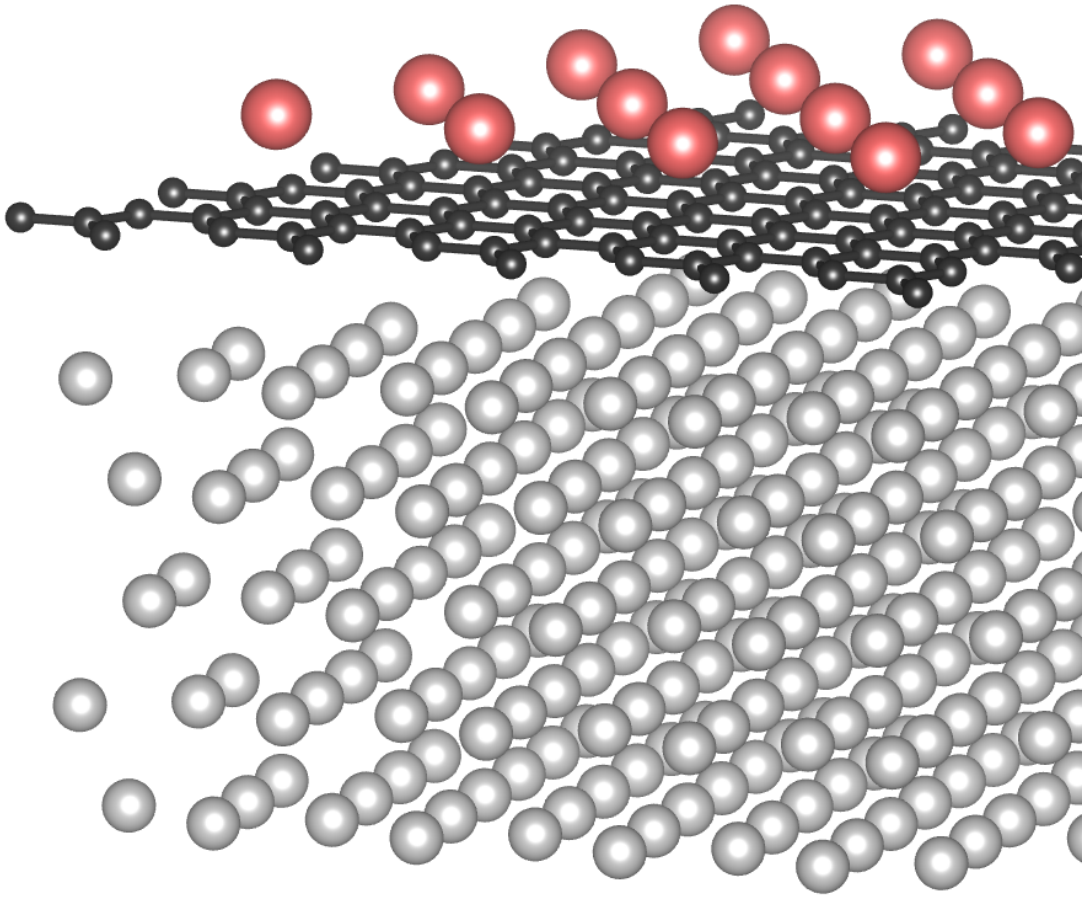

The objective of this chapter is to investigate the impact of a metallic substrate on the magnetic properties of Gd/Gr. Understanding the effects arising from the metallic substrate in graphene-based systems is essential, as experimental growth of van der Waals heterostructures often occurs on such surfaces. Two scenarios have been examined: a non-magnetic substrate, Ir(111), and a magnetic substrate, Co(111).

The chapter will be organized as follows:

- In Section 6.1, an initial investigation of Gr on an Ir(111) surface at two different distances of the graphene monolayer from the substrate is carried out.
- In Section 6.2 the investigation is expanded by simulating the adsorption of a Gd adatom on top of Gr/Ir(111), with attention given to differences between the two perpendicular heights of Gr from Ir(111).
- In Section 6.3, a magnetic substrate is exemplified by replacing the Ir atoms with Co atoms, and the effect of the magnetic surface will be analyzed by considering the experimental distance between Gr and Co(111).

Computational details

The following sections present results obtained using the FLAPW method within the DFT+U framework as implemented in FLEUR. The simulations were performed in a $\sqrt{3} \times \sqrt{3}$ simulation cell with the same lattice parameter as the previous studies of free-standing RE/Gr systems. A surface of Ir(111) (Co(111)) was constructed by stacking 5 layers of FCC Ir (Co) in the ABC stacking sequence beneath the Gr monolayer. The Gd adatom was positioned in the H-site of the Gr monolayer. The value of K_{max} was set to 4.5 a_0^{-1} for the SCF calculations and to 4.3 a_0^{-1} for the MAE calculations, and the maximal angular momentum inside the MT spheres was set to $l_{max} = 10$ for Gd, $l_{max} = 6$ for C atoms, and $l_{max} = 8$ for Ir and Co atoms. The SCF cycle was converged using the PBE prescription of GGA exchange-correlation functional and a k-point mesh of 20×20. The DFT+U parameters for Gd were set to $U = 6.7$ eV and $J = 0.7$ eV.

6.1 Graphene adsorbed on Ir(111)

It is widely acknowledged through experimental evidence that the growth of graphene on Ir(111) leads to a structural mismatch when superposing the two structures. This mismatch is primarily attributed to a lattice constant disparity of approximately 10% between the graphene lattice constant (2.46 Å) and that of Ir(111) (2.73 Å), which results in significant distortions within the system. This has been demonstrated

through a number of studies, including those conducted by Brako et al. (2010) [128], Coraux et al. (2008) [205], and Meng et al. (2012) [206]. A superperiodicity, known as a *Moiré* pattern, is generated as a result, in which the two structures only match perfectly after a certain number of Ir unit cells and Graphene unit cells have been covered, such that the center of the Graphene hexagon aligns with an Ir atom. To achieve this alignment, 10 Graphene unit cells must be present on 9 Ir unit cells in each surface direction, given the larger size of the Ir unit cell. Simulating such a large supercell requires significant computational resources, and therefore it is often more practical to simulate the different structural registries that appear within the Moiré pattern separately. The objective of the forthcoming investigation is to assess the effect of a metallic surface on the magnetic behavior of the RE/Gr complex. The Gr monolayer interacts with the Ir(111) metallic surface through van der Waals forces, and it is presumed that the crystal field surrounding the magnetic rare-earth (RE) atom is solely determined by the hexagonal carbon ring of the Gr. Therefore, to obtain computationally feasible outcomes, the varied structural configurations within the Moiré superstructure are disregarded, and solely the impact of a generic Ir(111) surface is examined. The simulation cell chosen for this study includes the previously adopted $\sqrt{3} \times \sqrt{3}$ cell of graphene with its corresponding lattice constant, along with five layers of Ir(111) consisting of a total of 6 carbon atoms and 15 Ir atoms (3 Ir atoms per layer), as illustrated in Figure 6.1. The Ir(111) interlayer distance has been evaluated as one third of the body diagonal of FCC bulk Ir, resulting in a value of 2.228 Å when a bulk lattice constant of 3.86 Å is used, as reported in [128].

As Gr grown on Ir(111) is not flat but instead presents corrugations with regions at different distances from the substrate, the Gr/Ir(111) system was investigated in this study at two distinct distances of the Gr from the Ir(111): the *valley* position at h_v = 3.2 Å, and the *hill* position at h_h = 3.6 Å, as observed in [207]. A sketch of the corrugated graphene monolayer on Ir, illustrating the simulated valley and hill positions, is presented in Fig. 6.2, along with the differential charge densities

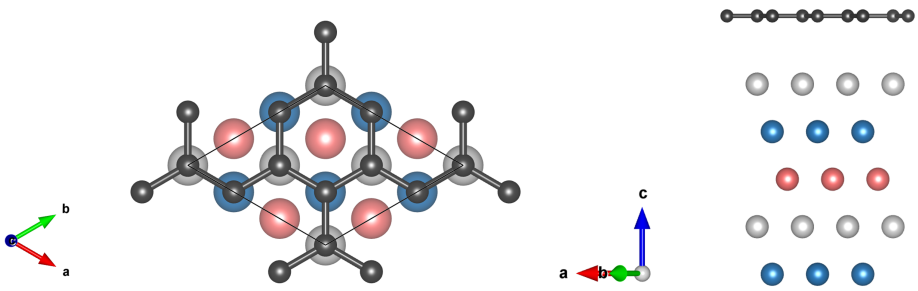

Figure 6.1: $\sqrt{3} \times \sqrt{3}$ simulation cell for Gr/Ir(111) illustrating the ABC stacking of the Ir(111) surface layers in different colors.

calculated as $n_{\mathrm{Gr/Ir}} - n_{\mathrm{Gr}} - n_{\mathrm{Ir}}$ for the valley and hill positions of the Gr monolayer on Ir. The calculations reveal significant variations in charge distribution between the two structures. The charge accumulation regions (positive values) are indicated in red, while the charge loss regions (negative values) are shown in blue. The data suggests that when the Gr is in closer proximity to the Ir surface, the interaction involves more charge. Notably, there is a stronger dipole in the interface region, with a negative pole located at the backside of Gr and a positive pole situated above the first layer of Ir. This charge separation is also observed in the hill position, albeit with less intensity. Fig. 6.3 illustrates the computed relative band structures, where the overall band structures for each of the two analyzed Gr-Ir distances are presented in black, while the contribution of Gr is depicted in red. The contribution of Gr is also displayed separately with more emphasis underneath. An important observation is that at the hill position h_h, the Dirac cone is distinctly visible above the Fermi energy, indicating a slight p-doping from the metal surface to the π orbitals of Gr that are

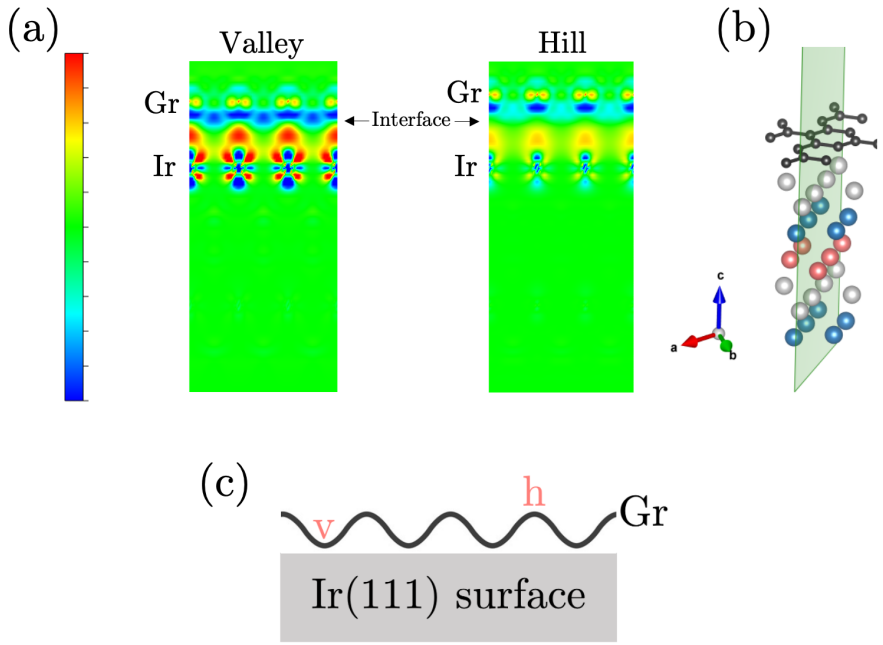

Figure 6.2: (a) The differential charge density in the Gr/Ir(111) system in the (1-10) plane is shown for the valley and hill positions of graphene from the first Ir layer. The two plots use the same color scale, ranging from −0.001 to 0.001 of saturation, to highlight the variations in charge distribution. (b) The (1-10) crystallographic plane. (c) A sketch of the corrugated graphene monolayer on Ir(111) illustrating the valley and hill positions is provided.

oriented perpendicular to the sheet. This phenomenon has also been experimentally observed [207, 208]. Additionally, it should be mentioned that an induced gap exists at the Dirac point due to the intervalley mixing. In contrast, the breaking of the Dirac cone observed at the valley position h_v can be attributed to the disruption of the AB sublattice symmetry of graphene as it approaches the Ir(111) surface in the chosen configuration, similar to what has been observed in graphene on Au(111) [209]. In Fig. 6.1, it can be seen that three carbon atoms are positioned directly above an Ir atom, while the remaining carbon atoms are located above the second layer of Ir atoms. However, at h_h, the distance is sufficient to prevent significant interaction between Gr and Ir(111), thereby preserving the symmetry of Gr. As a result, the proximity to Ir(111) has a considerable impact on the Gr structure at h_v, which is further supported by the observation that the Gr bands are pushed towards lower energies compared to the h_h configuration.

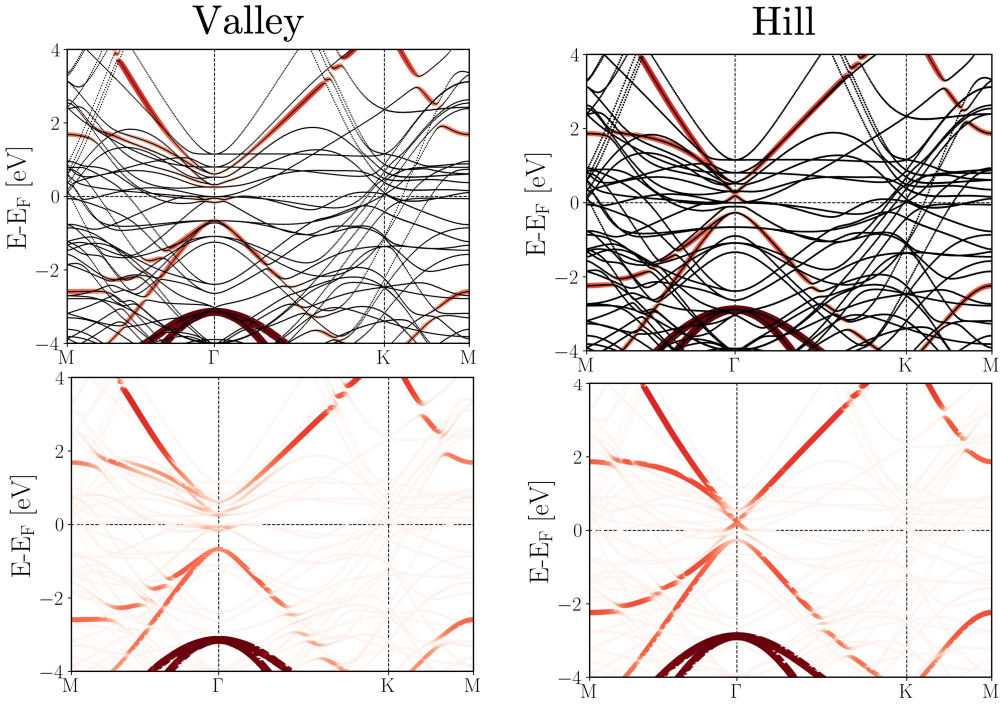

Figure 6.3: Computed band structures of Gr/Ir(111) system at valley distance (3.2 Å) and hill distance (3.6 Å) of Gr from Ir(111). Black denotes the overall band structure, and red illustrates the contribution of C atoms.

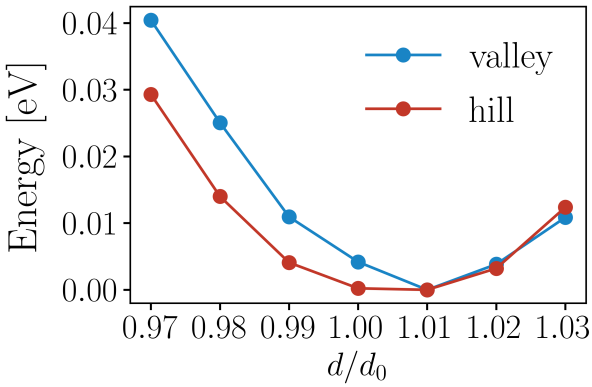

Figure 6.4: Optimization of the perpendicular distance between the Gd adatom and the Gr monolayer is shown for the two Gr-Ir(111) distances. The total energy is evaluated as a function of the relative distance d/d_0, where d_0 is the equilibrium distance obtained in the absence of Ir(111) and d represents the tested new position. The range of distance variation considered is from $d = 0.97d_0$ to $d = 1.03d_0$.

6.2 Gd on top of Gr/Ir(111)

The geometry of the Gd atom adsorbed onto Gr/Ir(111) maintains the same configuration as in the free-standing graphene systems, where the magnetic adatom occupies the H-site. To determine the Gd-Gr distance in the presence of the metal surface, the equilibrium distance of Gd/Gr, which is $d_0 = 2.236$ Å, was initially used and the perpendicular distance was varied by increasing and decreasing it by 3% in steps of 1%, while evaluating the total energy. The result, shown in Fig. 6.4, indicates that both systems favor a slightly higher position of the Gd from Gr, at $d/d_0 = 1.01$, corresponding to $d = 2.258$ Å. In the presence of a Gd adatom, the system exhibits spin polarization due to the large spin magnetic moment of Gd, which is approximately

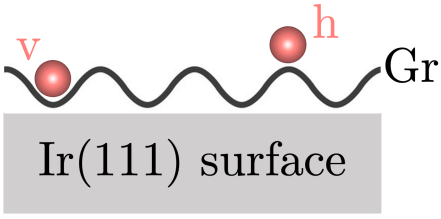

Figure 6.5: The diagram illustrates the two possible structural configurations of Gd/-Gr/Ir(111), with Gd adsorbed either in the valley position of Gr or in the hill position.

7.357 μ_B for h_v and 7.352 μ_B for h_h. Additionally, the d_{occ} and f_{occ} values show a high degree of similarity between the two distances. Specifically, in the valley distance, there are 0.853 d electrons and 7.013 $4f$ electrons, while in the hill distance, there are 0.858 d electrons and the same $4f$ electron count as in the valley distance. Thus, no significant differences are observed in the Gd atom between the two distances. By calculating the difference between the total spin-up charge density and the total spin-down charge density, a total magnetic moment of 8.021 μ_B for the valley and 7.939 μ_B for the hill is obtained. This indicates that both cases behave similarly to the free-standing Gd/Gr system, with the hill approaching that limit and the valley exhibiting a slightly increased total magnetic spin moment.

Fig. 6.6 depicts the spin-polarized electronic structure of the Gd/Gr/Ir(111) system

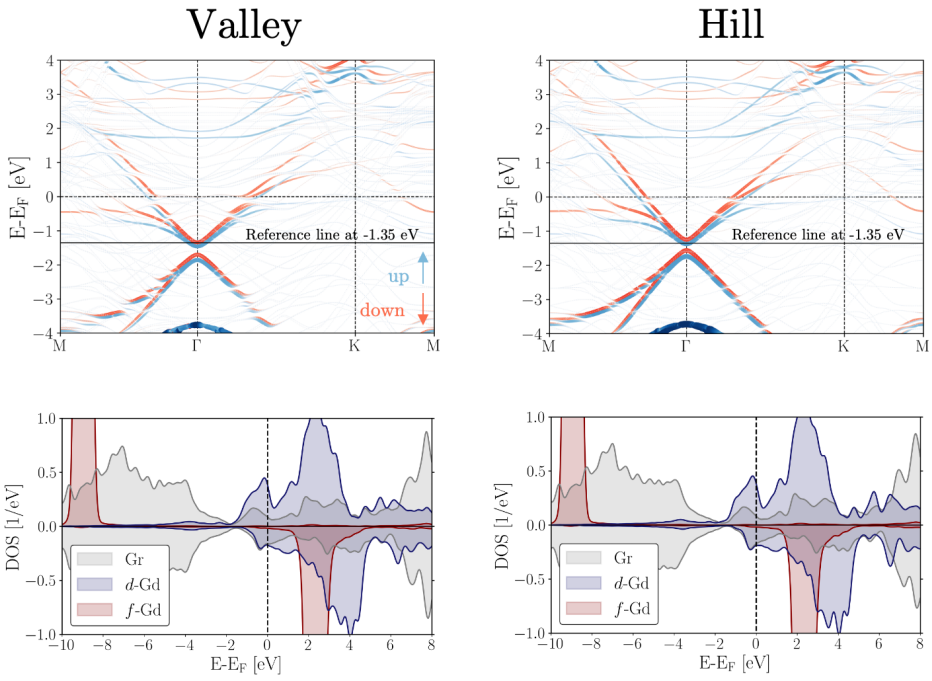

Figure 6.6: The upper panels show the spin-polarized band structure projected on the carbon atoms of Gd/Gr/Ir(111) in the valley and hill configurations, where blue represents the spin-up channel and red represents the spin-down channel. A reference line is plotted at -1.35 eV. The lower panels show the corresponding spin-polarized density of states of the carbon contribution (grey), the d electrons in Gd (blue), and the f electrons of Gd (red). All calculations were performed in presence of SOC.

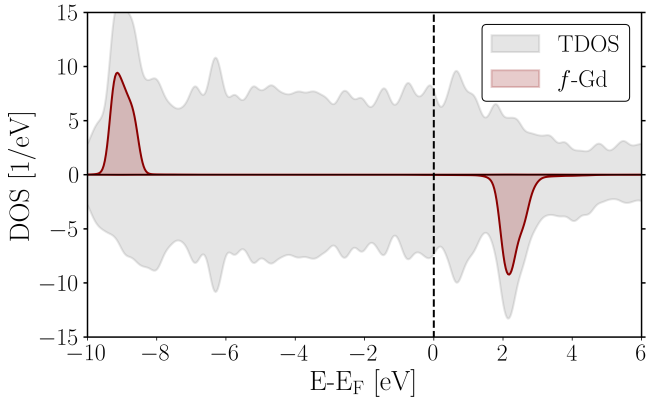

Figure 6.7: Spin-resolved total DOS (in grey) and $4f$ DOS (in red) of Gd/Gr/Ir(111) in the valley configuration.

with Gr at two different distances from Ir(111), calculated with SOC. The upper panels present the spin-polarized graphene contribution to the band structure, with blue and red representing the spin-up and spin-down channels, respectively, providing a clear view of the Dirac cone. The energy splitting between the spin-up and spin-down bands indicates the induced spin-polarization, which is comparable to the free-standing Gd/Gr exchange, as shown in Appendix C where the graphene band structure of Gd/Gr/Ir(111) at h_h is compared to that of the free-standing Gd/Gr without the metallic surface. In addition, the adsorption of the Gd adatom on the Gr/Ir(111) structure induces a clear n-doping effect, as evidenced by the shift of the Dirac cone below the Fermi energy. This suggests a charge transfer from the d electrons of Gd to the π orbitals, as previously discussed for Gd/Gr. The n-doping effect is slightly more pronounced in the valley configuration than in the hill, as indicated by the reference line at −1.35 eV. This is reflected in the position of the graphene bands, which are pushed further towards lower energies in the valley. Consequently, a stronger interaction is expected at h_v between the metal and Gr as qualitatively seen also in Appendix C.2, where the product between all the C contributions to the bands with the Ir contributions is mapped in a color scheme.

The spin-polarized DOS shown in the lower panel of Fig. 6.6 provides further evidence of the n-doping effect. The grey region represents the contribution of the carbon atoms and the Dirac point appears below the Fermi energy at 0 eV for both the valley and hill configurations. The spin-polarized d states of Gd are located around this energy and exhibit an induced magnetic moment due to the large $4f$ magnetic moment. The occupied spin-up $4f$ peak is situated at approximately −9 eV, with an energy gap of roughly 11 eV from the unoccupied spin-down peak. Additionally, Fig. 6.7 displays the TDOS of the h_v system along with the $4f$ states of Gd to provide a complete

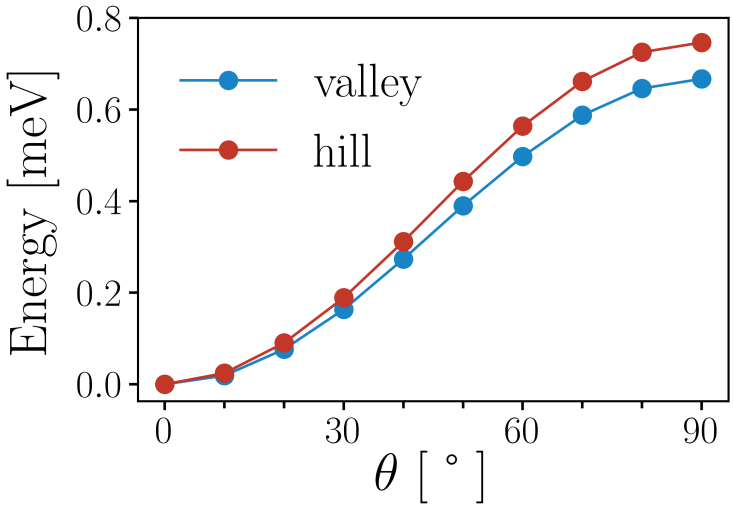

Figure 6.8: Magnetic anostropy curves: total energy against the angle between the z-axis and the direction of the magnetization. The MAE has been evaluated for both the valley and the hill configurations.

overview of the electronic structure. It is evident that most of the features arise from the Ir(111) surface, and the structure exhibits an overall metallic behavior. Furthermore, most of the spin-polarization is concentrated at and around the $4f$ peaks, suggesting that the magnetic moment arises from these states.

Additional exploration was conducted to examine the magnetic anisotropy in the system. Similarly to previous studies, the total energy was computed by rotating the magnetization in the zx-plane through varying the angle θ from 0° (perpendicular magnetization) to 90° (in-plane magnetization). The obtained results for both the valley and hill configurations of the Gr-Ir(111) distances are presented in Fig. 6.8. The system exhibits an out-of-plane easy-axis, and requires an energy of about 0.7 meV to rotate the magnetization in-plane. The energy scales observed are similar to those in free-standing Gd/Gr, indicating that the metallic substrate has a negligible effect on enhancing the MAE through crystal field effects or SOC. In fact, the contribution of Gr to the band structure computed without SOC showed no difference from the SOC calculations (discussed in Fig. 6.6), providing further evidence that Ir does not induce SOC in the Gd/Gr system. Although Ir(111) has a small influence on the system, as seen in Fig. 6.8, the MAE in the valley configuration is slightly reduced.

To qualitatively investigate this effect, the energy difference $\Delta E = E_{\parallel} - E_{\perp}$ was computed at h_h and h_v, with SOC turned off sequentially for Gd and Ir(111). In the valley configuration, neglecting SOC in Gd resulted in $\Delta E \sim -0.04$ meV, indicating

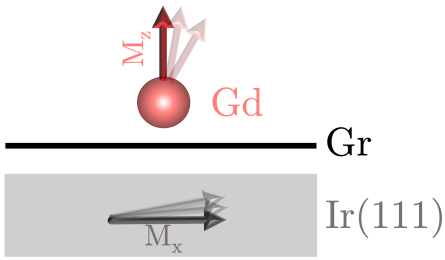

Figure 6.9: Visualization of the competition between the Gd out-of-plane easy-axis and the Ir(111) in-plane easy-axis.

an in-plane easy-axis, while turning off SOC in Ir resulted in $\Delta E \sim 0.77$ meV, indicating an out-of-plane easy-axis. Similarly, in the hill configuration, neglecting SOC in Gd resulted in $\Delta E \sim -0.01$ meV, while turning off SOC in Ir resulted in $\Delta E = 1.22$ meV, showing that Ir favors an in-plane magnetization while Gd favors an out-of-plane magnetization. Therefore, there is a competition between the two magnetization directions, as schematically illustrated in Fig. 6.9, leading to a reduction in the total energy required to rotate the magnetization in-plane as the Gd atom approaches the Ir(111) surface, due to the enhanced interaction with the metal.

In summary, due to its strong binding to the Gr monolayer and proximity to it, Gd has served as an excellent case study for investigating the influence of Ir(111) on magnetic anisotropy effects in RE/Gr systems. The effects of Ir(111) on the magnetic properties of Gd/Gr were found to be minor, with only slight changes observed when the complex was in close proximity to the substrate. The VdW interactions between Gr and Ir(111) resulted in a sufficient distance between the two, preventing the transfer of SOC or variations in the hexagonal crystal field induced by the substrate. However, further investigations are necessary, particularly for highly anisotropic RE atoms. Nonetheless, these findings demonstrate the potential of Ir(111) as a substrate for growing complex magnetic heterostructures.

6.3 Gd on top of Gr/Co(111)

To investigate the influence of the magnetic surface on Gd/Gr, a structural configuration has been selected in which the Gd-Gr distance is maintained at the equilibrium distance obtained for the free-standing complex, specifically $d_0 = 2.236$ Å, while the Gr-Co(111) distance is set to 2.157 Å based on previous findings in [210]. By comparison with the Gr-Ir(111) distance, it is evident that the presence of a Co surface brings the Gr much closer to the substrate. To enable comparison, the surface structure is kept identical to that of Ir(111), comprising five layers of ABC stacking, with the substitution of magnetic Co atoms for the Ir atoms.

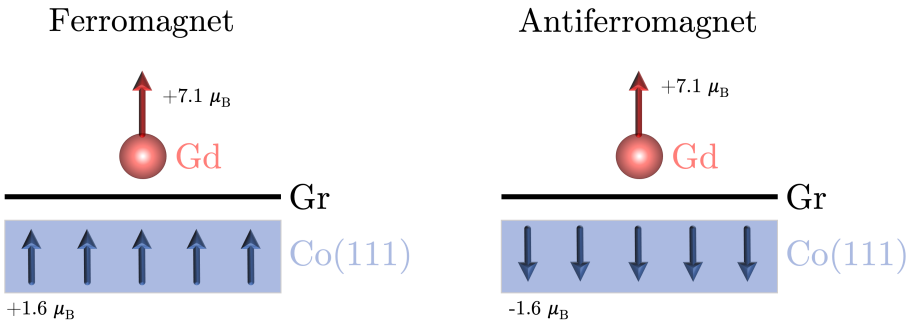

Figure 6.10: Ferromagnetic and antiferromagnetic configurations investigated in the system Gd/Gr/Co(111).

Two distinct magnetic configurations were examined in this study: a ferromagnetic (FM) state in which the Gd spin magnetic moment is aligned with the Co magnetic moments, and an antiferromagnetic (AFM) arrangement in which the magnetic moments of the two constituents are antiparallel, as depicted in Fig. 6.10. In the FM state, the magnetic moments are initially set to 7.1 μ_B and 1.6 μ_B. To obtain the AFM state, the sign of the Co atom's magnetic moment is reversed.
The computed values for d_{occ}, f_{occ}, and the spin magnetic moment of Gd are presented in Table 6.1, along with the MAE expressed as $\Delta E = E_{\parallel} - E_{\perp}$ for both magnetic configurations. In this context, $E_{\perp}$ denotes the total energy of the system in the FM or AFM state with magnetization perpendicular to the plane. On the other hand, $E_{\parallel}$ represents the total energy in the FM or AFM state when the magnetization is rotated by 90° from the perpendicular direction to an in-plane orientation.

Before discussing the MAE, a brief summary of the electronic properties in both FM and AFM configurations with a perpendicular magnetization direction is presented. Although the d and f occupations show little difference between the FM and AFM configurations, the spin magnetic moment of Gd is slightly greater in the FM configuration due to the increased spin polarization in the MT d orbitals of Gd. More precisely, the difference between the spin-up and spin-down d occupation, $n_{d_\uparrow} - n_{d_\downarrow}$, is

order	d_{occ}	f_{occ}	$m_s^{\mathrm{Gd}}[\mu_B]$	ΔE [meV]
FM	0.850	7.018	7.417	−0.533
AFM	0.844	7.022	7.262	−0.261

Table 6.1: The table summarizes the ground state properties of Gd/Gr/Co(111) in the FM and AFM orders, including the d and f occupations, spin m_s^{RE} of Gd, computed with a perpendicular magnetization, and the magnetic anisotropy of the system.

0.409 for the FM configuration and 0.267 for the AFM configuration. The magnetic moment of the Co atoms exhibits a small variation among the different layers, with the most significant difference occurring between the first and fifth layers, whereas the values in the three middle layers are relatively consistent. Specifically, the magnetic moment in the first layer is 1.657 μ_B, and it gradually increases up to the maximum value of 1.839 μ_B in the layer that is farthest from the surface. Conversely, the magnetic moment values in the second, third, and fourth layers fall within the range of $1.774 - 1.798$ μ_B, which are comparatively similar. A similar trend is observed in the AFM configuration with inverted sign.

The transition from FM to AFM is marked by a switch between the spin-up and spin-down channels, as evidenced by the TDOS (in light blue) shown in Fig. 6.11, with the exception of the Gd states. By closer inspection of the carbon atoms' contribution (shown in grey), it becomes evident that the change in magnetization also affects the graphene states, leading to an inversion of the spin-up and spin-down states. This indicates a strong influence of the metallic surface on the behavior of graphene, as depicted also in the spin-polarized band structure displaying the C atom's contributions in Fig. C.3 of Appendix C.3. Additionally, it is observed that significant n-doping

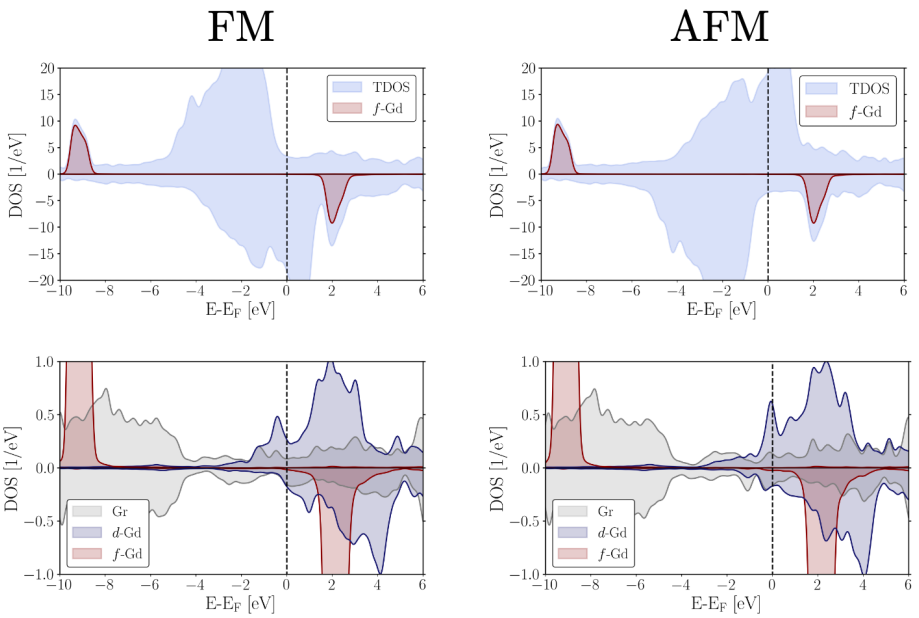

Figure 6.11: Spin-resolved DOS for the two magnetic orders: the top panels display the TDOS of the system and the $4f$ states of Gd, the lower panels display the relative $4f$, $5d$ of Gd and graphene contributions.

occurs in graphene, surpassing the levels found in free-standing Gd/Gr and Gd/-Gr/Ir(111), indicating an additional charge transfer from Co(111) to the graphene orbitals. Furthermore, it should be emphasized that upon evaluating the total energies of the FM and AFM configurations in Gd/Gr/Co(111), the FM configuration is found to be energetically favored, indicating a preference for a parallel alignment of the magnetic moments.

Upon examination of the ΔE values presented in Table 6.1, it is evident that both the FM and AFM configurations prefer an in-plane easy-axis. In the case of FM, disabling SOC on the Gd atom results in a ΔE of -1.016 meV, indicating Co's inclination towards an in-plane magnetization. Conversely, disabling SOC on the Co atoms yields a ΔE of 0.641 meV, signifying Gd's preference for a perpendicular easy-axis. These results suggest that, like the Ir(111) surface, Co(111) promotes an in-plane magnetization, while Gd promotes an out-of-plane magnetization. However, unlike Ir(111), which exhibits limited spin-polarization, the Co(111) surface generates a large magnetic moment that competes with Gd's magnetic moment, and thus can fully induce a shift in the easy-axis of the Gd/Gr system. In contrast to Ir(111), it can be inferred that Co(111) exerts a significant influence on a RE/Gr system, indicating that it is unsuitable for studying free-standing RE/Gr or similar heterostructures due to the strong electronic and magnetic interactions.

Further research is recommended to determine how to improve the MAE by selecting a metallic substrate that preserves the same easy-axis as the RE/Gr system, thereby enhancing the MAE. However, a small MAE, such as the one observed in Gd/Gr, in competition with the substrate, can lead to intriguing phenomena that ultimately result in a canting of the magnetization.

Chapter 7

Engineering spin-orbit effects and Berry curvature by deposition of a Eu monolayer on WSe_2

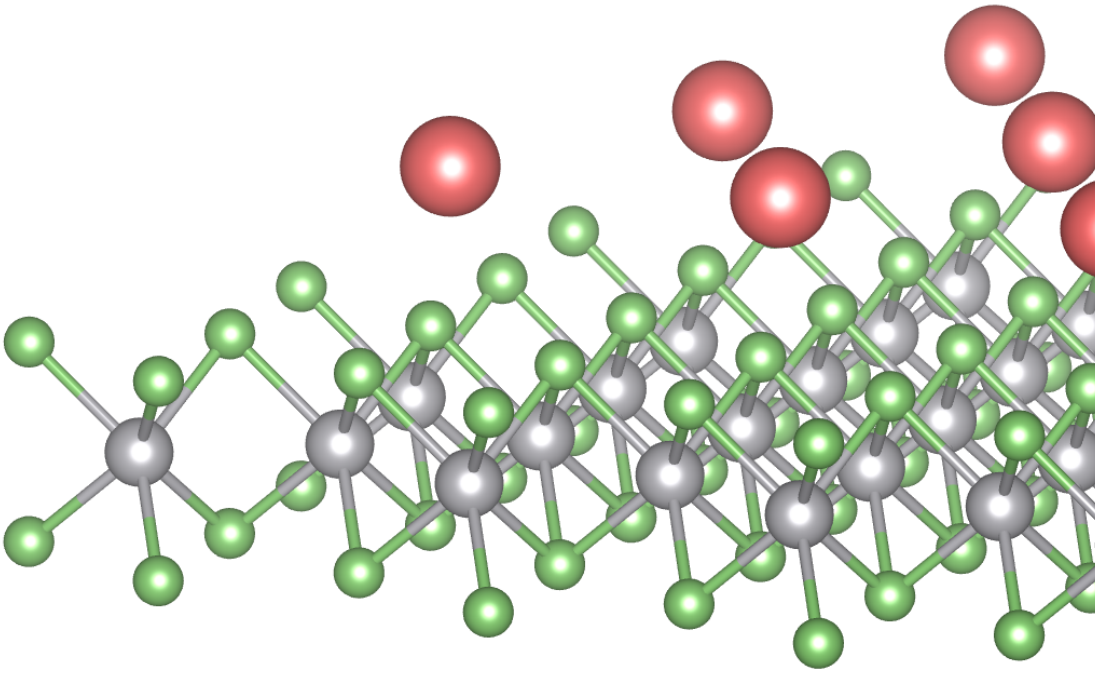

Motivated by recent advancements in 2D spintronics, the following chapter demonstrates the utilization of rare-earth atoms on 2D-materials to exploit magnetic anisotropy driven by the 4f electrons. Specifically, the study focuses on a Eu monolayer on a 1H-WSe_2 monolayer as a promising platform for engineering spin-orbit effects and Berry curvature. The Eu/WSe_2 system exhibits high magnetic anisotropy and valley-dependent polarization of spin and orbital angular momenta, originating from the interplay between localized 4f magnetic moments of Eu and mobile charge carriers of Eu and WSe_2, as well as magnetic and spin-orbit proximity effects at the interface. The magnetic properties analysis shows a ferromagnetic configuration with an out-of-plane easy-axis of the magnetization, promoting a pronounced anomalous Hall effect in the proposed system. Hence, the study proposes 4f-atoms deposited on transition-metal dichalcogenides as a promising platform for 2D spintronics. The findings are presented in the manuscript titled "Engineering spin-orbit effects and Berry curvature by deposition of a Eu monolayer on WSe_2" by Johanna P. Carbone, Dongwook Go, Yuriy Mokrousov, Gustav Bihlmayer, and Stefan Blügel [211].

The chapter is structured as follows:

- Section 7.1 provides an overview of the structural and electronic properties of Eu atoms adsorbed on WSe_2 in a high-coverage situation (1×1 unit cell), including symmetry considerations.
- In Section 7.2, the magnetic properties of the structure are analyzed, including magnetic anisotropy and the magnetic order.
- Section 7.3 discusses the spin and orbital texture produced in the material due to the interaction between different components.
- The observation of anomalous Hall effect is explained in Section 7.8, which discusses how the combination of properties arising from the various components in the system leads to this effect.
- Finally, in Section 7.5, the choice of the simulation cell is discussed by comparing a high-coverage situation of the Eu atom with a more dilute situation in a $\sqrt{3}\times\sqrt{3}$ supercell.

Computational details

The results presented in the following sections were obtained using the FLAPW method within the DFT+U framework, as implemented in FLEUR. A 1×1 unit cell was simulated, which included one Eu atom, two Se atoms, and one W atom, with a lattice constant of a = 3.327 Å, as illustrated in Fig. 7.1. The plane-wave basis cut-off was set to K_{max} = 4.0 a_0^{-1}, and the maximum angular momentum inside the MT spheres was set to l_{max} = 10 for Eu and l_{max} = 8 for W and Se. To converge the SCF cycle, the PBE prescription of the GGA exchange-correlation functional and a k-point mesh of 10×10 were used. The magnetic properties, such as the MAE and the spin-spiral, were computed using a 21×21 k-point mesh. To account for the highly localized $4f$ electrons of Eu, the DFT+U method was used with parameters set to U = 6.7 eV and J = 0.7 eV. In the simulations of the dilute case in a larger supercell (Fig. 7.9 (b)), the same parameters were adopted, with a 20×20 k-point mesh. The DFT energy bands are compared to the band structure obtained by constructing maximally-localized Wannier functions (MLWFs) in the FLAPW formalism [212] and the open-source code Wannier90 [213]. The initial projections for the Wannier functions are chosen to be s, d, f orbitals for the Eu atom, p orbitals for the Se atoms and s, d orbitals for the W atom. In this way, 50 MLWFs are constructed, where the frozen window maximum was set 0.4 eV above the Fermi energy. From the converged MLWFs, the Hamiltonian, spin, and orbital operators are written in real space, which are Fourier-transformed in an interpolated k-mesh for the calculation of spin-orbital texture, Berry curvature, and AHE.

7.1 Structural and electronic properties of Eu atoms on WSe_2

As mentioned in Section 3.2, the coexistence of strong SOC and a net magnetization is crucial for achieving AHC. This study aims to create this additional contribution to the Hall conductivity by combining Eu atoms with a monolayer of a TMDC material, namely WSe_2. This approach is motivated by the extensive research on magnetotransport properties in 2D-materials for the development of innovative magnetic storage devices. WSe_2 is a member of the TMDC family of materials and its 1H-phase monolayer has a triatomic structure with one layer of W sandwiched between two Se layers. Specifically, each W atom is covalently bonded to six Se atoms, resulting in a similar atom arrangement to that of graphene when viewed from above. Due to the presence of the heavy W atom in the structure, WSe_2 exhibits significant SOC effects, which play a crucial role in the phenomena under investigation.

The second essential ingredient is a strong magnetization, which is achieved by adsorbing a magnetic atom, in this case Eu. To determine the adsorption position of Eu on the TMDC, three sites were tested: on top of the W atom (T-W), on top of the Se atom (T-Se), and in the center of the hexagon formed by W and Se atoms (H). The

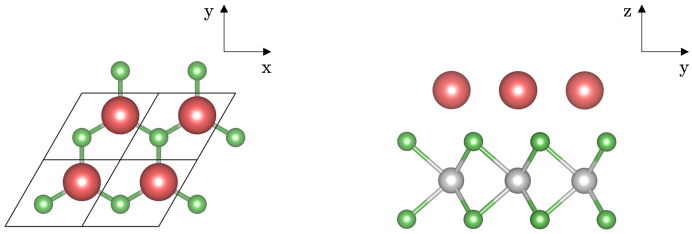

Figure 7.1: Left: 1×1 unit cell in a top-view of Eu (red spheres) monolayer deposited on top of the W atom (grey spheres) of a single layer of WSe_2. Se atoms are indicated by green spheres. Right: side-view of the Eu monlayer on top of the WSe_2 monolayer. The magnetic $4f$-atom is adsorbed on top of the W.

relaxation of the Eu atoms on top of the 2D-material was undertaken with subsequent calculations conducted on a 1×1 unit cell. For each adsorption site, Table 7.1 presents the calculated adsorption energy, the perpendicular distance from the first Se layer, the d and f electron occupations in the valence shell of Eu, and the spin magnetic moment of Eu. The adsorption energies were determined by computing the energy difference between the heterostructure and the individual components, specifically $E_{Eu/WSe_2} - E_{Eu} - E_{WSe_2}$. In all three instances, the f_{occ} generally adheres to Hund's rules, which is also evidenced by a large magnetic moment close to 7 μ_B. Any deviations from this value primarily stem from the spin-polarization of Eu d electrons due to intra-atomic exchange interactions between $4f$ and $5d$ electrons. By evaluating the difference $n_{d_\uparrow} - n_{d_\downarrow}$ within the MT spheres, the MT d magnetic moment is estimated to be 0.306 μ_B at the H-site, 0.463 μ_B at the T-Se site, and 0.2 μ_B at the T-W site. In all cases, smaller contributions to the magnetic moment also arise from spin-polarized intra-atomic s and p states.

It is apparent from the adsorption energies that the most advantageous site for adsorption is on the top of the W atoms, which also brings the Eu atom into closer proximity with the WSe2 monolayer. The unit cell and a side view of the structure

Site	E_{ads} [eV]	d_0 [Å]	d_{occ}	f_{occ}	$m_s^{RE}[\mu_B]$
H	−0.312	2.830	0.520	6.861	7.240
T-W	−0.474	2.500	0.522	6.865	7.130
T-Se	−0.341	3.119	0.550	6.858	7.440

Table 7.1: Ground state properties for Eu in the three adsorption sites on WSe_2: adsorption energy in eV, adsorption distance in Å, d and f occupation of the magnetic RE atom, and spin magnetic moment of the RE atom in μ_B. Calculations have been performed without SOC.

can be seen in Fig. 7.1. In the local framework of the RE atom, there are three nearest neighbors represented by Se atoms of the first layer, which generate a trigonal crystal field with C_{3v} symmetry.

An analysis of the spin-resolved DOS is shown in Fig. 7.2 (a) and (b), where the DOS is decomposed into its orbital contributions. Notably, the presence of the Eu monolayer leads to a closure of the semiconducting gap observed in pristine WSe_2, resulting in a metallic nature. Initially, the electronic structure of the system can be described by considering the electronic structure of the WSe_2 monolayer that acquires spin-polarized conduction electrons from Eu through hybridization. This causes the

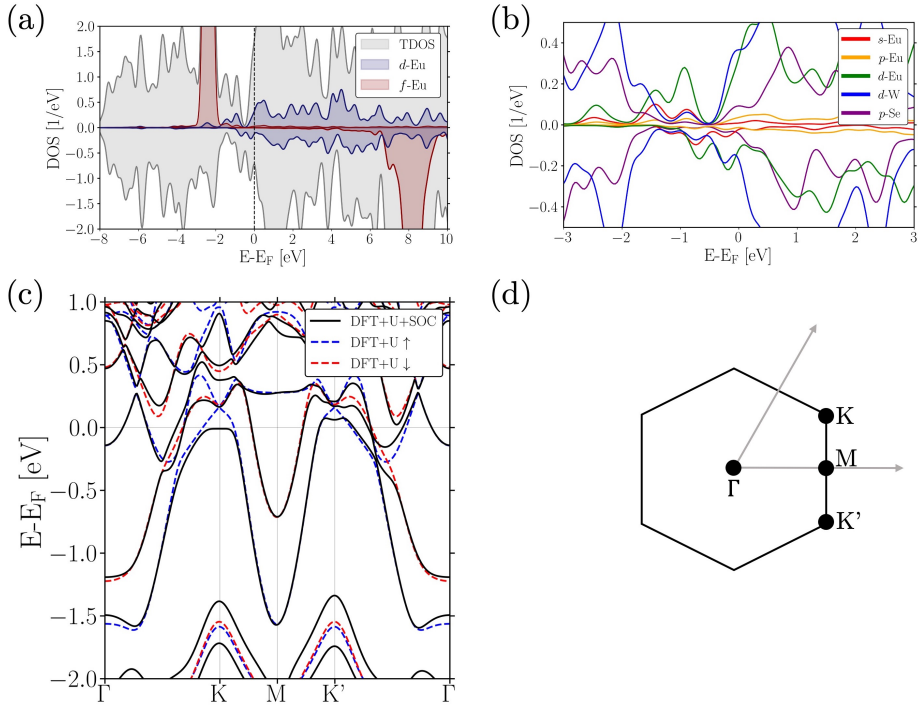

Figure 7.2: (a) Contribution to the local DOS of the f and d electrons of Eu. The total DOS (TDOS) is shown as grey shaded area. (b) Contribution to the local DOS of the s, p, d electrons of Eu, d electrons of W and p electrons of Se. Both DOS in (a) and (b) have been calculated without SOC. (c) Band structure of Eu/WSe_2 calculated with DFT+U (blue dashed line represents the majority channel and red dashed line represents the minority channel) and with DFT+U+SOC (black solid line). (d) First Brillouin zone with high-symmetry points.

Fermi surface to intersect the previously unoccupied conduction states of WSe_2. Consequently, mainly spin-polarized Eu d (and s) states hybridizing with W d-states are observed in the vicinity of the Fermi surface.

To provide more detailed insight, Fig. 7.2 (a) illustrates the TDOS, as well as the d (blue) and f (red) DOS of Eu. The upper panel represents the majority states, while the lower panel shows the minority states. The occupied $4f$ spin-up peak is located at approximately −2.5 eV, while the spin-down states that are unoccupied are situated around +8 eV, indicating an exchange splitting of about ~ 11 eV. The Eu d-states exhibit a significant band-width extending over more than 10 eV, indicative of their extensive delocalization and largely unoccupied nature. This behavior is consistent with the occupancy of a small fraction of Eu d-electrons, with $d_{\mathrm{occ}} = 0.522$ as shown in Tab. 7.1. Such occupancy results from the hybridization of the Eu atom with neighboring atoms when it is incorporated into the solid phase, in contrast to its isolated state as a single atom. A detailed discussion of this effect is provided in Section 7.5, in the case of quasi-single Eu atoms on top of WSe_2.

The TDOS exhibits spin-polarization as evidenced by the unequal spin-up and spin-down channels, which can also be observed in the orbital contributions of the s, p, d states of Eu, the d states of W, and the p states of Se, as highlighted in Fig. 7.2. The figure zooms in on the energy range close to the Fermi energy from −3 eV to +3 eV. In this energy range, large contributions from Eu-d, W-d, and Se-p states are found, along with strong spin-polarization. The strongest exchange splitting is observed for Eu-d electrons, which is a result of the intra-atomic ferromagnetic exchange coupling between localized $4f$ electrons and the delocalized d states of Eu. The large $4f$ magnetic moments also affect other states in the structure, as seen near the Fermi energy (±0.5 eV) for W-d, Se-p, and Eu-s. Concerning the hybridization effects arising in this energy window, Fig. 7.3 reports the calculated product between weights of different orbitals belonging to different chemical species. Close to the Fermi energy, it becomes evident that various hybridization processes are significant, such as those between Eu's more delocalized d and s electrons with W-d electrons, as well as interactions between Eu-s with Se-p. Between −1.5 eV and −2.5 eV, interactions between f states of Eu and d states of W can be found. These observations confirm the presence of an interaction between the substrate and the magnetic atom. To gain an understanding of the energy position of different states in the system, the orbital contributions to the band structure are presented in Fig. D.2 of Appendix D.

The role of the spin-orbit coupling is analyzed in Fig. 7.2 (c) displaying a comparison between the spin-resolved band structure in the vicinity of the Fermi energy along high-symmetry lines (for details see Fig. 7.2 (d)) neglecting the SOC by which majority states (blue lines) and minority states (red lines) are well-defined eigenstates with the ones calculated with SOC (black lines). A strong spin-orbit splitting is witnessed at the K and K'-points around −1.6 eV. These valley-shaped states have primarily W-d character and undergo spin-orbit splitting by about ±0.18 eV to −1.42 eV and

−1.78 eV. In the same way also the crossing point at K just above the Fermi energy is split up into two separated bands, while on the path between K and Γ just below the Fermi energy an avoided crossing is generated. This plays a crucial role in determining the strength of the magnetic anisotropy, in generating large Berry curvature and contributing to the AHE. Concerning the energy bands from K' to Γ, similar effects arise but it can be already noticed that the two high symmetry points K and K' are not equivalent due to the absence of structural inversion symmetry. As anticipated

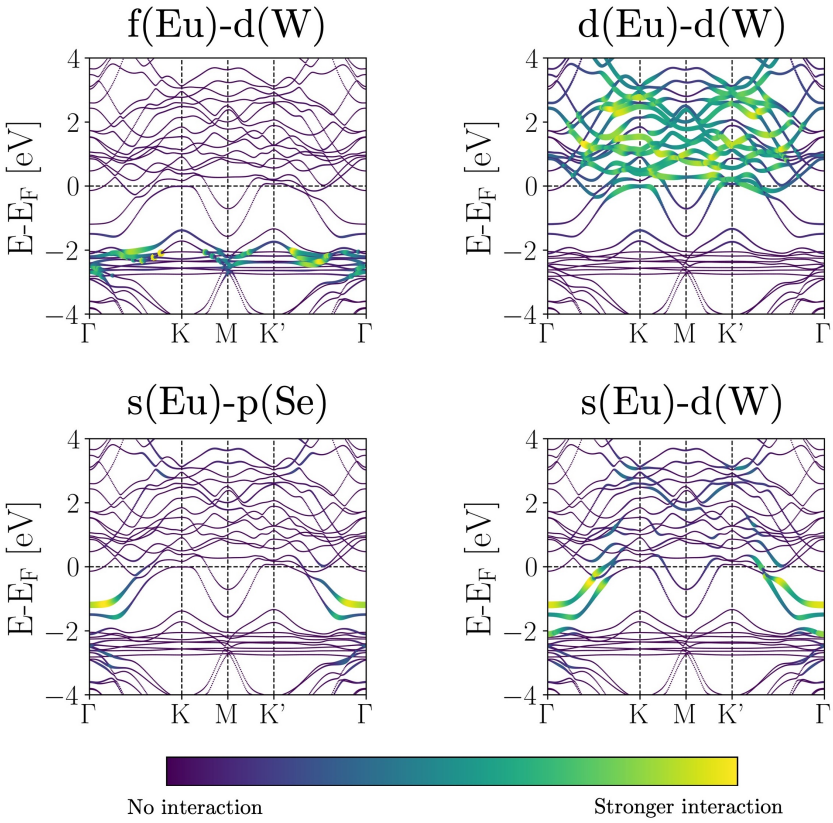

Figure 7.3: Hybridization analysis of electronic states with respect to different orbitals belonging to different chemical elements of the system for a monolayer of Eu on a WSe_2 monolayer: f electrons of Eu with d electrons of W, d electrons of Eu with d electrons of W, s electrons of Eu with p electrons of Se and s electrons of Eu with d electrons of W. The hybridization effects are calculated as the product of the weights of two different orbitals. Calculations are carried out including the spin-orbit coupling and explicit spin-analysis is neglected.

from the large DOS of W-d at the Fermi energy, discussed in Fig. 7.2 (b), in general, the SOC effect arises mainly from the W atom. The impact of increasing the SOC strength on the system is demonstrated in the band structure shown in Fig. D.1 in Appendix D. This augmentation results in energy gaps, avoided crossings, and an increase in spin splitting, including at the K-valley.

7.2 Magnetic properties

Upon examining the electronic properties and identifying significant orbital hybridizations and SOC effects, the next crucial step towards achieving AHC is the establishment of strong magnetism. High magnetic anisotropy energies are crucial for magnetic data-storage devices as they ensure the stability of a specific direction of the magnetic moments against external perturbations such as thermal fluctuations or scattering from conduction electrons. This stiffness of magnetization is a key ingredient for these devices to function effectively.

The total energy of the Eu/WSe_2 system is plotted as a function of the angle θ between the surface normal and the magnetization direction in Fig. 7.4 (a). By rotating the magnetization from the out-of-plane position ($\theta = 0°$) to the in-plane position ($\theta = 90°$) and calculating the total energy for each direction in 10-degree steps, it was found that the minimum energy state corresponds to an out-of-plane easy-axis of the magnetization, with a difference in energy of 1.75 meV per unit cell compared to the in-plane state. The magnetic anisotropy energy observed in Eu/WSe_2 is quite large for half-filled $4f$-shells, and can be attributed to the electronic hybridization between Eu and WSe_2.

This is mainly due to two aspects: 1) the direct $f - d$ interaction between Eu and W observed in Fig. 7.3; 2) the ferromagnetic spin-polarization of the Eu-d electrons, which results from intra-atomic exchange with $4f$ electrons, and the hybridization of the Eu and W d-electrons at the Fermi surface. Fig. 7.2 (c) shows a comparison of the band structure with and without SOC, which highlights the significant SOC influence on the Eu-W hybridization at the Fermi energy. By turning the spin-quantization axis of the Eu-$4f$ electrons, the spin-quantization axis of the Eu-d electrons follows. The spin-orbit dependent interaction between the spin-quantization axis of the Eu-d states and the crystal lattice dependent spin-orbit interaction of the W-d electrons leads to the observed magnetic anisotropy energy in Fig. 7.4 (a). Furthermore, the MAE is around two orders of magnitude smaller for Eu adsorbed on top of Gr (approximately 0.06 meV), where hybridization effects are minimal, which supports this hypothesis.

The significant MAE observed in the Eu system is a favorable outcome, given that maintaining a stable magnetization is essential. Moreover, the AHE indicates a linear relationship with the z component of magnetization expressed as $M\cos\theta$, thereby

rendering it a valuable technique for quantifying magnetization in magnetic materials [214, 215]. To explore the magnetic ordering in the ground state, the total energy is examined for specific spin-spiral states with a wave vector $\mathbf{q}$ (defined in reciprocal lattice vector units) along the high-symmetry lines in the 2D Brillouin zone. A spin-spiral state refers to a magnetic configuration where the magnetic moments are rotated by a constant angle from one atom to the next along a particular direction. It represents the exact mathematical solution of the classical Heisenberg model applied to periodic crystal lattices, and the q-state with the lowest energy is the magnetic ground state. The high-symmetry points of the Brillouin zone correspond to a certain periodic magnetic order in real space (for hexagonal lattices, see [216]). Specifically, the magnetization of an atom at position $\mathbf{R}$ can be expressed as

$$M(\mathbf{R}) = M \begin{pmatrix} \cos(\mathbf{q}\cdot\mathbf{R})\sin\beta \\ \sin(\mathbf{q}\cdot\mathbf{R})\sin\beta \\ \cos\beta \end{pmatrix}, \tag{7.1}$$

where β is defined as the angle between the magnetic moment and the rotation axis (see [217]). The generalized Bloch theorem [218], as implemented in the FLEUR code

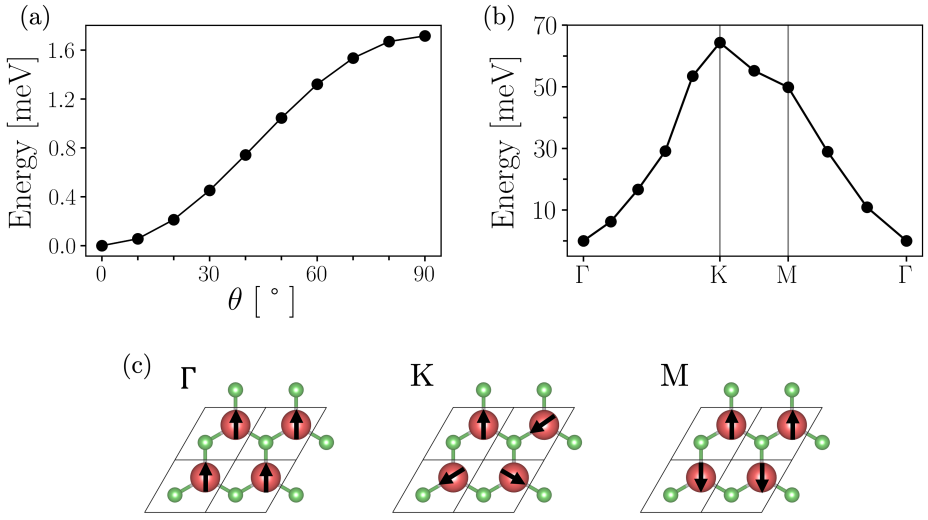

Figure 7.4: (a) Magnetic anisotropy energy curve: the total energy of the system is plotted versus the polar angle θ of the magnetization measured from the z-axis. (b) The energy of the spin-spiral states of a flat spiral, *i.e.* with cone angle $\beta = \pi/2$, computed for the values of the $\mathbf{q}$-vector along the Γ–K–M path, presented with respect to the ferromagnetic ground state at the Γ-point. (c) The magnetic configurations at the high-symmetry points.

[219], is a highly efficient numerical method for calculating the DFT total energy for a spin-spiral state. By applying this method, the energy is calculated for various values of the **q**-vector of a spin spiral along the Γ–K–M path, and the results are displayed in Fig. 7.4 (b). The inset in Fig. 7.2 (b) depicts the first Brillouin zone, which highlights the high-symmetry points. Moreover, an overview of the magnetic orders at these points is shown in Fig. 7.4 (c). The energy minimum is found at Γ, indicating that the system favors a ferromagnetic ground state. Additionally, the energy differences between Γ and the other two high-symmetry points, K (non-collinear 120°-Néel state) and M (row-wise antiferromagnetic state), are about 70 meV and 50 meV, respectively. Hence, the Néel and the antiferromagnetic state are not energetically favorable.

7.3 Spin and orbital textures

The spatial inversion symmetry (I) operation maps **k** to −**k**, resulting in degenerate bands around the Γ point for each spin direction, given by:

$$\epsilon(\mathbf{k},\uparrow) = \epsilon(-\mathbf{k},\uparrow) \quad \text{and} \quad \epsilon(\mathbf{k},\downarrow) = \epsilon(-\mathbf{k},\downarrow). \tag{7.2}$$

Furthermore, due to time-reversal symmetry, we have $\epsilon(\mathbf{k},\uparrow(\downarrow)) = \epsilon(-\mathbf{k},\downarrow(\uparrow))$, resulting in double-degenerate bands:

$$\epsilon(\mathbf{k},\uparrow) \overset{\mathrm{I}}{=} \epsilon(-\mathbf{k},\uparrow) \overset{\mathrm{TR}}{=} \epsilon(\mathbf{k},\downarrow) \overset{\mathrm{I}}{=} \epsilon(-\mathbf{k},\downarrow). \tag{7.3}$$

The breaking of structural inversion symmetry in a monolayer of TMDC results in the appearance of non-identical valleys K and K' in k-space, as illustrated in Fig. 7.5,

$$\epsilon(\mathbf{k},\uparrow) \overset{\mathrm{TR}}{=} \epsilon(-\mathbf{k},\downarrow) \overset{\mathrm{I}}{\neq} \epsilon(-\mathbf{k},\uparrow) \overset{\mathrm{TR}}{=} \epsilon(\mathbf{k},\downarrow), \tag{7.4}$$

leading to valley-specific orbital angular momentum and Berry curvature, giving rise to the valley-orbital Hall effect [220–222]. By depositing Eu atoms on WSe_2, the

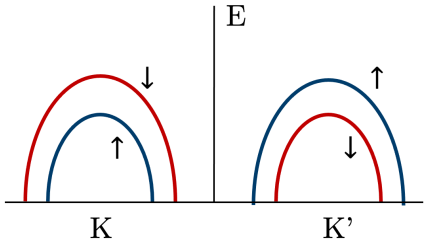

Figure 7.5: K–valley splitting in a monolayer of TMDCs due to the absence of inversion symmetry and enhanced by the presence of SOC.

Rashba effect can be induced by breaking the mirror symmetry with respect to the 2D plane [223, 224]. The breaking of symmetry results in the creation of a potential gradient on the surface that produces a SOC field when an electron travels through the resulting electric field, leading to a magnetic field interacting with its spin. The Rashba effect is induced not only on the spin but also on the orbital angular momentum, which is known as the orbital Rashba effect (ORE) [225–228], and plays a crucial role in magnetotransport phenomena. Similar to the Rashba effect, where the electron's spin is locked to its momentum, in the ORE, the electron's orbital angular momentum $\mathbf{L}$ is locked to its momentum $\mathbf{k}$. The Rashba Hamiltonian can be written to describe this effect, where the spin operator is replaced with the orbital angular momentum operator [227]:

$$\mathcal{H}_{\mathrm{OR}}(\mathbf{k}) = \frac{\alpha_{\mathrm{OR}}}{\hbar}\mathbf{L}\cdot(\hat{\mathbf{z}}\times\mathbf{k}), \tag{7.5}$$

where α_{OR} is the orbital Rashba parameter identifying the strength of the effect. The ORE is observed in situations where there is significant orbital hybridization at surfaces. In such cases, an electric dipole is generated, which couples to the electric field created by the breaking of inversion symmetry at the surface. This interaction affects states having different orbital angular momentum, leading to the splitting of the bands and the emergence of orbital textures in reciprocal space. Notably, the ORE occurs even in the absence of SOC, and the conventional spin Rashba effect arises only after SOC is introduced. Therefore, spin Rashba splitting is a secondary effect driven by the ORE.

Thus, the spin and orbital textures are essential for comprehending spin and orbital magneto-transport phenomena, as previously documented in [229, 230]. The following analysis provides an overview of the spin and orbital textures, represented as $\mathbf{S}_{\mathrm{FS}}(\mathbf{k})$ and $\mathbf{L}_{\mathrm{FS}}(\mathbf{k})$, respectively, in the k-space at the Fermi surface of Eu/WSe_2 (Fig. 7.3). Following Ref. [230], the orbital texture is evaluated as the expectation value of the orbital angular momentum operator $\mathbf{L}$ defined within the muffin-tin sphere of each atom,

$$\mathbf{L}_{\mathrm{FS}}(\mathbf{k}) \;=\; \sum_{n}\frac{2\,\langle u_{n\mathbf{k}}|\,\mathbf{L}\,|u_{n\mathbf{k}}\rangle}{1+\cosh[(E_{\mathrm{F}}-E_{n\mathbf{k}})/k_{\mathrm{B}}T]}, \tag{7.6}$$

Here, $u_{n\mathbf{k}}$ is the periodic part of the Bloch state with band index n. The denominator expresses the Fermi-Dirac temperature broadening of the Fermi surface. $k_{\mathrm{B}}T$ is set to $k_{\mathrm{B}}T = 25$ meV for broadening, where k_{B} is the Boltzmann constant and T is the temperature. $E_{n\mathbf{k}}$ corresponds to the energy band, and E_{F} to the Fermi energy. The spin texture is obtained replacing $\mathbf{L}$ by $\mathbf{S}$ in Eq. (7.6).

In general, the breaking of inversion symmetry results in the inequivalence of the K and K' valleys. As shown in Fig. 7.6 (a), the z component of the orbital angular momentum exhibits a 3-fold rotational symmetry as expected, along with valley-dependent orbital textures with opposite signs at the K and K' valleys, similar to the

conduction states of the bare WSe_2 [231]. The z component of the spin angular momentum is shown in Fig. 7.6 (b). Although it satisfies a three-fold rotation symmetry, it nearly exhibits a six-fold rotation symmetry. This is because the spin magnetism is mainly driven by Eu layer, which has a six-fold rotation symmetry if the substrate is absent. Slight deviation of the spin texture from the six-fold rotation symmetry indicates hybridization of Eu atoms with the substrate, where proximity-induced W d-states exhibit finite spin polarization via an indirect exchange interaction between itinerant Eu s, d-electrons and the spin moments of localized f electrons. These features are directly associated with the orbital contributions to the band structure discussed in Fig. 7.2 and in Fig. D.2. For example, around the Γ point, Eu-d majority states prevail, resulting in a positive value of $\langle S_z \rangle_{\mathrm{FS}}$. Concerning the K and K′ points

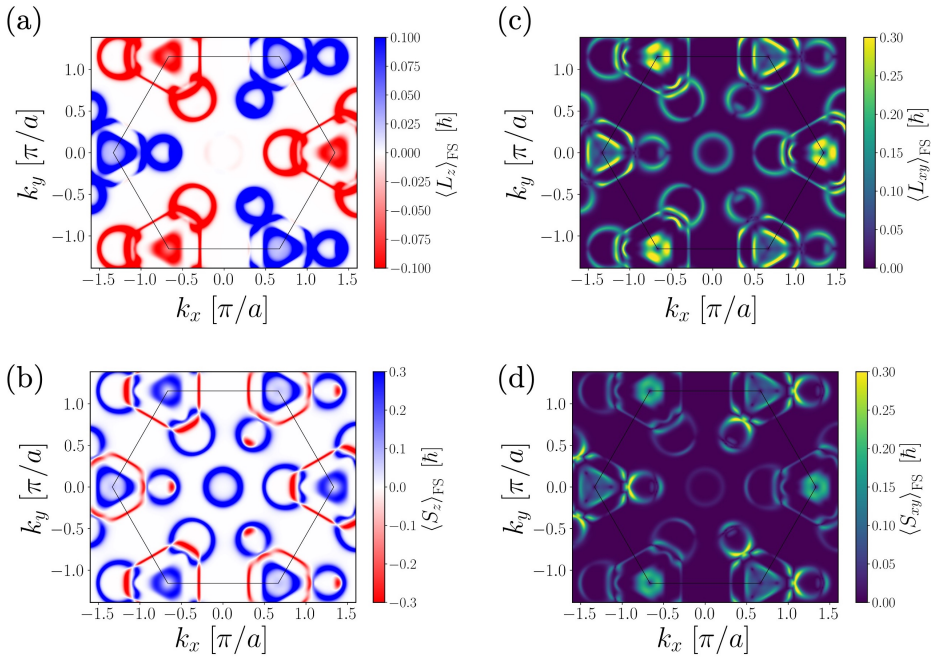

Figure 7.6: Spin and orbital texture in k-space at the Fermi surface. (a) Expectation value for the out-of-plane component of the orbital angular momentum at the Fermi surface $\langle L_z \rangle_{\mathrm{FS}}$. (b) Expectation value of the in-plane component of the orbital angular momentum $\langle L_{xy} \rangle_{\mathrm{FS}} = \sqrt{\langle L_x \rangle_{\mathrm{FS}}^2 + \langle L_y \rangle_{\mathrm{FS}}^2}$. Analogously, the z-component and the magnitude of the in-plane component for the spin expectation value at the Fermi surface are shown in (c) and (d), respectively. $\langle L_z \rangle_{\mathrm{FS}} > (<) 0$ and $\langle S_z \rangle_{\mathrm{FS}} > (<) 0$ (color blue (red)) corresponds the angular-momentum direction (anti-)parallel to the spin of Eu-4f electrons.

instead, the biggest contribution comes from the W-d states with a spin-orbit splitting that competes in energy with the exchange splitting of the hybridizing s and d electrons of Eu, causing the majority states to lie around the Fermi energy and a full quantum mixture of electronic states resulting in three-dimensional spin and angular moment textures. When comparing Figs. 7.6 (a) to (d) around the K and K′ points, it is evident that similar values for $\langle \mathbf{S} \rangle_{\mathrm{FS}}$ and $\langle \mathbf{L} \rangle_{\mathrm{FS}}$ for the out-of-plane in in-plane components are observed, respectively.

In Fig. 7.6 (c), the in-plane component of the orbital angular momentum, $\langle L_{xy} \rangle_{\mathrm{FS}} = \sqrt{\langle L_x \rangle_{\mathrm{FS}}^2 + \langle L_y \rangle_{\mathrm{FS}}^2}$, displays a Rashba-like texture, which arises from the hybridization between Eu and WSe_2 and the consequent breaking of z-reflection mirror symmetry. Notably, this orbital Rashba effect is independent of the SOC and is solely due to the orbital hybridization. When SOC is taken into account, an orbital texture emerges, coupled with the spin texture, which leads to the emergence of the spin Rashba effect, as shown in Fig. 7.6 (d). Remarkably, the in-plane orbital and spin textures share a striking resemblance, indicating that both have the same origin – the orbital hybridization. This similarity also explains why a three-fold rotation symmetry is evident in both the in-plane spin and orbital textures, but not for the out-of-plane component.

7.4 Anomalous Hall conductivity

The magnetic and orbital properties, coupled with the perpendicular ferromagnetic ordering, provide a promising starting point for investigating the anomalous conductivity in the system. The Berry curvature (Ω) is a useful quantity for characterizing this behavior. Breaking of spatial inversion symmetry ensures that the Berry curvature at opposite $\mathbf{k}$ points has opposite sign but equal magnitude, such that $\Omega(\mathbf{k}) = -\Omega(-\mathbf{k})$, leading to distinguishable behavior at the two K-valleys. However, the integration over the entire Brillouin zone results in vanishing values. To obtain finite values of Ω, an additional symmetry breaking mechanism must be considered, arising from the presence of magnetic Eu atoms, which breaks time-reversal symmetry and leads to markedly different behavior at the two K-valleys ($\Omega(\mathbf{k}) \neq -\Omega(-\mathbf{k})$).

The interplay between orbital hybridizations due to proximity and SOC can lead to small energy gaps or avoided crossings between the energy bands, as illustrated in Fig. 7.2. Such regions are expected to generate a significant Berry curvature. This is evident from the features in the Berry curvature depicted in Fig. 7.7 (a), where the calculated band structure along Γ–K–M–K'–Γ is displayed with the corresponding Berry curvature values in color scale. Regions of significant $\Omega_{n\mathbf{k}}$ can be identified at specific points where the degeneracy of energy bands is lifted by the SOC. This is particularly evident for the splitting of bands between Γ and K which results in a band inversion. Fig. 7.7 (b) illustrates the Berry curvature summed over all occupied states below the Fermi energy for the same k-path, confirming that hotspots in the

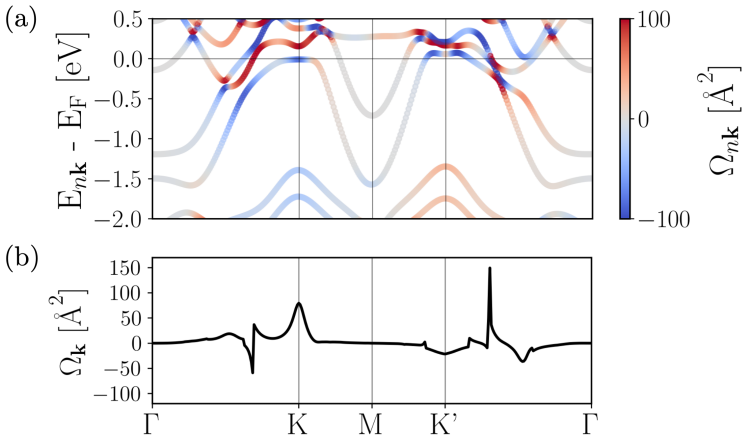

Figure 7.7: (a) Band structure around the Fermi energy with color scale indicating the value of the Berry curvature $\Omega_{n\mathbf{k}}$. (b) Berry curvature summed over all occupied states along the k-path Γ–K–M–K'–Γ.

Berry curvature arise from SOC-induced avoided crossings found along the Γ–K and Γ–K' paths. Furthermore, the two K and K' points exhibit different Berry curvature. Specifically, the K point has a positive peak, while the K' point displays a broad negative feature. Along the path K'–Γ an intense peak appears characterized by inverted sign with respect to the peak between Γ–K.

By integrating the Berry curvature over the Brillouin zone, it is possible to calculate the intrinsic anomalous Hall conductivity. Fig. 7.8 shows the anomalous conductivity as a function of the Fermi energy, which is varied with respect to the original value

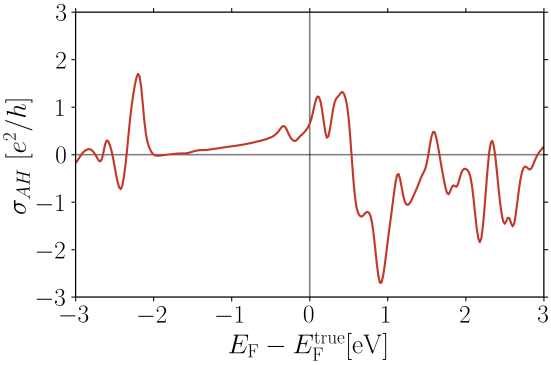

Figure 7.8: Anomalous Hall conductivity as a function of the Fermi level.

$E_{\mathrm{F}}^{\mathrm{true}}$. Major peaks are found around 2 eV below the Fermi energy, slightly above the Fermi energy, and 1 eV above the Fermi energy. These energies are where avoided band crossings induced by the SOC are found. A double-peak feature right above the Fermi energy implies an interesting possibility to tune the Hall response by electron doping, which may be experimentally observed. Meanwhile, the peak at −2 eV is where the K and K' valleys of WSe_2 in k-space are situated. From Fig. 7.2 (a) it is clear that SOC lifts the degeneracy of the band at the K and K' valleys which have predominantly d character from the W atom such that a contribution to the Berry curvature arises.

7.5 Effect of Eu coverage

In an experimental set-up, it is possible that the WSe_2 substrate may not be fully covered by Eu atoms. To examine the impact of Eu coverage on the electronic and magnetic properties, the electronic structures of Eu in two different unit cells are compared: the previous studied 1×1 unit cell (Fig. 7.9 (a)) and the $\sqrt{3}\times\sqrt{3}$ unit cell (Fig. 7.9 (b)), where Eu has 1/3 coverage compared to the 1×1 unit cell.

Table 7.2 summarizes the adsorption energies, distances from the substrate, total magnetic moment of the Eu atom, and its f- and d-state occupation for the $\sqrt{3}\times\sqrt{3}$ cell. In the scenario where Eu atoms sparsely cover the WSe_2 substrate, the behavior of Eu is similar to that of a single-atom adsorbate. Specifically, the adsorption energy slightly increases, suggesting a stronger bonding towards the substrate. Furthermore, the occupation number of Eu f-electrons approaches the atomic occupation of 7, and the occupation number of Eu d-electrons (d_{occ}) is reduced by a factor of 4. This leads to negligible d contributions to m_s^{RE}, in contrast to the scenario where the coverage is dense. Similar to the 1×1 cell, the preferred adsorption site is located on the top of a W atom.

Reducing the coverage of Eu on WSe_2 leads to a decrease in the magnetic proximity of WSe_2 due to the reduction in hybridization between Eu and W d-electrons. Simultaneously, the semiconducting properties of the WSe_2 monolayer reemerge. Upon

Site	E_{ads} [eV]	d_0 [Å]	d_{occ}	f_{occ}	$m_s^{\mathrm{RE}}[\mu_{\mathrm{B}}]$
H	−0.611	2.582	0.128	6.923	6.991
T-W	−0.690	2.500	0.158	6.923	6.994
T-Se	−0.401	3.112	0.085	6.922	7.000

Table 7.2: Adsorption energy, distance of the Eu atom from the WSe_2 layer, the magnetic moment and the f and d occupations in the muffin-tin sphere of the Eu atom for the different adsorption sites in the $\sqrt{3}\times\sqrt{3}$ cell. Calculations have been performed without SOC.

examination of the band structure of $(\sqrt{3}\times\sqrt{3})$-Eu/WSe_2 in Fig. 7.9 (d), a band gap of approximately ±0.4 eV around −1 eV is observed. However, $(\sqrt{3}\times\sqrt{3})$-Eu/WSe_2 becomes a conductor due to the doping of WSe_2 by Eu s, p, and d-electrons, albeit to a lesser extent than in the dense coverage case. When compared to the full coverage case depicted in Fig. 7.9 (c), the exchange splitting of the states at the Fermi energy (the energy difference between the red and blue lines) is significantly smaller, indicating indeed a reduction in magnetic proximity. Fig. D.3 in Appendix D displays the respective spin-polarized DOS. It is evident that the bands immediately below the Fermi energy primarily correspond to the s states of Eu and, to a lesser extent, to the d states.

The computed differential charge densities $(n_{\mathrm{Eu/WSe_2}} - n_{\mathrm{Eu}} - n_{\mathrm{WSe_2}})$ shown in Fig. 7.10 for both concentrations of the RE atom reveal less charge delocalization in the $\sqrt{3}\times\sqrt{3}$ supercell, when compared on the same color scale, with the high coverage situation.

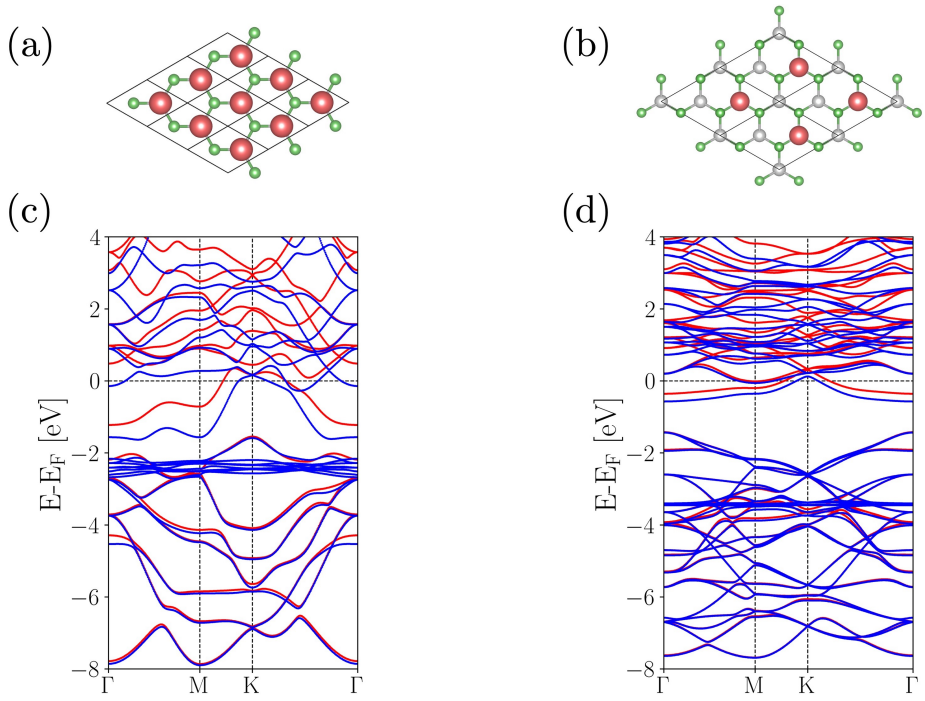

Figure 7.9: Comparison of the electronic structure of Eu monolayer on a WSe_2 monolayer for two simulation cells: (a) 1×1 unit cell (high coverage of Eu) and (b) $\sqrt{3}\times\sqrt{3}$ unit cell (low coverage of Eu). The corresponding band structures determined neglecting SOC are shown in (c) and (d), where blue and red lines indicate majority and minority states, respectively.

This is indicated by blue regions (loss of charge) and red regions (gain of charge) between the involved atoms. This enhanced charge transfer within the 1×1 unit cell leads to the disappearance of all semiconducting features of bare WSe_2 in the band structure.

Fig. 7.11 (a) displays the respective magnetic anisotropy energy as function of the magnetization direction in the dilute situation. In agreement with the full-coverage case, the easy-axis is out-of-plane and consistent with the explanation given in Section 7.2 that the interaction of spin carrying Eu and the spin-orbit carrying W d-electrons are the origin of the magnetocrystalline anisotropy. The energy of the in-plane hard axis is only 0.2 meV per $\sqrt{3} \times \sqrt{3}$ unit cell, much smaller than the 1.75 meV per 1×1 unit cell.
Figs. 7.11 (b) and (c) demonstrate the effect of turning off the spin-orbit coupling in the Eu and W muffin-tin spheres, respectively, in the low-coverage situation. These figures reveal that in this case, the MAE is solely driven by the substrate, particularly by the orbital interactions of W with its surrounding environment. Indeed, Fig. 7.11 (c) illustrates that the energy of the system remains unchanged when the spin moments of Eu and Se are rotated, indicating an atomic nature of Eu and a negligible Eu-substrate orbital hybridization compared to the 1×1 unit cell. Thus, a high coverage of Eu atoms appears to be necessary for inducing significant MAE by establishing strong orbital hybridizations and enabling measurements of the anomalous Hall effect.

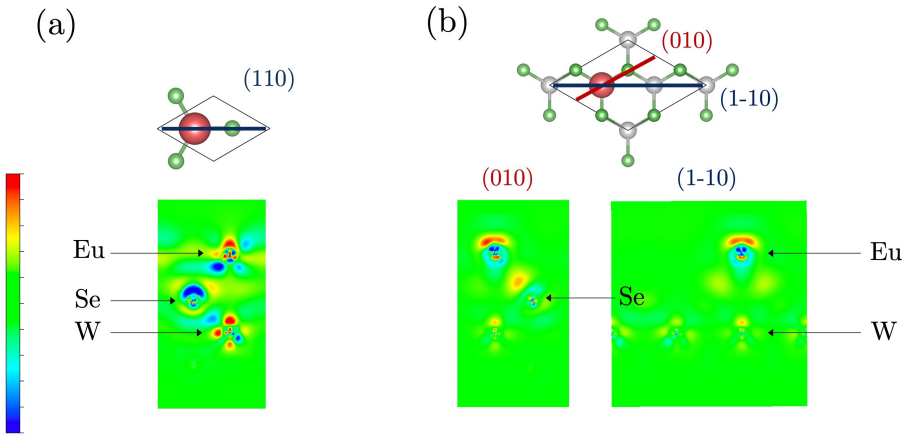

Figure 7.10: Differential charge density of Eu/WSe_2 in the two simulation cells. (a) The 1×1 unit cell in the (110) plane. (b) The $\sqrt{3} \times \sqrt{3}$ unit cell in the (010) and (1-10) planes. The color scale ranges from −0.005 to +0.005 and is consistent in both cases. The interaction between the Eu atom and the WSe_2 substrate involves more charge in the 1×1 unit cell compared to the $\sqrt{3} \times \sqrt{3}$ unit cell.

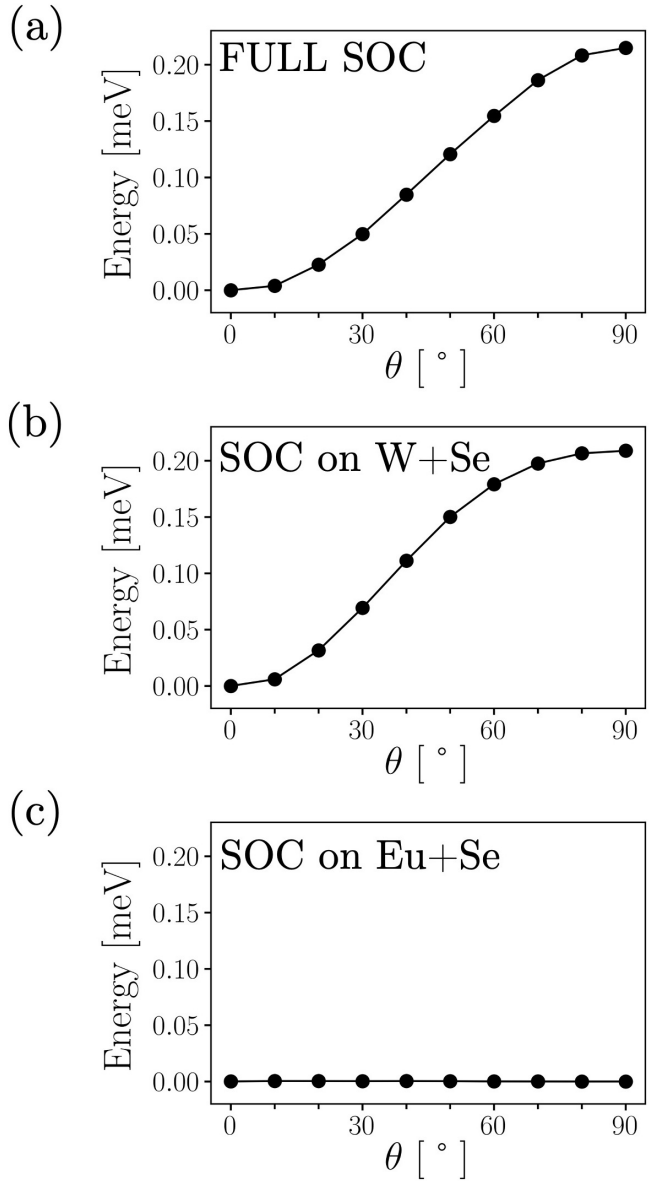

Figure 7.11: (a) The magnetic anisotropy curve in the zx-plane for the $\sqrt{3} \times \sqrt{3}$ simulation cell of Eu/WSe_2. Similar to the 1×1 cell, the dilute coverage situation exhibits an out-of-plane easy-axis. However, the magnetic anisotropy energy from the in-plane direction is significantly reduced to approximately ~ 0.2 meV. (b) MAE curve turning off SOC on the Eu and considering only the W+Se contributions. (c) MAE curve turning off SOC on the W and considering only the Eu+Se contributions.

Chapter 8

Gd and Ho atoms deposited on WSe_2: coverage dependence of magnetic properties

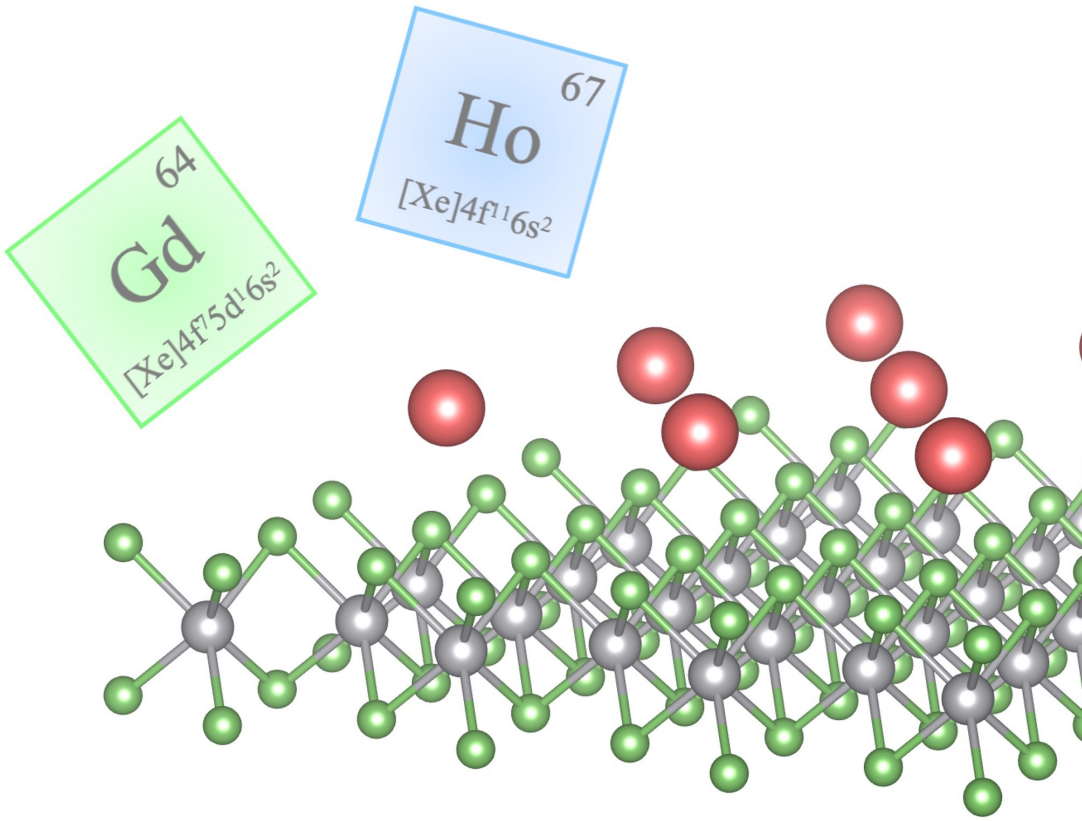

In the following chapter, a glimpse into the electronic and magnetic characteristics of Gd and Ho adsorbed onto a WSe_2 monolayer is provided. In light of the findings obtained for Eu on WSe_2, the inquiry naturally progresses towards examining other rare-earth elements that exhibit dissimilar chemical interactions, such as Gd, or that possess an open $4f$-shell, as in the case of Ho.

The chapter is structured as follows:

- Section 8.1 focuses on examining the structural and electronic properties of Gd atoms when adsorbed on WSe_2 in a high-coverage scenario (1×1 unit cell). The subsequent discussion delves into the magnetic anisotropy exhibited by the system.
- In Section 8.2, the study on a dilute distribution of Gd atoms on WSe_2 is presented, utilizing a $\sqrt{3}\times\sqrt{3}$ simulation cell. The electronic characteristics and magnetic anisotropy are examined, and the findings demonstrate that, unlike Eu/WSe_2, the magnetic anisotropy energy is increased by a low concentration of Gd atoms due to their chemically active $5d$ electrons.
- Sections 8.4 and 8.5 conclude the study by investigating the effect of replacing the half-filled $4f$-atoms with open $4f$-shell Ho atoms. The adsorption of Ho on WSe_2 and its corresponding magnetic anisotropy is discussed in both high and low coverage situations.

Computational details

The DFT and Hubbard parameters that were used in the Eu/WSe_2 system were also employed for the Gd/WSe_2 system. Additionally, for the Ho/WSe_2 system, the same DFT parameters as for Eu/WSe_2 were used, while the U and J parameters from Ho/Gr were employed, namely U = 7.03 eV and J = 0.83 eV.

8.1 Gd atoms deposited on 1×1 WSe_2: monolayer case

The Gd atom has been adsorbed on the three different adsorption sites of 1×1 WSe_2 and the respective adsorption energies, perpendicular distances from the first Se layer, as well as d and f occupations of the Gd atom and its spin magnetic moment are summarized in Table 8.1. In general, Gd tends to follow Hund's rules with an f occupation close to 7 electrons, which reflects in the very large magnetic moment of Gd > 7 μ_B. The deviations from a 7 μ_B magnetic moment in all cases can be attributed to the presence of one $5d$ electron, which results in magnetic moments of approximately 0.55 μ_B on the H-site, 0.46 μ_B on the T-W site, and 0.52 μ_B on the T-Se site, for the d states. Similar to the Eu/WSe_2 case, the adsorption energies indicate a preference for on-top adsorption on the W atoms, with similar magnitudes

Table 8.1: Ground state properties for Gd in the three adsorption sites on 1×1 WSe_2: adsorption energy in eV, adsorption distance in Å, d and f occupation of the magnetic RE atom, and spin magnetic moment of the RE atom in μ_B. Calculations have been performed without SOC.

Site	E_{ads} [eV]	d_0 [Å]	d_{occ}	f_{occ}	$m_s^{RE}[\mu_B]$
H	−0.319	2.716	1.011	6.980	7.589
T-W	−0.507	2.377	1.020	6.990	7.509
T-Se	−0.415	3.001	1.000	6.977	7.564

across all sites and in comparison to Eu/WSe_2. This places the Gd atoms in close proximity to the TMDC monolayer.

In Fig. 8.1 (a), the spin-polarized density of states of the system is depicted. The grey region represents the TDOS, while the red and blue regions correspond to the f and d states of the Gd atom, respectively. The d states exhibit a broad energy range due to their delocalization, while the f states exhibit two sharp peaks at approximately −8 eV and 3 eV. The presence of the magnetic Gd atom leads to a strongly spin-polarized electronic structure, as demonstrated by the spin-polarized band structure shown in Fig. 8.1 (b). In this figure, the blue and red colors indicate the spin-up and spin-down states, respectively. The overall band structure is similar to that observed in Eu/WSe_2, albeit with a slightly higher degree of spin-splitting due to the increased magnetic interaction compared to Eu.

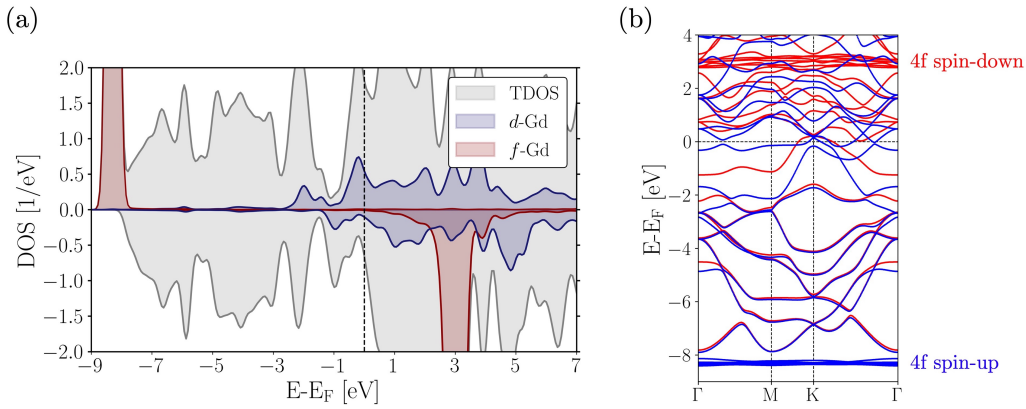

Figure 8.1: (a) Spin-resolved DOS of 1 × 1 Gd/WSe_2: grey represents the TDOS, red and blue the f and d states of Gd. (b) Spin-resolved band structure highlighting the $4f$ states. Calculations were performed without SOC.

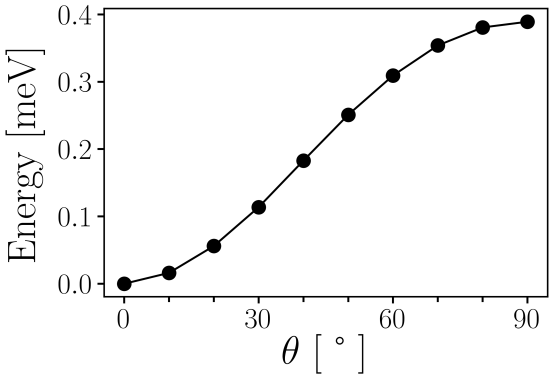

Figure 8.2: The magnetic anisotropy energy curve of Gd on 1×1 WSe_2 exhibits an easy-axis oriented out-of-plane, and an energy difference of around ~ 0.4 meV relative to the in-plane direction.

The MAE calculation results (refer to Fig. 8.2) reveal an out-of-plane easy-axis and a four times smaller anisotropy than the one observed in 1×1 Eu/WSe_2 of approximately 0.4 meV. This phenomenon may be explained by taking into account that the occupied $4f$ states are located at a considerable depth in energy, which means they cannot interact with the substrate states. The evaluation of the interaction between various orbital contributions, as depicted in the band structures in Fig. 8.3, supports this observation. The color scale represents the product of weights attributed to different orbitals and species. It is evident that, unlike in Eu/WSe_2 (Fig. 7.3), the occupied $4f$ states are not within the same energy range as other states and are not visible around the Fermi energy. Consequently, they do not hybridize with the delocalized d electrons of W. Nevertheless, interaction occurs between the delocalized electrons of Gd and WSe_2, which is also observed in Eu/WSe_2. The band structures presented exhibit significant splittings between the bands at the K-valleys and various points near the Fermi energy, which are attributed to the influence of SOC that was taken into account during the computations. However, regarding the goal of creating a stable anomalous Hall conductor, as previously discussed, the magnetization of 1×1 Gd/WSe_2 is less stable than that of 1×1 Eu/WSe_2, indicating it can be more susceptible to perturbations. Further information is presented in Fig. D.4 of Appendix D, illustrating the impact of disabling SOC for different elements on the MAE curve. First, SOC is deactivated on the Gd atom to isolate the substrate contribution to the MAE. Subsequently, SOC on the W atom is disabled to examine the MAE resulting from Gd and Se.

It is important to emphasize that Gd and Eu exhibit differing chemical behaviors due to the outer $5d$ electron in Gd. While Eu lacks occupied outer d electrons and can only acquire d occupation through transfer from neighboring or underlying atoms, Gd

already has a $5d$ electron, and a full occupation may indicate a reluctance to hybridize with the surrounding environment. Upon examining the orbital contributions in the Appendix in Fig. D.2, it is apparent that the bands near the Fermi energy on the K–M–K' path display d electron contributions of Eu in Eu/WSe_2, which arise from charge transfer. On the other hand, in Gd, these bands originate from Gd's own electron and, as a result, have a higher occupation. Consequently, they are shifted towards the lower energy region near the K-valleys, where they exhibit slight interaction. This suggests that Eu generally interacts more with the substrate through charge transfer, while Gd behaves more atomically, with its states pushed onto the WSe_2 states. However, given that the distinguishing factor between 1×1 Eu/WSe_2 and 1×1 Gd/WSe_2 is the interatomic $f-d$ hybridization, it seems that this interaction is the primary contributor to the MAE in high-coverage situations.

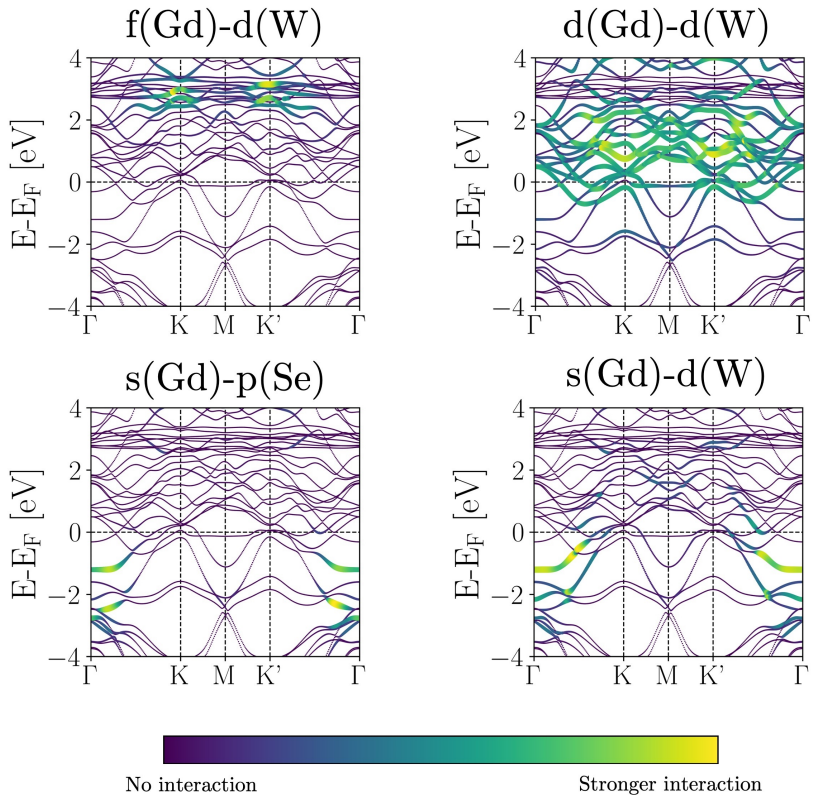

Figure 8.3: SOC-included calculations of orbital interactions in Gd/WSe_2 along the Γ–K–K'–Γ path. The interactions include: f states of Gd with d states of W, d states of Gd with d states of W, s states of Gd with p states of Se, and s states of Gd with d states of W.

Table 8.2: Ground state properties for Gd in the three adsorption sites on $\sqrt{3} \times \sqrt{3}$ WSe_2: adsorption energy in eV, adsorption distance in Å, d and f occupation of the magnetic RE atom, and spin magnetic moment of the RE atom in μ_B. Calculations have been performed without SOC.

Site	E_{ads} [eV]	d_0 [Å]	d_{occ}	f_{occ}	$m_s^{RE}[\mu_B]$
H	−1.106	2.162	0.756	7.004	7.433
T-W	−1.451	2.049	0.831	7.012	7.407
T-Se	−0.688	2.796	0.684	6.984	7.530

8.2 Gd atoms deposited on $\sqrt{3} \times \sqrt{3}$ WSe_2: dilute limit

As we move towards a less concentrated state in which the Gd atom coverage on WSe_2 is reduced to 1/3 of the 1×1 unit cell, various distinctions can be observed upon examining the adsorption properties listed in Table 8.2. One primary observation is that the adsorption energy is substantially larger than that in the high-coverage condition, and in the preferred T-W site, the Gd atom moves significantly closer towards the substrate, exhibiting a more pronounced proximity compared also to $\sqrt{3} \times \sqrt{3}$ Eu/WSe_2. Secondly, a slight loss in the d occupation is noticeable, which suggests a stronger interaction with the substrate.

Fig. 8.4 displays the corresponding electronic structure, where (a) presents the spin-resolved DOS and (b) displays the spin-resolved band structure, both calculated without SOC. It is noticeable that, once more, the system exhibits "semiconduct-

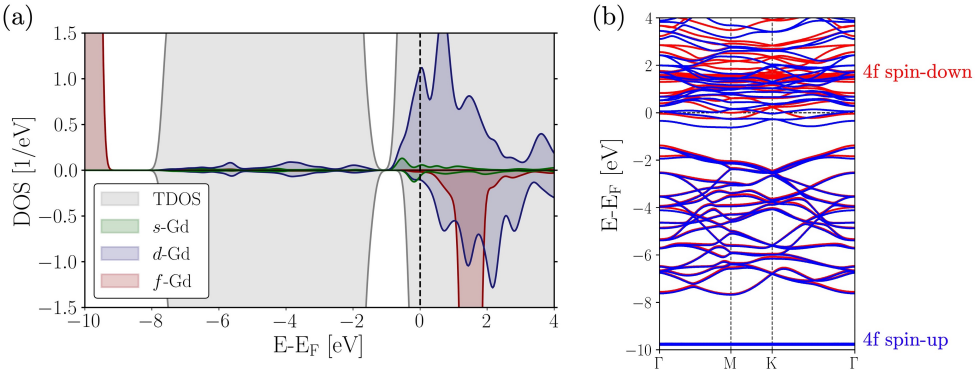

Figure 8.4: (a) Spin-resolved DOS of $\sqrt{3} \times \sqrt{3}$ Gd/WSe_2: grey represents the TDOS, green, red and blue the s, f and d states of Gd. (b) Spin-resolved band structure highlighting the $4f$ states. Calculations were performed without SOC.

ing" characteristics in this low coverage scenario, with an energy gap present in both spin channels below the Fermi energy. The spin-splitting in the system seems to be slightly stronger than in the $\sqrt{3} \times \sqrt{3}$ Eu/WSe_2 scenario due to the larger $m_s^{Gd} \sim 7.4$ μ_B, in comparison to $m_s^{Eu} \sim 7.0$ μ_B. Once again, the $4f$ peaks are widely separated in energy, with the occupied spin-up peak at around ~ -10 eV and the unoccupied spin-down peak at approximately ~ 1.8 eV. Nonetheless, the most significant aspect to observe is the existence of a significant DOS originating from the d occupation on and below the Fermi energy, in addition to the previously observed s occupation in the $\sqrt{3} \times \sqrt{3}$ Eu/WSe_2 case.

For a qualitative analysis of the electronic charge displacement involved in the heterostructure formation, the differential charge density was computed in the same saturation range as that of the $\sqrt{3} \times \sqrt{3}$ Eu/WSe_2 case, as discussed in Fig. 7.10 (b). For comparison purposes, the figure is presented again in Fig. 8.5. Observing the differential charge density in the Gd case reveals stronger intensities, indicating greater charge gain/loss in the respective red/blue areas. Furthermore, it seems that the Gd atom not only interacts with the W atom underneath, but some charge also appears to be involved on the second and third nearest W atoms. Another noteworthy feature is the symmetry of the charge lobes on Gd, which exhibit more pronounced features in the xy-plane. The orbital-specific d DOS of Gd is analyzed in Fig. 8.6 to confirm this observation. Firstly, it should be pointed out that due to the C_{3v} symmetry of the system, the $d_{x^2-y^2}$ and d_{xy} orbitals, as well as the d_{yz} and d_{xz} orbitals, are degenerate. Secondly, the ($d_{x^2-y^2}$, d_{xy}) orbitals, oriented in the xy plane of the WSe_2, have the largest orbital contribution in the occupied region, followed by the (d_{yz}, d_{xz})

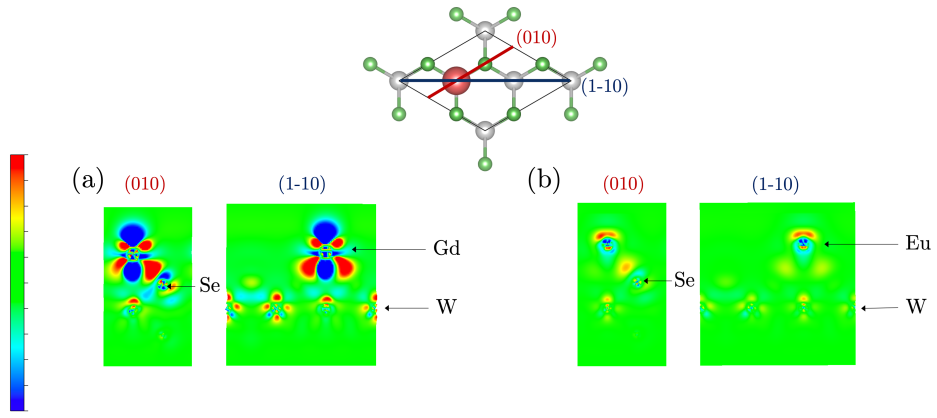

Figure 8.5: (a) Differential charge density of $\sqrt{3} \times \sqrt{3}$ Gd/WSe_2 in the (010) and (1-10) planes. (b) Differential charge density of $\sqrt{3} \times \sqrt{3}$ Eu/WSe_2 in the (010) and (1-10) planes. The color scale ranges from −0.005 to +0.005 and is consistent in both cases.

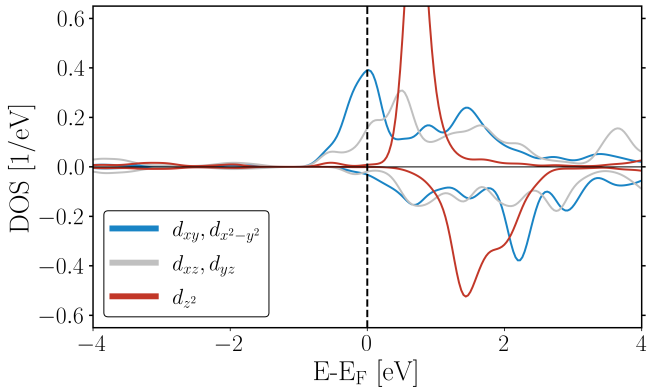

Figure 8.6: Orbital-resolved d density of states of Gd in $\sqrt{3}\times\sqrt{3}$ Gd/WSe_2: the $d_{x^2-y^2}$ and d_{xy} orbitals, as well as the d_{yz} and d_{xz} orbitals, are degenerate due to the C_{3v} symmetry of the system.

orbitals that introduce a z component. Lastly, a small red peak can be observed around ~ −0.5 eV from the d_{z^2} orbitals.

Shifting our attention to the influence of d chemistry on the MAE, we turn to examine Fig. 8.7. This figure displays the total energy as a function of the magnetization direction, indicating a significantly larger magnetic anisotropy compared to all other cases investigated where a half-filled $4f$-shell was present (recall that Gd/Gr yielded a MAE of ~ 0.6 meV), and close to the energy magnitudes observed in open $4f$-shells,

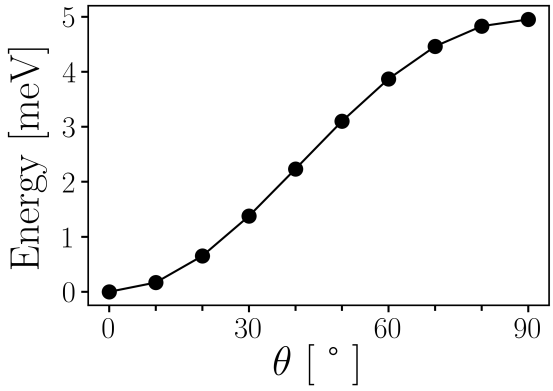

Figure 8.7: The magnetic anisotropy energy curve of Gd on $\sqrt{3}\times\sqrt{3}$ WSe_2 exhibits an easy-axis oriented out-of-plane, and an energy of around ~ 5 meV relative to the in-plane direction.

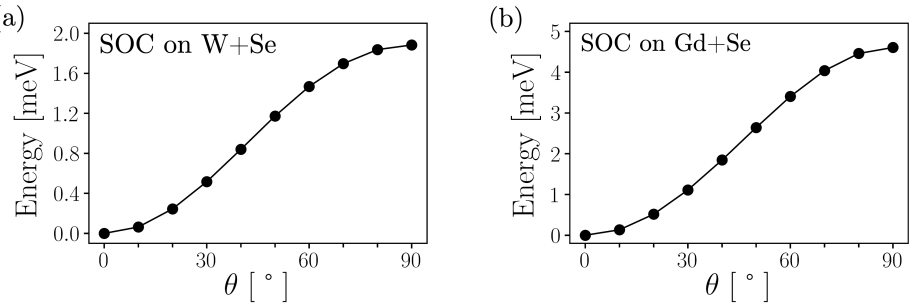

Figure 8.8: Magnetic anisotropy curves in the zx-plane for the $\sqrt{3} \times \sqrt{3}$ simulation cell of Gd/WSe_2 by turning off SOC on (a) the Gd atom and (b) on the W atoms.

albeit with a lower order anisotropy. The substantial energy difference observed is surprising, especially when considering the experience gained from the Eu/WSe_2 system where the dilution of the RE atom led to a smaller MAE.

The difference with the Gr systems can be explained by considering that Gr, in comparison to WSe_2, leads to weaker hybridization effects, resulting in the MAE arising solely from the Gd atom in the hexagonal crystal field. In the present case, the MAE is driven by both the Gd atom in the C_{3v} crystal field and the effects of orbital hybridizations and spin-polarization. The Gd spin-polarizes the environment and, via orbital hybridizations at the Fermi energy, leads to a rotation of the magnetic moments of other spin-polarized electrons in the system. Analyzing the effect of SOC supports this idea, as demonstrated in Fig. 8.8. Specifically, SOC has been turned off for both the Gd atom (Fig. 8.8 (a)) and the W atoms (Fig. 8.8 (b)). The results show that the substrate atoms themselves lead to a substantial MAE, even when SOC on Gd is disregarded, though most of the contribution appears to arise from the Gd atom. Additionally, it should be noted that the contributions from the two species are not additive.

Another difference to the $\sqrt{3} \times \sqrt{3}$ Eu/WSe_2 system arises from the DOS in the occupied region close to the Fermi energy: the Eu system does not exhibit a large d occupation as the Gd system, which is reflected in a generally smaller interaction with the substrate. Additionally, it is important to note that, while the distance between the Eu atom and WSe_2 does not appear to be greatly affected by dilution, in the case of Gd, dilution results in the RE atom being brought much closer to the substrate. As such, further investigations are recommended to gain a deeper understanding of how the concentration of RE atoms impacts their adsorption distance, taking into consideration the nature of the RE atom, and how this in turn affects the MAE and any possible magnetoelastic phenomena.

8.3 Eu/WSe_2 and Gd/WSe_2: takeaways

The primary conclusion is that MAE in the systems is mainly generated by $4f$ electrons, either through direct interaction with the chemical environment or indirectly through induced magnetic moments. Another important finding is the significant impact of an additional $5d$ electron on the MAE. Based on these observations, the following conclusions can be inferred:

1. In cases of high coverage (1×1 unit cells), the dominant factor influencing the MAE is the positioning of the $4f$ states in the gapless energy spectrum. When $4f$ states are in close proximity to other states in the system (Eu), they may hybridize and cause significant MAE. On the other hand, when $4f$ states are distant from other states (Gd), they may induce only minor anisotropies via spin-polarization of other states. This contribution is also present in the first scenario.

2. For the low coverage situations ($\sqrt{3} \times \sqrt{3}$ simulation cells), the key factor impacting MAE is the spin-polarization of states at E_F above the energy gap of the semiconducting WSe_2 substrate, induced by the $4f$ electrons. For Eu, a low density of states of the RE atom close to the Fermi energy is observed, while for Gd, a significant spin-polarized d DOS is found, which primarily contributes to the MAE.

3. When comparing the $\sqrt{3} \times \sqrt{3}$ Eu and Gd systems on WSe_2 to their respective systems on Gr, it becomes clear that the choice of 2D-material plays a crucial role in determining the MAE of the system. In this case, WSe_2 seems to amplify the MAE of both RE atoms compared to Gr. The effect is particularly striking for Gd and can be attributed to various factors such as orbital hybridizations, stronger SOC, and a different symmetry of the crystal field.

4. By carefully selecting the substrate and the coverage of the RE atom, it is feasible to manipulate the magnetic anisotropy of half-filled $4f$-atoms.

RE	mechanism	1×1 MAE	$\sqrt{3} \times \sqrt{3}$ MAE	d_{occ}
Eu	4f hybridization with substrate, intra-atomic f-d spin-polarization and d(Eu)-d(W) hybridization	1.7 meV f states close to other states	0.2 meV small 5d DOS at E_F	Larger in the monolayer compared to the dilute case
Gd	Intra-atomic f-d spin-polarization and d(Gd)-d(W) hybridization	0.4 meV f states deep in energy	5 meV large 5d DOS at E_F	Larger in the monolayer compared to the dilute case

Table 8.3: A summary of the main findings regarding the electronic and magnetic properties of Eu and Gd adsorbed on WSe_2.

8.4 Ho atoms deposited on 1×1 WSe_2: monolayer case

After investigating the behavior of half-filled $4f$-shells in two different packing densities of the RE atoms and two valence configurations (Eu vs. Gd), the next sections will provide a brief account on of the chemical and magnetic properties of an open $4f$-shell RE atom on WSe_2, with a focus on Ho. Chemically, Ho behaves more similarly to Eu (without an external $5d$ electron). Therefore, this compares the effect of the non-half-filled $4f$-shell on the magnetic anisotropy. The first step is to examine the high-coverage scenario by simulating a 1×1 unit cell containing one Ho atom per W atom, effectively representing an entire monolayer of Ho atoms on the surface of the substrate. Subsequently, the study will briefly address the more dilute situation in the $\sqrt{3} \times \sqrt{3}$ simulation cell.

Table 8.4 summarizes the adsorption properties of Ho, indicating that it prefers to adsorb on top of the W atom, as evidenced by the adsorption energies. Similarly to the case of Eu, Ho gains a fraction of d electrons that were not present in the isolated Ho atom and moves closer to the substrate when adsorbed on this site compared to other tested positions. The $4f$ occupation closely follows Hund's rules, with almost 11 electrons in the shell, leading to a magnetic moment close to 3 μ_B. This magnetic moment induces a small spin-polarization in other states, such as the d states which exhibit a magnetic moment of ~ 0.05 μ_B, much smaller than those observed in Eu and Gd/WSe_2 due to the smaller $4f$ magnetic moment. However, the orbital magnetic moment is approximately 1 μ_B smaller than the value predicted by Hund's rules (6 μ_B). This suggests a competition between Hund's rules and the crystal field effect, which causes quenching of the orbital moment. It appears that one $4f$ electron moves from the orbital with orbital quantum number $m_l = 0$ to $m_l = -1$, inducing the reduction of the total orbital angular momentum.

The electronic structure of the system is shown in Fig. 8.9. The spin-polarized DOS in Fig. 8.9 (a) indicates that the $4f$ states occupy a wide energy range, with the occupied states ranging from approximately −4 eV to −0.5 eV, while the unoccupied states are located at approximately 7 eV. The d states are highly delocalized, with a small

Site	E_{ads} [eV]	d_0 [Å]	d_{occ}	f_{occ}	$m_s^{RE}[\mu_B]$	$m_l^{RE}[\mu_B]$
H	−0.511	2.672	0.395	10.853	3.085	4.897
T-W	−0.946	2.404	0.440	10.846	3.068	4.888
T-Se	−0.780	3.101	0.405	10.849	3.107	4.899

Table 8.4: Ground state properties for Ho in the three adsorption sites on 1×1 WSe_2: adsorption energy in eV, adsorption distance in Å, d and f occupation of the magnetic RE atom, and spin and orbital magnetic moment of the RE atom in μ_B. Calculations for E_{ads} and d_0 have been performed without SOC, all the other properties have been calculated including SOC.

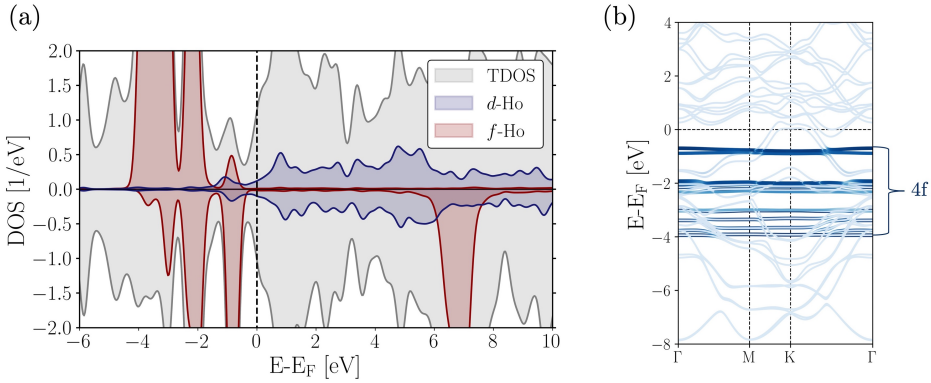

Figure 8.9: (a) Spin-resolved DOS of 1×1 Gd/WSe_2: grey represents the TDOS, red and blue the f and d states of Ho. (b) Band structure highlighting the occupied $4f$ states. Calculations were performed with SOC.

fraction of them being occupied and overlapping in energy with some of the $4f$ states. This suggests the possibility of an intra-atomic $f-d$ interaction. In Fig. 8.9 (b), the band structure exhibits characteristics similar to the 1×1 Eu and Gd/WSe_2 systems. However, it is noteworthy that the bands originating from the $4f$ electrons of Ho are exceptionally flat, in the displayed occupied region. These bands are situated in close proximity to the Fermi energy and are expected to significantly impact the magnetic properties of the system. It is also noted that the exchange splitting of the electronic structure is diminished in comparison to that of Eu and Gd. However, the spin-orbit coupling splitting, which is notably visible in the K-valleys, appears to be of similar magnitude for all the systems, as can be observed in the subsequent Fig. 8.10.

In these plots, the band structure is shown for the path Γ–K–M–K'–Γ, with the valence band maxima of WSe_2 at the K-valleys being noticeable at around −2 eV. The figures illustrate the interaction between different types of electrons in the system, which appear to be comparable to those observed in the 1×1 Eu/WSe_2 structure. Specifically, the delocalized Ho s, d electrons interact with the delocalized electrons of the substrate, while the $4f$ electrons interact with the d electrons of W, which are in the same energy range close to the Fermi energy. As a result, one may expect a magnetic anisotropy energy of at least a similar order of magnitude as observed for Eu/WSe_2 and greater than that of Gd/WSe_2, in which the $4f$ states were considerably distant from the substrate states. In the same region as these $4f$ states, other states of the Ho atom, such as the d and s states, also appear to interact intra-atomically with the $4f$ band at around −1 eV.

In order to examine the impact of an open $4f$-shell on the magnetic anisotropy, the out-of-plane MAE curve has been calculated and is presented in Fig. 8.11. The blue

dots denote the DFT+U data, and the red curve represents the fitting obtained using Eq. 2.19 for a C_{3v} crystal field, with $\varphi = 0$ and only considering a single $\sin^6\theta$ term. In other words, the extracted magnetic anisotropy constants are K_1, K_2, K_2', K_3, and K_5. Similar to open $4f$-shells in graphene systems, the magnetic easy-axis for Ho on a WSe_2 surface is observed to appear at a canted θ angle, around 70°, with a larger in-plane component than the out-of-plane one. The large values of MAE obtained are noteworthy, with the maximum energy from the magnetic ground state being approximately 15 meV, an order of magnitude greater than the MAE observed in 1×1 Eu/WSe_2. The hard-axis is found at $\theta \sim 30°$, while the perpendicular magnetization direction ($\theta = 0°$) is slightly lower in energy, at ~ 10 meV from the ground state. The overall behavior is highly anisotropic, as expected for a non-spherical $4f$ charge cloud

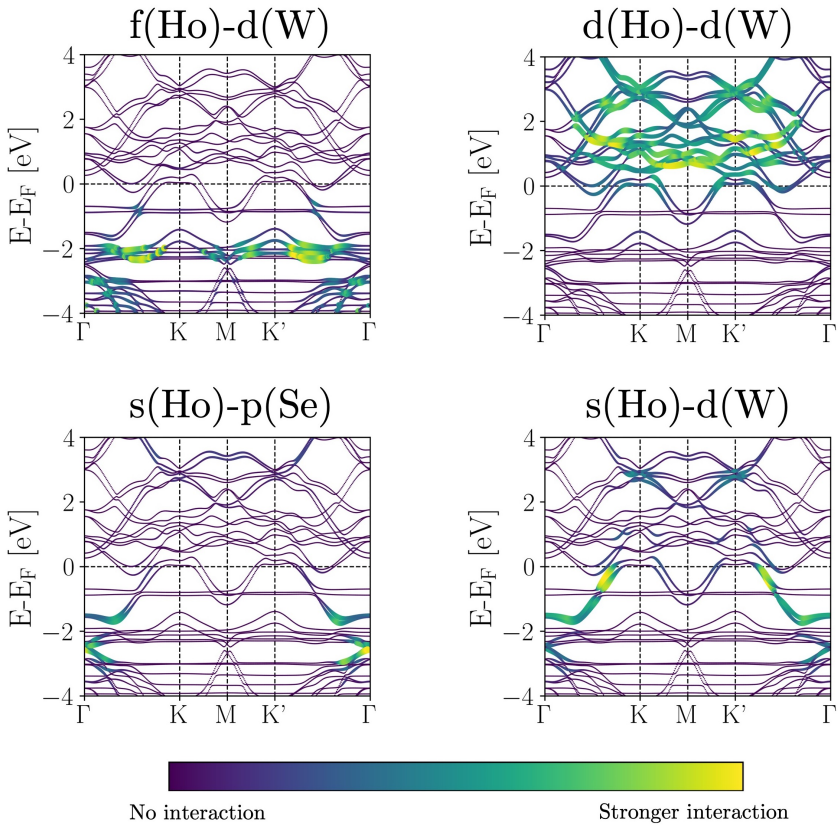

Figure 8.10: SOC-included calculations of orbital interactions in Ho/WSe_2 along the Γ–K–K'–Γ path. The interactions include: f states of Ho with d states of W, d states of Ho with d states of W, s states of Ho with p states of Se, and s states of Ho with d states of W.

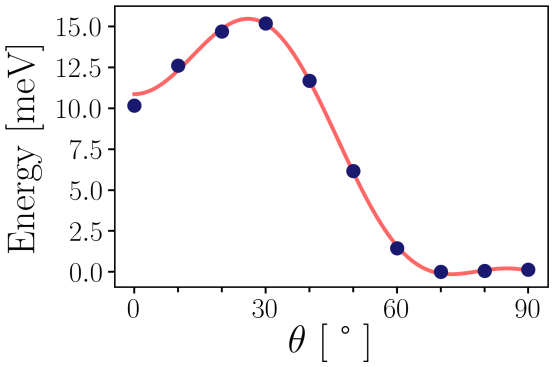

Figure 8.11: The magnetic anisotropy energy curve for Ho on a 1×1 WSe_2 monolayer in the zx-plane. The DFT+U data is denoted by blue dots, while the fitting function is represented by a continuous red line.

with non-zero angular momentum. The large MAE values and high-order anisotropic behavior can be attributed to the indirect effect of the $4f$ magnetic moment polarizing other states, which generate MAE contributions through SOC, and the effect of the $4f$ states interacting with neighboring states, where the crucial difference from the Eu system is that the $4f$ charge cloud exhibits a high degree of anisotropy in space, leading to a pronounced angular dependence of the energy. The magnetic anisotropy constants obtained from the fitting of the self-consistent data are presented in Table 8.5 in units of meV and K.

It is worth noting that in the Ho/WSe_2 system, the interactions between $4f$ electrons and the substrate consist of electrostatic interactions and potentially involve more complex hybridization effects. The increased diversity of chemical species and electrons in the Ho/WSe_2 system, in contrast to the graphene complexes discussed in Chapter 5, contributes to this distinction. Consequently, conducting further analysis utilizing crystal field theory could provide valuable insights into the accuracy of the point charge model employed in these TMDC systems, which exclusively considers electrostatic interactions.

Unit	K_1	K_2	K_2'	K_3	K_5
meV	56.061	−160.875	6.704	94.143	−16.701
K	650.565	−1866.888	77.797	1092.491	−193.808

Table 8.5: Magnetic anisotropy constants obtained via fitting of DFT+U data depicted in Fig. 8.11 for 1×1 Ho/WSe_2. The values are reported in meV and K.

8.5 Ho atoms deposited on $\sqrt{3} \times \sqrt{3}$ WSe_2: dilute limit

Moving on to the dilute scenario, Table 8.6 presents a summary of the adsorption properties on different sites. Notably, in the H-site, the orbital moment approaches the Hund's rule value of 6 μ_B, unlike in the monolayer where all sites had values close to 5 μ_B. This difference can be attributed to the larger distance from the substrate, of approximately Δd_0 = 0.4 Å, resulting in a more atomic-like behavior of the Ho atoms. However, the orbital moment is quenched by 1 μ_B when located on the Se and W atoms, suggesting the presence of a stronger crystal field effect or convergence towards a local energy minimum. At the T-W site, two distinct energy minima were identified: one characterized by full Hund's rule values and another where the orbital moment is quenched. The latter represents the ground state, which has a lower energy by 0.33 eV, and was obtained by considering the same adsorption distance as the Hund's rules case (the adsorption energy in this configuration has not been evaluated).

The DOS for the two energy minima can be found in Fig. 8.12. Similar to the case of $\sqrt{3} \times \sqrt{3}$ Eu/WSe_2, the d occupation is negligible, resulting in a minimal contribution to the MAE of the system. In both cases, the $4f$ occupation gives rise to spiky peaks located below the Fermi energy, which are separated by a significant energy gap from the unoccupied counterpart. The distinctive shape of the $4f$ peaks, reflecting the different orbital moment, induces other disparities in the electronic structure. To be more precise, in both spin channels, the deviation from Hund's rules (Fig. 8.12 (a)) leads to an energy gap of approximately 1 eV between the f states and the s states of Ho. In contrast to the Hund's rules case (Fig. 8.12 (b)), where the $4f$ states close the gap, the $4f$ states are slightly lower in energy, as demonstrated also by the band structures displayed in Figs. 8.12 (c) and (d). Large MAE is expected in both cases due to the presence of an open $4f$-shell. However, further investigations are needed

Site	E_{ads} [eV]	d_0 [Å]	d_{occ}	f_{occ}	$m_s^{RE}[\mu_B]$	$m_l^{RE}[\mu_B]$
H	−0.374	3.069	0.039	10.910	3.005	5.944
T-W	−0.634	2.428	0.141	10.910	3.012	5.935
T-W_{GS}	-	2.428	0.141	10.910	3.009	4.948
T-Se	−0.382	3.120	0.056	10.911	3.008	4.956

Table 8.6: Ground state properties for Ho in the three adsorption sites on $\sqrt{3} \times \sqrt{3}$ WSe_2: adsorption energy in eV, adsorption distance in Å, d and f occupation of the magnetic RE atom, and spin and orbital magnetic moment of the RE atom in μ_B. Calculations for E_{ads} and d_0 have been performed without SOC, all the other properties have been calculated including SOC. For the T-W_{GS} case, the adsorption energy has not been evaluated, and the distance from the first Se layer is assumed to be the same as in the Hund's rule case.

to elucidate the potential impact of the difference in orbital moment on the magnetic anisotropy energy, for example within the framework of the crystal field theory model employed for the RE/Gr systems.

Fig. 8.13 presents the computed magnetic anisotropy for the $m_l^{\mathrm{Ho}} = 6\ \mu_{\mathrm{B}}$ scenario, where the DFT+U outcomes are indicated with blue dots and the fitting function for a C_{3v} symmetry is depicted with a red line. When comparing to the other $\sqrt{3} \times \sqrt{3}$ systems (Eu and Gd), it becomes apparent that the energy involved in the magnetization rotation is higher than for Eu and in the same order of magnitude as for Gd. However, in contrast to Gd, where a large d occupation at the Fermi energy drives the phenomenon, in this case, it arises from the $4f$ electrons. These $4f$ electrons not only result in an energy difference between the magnetic ground state (at approximately $\theta = 50°$) and the hard axis (perpendicular direction, $\theta = 0°$) of about ~ 6 meV but also produce a highly anisotropic behavior, resulting in high-order terms in the energy functional expansion (see Table 8.7). In contrast, when comparing with Ho on graphene, it is apparent that although both exhibit a tilted magnetic ground state,

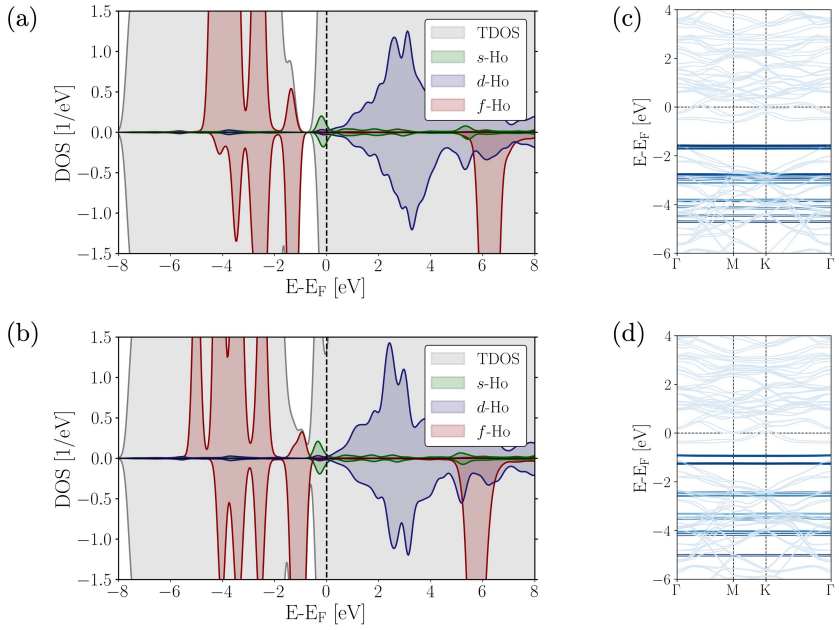

Figure 8.12: Spin-resolved DOS of $\sqrt{3} \times \sqrt{3}$ Ho/WSe_2: (a) In the $m_l^{\mathrm{Ho}} = 5\ \mu_{\mathrm{B}}$ case. (b) In the $m_l^{\mathrm{Ho}} = 6\ \mu_{\mathrm{B}}$ (Hund's rules) case. Grey represents the TDOS, red and blue the f and d states of Ho. Figures (c) and (d) are the respective band structures highlighting the occupied $4f$ states. Calculations were peformed with SOC and GGA+U.

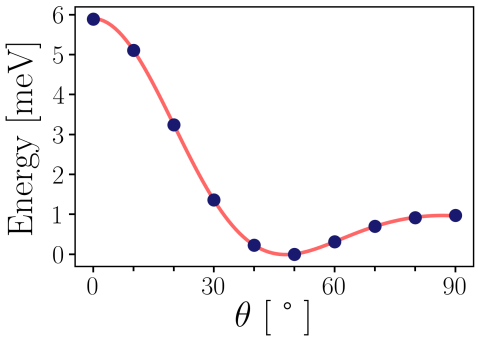

Figure 8.13: The magnetic anisotropy energy curve for Ho with m_l^{Ho} = 6 μ_{B} on a $\sqrt{3}\times\sqrt{3}$ WSe_2 monolayer in the zx-plane. The DFT+U data is denoted by blue dots, while the fitting function is represented by a continuous red line.

the shape of the curve is distinctly different, possibly due to the varying symmetries of the surrounding crystal field as well as the chemical makeup of the 2D-material, which can have an impact on the orbital hybridization effect.

Overall, it can be concluded that Ho on WSe_2 displays a canted magnetization direction and high anisotropy values that can be controlled by adjusting the coverage of the magnetic atom. Unlike half-filled $4f$-shells, the magnetic anisotropy can attain significant magnitudes even without the presence of delocalized d occupation, as observed in the $\sqrt{3}\times\sqrt{3}$ case, due to the significant direct contributions from the bare anisotropic $4f$ charge cloud. However, increasing the Ho coverage and, therefore, the d occupation of Ho and the interface hybridization, results in larger anisotropy values than any other system studied, likely driven by the $4f$ charge cloud and the intra-atomically spin-polarized d occupation, as well as the $4f$-$4f$ repulsion. Indeed, in a monolayer of Ho atoms, the anisotropic nature of the $4f$ charge clouds themselves can contribute to the crystal field effect. However, this contribution becomes negligible in half-filled $4f$-shells. Therefore, the optimal approach to achieving high magnetic anisotropies may be to employ open $4f$-shells at a high concentration.

Unit	K_1	K_2	K_2'	K_3	K_5
meV	−28.095	37.341	1.515	−14.189	3.950
K	−326.031	433.328	17.581	−164.658	45.838

Table 8.7: Magnetic anisotropy constants obtained via fitting of DFT+U data depicted in Fig. 8.13 for $\sqrt{3}\times\sqrt{3}$ Ho/WSe_2. The values are reported in meV and K.

Chapter 9

Conclusions

This thesis offers a comprehensive investigation of the electronic and magnetic properties of various rare-earth atoms adsorbed on different 2D-materials based on first-principles DFT calculations. By examining two distinct 2D materials as substrates for the rare-earth atoms, it becomes possible to explore a range of chemical environments. This exploration encompasses examining varying interactions, contributions from spin-orbit coupling, and different symmetries of the crystal field. Furthermore, the study uncovers the magnetic behavior based on the orbital occupation by analyzing both half-filled $4f$-shells and open $4f$-shells. The findings reveal that, in general, the significant magnetic anisotropies are primarily driven by the spin and orbital magnetic moments resulting from the interplay between the $4f$ electrons and the surrounding crystal field. Notably, the magnetic anisotropies are particularly large for open $4f$-shells. Moreover, the involvement of $5d$ electrons becomes crucial in specific cases, as they can contribute to the magnetic anisotropy and influence the chemistry of the rare-earth atoms. Additionally, the study demonstrates that the magnetic anisotropy can be modified through mechanical deformation and variations in the adsorption coverage.

The investigation of $4f$-atoms adsorbed on a graphene monolayer elucidated that rare-earth elements lacking an additional $5d$ electron in their valence shell exhibit similar chemical behavior, while those with $5d$ electrons, such as Gd, interact differently with graphene. All studied RE/Gr complexes displayed large spin magnetic moments and significant orbital magnetic moments for open $4f$-shell configurations (Dy, Ho, and Tm). The values of the spin and orbital moments conform with Hund's rule orbital occupation in all cases except for Dy/Gr, where a lower energy configuration with a smaller orbital moment was discovered.

Adsorption of $4f$-atoms onto graphene causes n-doping in the 2D-material, resulting in metallic behavior driven by the delocalized d occupation of the RE atoms. The $4f$ states remain localized and detached from the Fermi energy, and are the primary source of magnetic anisotropy. Eu/Gr and Gd/Gr exhibit negligible magnetic anisotropies in magnitude, which are well described by low orders in the energy functional $E(\theta, \phi)$ due to the almost absent orbital moment in the half-filled $4f$ situation.

In contrast, Dy, Ho, and Tm exhibit magnetic anisotropies on the order of several meV, which necessitate high-order contributions to fit well with the energy functional $E(\theta, \phi)$ for hexagonal systems. A detailed analysis of the energy as a function of magnetization direction reveals that Ho/Gr and Tm/Gr favor a canted easy-axis, while Dy/Gr exhibits an in-plane easy-axis. Fitting the magnetic anisotropy curves allowed for determination of the magnetic anisotropy constants, which were then reverse-engineered in the quantum framework for the crystal field parameters. The crystal field parameters were utilized to compute the multiplet structures, revealing that Ho/Gr and Tm/Gr are protected against direct quantum tunneling of magnetization, whereas Dy/Gr generates tunnel-split doublets that can potentially destabilize the magnetization. However, in the case of Dy/Gr, a single magnetic ground state at $\langle J_z = 0 \rangle$ was identified, consequently ruling out the possibility of magnetization reversal.
By examining the effect of an induced perpendicular strain on the $4f$-atoms, it was observed that compressing the atoms towards the graphene monolayer results in an increased magnetic anisotropy, indicating a promising approach for enhancing magnetic stability. Furthermore, application of strain has been observed to cause pressure-induced magnetization switching by changing the easy-axis in Dy/Gr. The results of the magnetoelastic analysis indicate that the force constants and vibrational frequencies of the RE/Gr complexes reflect the d occupations and are sensitive to the direction of magnetization.

In the investigation of Dy/Gr, a notable finding involves the study of its two different energy minima corresponding to two orbital configurations, namely $J = 7$ and $J = 8$. The presence of the $J = 7$ occupation implies a conflict between the intra-atomic exchange and the crystal field effect. It has been demonstrated that a significant modification in the magnetic anisotropy is observed when one $4f$ electron is shifted into a different f orbital from the one expected by Hund's rules. It is evident from this that a precise description of the $4f$ electrons holds immense significance in unraveling magnetic anisotropies with utmost accuracy.

Finally, the dilution of $4f$-atoms adsorbed on graphene leads to a more atomic-like behavior, as reflected in the electron occupations. Surprisingly, the s states show sharper and stronger spin-polarized peaks in the density of states upon dilution. This leads to a flat band close to the Fermi energy in the 4×4 supercell.

The investigation of the effect of metallic substrates on the magnetic anisotropy of Gd/Gr has revealed a dependence on the magnetic properties and interaction of the substrate with graphene. In this study, Ir(111) was selected as a non-magnetic substrate, and the investigation revealed that the weak van der Waals interaction with graphene resulted in a minimal impact on the MAE of Gd/Gr. Only when the Gd atom adsorbs in the valley regions of the corrugated graphene, bringing it closer to the Ir surface, slight effects on the overall out-of-plane MAE are observed. Specifically, the decrease in MAE can be ascribed to the preferred in-plane magnetization direc-

tion of the induced magnetic moment in the metallic substrate, which slightly reduces the hardness of the perpendicular easy-axis of Gd/Gr. However, given the very low energy scales involved, it can be concluded that Ir(111) has a minimal impact and is thus a suitable substrate for investigating the magnetic anisotropy effects of RE/Gr systems or other 2D magnetic nanostructures.

To examine the impact of a magnetic metallic substrate, simulations were performed with a Co(111) surface as a substrate for Gd/Gr. The easy-axis of the system was found to be in-plane, indicating a strong influence of the magnetic Co(111) substrate on the magnetic properties of Gd/Gr, which otherwise exhibits a perpendicular easy-axis. Therefore, the Co(111) magnetism and its interaction with Gd/Gr are significant enough to modify the magnetic properties of the graphene complex. As such, a magnetic substrate such as Co(111) can be employed to induce changes in the magnetic properties of RE/Gr systems.

The study of rare-earth atoms adsorbed on a TMDC substrate, namely WSe_2, has yielded notable and compelling findings with regard to both magnetic characteristics and transport properties. The systems were analyzed considering different degrees of coverage of the RE atom on WSe_2.
The investigation of Eu atoms deposited on a WSe_2 monolayer at high coverage has revealed promising features for the development of magnetotransport applications. The proximity-induced orbital hybridizations, spin-orbit coupling, spin-polarization, and broken symmetries provide the potential to influence the magnetic anisotropy, spin-orbital textures, and Berry curvature. High concentration of Eu atoms generates an overall metallic system with a large density of states around the Fermi energy, which plays a fundamental role in the generation of magnetic anisotropy. The spin-polarization induced by the large local $4f$ moment of Eu, along with the observed hybridizations between Eu electrons and the delocalized electrons of the substrate, are responsible for generating a prominent magnetic anisotropy ($\sim$ 1.75 meV) even in the presence of a half-filled $4f$-shell, with a perpendicular easy-axis. Moreover, the calculations predict a ferromagnetic configuration, while the spin-orbital texture on the Fermi surface evidences the presence of magnetic interactions and orbital hybridizations. The synergy between these features induces Berry curvature hotspots in k-space, which lead to a sizable anomalous Hall conductivity in the sample. This example of RE/TMDC heterostructure expands the design portfolio of potential future spintronic devices in 2D.

Upon exploring the magnetic anisotropy of the Eu/TMDC system at a reduced coverage of Eu atoms, *i.e.*, in a $\sqrt{3}\times\sqrt{3}$ simulation cell, the magnetic anisotropy was found to be almost quenched, with values in the range of ~ 0.2 meV. This significant reduction in magnetic anisotropy is attributed to the decreased magnetic proximity effects resulting from weaker hybridizations between Eu and WSe_2, as well as between Eu atoms. The exchange splitting is reasonably smaller than that in the high-coverage scenario, and the overall electronic structure displays a reemergence of the semicon-

ducting features of WSe_2 with a band gap close to the Fermi energy. These findings indicate that a high coverage of Eu atoms is crucial to achieve significant magnetic anisotropies when Eu is the chosen rare-earth atom. Furthermore, the observation holds significant implications for experimental realizations and suggests that high coverage is also essential for measuring the anomalous Hall effect.

The study of Gd/WSe_2 is of interest due to the chemical dissimilarity between Gd and Eu, which arises from the outer $5d$ electron. Comparing the high and low coverage situations of the two $4f$-atoms on the TMDC reveals that Gd exhibits opposite behavior to Eu. Specifically, a small magnetic anisotropy was found for high coverage, whereas extraordinarily large values were obtained in the dilute situation. Inspection of the electronic structures of the two cases reveals that, in the high coverage case, the magnetic anisotropy is significantly influenced by the energy location of the $4f$ states in the energy spectrum and their overlapping with the substrate states near the Fermi energy. For Gd, these states are much deeper in energy than for Eu, which causes them to not contribute to direct interactions with other electrons. In contrast, the key factor in the dilute case appears to be the presence of spin-polarized states above the energy gap close to the Fermi energy. While Eu exhibits a low density of states in this energy area, Gd is characterized by a large density of states, primarily originating from d states. These states are spin-polarized intra-atomically by the $4f$ magnetic moment and hybridize with the electrons of the substrate. Another crucial aspect to consider relative to the unique chemistry of Gd is its closer adsorption to the TMDC monolayer in the dilute scenario. This proximity significantly amplifies the interaction between the Gd adatom and the crystal field.
Additionally, when comparing the dilute cases of Eu and Gd on WSe_2 with the respective graphene systems, it was found that the magnetic anisotropy is generally amplified by the TMDC. The details of this amplification depend on the factors discussed above. These results highlight the crucial role of both the $4f$-atom and the 2D-material in tailoring the magnetic anisotropy.

To determine the influence of a non-spherical $4f$ charge distribution on the magnetic anisotropy of WSe_2, Ho atoms were simulated on the surface of the material in both high and low coverage scenarios. When Ho atoms are densely packed, the electronic structure is similar to that of Eu/WSe_2 with the $4f$ states situated near the Fermi energy. As a result, the magnetic anisotropy energy reaches significant values (around 15 meV) and exhibits a highly anisotropic behavior with respect to the magnetization direction. These characteristics distinguish Ho from Eu and Gd, as the non-spherical $4f$ distribution of Ho, due to its large orbital moment, interacts differently with the surrounding crystal field under rotation of the magnetization. To gain a comprehensive understanding of the significant magnetic anisotropy, it is crucial also to consider the contribution of the crystal field originating from the open $4f$-shells, which results in $4f$-$4f$ interactions. When the Ho atoms are less concentrated, similar to the Eu case, the magnetic anisotropy decreases but remains relatively high, indicating that adjusting the coverage of Ho controls the magnetic anisotropy. Furthermore, it is

essential to note that changing the 2D-material from graphene to WSe_2 leads to a different local symmetry in the crystal field theory, resulting in a varied dependence on the magnetization direction.

In conclusion, these years of research on rare-earth atoms in 2D-materials have revealed a deeper understanding of the behavior of magnetic anisotropy resulting from the interaction between $4f$ electrons and the crystal field, as well as complex hybridization effects involving other types of electrons. Intra-atomic and inter-atomic spin-polarization, spin-orbit coupling, orbital hybridizations, and symmetry conditions all play important roles in this complex picture. While a point charge model may suffice for treating $4f$-atoms in graphene systems with small interactions, it becomes more challenging when dealing with complex structures containing various chemical elements. In such cases, a thorough understanding of many parallel effects is crucial for discernment. The beauty of this field lies in the fusion of physics and chemistry to provide important insights into the behavior of rare-earth atoms in their environments.

Hopefully, the insights gained from these studies will not only expand our fundamental understanding of the complex behavior of $4f$-atoms, but also provide important guidelines for designing new magnetic materials with tailored properties for both fundamental scientific knowledge and practical applications in the future.

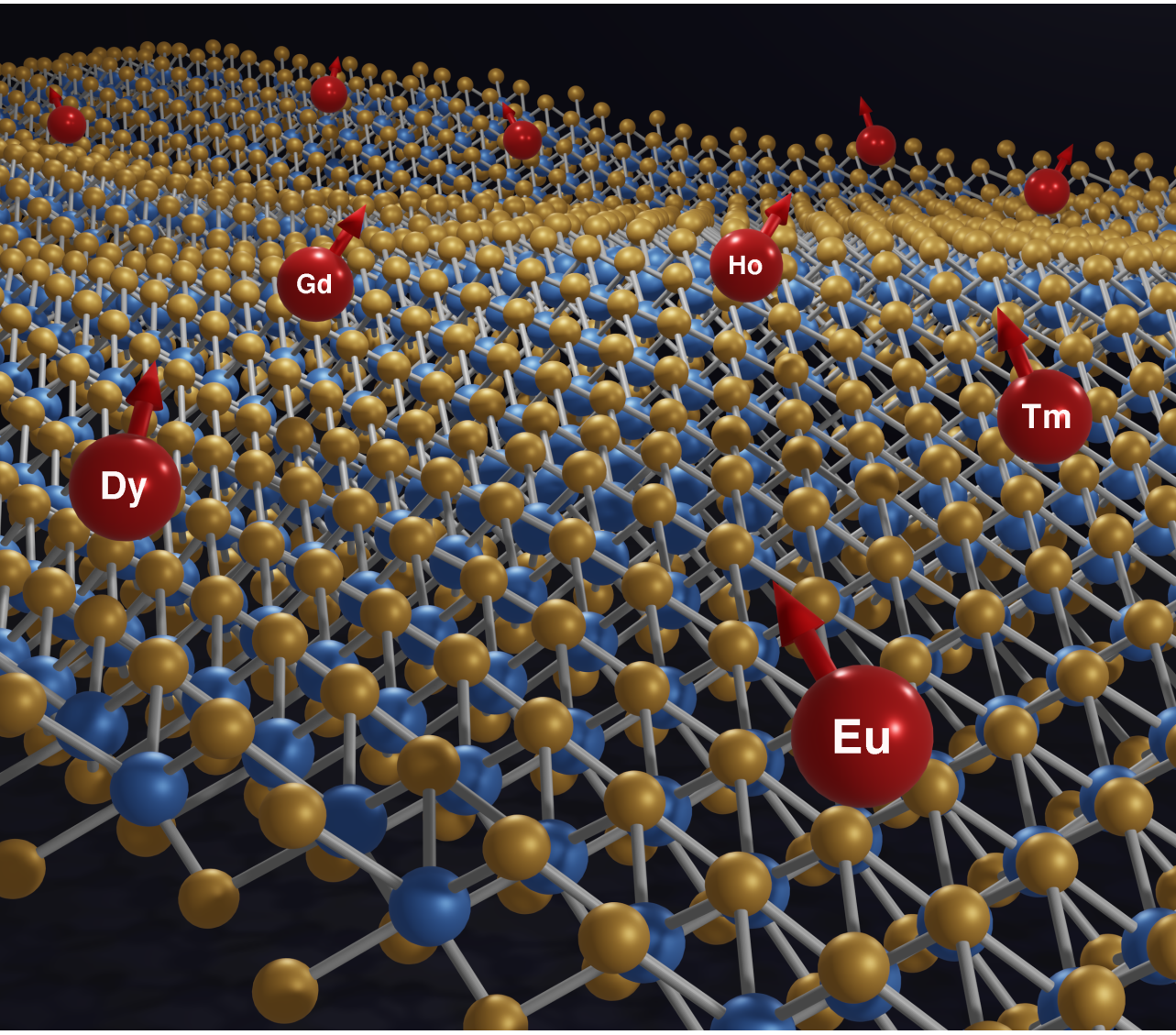

A graphical representation illustrating the magnetic rare-earth atoms investigated in this thesis, adsorbed on a monolayer of transition metal dichalcogenide. Credit for the design of this image goes to Daniele Valente.

Appendix A

A.1 Character Tables

In general, the characters of a system with total angular momentum J undergoing a rotation of an angle α can be calculated as follows:

$$\chi^J(\alpha) = \frac{\sin[(J+\frac{1}{2})\alpha]}{\sin\frac{\alpha}{2}}. \tag{A.1}$$

However, it is important to note that the transformation $\alpha \to \alpha+2\pi$ behaves differently for integer and half-integer values of J. Specifically, when evaluating the rotation $\alpha + 2\pi$, we have [232]:

$$\chi^J(\alpha+2\pi) = \frac{\sin[(J+\frac{1}{2})(\alpha+2\pi)]}{\sin\frac{\alpha+2\pi}{2}} = \frac{\sin(J+\frac{1}{2})\alpha\cdot\cos(J+\frac{1}{2})2\pi}{\sin\frac{\alpha}{2}\cdot\cos\pi}, \tag{A.2}$$

where the value of $\cos(J+\frac{1}{2})2\pi$ is negative for integer J values and positive for half-integer J values. Therefore, it is possible to express this as:

$$\chi^J(\alpha+2\pi) = \chi^J(\alpha)(-1)^{2J}, \tag{A.3}$$

Based on this, it can be can be inferred that for systems with integer J, rotations of $\alpha + n\pi$, where $n = 2, 4, 6, \ldots$, result in the same outcome. However, for half-integer spin systems, rotations of 2π and 4π do not produce the same character:

$$\begin{aligned}\chi^J(\alpha\pm 2\pi) &= -\chi^J(\alpha)\\ \chi^J(\alpha\pm 4\pi) &= +\chi^J(\alpha).\end{aligned} \tag{A.4}$$

This implies that in the latter case, the identity operation is defined differently. In other words, a rotation of 2π does not leave the system unchanged, but a rotation of 4π is required. Due to this characteristic of half-integer spin systems, it becomes necessary to introduce an additional group element to represent the 2π rotation (as the identity corresponds to the 4π rotation). As a consequence, the point group experiences a doubling of the number of symmetries, encompassing both the original operations and the composite operations obtained by applying the 2π rotation to the original ones.

An example of double group character table can be seen in Table A.1, which shows the double C_{6v} point group for half-integer spin and the spherically symmetric K_h group with $J = 7/2, 15/2$. Table A.2 displays the standard character table of the C_{6v} and K_h group with $J = 8$.

C_{6v}	E	$\bar{E}$	C_2 $\bar{C}_2$	$2C_3$	$2\bar{C}_3$	$2C_6$	$2\bar{C}_6$	$3\sigma_d$ $3\bar{\sigma}_d$	$3\sigma_v$ $3\bar{\sigma}_v$
Γ_1	1	1	1	1	1	1	1	1	1
Γ_2	1	1	1	1	1	1	1	−1	−1
Γ_3	1	1	−1	1	1	−1	−1	1	−1
Γ_4	1	1	−1	1	1	−1	−1	1	1
Γ_5	2	2	−2	−1	−1	1	1	0	0
Γ_6	2	2	2	−1	−1	−1	−1	0	0
Γ_7	2	−2	0	1	−1	$\sqrt{3}$	$-\sqrt{3}$	0	0
Γ_8	2	−2	0	1	−1	$-\sqrt{3}$	$\sqrt{3}$	0	0
Γ_9	2	−2	0	−2	2	0	0	0	0
$J = 7/2\ K_h$	8	−8	0	1	−1	$-\sqrt{3}$	$\sqrt{3}$	0	0
$J = 15/2\ K_h$	16	−16	0	−1	1	$\sqrt{3}$	$-\sqrt{3}$	0	0

Table A.1: Character table of the C_{6v} symmetry double group and of the rotational invariant atom with total angular momentum $J = 7/2, 15/2$.

C_{6v}	E	$2C_6$	$2C_3$	$2C_2$	$3\sigma_d$	$3\sigma_v$
Γ_1	1	1	1	1	1	1
Γ_2	1	1	1	1	−1	−1
Γ_3	1	−1	1	−1	1	−1
Γ_4	1	−1	1	−1	−1	1
Γ_5	2	1	−1	−2	0	0
Γ_6	2	−1	−1	2	0	0
$J = 8\ K_h$	17	1	−1	1	−1	−1

Table A.2: Character table of the C_{6v} symmetry point group and of the rotational invariant atom with total angular momentum $J = 8$.

A.2 C_{6v} Crystal Field matrix elements for $J = 8$

The crystal field matrix elements for $J = 8$ are presented in accordance with Ref. [67]:

$$\langle J_z = 8|\mathcal{H}_{6v}|J_z = 8\rangle = \langle J_z = -8|\mathcal{H}_{6v}|J_z = -8\rangle = 120C_2^0 + 21840C_4^0 + 1441440C_6^0$$

$$\langle J_z = 7|\mathcal{H}_{6v}|J_z = 7\rangle = \langle J_z = -7|\mathcal{H}_{6v}|J_z = -7\rangle = 75C_2^0 - 5460C_4^0 - 2342340C_6^0$$

$$\langle J_z = 6|\mathcal{H}_{6v}|J_z = 6\rangle = \langle J_z = -6\mathcal{H}_{6v}|J_z = -6\rangle = 36C_2^0 - 16380C_4^0 - 1081080C_6^0$$

$$\langle J_z = 5|\mathcal{H}_{6v}|J_z = 5\rangle = \langle J_z = -5|\mathcal{H}_{6v}|J_z = -5\rangle = 3C_2^0 - 16380C_4^0 + 900900C_6^0$$

$$\langle J_z = 4|\mathcal{H}_{6v}|J_z = 4\rangle = \langle J_z = -4|\mathcal{H}_{6v}|J_z = -4\rangle = -24C_2^0 - 10080C_4^0 + 1774080C_6^0$$

$$\langle J_z = 3|\mathcal{H}_{6v}|J_z = 3\rangle = \langle J_z = -3|\mathcal{H}_{6v}|J_z = -3\rangle = -45C_2^0 - 1260C_4^0 + 1288980C_6^0$$

$$\langle J_z = 2|\mathcal{H}_{6v}|J_z = 2\rangle = \langle J_z = -2|\mathcal{H}_{6v}|J_z = -2\rangle = -60C_2^0 + 7140C_4^0 + 27720C_6^0$$

$$\langle J_z = 1|\mathcal{H}_{6v}|J_z = 1\rangle = \langle J_z = -1|\mathcal{H}_{6v}|J_z = -1\rangle = -69C_2^0 + 13020C_4^0 - 1178100C_6^0$$

$$\langle J_z = 0|\mathcal{H}_{6v}|J_z = 0\rangle = -72C_2^0 + 15120C_4^0 - 1663200C_6^0$$

$$\langle J_z = 8|\mathcal{H}_{6v}|J_z = 2\rangle = \langle J_z = 2|\mathcal{H}_{6v}|J_z = 8\rangle = \langle J_z = -8|\mathcal{H}_{6v}|J_z = -2\rangle = \langle J_z = -2|\mathcal{H}_{6v}|J_z = -8\rangle = 720\sqrt{2002}C_6^6$$

$$\langle J_z = 7|\mathcal{H}_{6v}|J_z = 1\rangle = \langle J_z = 1|\mathcal{H}_{6v}|J_z = 7\rangle = \langle J_z = -7|\mathcal{H}_{6v}|J_z = -1\rangle = \langle J_z = -1|\mathcal{H}_{6v}|J_z = -7\rangle = 2520\sqrt{715}C_6^6$$

$$\langle J_z = 6|\mathcal{H}_{6v}|J_z = 0\rangle = \langle J_z = 0|\mathcal{H}_{6v}|J_z = 6\rangle = \langle J_z = -6|\mathcal{H}_{6v}|J_z = 0\rangle = \langle J_z = 0|\mathcal{H}_{6v}|J_z = -6\rangle = 5040\sqrt{429}C_6^6$$

$$\langle J_z = 5|\mathcal{H}_{6v}|J_z = -1\rangle = \langle J_z = -1|\mathcal{H}_{6v}|J_z = 5\rangle = \langle J_z = -5|\mathcal{H}_{6v}|J_z = 1\rangle = \langle J_z = 1|\mathcal{H}_{6v}|J_z = -5\rangle = 4320\sqrt{1001}C_6^6$$

$$\langle J_z = 4|\mathcal{H}_{6v}|J_z = -2\rangle = \langle J_z = -2|\mathcal{H}_{6v}|J_z = 4\rangle = \langle J_z = -4|\mathcal{H}_{6v}|J_z = 2\rangle = \langle J_z = 2|\mathcal{H}_{6v}|J_z = -4\rangle = 15120\sqrt{110}C_6^6$$

$$\langle J_z = 3|\mathcal{H}_{6v}|J_z = -3\rangle = \langle J_z = -3|\mathcal{H}_{6v}|J_z = 3\rangle = 166320C_6^6$$

A.3 C_{6v} Crystal Field matrix elements for $J = 15/2$

The crystal field matrix elements for $J = 15/2$ are presented in accordance with Ref. [67]:

$$\langle J_z = \tfrac{15}{2}|\mathcal{H}_{6v}|J_z = \tfrac{15}{2}\rangle = \langle J_z = -\tfrac{15}{2}|\mathcal{H}_{6v}|J_z = -\tfrac{15}{2}\rangle = 105C_2^0 + 16380C_4^0 + 900900C_6^0$$

$$\langle J_z = \tfrac{13}{2}|\mathcal{H}_{6v}|J_z = \tfrac{13}{2}\rangle = \langle J_z = -\tfrac{13}{2}|\mathcal{H}_{6v}|J_z = -\tfrac{13}{2}\rangle = 63C_2^0 - 5460C_4^0 - 1621620C_6^0$$

$$\langle J_z = \tfrac{11}{2}|\mathcal{H}_{6v}|J_z = \tfrac{11}{2}\rangle = \langle J_z = -\tfrac{11}{2}|\mathcal{H}_{6v}|J_z = -\tfrac{11}{2}\rangle = 27C_2^0 - 13260C_4^0 + 540540C_6^0$$

$$\langle J_z = \tfrac{9}{2}|\mathcal{H}_{6v}|J_z = \tfrac{9}{2}\rangle = \langle J_z = -\tfrac{9}{2}|\mathcal{H}_{6v}|J_z = -\tfrac{9}{2}\rangle = -3C_2^0 - 12060C_4^0 - 817740C_6^0$$

$$\langle J_z = \tfrac{7}{2}|\mathcal{H}_{6v}|J_z = \tfrac{7}{2}\rangle = \langle J_z = -\tfrac{7}{2}|\mathcal{H}_{6v}|J_z = -\tfrac{7}{2}\rangle = -27C_2^0 - 6060C_4^0 + 1205820C_6^0$$

$$\langle J_z = \tfrac{5}{2}|\mathcal{H}_{6v}|J_z = \tfrac{5}{2}\rangle = \langle J_z = -\tfrac{5}{2}|\mathcal{H}_{6v}|J_z = -\tfrac{5}{2}\rangle = -45C_2^0 - 1380C_4^0 + 623700C_6^0$$

$$\langle J_z = \tfrac{3}{2}|\mathcal{H}_{6v}|J_z = \tfrac{3}{2}\rangle = \langle J_z = -\tfrac{3}{2}|\mathcal{H}_{6v}|J_z = -\tfrac{3}{2}\rangle = -57C_2^0 + 77400C_4^0 - 346500C_6^0$$

$$\langle J_z = \tfrac{1}{2}|\mathcal{H}_{6v}|J_z = \tfrac{1}{2}\rangle = \langle J_z = -\tfrac{1}{2}|\mathcal{H}_{6v}|J_z = -\tfrac{1}{2}\rangle = -63C_2^0 + 11340C_4^0 - 1039500C_6^0$$

$$\langle J_z = \tfrac{15}{2}|\mathcal{H}_{6v}|J_z = \tfrac{3}{2}\rangle = \langle J_z = -\tfrac{15}{2}|\mathcal{H}_{6v}|J_z = -\tfrac{3}{2}\rangle = \langle J_z = -\tfrac{3}{2}|\mathcal{H}_{6v}|J_z = -\tfrac{15}{2}\rangle =$$
$$\langle J_z = \tfrac{3}{2}|\mathcal{H}_{6v}|J_z = \tfrac{15}{2}\rangle = 360\sqrt{11}\sqrt{455}C_6^6$$

$$\langle J_z = \tfrac{13}{2}|\mathcal{H}_{6v}|J_z = \tfrac{1}{2}\rangle = \langle J_z = -\tfrac{13}{2}|\mathcal{H}_{6v}|J_z = -\tfrac{1}{2}\rangle = \langle J_z = -\tfrac{1}{2}|\mathcal{H}_{6v}|J_z = -\tfrac{13}{2}\rangle =$$
$$\langle J_z = \tfrac{1}{2}|\mathcal{H}_{\text{hex.}}|J_z = \tfrac{13}{2}\rangle = 7 \cdot 360\sqrt{11}\sqrt{39}C_6^6$$

$$\langle J_z = \tfrac{11}{2}|\mathcal{H}_{6v}|J_z = -\tfrac{1}{2}\rangle = \langle J_z = -\tfrac{11}{2}|\mathcal{H}_{6v}|J_z = \tfrac{1}{2}\rangle = \langle J_z = \tfrac{1}{2}|\mathcal{H}_{6v}|J_z = -\tfrac{11}{2}\rangle =$$
$$\langle J_z = -\tfrac{1}{2}|\mathcal{H}_{6v}|J_z = \tfrac{11}{2}\rangle = 4 \cdot 360\sqrt{11}\sqrt{273}C_6^6$$

$$\langle J_z = \tfrac{9}{2}|\mathcal{H}_{6v}|J_z = -\tfrac{3}{2}\rangle = \langle J_z = -\tfrac{9}{2}|\mathcal{H}_{6v}|J_z = \tfrac{3}{2}\rangle = \langle J_z = \tfrac{3}{2}|\mathcal{H}_{6v}|J_z = -\tfrac{9}{2}\rangle =$$
$$\langle J_z = -\tfrac{3}{2}|\mathcal{H}_{6v}|J_z = \tfrac{9}{2}\rangle = 84 \cdot 360\sqrt{11}C_6^6$$

$$\langle J_z = \tfrac{7}{2}|\mathcal{H}_{6v}|J_z = -\tfrac{5}{2}\rangle = \langle J_z = -\tfrac{5}{2}|\mathcal{H}_{6v}|J_z = \tfrac{5}{2}\rangle = \langle J_z = \tfrac{5}{2}|\mathcal{H}_{6v}|J_z = -\tfrac{7}{2}\rangle =$$
$$\langle J_z = -\tfrac{5}{2}|\mathcal{H}_{6v}|J_z = \tfrac{7}{2}\rangle = 42 \cdot 360\sqrt{11}\sqrt{5}C_6^6$$

A.4 Stevens' factors

In the following the Stevens factors adapted from [40] are reported.

Ion^{3+}	$\alpha \times 10^2$	$\beta \times 10^4$	$\gamma \times 10^6$
Ce	−5.714	63.49	0
Pr	−2.101	−7.346	60.99
Nd	−0.6428	−2.911	−37.99
Pm	0.7714	4.076	60.78
Sm	4.127	25.01	0
Tb	−1.0101	1.224	−1.121
Dy	−0.6349	−0.5920	1.035
Ho	−0.2222	−0.3330	−1.294
Er	0.2540	0.4440	2.070
Tm	1.0101	1.632	−5.606
Yb	3.175	−17.32	148.0

Table A.3: Stevens' factors for RE ions in the 3+ oxidation state.

Appendix B

B.1 Band structures of open $4f$-shell atoms on $\sqrt{3} \times \sqrt{3}$ graphene

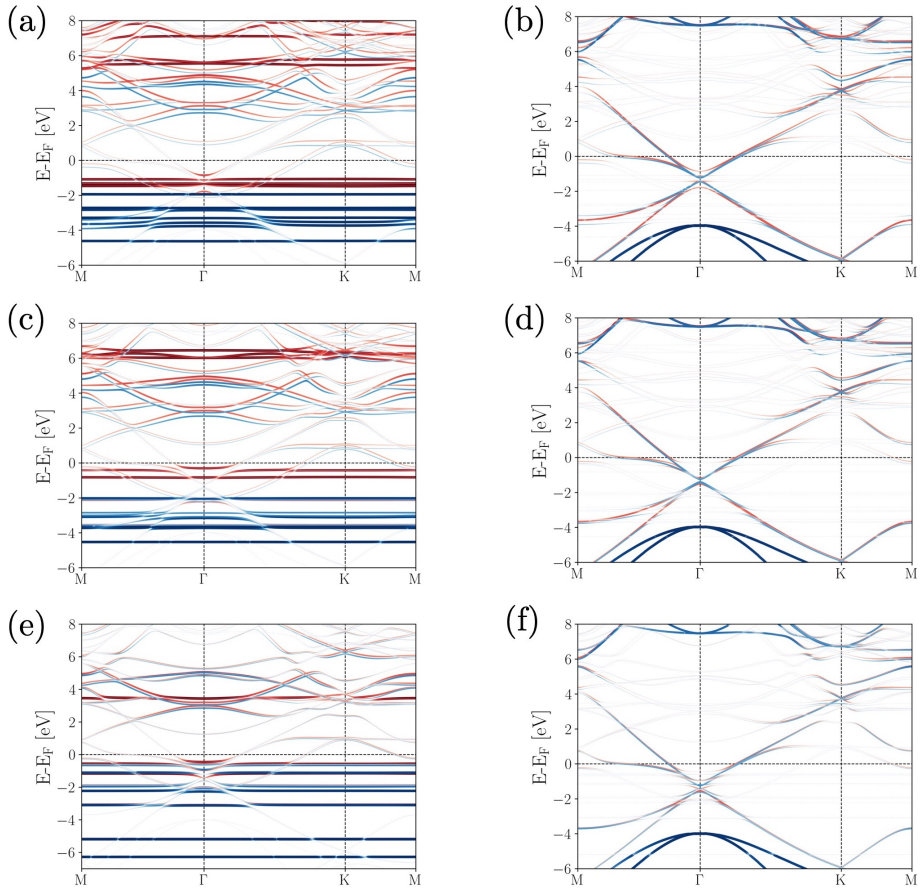

Figure B.1: RE/Gr band structures. (a)-(b) Dy contribution (left) and C contribution (right) in Dy/Gr; (c)-(d) Ho contribution (left) and C contribution (right) in Ho/Gr; (e)-(f) Tm contribution (left) and C contribution (right) in Tm/Gr.

B.2 Crystal field parameters at equilibrium distance in standard and Waybourne notation

The table below displays the crystal field parameters at equilibrium distance calculated as $A_l^m = C_l^m/\alpha_l$, where α_l represents the Stevens' factor for a specific total angular momentum J. For the Gr-complex under investigation, Dy has a J value of 8, corresponding to the Ho^{3+} configuration, with the associated Stevens' factors of $(\alpha_2, \alpha_4, \alpha_6) = (-0.222 \cdot 10^{-2}, -0.333 \cdot 10^{-4}, -1.3 \cdot 10^{-6})$, as presented in Table A.3. Similarly, the Stevens' factors for Ho ($J = 15/2$) correspond to the Er^{3+} values, and for Tm ($J = 7/2$), the values associated with Yb^{3+} are assumed.

Unit	A_2^0	A_4^0	A_6^0	A_6^6
Dy adatom on graphene				
meV	−11.287	5.156	0.057	3.765
K	−130.980	59.833	0.659	43.691
Ho adatom on graphene				
meV	−15.312	8.793	0.096	3.089
K	−177.688	102.039	1.114	35.846
Tm adatom on graphene				
meV	−5.990	−5.329	−0.054	−13.556
K	−69.511	−61.841	−0.627	−157.311

Table B.1: Crystal field parameters in standard notation at equilibrium distance. The values are reported in meV and K.

The CFP in the Waybourne convention, $B_l^m = C_l^m/\alpha_l\theta_l^m$, are summarized in Table B.2.

Unit	B_2^0	B_4^0	B_6^0	B_6^6
Dy adatom on graphene				
meV	−22.573	41.246	0.908	3.964
K	−261.949	478.640	10.537	46
Ho adatom on graphene				
meV	−30.623	70.345	1.540	3.252
K	−355.365	816.320	17.871	37.738
Tm adatom on graphene				
meV	−11.979	−42.630	−0.868	−14.271
K	−139.011	−494.701	−10.073	−165.608

Table B.2: Crystal field parameters in Waybourne notation at equilibrium distance. The values are reported in meV and K.

B.3 Phase diagrams of $\langle J_z \rangle$ for $J = 7/2, 8, 15/2$

Considering the CF Hamiltonian for a hexagonal symmetry in Eq. 2.37, and dividing it by the first CFP (C_2^0) neglecting the transverse term ($C_6^6 = 0$), leads to

$$\frac{\mathcal{H}_{6v}}{C_2^0} = \hat{O}_2^0 + \frac{C_4^0}{C_2^0}\hat{O}_4^0 + \frac{C_6^0}{C_2^0}\hat{O}_6^0. \tag{B.1}$$

The diagonalization of Eq. B.1 can be done for a range of C_4^0 and C_6^0 values with fixed C_2^0, resulting in a series of multiplet structures. For each spectrum, the magnetic ground state (lowest lying state in energy) can be identified and its expectation value, $\langle J_z \rangle$, is plotted in a phase diagram. Fig. B.2 shows the phase diagrams for $J = 7/2,\ 15/2,\ 8$.

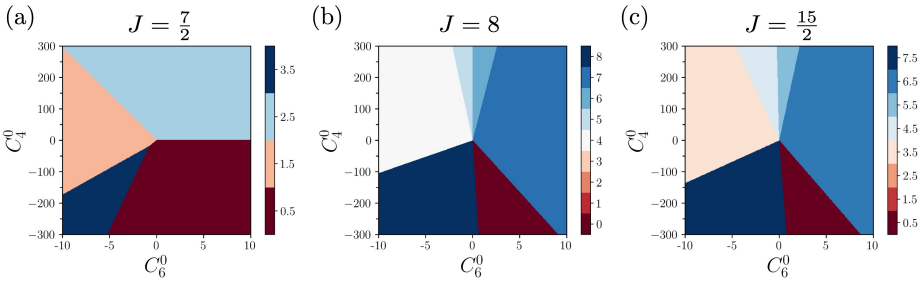

Figure B.2: Phase diagrams of the magnetic ground state for multiplet structures with varying C_4^0/C_2^0 and C_6^0/C_2^0 ratios for systems with total angular momentum (a) $J = 7/2$ (b) $J = 8$ and (c) $J = 15/2$.

Each diagram scans the ground state for CFP spanning the ranges $-300 \leq C_4^0 \leq 300$ and $-10 \leq C_6^0 \leq 10$. Since the spectrum is always symmetric around $\langle J_z \rangle$, only the ground state with $\langle J_z \rangle \geq 0$ has been considered. As an example case, C_2^0 is set to 100 (arbitrary units), allowing the phase diagrams to show the magnetic ground state for ratios $-3 < C_4^0/C_2^0 < 3$ and $-0.1 < C_6^0/C_2^0 < 0.1$. These values are chosen based on the most visible information obtained from trial values, starting from large ranges and narrowing in on the region where most phase transitions occur. The magnetic ground state varies depending on the values of the CFP with fixed C_2^0, and further analysis can be carried out by extending the code to all possible J values across the $4f$ series and by integrating symmetries other than C_{6v}.

Appendix C

C.1 Gd/Gr/Ir(111) vs. Gd/Gr: graphene contribution

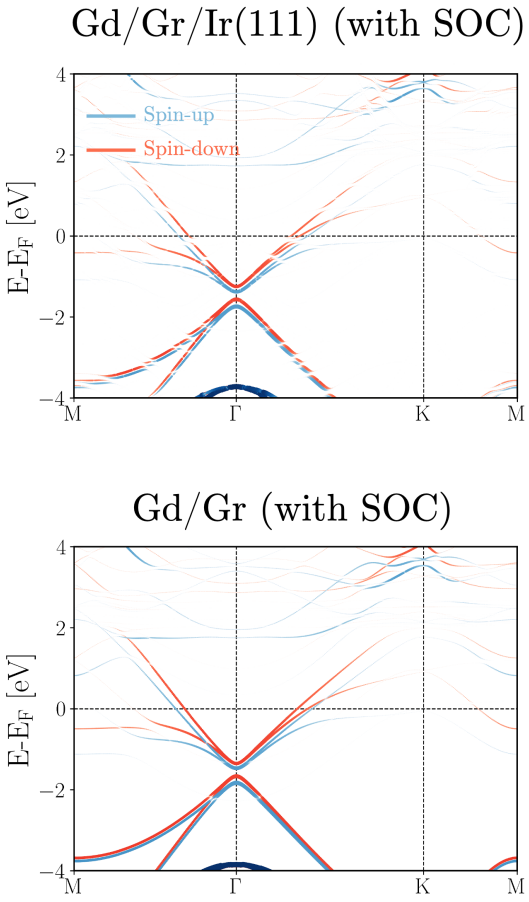

Figure C.1: The figure compares the band structure contributions of graphene in Gd/-Gr/Ir(111) with Gr positioned at h_h, and that of free-standing Gd/Gr. The spin-up channel is represented in blue, and the spin-down channel is shown in red. These calculations were performed with the inclusion of spin-orbit coupling.

C.2 Gd/Gr/Ir(111): Gr-Ir(111) interaction with distance

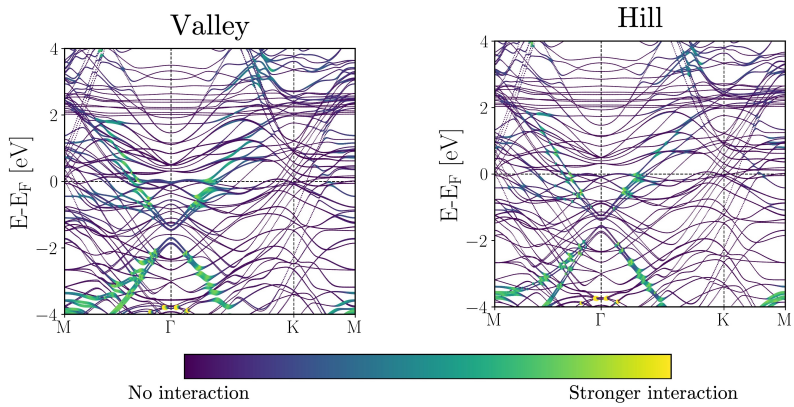

Figure C.2: Band structure of Gd/Gr/Ir(111) at the valley and hill positions, highlighting the strength of Gr-Ir interaction using a colormap based on the product of the sum of all carbon contributions and the sum of all Ir contributions. The valley configuration shows a higher degree of interaction.

C.3 Gd/Gr/Co(111): spin-polarized band structure of graphene

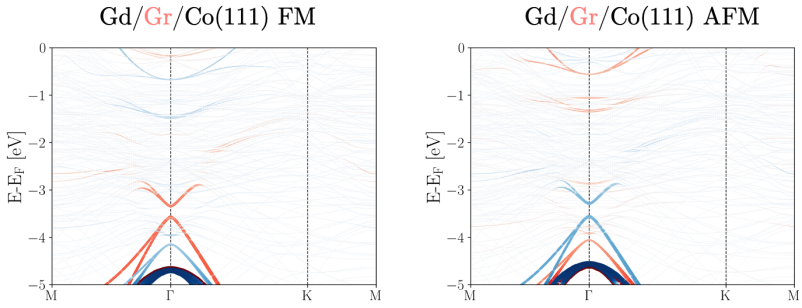

Figure C.3: Spin-polarized band structure of carbon atoms in the ferromagnetic and antiferromagnetic configurations of Gd/Gr/Co(111). The calculations were performed with the inclusion of SOC.

Appendix D

D.1 Eu on 1×1 WSe_2: spin-orbit coupling scaling

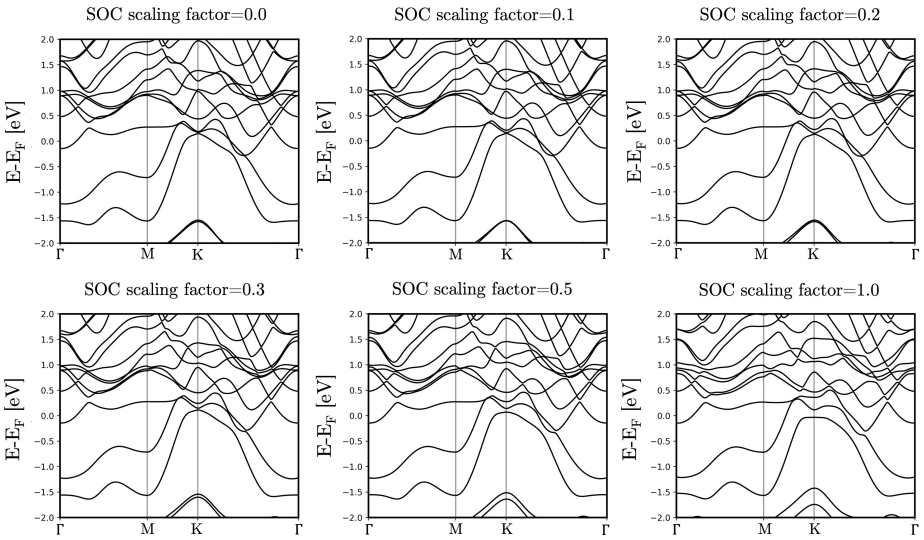

Figure D.1: The scaling effect of spin-orbit coupling in 1×1 Eu/WSe_2 can be observed in the simulated band structure along the Γ-M-K-Γ path in reciprocal space. As the strength of spin-orbit coupling increases, energy gaps form, leading to the removal of degeneracies and the appearance of avoided crossings. This effect is particularly evident in the K-valley, where the spin-up and spin-down channels are split.

D.2 Eu on 1×1 WSe_2: orbital contributions to the band structure

Fig. D.2 reports the band structure of a monolayer of Eu atoms deposited on 1H-WSe_2, which illustrates the contribution coming from different chemical elements and orbitals. Specifically the contribution of the f, s, d electrons of Eu, the p electrons of Se and the d electrons of W are shown. The shown contribution for Se only includes the atom of the upper layer, which is the one closer to the adatom and thus exhibits stronger interaction.

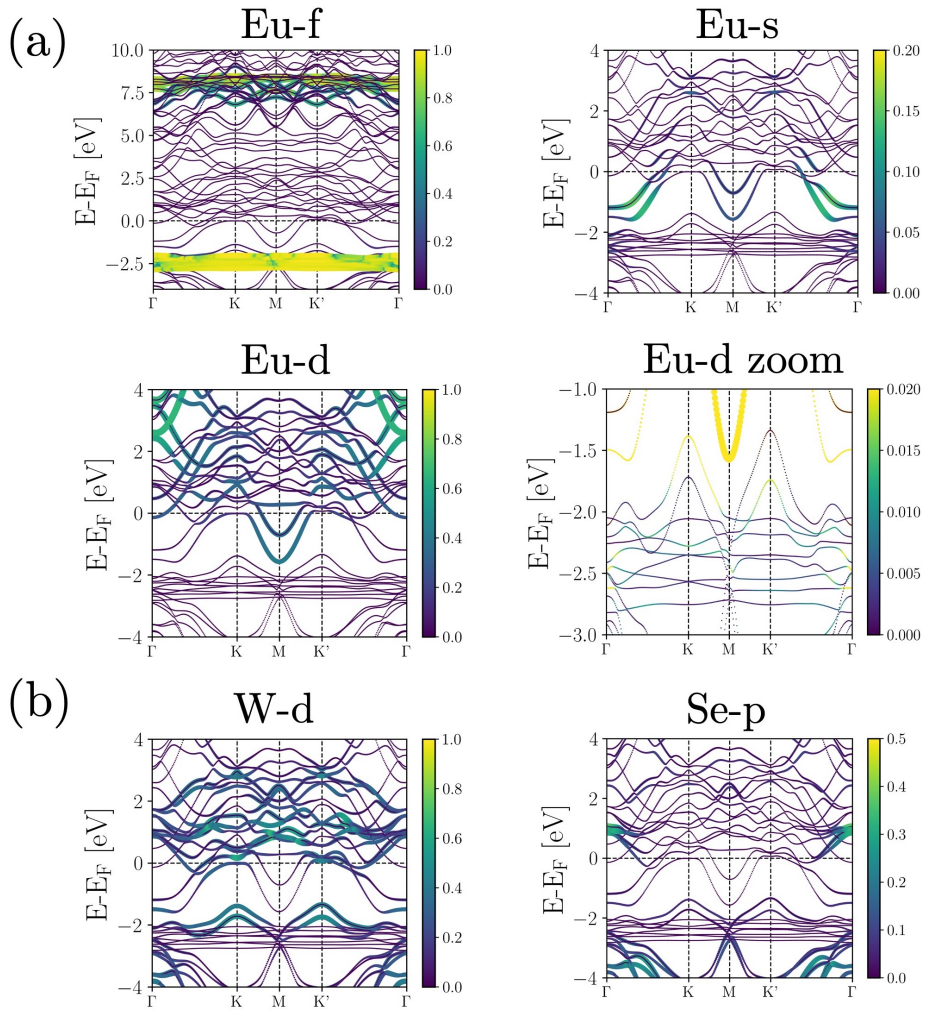

Figure D.2: Orbital contributions to the band structure of a monolayer of Eu on a WSe_2 monolayer are depicted for the various chemical elements present in the system. Specifically, panel (a) illustrates the f, s, and d contributions of Eu, with a zoomed-in view of the d contribution near the energy range of occupied f states. In panel (b), the d contribution of W and the p contribution of Se from the substrate are displayed. The color scale indicates the weights of the orbital characters. The calculations include the consideration of spin-orbit coupling.

D.3 Eu on $\sqrt{3}\times\sqrt{3}$ WSe_2: density of states

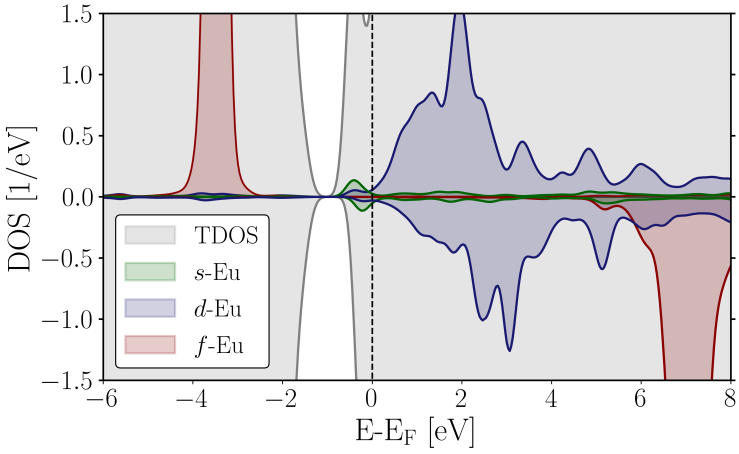

Figure D.3: Spin-resolved density of states of $\sqrt{3}\times\sqrt{3}$ Eu/WSe_2. Grey represents the TDOS, green, red and blue the s, f and d states of the Eu atom.

D.4 Gd on 1×1 WSe_2: magnetic anisotropy contributions

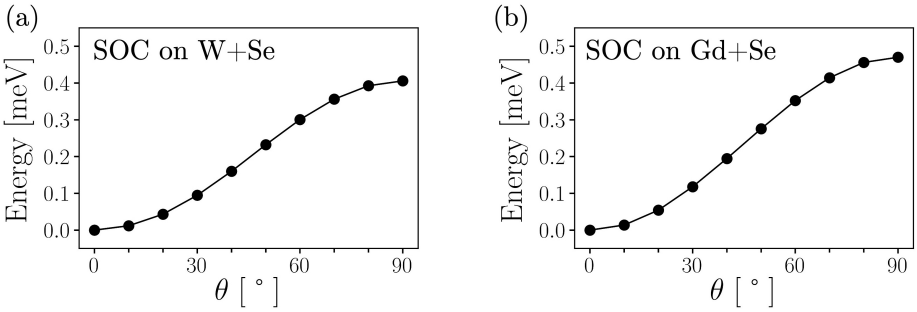

Figure D.4: Out-of-plane magnetic anisotropy curves in the xz-plane for the 1×1 simulation cell of Gd/WSe_2 are shown by disabling spin-orbit coupling on (a) the Gd atom and (b) the W atoms.

Appendix E

Presented below are several examples of FLEUR input files for the input generator `inpgen` of the investigated systems. These input files contain information about the hexagonal lattice geometry of the studied systems, including atomic positions, as well as specifications such as the k-point mesh and spin-orbit coupling. It is worth noting that, for the calculation of magnetic anisotropy curves, the line `&soc 0.37 0.10` is employed, which leads to a breaking of symmetries. For each (θ, φ) point, the orientation of the spin quantization axis is then adjusted in the corresponding `inp.xml` file.

E.1 Input file sample for FLEUR: Eu atom on $\sqrt{3} \times \sqrt{3}$ graphene

```
&input  film=t  /
&lattice latsys=hdp  a=8.0518  /

7
63   1.0  2.0    1.8000953146
6    0.0  0.0   -3.0
6    1.0  1.0   -3.0
6    2.0  2.0   -3.0
6    1.0  0.0   -3.0
6    0.0  2.0   -3.0
6    2.0  1.0   -3.0

&factor 3.0  3.0 1.0 /
&soc    0.37 0.10 /
&kpt    div1=20 div2=20 div3=1 /
```

The input files for Gd/Gr, Dy/Gr, Ho/Gr, and Tm/Gr share identical structures, except for the adjusted distance between the rare-earth atom and the Gr monolayer and the atomic number of the first listed atom.

E.2 Input file sample for FLEUR: Gd atom on $\sqrt{3} \times \sqrt{3}$ Gr/Ir(111)

```
&input  film=t  /
&lattice latsys=hdp a=8.0518 /

22
64   1.0  2.0    13.31797096
6    0.0  0.0     9.09219959035
6    1.0  1.0     9.09219959035
6    2.0  2.0     9.09219959035
6    1.0  0.0     9.09219959035
6    0.0  2.0     9.09219959035
6    2.0  1.0     9.09219959035
77   0.0  0.0     3.04519959035
77   1.0  1.0     3.04519959035
77   2.0  2.0     3.04519959035
77   1.0  0.0    -1.1668004096499995
77   0.0  2.0    -1.1668004096499995
77   2.0  1.0    -1.1668004096499995
77   0.0  1.0    -5.378800409649999
77   2.0  0.0    -5.378800409649999
77   1.0  2.0    -5.378800409649999
77   0.0  0.0    -9.590800409649999
77   1.0  1.0    -9.590800409649999
77   2.0  2.0    -9.590800409649999
77   1.0  0.0    -13.802800409649999
77   0.0  2.0    -13.802800409649999
77   2.0  1.0    -13.802800409649999

&factor 3.0 3.0 1.0 /
&kpt div1=20 div2=20 div3=1 /
```

The above corresponds to the structure with Gr in the valley position on Ir(111).

E.3 Input file sample for FLEUR: Eu atom on 1×1 WSe_2

```
&input  film=t /
&lattice latsys=hcp  a=6.287113491   /

4
63   1.0  2.0    4.9538123666
34   2.0  1.0    0.2365412966
74   1.0  2.0   -2.9964573580
34   2.0  1.0   -6.175900000

&factor 3.0 3.0 1.0 /
&soc 0.0 0.0 /
&kpt 64 /
```

The provided input generates the structure of the 1×1 Eu/WSe_2 simulation cell with a k-point mesh consisting of 64 k-points. Subsequently, the k-point mesh has been appropriately modified for the actual calculations with the command line: `inpgen -inp.xml -kpt gamma@grid=10,10,1`.

E.4 Input file sample for FLEUR: Eu atom on $\sqrt{3} \times \sqrt{3}$ WSe_2

```
&input  film=t  /
&lattice latsys=hdp  a=10.8896   /

10
63    1.0  1.0    4.9538123666
74    0.0  0.0   -2.9992581821
74    1.0  1.0   -2.9964573580
74    2.0  2.0   -2.9992624865
34    1.0  0.0    0.2365412966
34    1.0  0.0   -6.1759
34    0.0  2.0    0.2365412966
34    0.0  2.0   -6.1759
34    2.0  1.0    0.2365412966
34    2.0  1.0   -6.1759

&factor 3.0 3.0 1.0 /
&kpt div1=20 div2=20 div3=1 /
```

Bibliography

[1] P. Ajayan, P. Kim, and K. Banerjee. "van der Waals materials". In: *Phys. Today* 69.9 (2016), p. 38.

[2] K. Zhang et al. "Two dimensional hexagonal boron nitride (2D-hBN): synthesis, properties and applications". In: *Journal of Materials Chemistry C* 5.46 (2017), pp. 11992–12022.

[3] A. V. Kolobov and J. Tominaga. *Two-dimensional transition-metal dichalcogenides*. Vol. 239. Springer, 2016.

[4] M. A McGuire. "Cleavable magnetic materials from van der Waals layered transition metal halides and chalcogenides". In: *Journal of Applied Physics* 128.11 (2020), p. 110901.

[5] M. Abramchuk et al. "Controlling magnetic and optical properties of the van der Waals crystal CrCl3- xBrx via mixed halide chemistry". In: *Advanced materials* 30.25 (2018), p. 1801325.

[6] A. K. Geim and I. V. Grigorieva. "Van der Waals heterostructures". In: *Nature* 499.7459 (2013), pp. 419–425.

[7] E. Rossi and C. Triola. "Van Der Waals Heterostructures with Spin-Orbit Coupling". In: *Annalen der Physik* 532.2 (2020), p. 1900344.

[8] K. Zollner, M. Gmitra, and J. Fabian. "Swapping exchange and spin-orbit coupling in 2d van der waals heterostructures". In: *Physical Review Letters* 125.19 (2020), p. 196402.

[9] D. Zhong et al. "Layer-resolved magnetic proximity effect in van der Waals heterostructures". In: *Nature nanotechnology* 15.3 (2020), pp. 187–191.

[10] P. Nagler et al. "Giant magnetic splitting inducing near-unity valley polarization in van der Waals heterostructures". In: *Nature communications* 8.1 (2017), p. 1551.

[11] S. K. Behura et al. "Moiré physics in twisted van der Waals heterostructures of 2D materials". In: *Emergent Materials* 4 (2021), pp. 813–826.

[12] Q. Xu, Y. Guo, and L. Xian. "Moiré flat bands in twisted 2D hexagonal vdW materials". In: *2D Materials* 9.1 (2021), p. 014005.

[13] F. He et al. "Moiré patterns in 2D materials: a review". In: *ACS nano* 15.4 (2021), pp. 5944–5958.

[14] M. Tian et al. "Two-dimensional van der Waals materials for spin-orbit torque applications". In: *Frontiers in Nanotechnology* 3 (2021), p. 732916.

[15] W. Zhang et al. "Van der Waals stacked 2D layered materials for optoelectronics". In: *2D Materials* 3.2 (2016), p. 022001.

[16] D. Jariwala et al. “Van der Waals materials for atomically-thin photovoltaics: promise and outlook”. In: *Acs Photonics* 4.12 (2017), pp. 2962–2970.

[17] H. Li, S. Ruan, and Y.-J. Zeng. “Intrinsic van der Waals magnetic materials from bulk to the 2D limit: new frontiers of spintronics”. In: *Advanced Materials* 31.27 (2019), p. 1900065.

[18] J. F. Sierra et al. “Van der Waals heterostructures for spintronics and opto-spintronics”. In: *Nature Nanotechnology* 16.8 (2021), pp. 856–868.

[19] K. S Burch, D. Mandrus, and J.-G. Park. “Magnetism in two-dimensional van der Waals materials”. In: *Nature* 563.7729 (2018), pp. 47–52.

[20] Q. H. Wang et al. “The magnetic genome of two-dimensional van der Waals materials”. In: *ACS nano* 16.5 (2022), pp. 6960–7079.

[21] J. Arneth et al. “Uniaxial pressure effects in the two-dimensional van der Waals ferromagnet CrI 3”. In: *Physical Review B* 105.6 (2022), p. L060404.

[22] E. Aguilera et al. “Topological magnonics in the two-dimensional van der Waals magnet CrI 3”. In: *Physical Review B* 102.2 (2020), p. 024409.

[23] C. Tan et al. “Hard magnetic properties in nanoflake van der Waals Fe3GeTe2”. In: *Nature communications* 9.1 (2018), p. 1554.

[24] X. Wang et al. “Current-driven magnetization switching in a van der Waals ferromagnet Fe3GeTe2”. In: *Science advances* 5.8 (2019), eaaw8904.

[25] D. Afanasiev et al. “Controlling the anisotropy of a van der Waals antiferromagnet with light”. In: *Science advances* 7.23 (2021), eabf3096.

[26] Z. Wang et al. “Electric-field control of magnetism in a few-layered van der Waals ferromagnetic semiconductor”. In: *Nature nanotechnology* 13.7 (2018), pp. 554–559.

[27] N. Sethulakshmi et al. “Magnetism in two-dimensional materials beyond graphene”. In: *Materials today* 27 (2019), pp. 107–122.

[28] S. N. Reed-Lingenfelter et al. “Surface Functionalization for Magnetic Property Tuning of Nonmagnetic 2D Materials”. In: *Advanced Materials Interfaces* 9.3 (2022), p. 2100463.

[29] J. Hong et al. “Atomic defects in two-dimensional materials: From single-atom spectroscopy to functionalities in opto-/electronics, nanomagnetism, and catalysis”. In: *Advanced Materials* 29.14 (2017), p. 1606434.

[30] M. Gobbi, E. Orgiu, and P. Samori. “When 2D materials meet molecules: opportunities and challenges of hybrid organic/inorganic van der Waals heterostructures”. In: *Advanced Materials* 30.18 (2018), p. 1706103.

[31] E. Coronado. “Molecular magnetism: from chemical design to spin control in molecules, materials and devices”. In: *Nature Reviews Materials* 5.2 (2020), pp. 87–104.

[32] M. Gibertini et al. “Magnetic 2D materials and heterostructures”. In: *Nature nanotechnology* 14.5 (2019), pp. 408–419.

[33] R. Sessoli. “Single-atom data storage”. In: *Nature* 543.7644 (2017), pp. 189–190.

[34] N. Ishikawa et al. “Lanthanide double-decker complexes functioning as magnets at the single-molecular level”. In: *Journal of the American Chemical Society* 125.29 (2003), pp. 8694–8695.

[35] L. Bogani and W. Wernsdorfer. “Molecular spintronics using single-molecule magnets”. In: *Nature materials* 7.3 (2008), pp. 179–186.

[36] J. D. Rinehart and J. R. Long. “Exploiting single-ion anisotropy in the design of f-element single-molecule magnets”. In: *Chemical Science* 2.11 (2011), pp. 2078–2085.

[37] S. T. Liddle and J. van Slageren. “Improving f-element single molecule magnets”. In: *Chemical Society Reviews* 44.19 (2015), pp. 6655–6669.

[38] F. Donati et al. “Magnetic remanence in single atoms”. In: *Science* 352.6283 (2016), pp. 318–321.

[39] F. D. Natterer et al. “Reading and writing single-atom magnets”. In: *Nature* 543.7644 (2017), pp. 226–228.

[40] J. Jensen and A. R. Mackintosh. *Rare earth magnetism*. Clarendon Press Oxford, 1991.

[41] S. Cotton. *Lanthanide and actinide chemistry*. John Wiley & Sons, 2013.

[42] H.G. Friedman Jr, G.R. Choppin, and D.G. Feuerbacher. “The shapes of the f orbitals”. In: *Journal of Chemical Education* 41.7 (1964), p. 354.

[43] J. Townsend, J. K. Kirkland, and K. D. Vogiatzis. “Chapter 3 - Post-Hartree-Fock methods: configuration interaction, many-body perturbation theory, coupled-cluster theory”. In: *Mathematical Physics in Theoretical Chemistry*. Ed. by S.M. Blinder and J.E. House. Developments in Physical & Theoretical Chemistry. Elsevier, 2019, pp. 63–117.

[44] B. Himmetoglu et al. “Hubbard-corrected DFT energy functionals: The LDA+ U description of correlated systems”. In: *International Journal of Quantum Chemistry* 114.1 (2014), pp. 14–49.

[45] A. Paul and T. Birol. “Applications of DFT+ DMFT in materials science”. In: *Annual Review of Materials Research* 49 (2019), pp. 31–52.

[46] T. Tsuneda and K. Hirao. “Self-interaction corrections in density functional theory”. In: *The Journal of chemical physics* 140.18 (2014), 18A513.

[47] F. Hund. “Zur deutung der molekelspektren. i”. In: *Zeitschrift für Physik* 40.10 (1927), pp. 742–764.

[48] F. Hund. “Zur deutung der molekelspektren. II”. In: *Zeitschrift für Physik* 42.2 (1927), pp. 93–120.

[49] N. Manini. *Introduction to the Physics of Matter: Basic Atomic, Molecular, and Solid-state Physics*. Springer Nature, 2020.

[50] R. A. Layfield and M. Murugesu. *Lanthanides and actinides in molecular magnetism*. John Wiley & Sons, 2015.

[51] A. K. Geim. "Graphene: status and prospects". In: *science* 324.5934 (2009), pp. 1530–1534.

[52] K. S. Novoselov et al. "A roadmap for graphene". In: *nature* 490.7419 (2012), pp. 192–200.

[53] M. Xu et al. "Graphene-like two-dimensional materials". In: *Chemical reviews* 113.5 (2013), pp. 3766–3798.

[54] S. Manzeli et al. "2D transition metal dichalcogenides". In: *Nature Reviews Materials* 2.8 (2017), pp. 1–15.

[55] W. Choi et al. "Recent development of two-dimensional transition metal dichalcogenides and their applications". In: *Materials Today* 20.3 (2017), pp. 116–130.

[56] L. D. Landau et al. *Electrodynamics of continuous media*. Vol. 8. elsevier, 2013.

[57] R. Skomski, P. Manchanda, and A. Kashyap. "Anisotropy and Crystal Field". In: *Handbook of Magnetism and Magnetic Materials* (2020), pp. 1–83.

[58] E. W. Lee. "Magnetostriction and magnetomechanical effects". In: *Reports on progress in physics* 18.1 (1955), p. 184.

[59] N. B. Ekreem et al. "An overview of magnetostriction, its use and methods to measure these properties". In: *Journal of Materials Processing Technology* 191.1-3 (2007), pp. 96–101.

[60] J. O'Donnell et al. "Magnetoelastic coupling and magnetic anisotropy in La 0.67 Ca 0.33 MnO 3 films". In: *Applied Physics Letters* 72.14 (1998), pp. 1775–1777.

[61] E. R. Callen and H. B. Callen. "Static Magnetoelastic Coupling in Cubic Crystals". In: *Phys. Rev.* 129 (2 Jan. 1963), pp. 578–593.

[62] V. A. Chernenko et al. "Giant magnetoelastic response in MnAs". In: *Journal of applied physics* 85.11 (1999), pp. 7833–7837.

[63] S. B. Roy. "First order magneto-structural phase transition and associated multi-functional properties in magnetic solids". In: *Journal of Physics: Condensed Matter* 25.18 (2013), p. 183201.

[64] T. Saerbeck et al. "Coupling of magnetism and structural phase transitions by interfacial strain". In: *Journal of Materials Research* 29.20 (2014), pp. 2353–2365.

[65] C. Kittel. "Physical Theory of Ferromagnetic Domains". In: *Rev. Mod. Phys.* 21 (4 Oct. 1949), pp. 541–583.

[66] A. Del Moral. "Magnetostriction and magnetoelasticity theory: A modern view". In: *Handbook of Magnetism and Advanced Magnetic Materials* (2007).

[67] M. T. Hutchings. "Point-charge calculations of energy levels of magnetic ions in crystalline electric fields". In: *Solid state physics*. Vol. 16. Elsevier, 1964, pp. 227–273.

[68] P. Fulde and M. Loewenhaupt. "Magnetic excitations in crystal-field split 4f systems". In: *Advances in Physics* 34.5 (1985), pp. 589–661.

[69] G. B. Arfken and H. J. Weber. *Mathematical methods for physicists*. 1999.

[70] K. W. H. Stevens. "Matrix elements and operator equivalents connected with the magnetic properties of rare earth ions". In: *Proceedings of the Physical Society. Section A* 65.3 (1952), p. 209.

[71] R. J. Radwański and J. J. M. Franse. "Magnetocrystalline anisotropy and crystal field in Ho2Co17". In: *Physica B: Condensed Matter* 154.2 (1989), pp. 181–188.

[72] R. Baltic et al. In: *Phys. Rev. B* 98 (2 2018), p. 024412.

[73] D. Gatteschi and R. Sessoli. "Quantum tunneling of magnetization and related phenomena in molecular materials". In: *Angewandte Chemie International Edition* 42.3 (2003), pp. 268–297.

[74] M. Tinkham. *Group theory and quantum mechanics*. Courier Corporation, 2003.

[75] R. Baltic. *Magnetic Stability of Single Lanthanide Atoms on Graphene*. Tech. rep. EPFL, 2018.

[76] T. Miyamachi et al. "Stabilizing the magnetic moment of single holmium atoms by symmetry". In: *Nature* 503.7475 (2013), pp. 242–246.

[77] C. Romeike et al. "Quantum-Tunneling-Induced Kondo Effect in Single Molecular Magnets". In: *Phys. Rev. Lett.* 96 (19 2006), p. 196601.

[78] A. B. Shick et al. "Magnetic anisotropy of a Dy atom on a graphene/Cu (111) surface". In: *Physical Review B* 102.6 (2020), p. 064402.

[79] C. E Patrick, G. A. Marchant, and J. B. Staunton. "Spin orientation and magnetostriction of Tb 1- x Dy x Fe 2 from first principles". In: *Physical Review Applied* 14.1 (2020), p. 014091.

[80] J. Sievers. "Asphericity of 4f-shells in their Hund's rule ground states". In: *Zeitschrift für Physik B Condensed Matter* 45.4 (1982), pp. 289–296.

[81] M. Yamada et al. "Crystal-field analysis of the magnetization process in a series of Nd 2 Fe 14 B-type compounds". In: *Physical Review B* 38.1 (1988), p. 620.

[82] C. E. Patrick and J. B. Staunton. "Crystal field coefficients for yttrium analogues of rare-earth/transition-metal magnets using density-functional theory in the projector-augmented wave formalism". In: *Journal of Physics: Condensed Matter* 31.30 (2019), p. 305901.

[83] D. J. Newman and B. Ng. "The superposition model of crystal fields". In: *Reports on Progress in Physics* 52.6 (1989), p. 699.

[84] P. Miró, M. Audiffred, and T. Heine. "An atlas of two-dimensional materials". In: *Chemical Society Reviews* 43.18 (2014), pp. 6537–6554.

[85] S. Das et al. "Synthesis, properties, and applications of 2-D materials: A comprehensive review". In: *Critical Reviews in Solid State and Materials Sciences* 39.4 (2014), pp. 231–252.

[86] A. J. Mannix et al. "Synthesis and chemistry of elemental 2D materials". In: *Nature Reviews Chemistry* 1.2 (2017), pp. 1–14.

[87] Y. Liu et al. "Van der Waals heterostructures and devices". In: *Nature Reviews Materials* 1.9 (2016), pp. 1–17.

[88] J. Sławińska and J. I. Cerdá. "Spin–orbit proximity effect in graphene on metallic substrates: decoration versus intercalation with metal adatoms". In: *New Journal of Physics* 21.7 (2019), p. 073018.

[89] S. P. Koenig et al. "Electron doping of ultrathin black phosphorus with Cu adatoms". In: *Nano Letters* 16.4 (2016), pp. 2145–2151.

[90] K.T. Chan, J. B. Neaton, and M. L. Cohen. "First-principles study of metal adatom adsorption on graphene". In: *Phys. Rev. B* 77 (23 June 2008), p. 235430.

[91] E. Simon et al. "Exchange interaction between magnetic adatoms on surfaces of noble metals". In: *Phys. Rev. B* 83 (22 June 2011), p. 224416.

[92] K. R. Sahoo et al. "Probing Proximity-Tailored High Spin–Orbit Coupling in 2D Materials". In: *Advanced Quantum Technologies* 3.9 (2020), p. 2000042.

[93] B. Fülöp et al. "Boosting proximity spin–orbit coupling in graphene/WSe2 heterostructures via hydrostatic pressure". In: *npj 2D Materials and Applications* 5.1 (2021), pp. 1–6.

[94] Z. Tu et al. "Spin–orbit coupling proximity effect in MoS2/Fe3GeTe2 heterostructures". In: *Applied Physics Letters* 120.4 (2022), p. 043102.

[95] C. Zhao et al. "Enhanced valley splitting in monolayer WSe2 due to magnetic exchange field". In: *Nature nanotechnology* 12.8 (2017), pp. 757–762.

[96] J. Hu et al. "Magnetic proximity effect at the interface of two-dimensional materials and magnetic oxide insulators". In: *Journal of Alloys and Compounds* (2022), p. 164830.

[97] X. Liang et al. "The magnetic proximity effect and electrical field tunable valley degeneracy in MoS 2/EuS van der Waals heterojunctions". In: *Nanoscale* 9.27 (2017), pp. 9502–9509.

[98] M. Bora and P. Deb. "Magnetic proximity effect in two-dimensional van der Waals heterostructure". In: *Journal of Physics: Materials* 4.3 (2021), p. 034014.

[99] B. Karpiak et al. "Magnetic proximity in a van der Waals heterostructure of magnetic insulator and graphene". In: *2D Materials* 7.1 (2019), p. 015026.

[100] S. H. Su et al. "Topological Proximity-Induced Dirac Fermion in Two-Dimensional Antimonene". In: *ACS nano* 15.9 (2021), pp. 15085–15095.

[101] T. Shoman et al. "Topological proximity effect in a topological insulator hybrid". In: *Nature communications* 6.1 (2015), pp. 1–6.

[102] C. X. Trang et al. "Conversion of a conventional superconductor into a topological superconductor by topological proximity effect". In: *Nature communications* 11.1 (2020), pp. 1–6.

[103] I. Žutić et al. "Proximitized materials". In: *Materials Today* 22 (2019), pp. 85–107.

[104] H.-W. Guo et al. "Stacking of 2D materials". In: *Advanced Functional Materials* 31.4 (2021), p. 2007810.

[105] K.S. Novoselov et al. "2D materials and van der Waals heterostructures". In: *Science* 353.6298 (2016), aac9439.

[106] E. C. Ahn. "2D materials for spintronic devices". In: *npj 2D Materials and Applications* 4.1 (2020), pp. 1–14.

[107] F. Donati and A. J. Heinrich. "A perspective on surface-adsorbed single atom magnets as atomic-scale magnetic memory". In: *Applied Physics Letters* 119.16 (2021), p. 160503.

[108] M. Grimm et al. "Universal Quantum Computing Using Electronuclear Wavefunctions of Rare-Earth Ions". In: *PRX Quantum* 2 (1 Jan. 2021), p. 010312.

[109] S. Bertaina et al. "Rare-earth solid-state qubits". In: *Nature nanotechnology* 2.1 (2007), pp. 39–42.

[110] M. Pivetta et al. "Measuring the Intra-Atomic Exchange Energy in Rare-Earth Adatoms". In: *Phys. Rev. X* 10 (3 Sept. 2020), p. 031054.

[111] C. Nistor et al. "Structure and magnetism of Tm atoms and monolayers on W(110)". In: *Phys. Rev. B* 90 (6 Aug. 2014), p. 064423.

[112] E. Fernandes et al. "Adsorption sites of individual metal atoms on ultrathin MgO(100) films". In: *Phys. Rev. B* 96 (4 July 2017), p. 045419.

[113] A. Singha et al. "$4f$ occupancy and magnetism of rare-earth atoms adsorbed on metal substrates". In: *Phys. Rev. B* 96 (22 Dec. 2017), p. 224418.

[114] A. B. Shick et al. "Magnetic character of holmium atom adsorbed on platinum surface". In: *Scientific reports* 7.1 (2017), pp. 1–6.

[115] A. Singha et al. "Mapping Orbital-Resolved Magnetism in Single Lanthanide Atoms". In: *ACS nano* 15.10 (2021), pp. 16162–16171.

[116] A. Singha et al. "Engineering atomic-scale magnetic fields by dysprosium single atom magnets". In: *Nature Communications* 12.1 (2021), pp. 1–6.

[117] A. B. Shick and A. Y. Denisov. "Magnetism of 4f-atoms adsorbed on metal and graphene substrates". In: *Journal of Magnetism and Magnetic Materials* 475 (2019), pp. 211–215.

[118] A. L. Kozub et al. “Electronic structure and magnetism of samarium and neodymium adatoms on free-standing graphene”. In: *Physical Review B* 94.12 (2016), p. 125113.

[119] F. Donati et al. “Magnetism of Ho and Er Atoms on Close-Packed Metal Surfaces”. In: *Phys. Rev. Lett.* 113 (23 Dec. 2014), p. 237201.

[120] F. Donati et al. “Correlation between electronic configuration and magnetic stability in dysprosium single atom magnets”. In: *Nano Letters* 21.19 (2021), pp. 8266–8273.

[121] T. Schuh et al. “Magnetic excitations of rare earth atoms and clusters on metallic surfaces”. In: *Nano letters* 12.9 (2012), pp. 4805–4809.

[122] R. Baltic et al. “Superlattice of single atom magnets on graphene”. In: *Nano letters* 16.12 (2016), pp. 7610–7615.

[123] V. Bellini et al. “Slow Magnetic Relaxation of Dy Adatoms with In-Plane Magnetic Anisotropy on a Two-Dimensional Electron Gas”. In: *ACS nano* 16.7 (2022), pp. 11182–11193.

[124] Z. Xu and M. J. Buehler. “Interface structure and mechanics between graphene and metal substrates: a first-principles study”. In: *Journal of Physics: Condensed Matter* 22.48 (2010), p. 485301.

[125] P. A. Khomyakov et al. “First-principles study of the interaction and charge transfer between graphene and metals”. In: *Phys. Rev. B* 79 (19 May 2009), p. 195425.

[126] J. Tao et al. “Modeling the physisorption of graphene on metals”. In: *Phys. Rev. B* 97 (16 Apr. 2018), p. 165403.

[127] J. Wintterlin and M.-L. Bocquet. “Graphene on metal surfaces”. In: *Surface Science* 603.10-12 (2009), pp. 1841–1852.

[128] R. Brako et al. “Graphene on the Ir (111) surface: from van der Waals to strong bonding”. In: *New Journal of Physics* 12.11 (2010), p. 113016.

[129] J. Kim and Z. Lee. In: *Applied Microscopy* 48 (June 2018), pp. 43–48.

[130] D. Voiry, A. Mohite, and M. Chhowalla. “Phase engineering of transition metal dichalcogenides”. In: *Chemical Society Reviews* 44.9 (2015), pp. 2702–2712.

[131] A. Kuc, N. Zibouche, and T. Heine. “Influence of quantum confinement on the electronic structure of the transition metal sulfide TS_2”. In: *Physical Review B* 83.24 (2011), p. 245213.

[132] J. A. Wilson and A. D. Yoffe. “The transition metal dichalcogenides discussion and interpretation of the observed optical, electrical and structural properties”. In: *Advances in Physics* 18.73 (1969), pp. 193–335.

[133] K. F. Mak et al. “Atomically thin MoS_2: a new direct-gap semiconductor”. In: *Physical review letters* 105.13 (2010), p. 136805.

[134] Y. Ding et al. "First principles study of structural, vibrational and electronic properties of graphene-like MX_2 (M= Mo, Nb, W, Ta; X= S, Se, Te) monolayers". In: *Physica B: Condensed Matter* 406.11 (2011), pp. 2254–2260.

[135] N. E. Staley et al. "Electric field effect on superconductivity in atomically thin flakes of $NbSe_2$". In: *Physical Review B* 80.18 (2009), p. 184505.

[136] C. Ataca, H. Sahin, and S. Ciraci. "Stable, single-layer MX_2 transition-metal oxides and dichalcogenides in a honeycomb-like structure". In: *The Journal of Physical Chemistry C* 116.16 (2012), pp. 8983–8999.

[137] Y. Li, K.-A. N. Duerloo, and E. J. Wauson K.and Reed. "Structural semiconductor-to-semimetal phase transition in two-dimensional materials induced by electrostatic gating". In: *Nature communications* 7.1 (2016), pp. 1–8.

[138] A. Ciarrocchi et al. "Thickness-modulated metal-to-semiconductor transformation in a transition metal dichalcogenide". In: *Nature communications* 9.1 (2018), pp. 1–6.

[139] D. Yan et al. "NbSeTe - a new layered transition metal dichalcogenide superconductor". In: *Journal of Physics: Condensed Matter* 32 (2020), p. 025702.

[140] Y. Liu et al. "Valleytronics in transition metal dichalcogenides materials". In: *Nano Research* 12.11 (2019), pp. 2695–2711.

[141] N. Zibouche et al. "Transition-metal dichalcogenides for spintronic applications". In: *Annalen der Physik* 526.9-10 (2014), pp. 395–401.

[142] D. Xiao et al. "Coupled spin and valley physics in monolayers of MoS 2 and other group-VI dichalcogenides". In: *Physical review letters* 108.19 (2012), p. 196802.

[143] N. Nagaosa et al. "Anomalous hall effect". In: *Reviews of modern physics* 82.2 (2010), p. 1539.

[144] M. Born and V. Fock. "Beweis des adiabatensatzes". In: *Zeitschrift für Physik* 51.3 (1928), pp. 165–180.

[145] B. R. Holstein. "The adiabatic theorem and Berry's phase". In: *American Journal of Physics* 57.12 (1989), pp. 1079–1084.

[146] D. Vanderbilt. *Berry phases in electronic structure theory: electric polarization, orbital magnetization and topological insulators*. Cambridge University Press, 2018.

[147] M. Gradhand et al. "First-principle calculations of the Berry curvature of Bloch states for charge and spin transport of electrons". In: *Journal of Physics: Condensed Matter* 24.21 (2012), p. 213202.

[148] R. Resta. *Lecture notes in Geometry and Topology in Electronic Structure Theory*. Feb. 2022.

[149] R. Kubo. "Statistical-mechanical theory of irreversible processes. I. General theory and simple applications to magnetic and conduction problems". In: *Journal of the Physical Society of Japan* 12.6 (1957), pp. 570–586.

[150] Y. Yao et al. "First principles calculation of anomalous Hall conductivity in ferromagnetic bcc Fe". In: *Physical review letters* 92.3 (2004), p. 037204.

[151] C. J. Cramer. *Essentials of computational chemistry: theories and models*. John Wiley & Sons, 2013.

[152] M. Born and W. Heisenberg. "Zur quantentheorie der molekeln". In: *Original Scientific Papers Wissenschaftliche Originalarbeiten*. Springer, 1985, pp. 216–246.

[153] J.-M. Combes, P. Duclos, and R. Seiler. "The born-oppenheimer approximation". In: *Rigorous atomic and molecular physics*. Springer, 1981, pp. 185–213.

[154] A. Szabo and N. S. Ostlund. *Modern quantum chemistry: introduction to advanced electronic structure theory*. Courier Corporation, 2012.

[155] P. Hohenberg and W. Kohn. "Inhomogeneous electron gas". In: *Physical review* 136.3B (1964), B864.

[156] W. Kohn and L. J. Sham. "Self-consistent equations including exchange and correlation effects". In: *Physical review* 140.4A (1965), A1133.

[157] P. W. Atkins and R. S. Friedman. *Molecular quantum mechanics*. Oxford university press, 2011.

[158] U. Von Barth and L. Hedin. "A local exchange-correlation potential for the spin polarized case. i". In: *Journal of Physics C: Solid State Physics* 5.13 (1972), p. 1629.

[159] M. M. Pant and A.K. Rajagopal. "Theory of inhomogeneous magnetic electron gas". In: *Solid State Communications* 10.12 (1972), pp. 1157–1160.

[160] G. Bihlmayer. "Density-functional Theory of Magnetism". In: *Handbook of magnetism and advanced magnetic materials* (2007).

[161] R. Zeller. "Spin-polarized dft calculations and magnetism". In: *Computational Nanoscience: Do It Yourself* 31 (2006), pp. 419–445.

[162] M. Cococcioni. "The LDA+ U approach: a simple Hubbard correction for correlated ground states". In: *Correlated Electrons: From Models to Materials Modeling and Simulation* 2 (2012).

[163] E. Pavarini et al. *The LDA+ DMFT approach to strongly correlated materials*. Tech. rep. Theoretische Nanoelektronik, 2011.

[164] V. I. Anisimov, F. Aryasetiawan, and A. I. Lichtenstein. "First-principles calculations of the electronic structure and spectra of strongly correlated systems: the LDA+ U method". In: *Journal of Physics: Condensed Matter* 9.4 (1997), p. 767.

[165] A. I. Liechtenstein, V. I Anisimov, and J. Zaanen. "Density-functional theory and strong interactions: Orbital ordering in Mott-Hubbard insulators". In: *Physical Review B* 52.8 (1995), R5467.

[166] B. Himmetoglu et al. "Hubbard-corrected DFT energy functionals: The LDA+ U description of correlated systems". In: *International Journal of Quantum Chemistry* 114.1 (2014), pp. 14–49.

[167] F. Aryasetiawan et al. "Calculations of Hubbard U from first-principles". In: *Physical Review B* 74.12 (2006), p. 125106.

[168] M. Tas et al. "Ab initio calculation of the Hubbard U and Hund exchange J in local moment magnets: The case of Mn-based full Heusler compounds". In: *Phys. Rev. Mater.* 6 (11 2022), p. 114401.

[169] F. Nilsson, R. Sakuma, and F. Aryasetiawan. "Ab initio calculations of the Hubbard U for the early lanthanides using the constrained random-phase approximation". In: *Phys. Rev. B* 88 (12 2013), p. 125123.

[170] M. Cococcioni and St. de Gironcoli. "Linear response approach to the calculation of the effective interaction parameters in the LDA + U method". In: *Phys. Rev. B* 71 (3 Jan. 2005), p. 035105.

[171] J. C. Slater. "Atomic shielding constants". In: *Physical Review* 36.1 (1930), p. 57.

[172] P. M. W. Gill. "Molecular integrals over Gaussian basis functions". In: *Advances in quantum chemistry*. Vol. 25. Elsevier, 1994, pp. 141–205.

[173] F. Jensen. "Atomic orbital basis sets". In: *Wiley Interdisciplinary Reviews: Computational Molecular Science* 3.3 (2013), pp. 273–295.

[174] G. Michalicek. "Extending the precision and efficiency of the all-electron full-potential linearized augmented plane-wave density-functional theory method". PhD thesis. Dissertation, Aachen, Techn. Hochsch., 2014, 2015.

[175] S. Blügel and G. Bihlmayer. "Full-potential linearized augmented planewave method". In: *Computational nanoscience: do it yourself* 31 (2006), pp. 85–129.

[176] D. J. Singh and L. Nordstrom. *Planewaves, Pseudopotentials, and the LAPW method*. Springer Science & Business Media, 2006.

[177] E. Sjöstedt. "Augmented Planewaves, Developments and Applications to Magnetism". PhD thesis. Acta Universitatis Upsaliensis, 2002.

[178] O. K. Andersen. "Linear methods in band theory". In: *Physical Review B* 12.8 (1975), p. 3060.

[179] E. Wimmer et al. "Full-potential self-consistent linearized-augmented-plane-wave method for calculating the electronic structure of molecules and surfaces: O 2 molecule". In: *Physical Review B* 24.2 (1981), p. 864.

[180] `www.flapw.de`.

[181] J. P. Carbone et al. “Magnetic properties of $4f$ adatoms on graphene: Density functional theory investigations”. In: *Phys. Rev. B* 108 (2023), p. 174431.

[182] D. F. Förster et al. “Phase coexistence of clusters and islands: europium on graphene”. In: *New Journal of Physics* 14.2 (2012), p. 023022.

[183] M. Jugovac et al. “Inducing Single Spin-polarized Flat Bands in Monolayer Graphene”. In: *Advanced Materials* (2023), p. 2301441.

[184] J. P. Perdew, K. Burke, and M. Ernzerhof. “Generalized gradient approximation made simple”. In: *Physical review letters* 77.18 (1996), p. 3865.

[185] I. L. M. Locht et al. “Standard model of the rare earths analyzed from the Hubbard I approximation”. In: *Physical Review B* 94.8 (2016), p. 085137.

[186] A. B. Shick, A. I. Liechtenstein, and W. E. Pickett. “Implementation of the LDA+ U method using the full-potential linearized augmented plane-wave basis”. In: *Physical Review B* 60.15 (1999), p. 10763.

[187] Ph. Kurz, G. Bihlmayer, and S. Blügel. “Magnetism and electronic structure of hcp Gd and the Gd (0001) surface”. In: *Journal of Physics: Condensed Matter* 14.25 (2002), p. 6353.

[188] D. Van der Marel and G. A. Sawatzky. “Electron-electron interaction and localization in d and f transition metals”. In: *Physical Review B* 37.18 (1988), p. 10674.

[189] C. Wang et al. “Direct observation of global elastic intervalley scattering induced by impurities on graphene”. In: *Nano Letters* 21.19 (2021), pp. 8258–8265.

[190] C. Wang et al. “Suppression of Intervalley Coupling in Graphene via Potassium Doping”. In: *The Journal of Physical Chemistry Letters* 13.40 (2022), pp. 9396–9403.

[191] J. Ding et al. “Engineering quantum anomalous/valley Hall states in graphene via metal-atom adsorption: An ab-initio study”. In: *Physical Review B* 84.19 (2011), p. 195444.

[192] Y. Ren et al. “Single-valley engineering in graphene superlattices”. In: *Physical Review B* 91.24 (2015), p. 245415.

[193] X. Liu et al. “Adsorption and growth morphology of rare-earth metals on graphene studied by ab initio calculations and scanning tunneling microscopy”. In: *Physical Review B* 82.24 (2010), p. 245408.

[194] X. Liu et al. “Metals on graphene: correlation between adatom adsorption behavior and growth morphology”. In: *Physical chemistry chemical physics* 14.25 (2012), pp. 9157–9166.

[195] S. Kraus et al. In: *Journal of the American Chemical Society* 144.24 (2022), pp. 11003–11009.

[196] F. Huttmann et al. In: *Physical review letters* 115.23 (2015), p. 236101.

[197] S. Schumacher et al. In: *Nano letters* 13.11 (2013), pp. 5013–5019.

[198] J. Cenker et al. "Reversible strain-induced magnetic phase transition in a van der Waals magnet". In: *Nature Nanotechnology* 17.3 (2022), pp. 256–261.

[199] D. C. Jiles and C. C. H. Lo. "The role of new materials in the development of magnetic sensors and actuators". In: *Sensors and Actuators A: Physical* 106.1-3 (2003), pp. 3–7.

[200] X. Hu et al. "Enhanced ferromagnetism and tunable magnetism in Fe3GeTe2 monolayer by strain engineering". In: *ACS applied materials & interfaces* 12.23 (2020), pp. 26367–26373.

[201] Ph. M. Morse. "Diatomic molecules according to the wave mechanics. II. Vibrational levels". In: *Physical review* 34.1 (1929), p. 57.

[202] V. I. Minkin. "Glossary of terms used in theoretical organic chemistry". In: *Pure and Applied Chemistry* 71.10 (1999), pp. 1919–1981.

[203] V. A. Basiuk, O. V. Prezhdo, and E. V. Basiuk. "Adsorption of Lanthanide Atoms on Graphene: Similar, Yet Different". In: *The Journal of Physical Chemistry Letters* 13.26 (2022), pp. 6042–6047.

[204] Qi. X. Zhou et al. "Electronic and magnetic properties of Rare-Earth atoms absorbed on graphene sheet: A theoretical study". In: *Key Engineering Materials*. Vol. 645. Trans Tech Publ. 2015, pp. 40–44.

[205] J. Coraux et al. "Structure of epitaxial graphene on Ir (111)". In: *New Journal of Physics* 10.4 (2008), p. 043033.

[206] L. Meng et al. "Multi-oriented moiré superstructures of graphene on Ir (111): experimental observations and theoretical models". In: *Journal of Physics: Condensed Matter* 24.31 (2012), p. 314214.

[207] C. Busse et al. "Graphene on Ir(111): Physisorption with Chemical Modulation". In: *Phys. Rev. Lett.* 107 (3 July 2011), p. 036101.

[208] I. Pletikosić et al. "Dirac cones and minigaps for graphene on Ir (111)". In: *Physical review letters* 102.5 (2009), p. 056808.

[209] D. Marchenko et al. "Giant Rashba splitting in graphene due to hybridization with gold". In: *Nature communications* 3.1 (2012), p. 1232.

[210] J. C. W. Swart et al. "Interaction of graphene with FCC–Co (111)". In: *Physical Chemistry Chemical Physics* 11.5 (2009), pp. 803–807.

[211] J. P. Carbone et al. "Engineering spin-orbit effects and Berry curvature by deposition of a monolayer of Eu on WSe 2". In: *Physical Review B* 106.6 (2022), p. 064401.

[212] F. Freimuth et al. "Maximally localized Wannier functions within the FLAPW formalism". In: *Physical Review B* 78.3 (2008), p. 035120.

[213] A. A. Mostofi et al. “An updated version of wannier90: A tool for obtaining maximally-localised Wannier functions”. In: *Computer Physics Communications* 185.8 (2014), pp. 2309–2310.

[214] K. Okamoto. “A new method for analysis of magnetic anisotropy in films using the spontaneous Hall effect”. In: *Journal of magnetism and magnetic materials* 35.1-3 (1983), pp. 353–355.

[215] S. de Haan, C. Lodder, and T. J. A. Popma. “The (anomalous) hall magnetometer as an analysis tool for high density recording media”. In: *Journal of the Magnetics Society of Japan* 15.Suppl. 2 (1991), pp. 349–354.

[216] D. Wortmann et al. “Resolving complex atomic-scale spin structures by spin-polarized scanning tunneling microscopy”. In: *Physical review letters* 86.18 (2001), p. 4132.

[217] Ph. Kurz. *Non-collinear magnetism at surfaces and in ultrathin films*. Tech. rep. Elektronische Eigenschaften, 2001.

[218] L. M. Sandratskii. “Energy band structure calculations for crystals with spiral magnetic structure”. In: *physica status solidi (b)* 136.1 (1986), pp. 167–180.

[219] Ph. Kurz et al. “Ab initio treatment of noncollinear magnets with the full-potential linearized augmented plane wave method”. In: *Physical Review B* 69.2 (2004), p. 024415.

[220] S. Bhowal and S. Satpathy. “Intrinsic orbital moment and prediction of a large orbital Hall effect in two-dimensional transition metal dichalcogenides”. In: *Physical Review B* 101.12 (2020), p. 121112.

[221] S. Bhowal and G. Vignale. “Orbital Hall effect as an alternative to valley Hall effect in gapped graphene”. In: *Physical Review B* 103.19 (2021), p. 195309.

[222] T. P. Cysne et al. “Disentangling orbital and valley Hall effects in bilayers of transition metal dichalcogenides”. In: *Physical review letters* 126.5 (2021), p. 056601.

[223] Y. A Bychkov and É. I. Rashba. “Properties of a 2D electron gas with lifted spectral degeneracy”. In: *JETP lett* 39.2 (1984), p. 78.

[224] A. Manchon et al. “New perspectives for Rashba spin–orbit coupling”. In: *Nature Materials* 14.9 (Sept. 2015), pp. 871–882.

[225] S. R. Park et al. “Orbital-angular-momentum based origin of Rashba-type surface band splitting”. In: *Phys. Rev. Lett.* 107 (15 2011), p. 156803.

[226] J. H. Park et al. “Orbital chirality and Rashba interaction in magnetic bands”. In: *Phys. Rev. B* 87 (4 2013), 041301(R).

[227] D. Go et al. “Toward surface orbitronics: giant orbital magnetism from the orbital Rashba effect at the surface of sp-metals”. In: *Scientific Reports* 7.1 (2017), p. 46742.

[228] V. Sunko et al. "Maximal Rashba-like spin splitting via kinetic-energy-coupled inversion-symmetry breaking". In: *Nature* 549.7673 (2017), pp. 492–496.

[229] D. Go et al. "Intrinsic spin and orbital Hall effects from orbital texture". In: *Physical Review Letters* 121.8 (2018), p. 086602.

[230] D. Go et al. "Orbital Rashba effect in a surface-oxidized Cu film". In: *Phys. Rev. B* 103 (12 2021), p. L121113.

[231] X. Xu et al. "Spin and pseudospins in layered transition metal dichalcogenides". In: *Nature Physics* 10.5 (2014), pp. 343–350.

[232] M. S Dresselhaus, G. Dresselhaus, and A. Jorio. *Group theory: application to the physics of condensed matter*. Springer Science & Business Media, 2007.

List of Publications

Published

1. *An analysis of the performance of coupled cluster methods for K-edge core excitations and ionizations using standard basis sets*,
   J. P. Carbone, L. Cheng, R. H. Myhre, D. Matthews, H. Koch, and S. Coriani,
   Advances in Quantum Chemistry, Vol. 79. Elsevier, (2019), pp. 241–261

2. *Engineering spin-orbit effects and Berry curvature by deposition of a monolayer of Eu on WSe_2*,
   J. P. Carbone, D. Go, Y. Mokrousov, G. Bihlmayer, and S. Blügel,
   Physical Review B 106.6 (2022), p. 064401

3. *Spin and orbital transport in rare-earth dichalcogenides: The case of EuS_2*,
   M. Zeer, D. Go, **J. P. Carbone**, T. G. Saunderson, M. Redies, M. Kläui, J. Ghabboun, W. Wulfhekel, S. Blügel, and Y. Mokrousov,
   Physical Review Materials 6.7 (2022), p. 074004

4. *Magnetic properties of $4f$ adatoms on graphene: Density functional theory investigations*,
   J. P. Carbone, J. Bouaziz, G. Bihlmayer, and S. Blügel,
   Physical Review B 108.17 (2023), p. 174431

In preparation

5. *Effect of metallic substrates on the magnetic properties of graphene-adsorbed Gd atoms*,
   J. P. Carbone, N. Atodiresei, G. Bihlmayer, and S. Blügel

6. *Coverage dependence of the magnetocrystalline anisotropy of $4f$-atoms on a transition-metal dichalcogenide monolayer*,
   J. P. Carbone, G. Bihlmayer, and S. Blügel

List of Figures

List of Tables

Acknowledgements

The project has been funded by the Deutsche Forschungsgemeinschaft (DFG) through CRC 1238, Control and Dynamics of Quantum Materials: Spin orbit coupling, correlations, and topology (Project No. 277146847 C01). Acknowledgements go to computing resources granted by RWTH Aachen University under Project No. jara0219.

The artwork for the cover of this thesis has been designed by Daniele Valente.

The years spent pursuing my PhD have been intense and challenging, and I've come to realize that while I've always aspired to a career in research and being part of the scientific community, the support of those around me has been, and will always be, fundamental to achieving my life goals. Therefore, I would like to express my acknowledgements to all the individuals who have been by my side during this life-changing experience.

I am immensely grateful to Prof. Dr. Stefan Blügel for providing me with the opportunity to work in an exceptional environment and for being a caring and understanding supervisor who constantly inspires me to do my best and shares valuable ideas and possibilities. I also want to thank him for allowing me to continue my family tradition and create new memories in a place that holds cherished childhood memories.

My sincere thanks also goes to Dr. Gustav Bihlmayer for his meticulous guidance throughout these years and for always being available whenever I needed assistance. I have learned from him not only physics, but also the importance of patience and calm in achieving sound scientific results and maintaining the right mindset to tackle any questions or problems that may arise in our work.

I am grateful to Dr. Juba Bouaziz for the fruitful discussions and support, and to Henning Janssen for sharing this experience (and the office) with me from day one.

I express my thanks to Dr. Nicolae Atodiresei for his availability and enthusiastic discussions with me. Our meetings always left me brimming with new ideas.

I would like to extend my appreciation to all the members of PGI-1/IAS-1 with whom I have shared my days. A special mention goes to the *Quantum Lounge* people who accepted me despite coming from the main building. Thank you for the incredibly long and nonsensical discussions after lunch, and for always appreciating my italian coffee - I will miss those moments. I specifically want to thank Daniela for being my pillar at the institute and a supportive friend.

I would like to give special recognition to Dr. Dongwook Go, who, apart from being

one of my closest friends, has been an important figure in supporting me throughout my journey. As I started my doctoral studies, the pandemic also began, presenting numerous challenges for a new PhD student. Despite the limitations of not being able to access the office, Dongwook has been a constant source of support. Through online meetings and chats, he has provided guidance in completing my initial projects and has helped uplift my spirits.

I also want to express my gratitude to Dr. Gregor Michalicek for continuously checking if I am happy since my master's thesis. Thank you for always being available to listen and help resolve any FLEUR problems.

Outside of Forschungszentrum Jülich, I would like to thank the individuals who have broadened my perspective of the research field and provided me with new experiences to keep my mind open:

First and foremost, I want to thank Prof. Dr. Pietro Gambardella and Prof. Dr. Nicola Spaldin for hosting me in their research groups at ETH Zürich. This was my first scientific exchange experience after the pandemic and marked the beginning of my research activities from a broader perspective. The opportunity to visit labs, see science beyond my computer screen, and engage in discussions with numerous researchers had a profound impact on shaping me as a scientist.

I am grateful to the CRC collaboration for organizing enjoyable and intellectually stimulating scientific retreats. These retreats provided me with the opportunity to meet fellow young researchers, exchange experiences and ideas, and gain insights into various theoretical and experimental aspects of condensed matter physics.

I would like to thank Dr. Stefano Rusponi of EPFL Lausanne for generously sharing his time and expertise in discussing rare-earth atoms on surfaces and shedding light on experimental possibilities in the field.

I would like to express my gratitude to the group of Prof. Dr. Thomas Michely at Universität zu Köln for their insightful discussions during the CRC retreats.

I also express my gratitude to Prof. Dr. Morgenstern of RWTH Aachen for agreeing to be my second referee.

Lastly, I want to thank Prof. Dr. Cesare Franchini at the University of Vienna and Prof. Dr. Andreas Grüneis at Technische Universität Wien for hosting me and providing me with the opportunity to share my work with their research groups. The enriching discussions we had and the exposure to fascinating phenomena and methods beyond my project were invaluable to my growth as a researcher.

I would like to take a moment to express my heartfelt appreciation to my friends. These remarkable individuals have been by my side through thick and thin, always unwavering in their support, regardless of the circumstances or distance between us. Anoop, Sara, Stefano, Chiara, Emanuele, Nicoletta, Matteo, Giovanni, Sabastian and David - your presence in my life has been a precious gift, filling it with moments of joy and growth. I am truly grateful for the years and accomplishments we have experienced together. *Thank you.*

I extend my heartfelt gratitude to Eduardo, whom I affectionately call Edu, despite his esteemed title as Prof. Dr. Eduardo Mendive Tapia. Edu's brilliance as a scientist and teacher is matched only by his steadfast and caring friendship, for which I am immensely grateful. Your constant support and enduring presence, even during the most challenging times, are invaluable to me, and I wholeheartedly appreciate your boundless generosity. In simple words, thank you for everything.

Thanks go out to my friends in the *Flamingo* community. I believe we are a demonstration to the fact that friendship transcends distances and strengthens over time. I sincerely appreciate your support throughout all these years and cherish the memories of all our incredible adventures together.

I am filled with profound gratitude for Riccardo, whose immense and genuine support has meant the world to me. The precious moments and experiences we have shared throughout the years hold a special place in my heart. Thank you for always bringing light into situations where I may not see it, and for your constant presence in my life.

Finally, I want to express my heartfelt gratitude to my family on both sides of the Alps. I am also grateful for my cousin Sophie, who has shared numerous Aachener adventures with me.

My utmost gratitude goes to the two most influential and inspiring scientists in my life, my mother and father. Thank you for your limitless support and encouragement: your understanding and belief in me have been a guiding light throughout my doctoral journey, and for that, I am truly grateful. It is incredibly rare to say that my parents not only understand, but probably even better than me, my doctoral thesis. Thank you for sharing in both my academic and personal journey.

Last but not least, I wish to express my deepest appreciation to someone whom I believe I've never truly thanked enough - my brother, Giulio. I may not excel in demonstrating my gratitude mostly, so I find it fitting to take a few extra words for you. Thank you for always being a source of calm, peace, and rationality in the face of difficulties and the challenges of life. The immeasurable joy I experience when we meet and the healing effect of our time together are truly invaluable. I genuinely thank you for your ongoing support and understanding, providing a comforting presence whenever I need it. Here's to us—cheers!

The best advice I've ever received is, "No one else knows what they're doing either".

Ricky Gervais

Band / Volume 269
The complex inositol metabolism of *Corynebacterium glutamicum* and its application for the production of rare inositols
P. Ramp (2023), VI, 161 pp
ISBN: 978-3-95806-699-1

Band / Volume 270
Spin- and orbital-dependent band structure of unconventional topological semimetals
K. Hagiwara (2023), v, 115 pp
ISBN: 978-3-95806-701-1

Band / Volume 271
Neutron scattering
Experimental Manuals of the JCNS Laboratory Course held at Forschungszentrum Jülich and at the Heinz-Maier-Leibnitz Zentrum Garching edited by T. Brückel, S. Förster, K. Friese, M. Kruteva, M. Zobel and R. Zorn (2023), ca 150 pp
ISBN: 978-3-95806-705-9

Band / Volume 272
Ab-initio investigation of the interplay between the hyperfine interaction and complex magnetism at the nanoscale
S. R. S. Shehada (2023), ix, xi, 119 pp
ISBN: 978-3-95806-718-9

Band / Volume 273
Analysis of the signal transduction cascade tuning the 2-oxoglutarate dehydrogenase activity in *Corynebacterium glutamicum*
L. Sundermeyer (2023), VI, 119 pp
ISBN: 978-3-95806-722-6

Band / Volume 274
Multicellular defense against phage infection in *Streptomyces* – impact of secondary metabolites and mycelial development
L. Kever (2023), iv, 246 pp
ISBN: 978-3-95806-724-0

Band / Volume 275
Investigation of the electronic band structure of 2D transition metal dichalcogenides via angle-resolved photoemission spectroscopy
B. Parashar (2023), xvii, 156 pp
ISBN: 978-3-95806-725-7

Schriften des Forschungszentrums Jülich
Reihe Schlüsseltechnologien / Key Technologies

Band / Volume 276
Strain- and process engineering for polyketides production with *Pseudomonas taiwanensis* VLB120 in two-phase cultivations
T. P. Schwanemann (2023), 230 pp
ISBN: 978-3-95806-726-4

Band / Volume 277
Quantitative atomic-level investigation of solid materials through multidimensional electron diffraction measurements
H. L. Lalandec-Robert (2024), xxi, 152 pp
ISBN: 978-3-95806-735-6

Band / Volume 278
Studies on the cAMP-responsive regulatory network of *Corynebacterium glutamicum*
N. Wolf (2024), iii, 122 pp
ISBN: 978-3-95806-736-3

Band / Volume 279
Rare-earth atoms on two-dimensional materials: *ab initio* investigation of magnetic properties
J. P. Carbone (2024), 235 pp
ISBN: 978-3-95806-740-0

Weitere ***Schriften des Verlags im Forschungszentrum Jülich*** unter
http://wwwzb1.fz-juelich.de/verlagextern1/index.asp

Schlüsseltechnologien / Key Technologies
Band / Volume 279
ISBN 978-3-95806-740-0

Mitglied der Helmholtz-Gemeinschaft

JÜLICH
Forschungszentrum